Nanoparticle doping in nematic liquid crystals

Von der Fakultät für Naturwissenschaften

der Universität Paderborn

genehmigte

Dissertation

zur Erlangung des akademischen Grades

Doktor der Naturwissenschaften

- Dr. rer. Nat. -

von

Martin Urbanski, M. Sc.

aus Paderborn

Januar 2013

Die vorliegende Dissertation entstand im Zeitraum von Oktober 2009 bis Januar 2013 im Fachbereich für Physikalische Chemie (Arbeitskreis Prof. Kitzerow) an der Fakultät für Naturwissenschaften der Universität Paderborn.

1. Gutachter: Prof. Dr. Heinz-Siegfried Kitzerow
2. Gutachter: Prof. Dr. Torsten Hegmann

Die Arbeit wurde eingereicht am: 16.01.2013
Tag der mündlichen Prüfung: 19.02.2013

Danksagung

An dieser Stelle möchte ich mich bei den Menschen bedanken, die auf unterschiedliche Art und Weise zum Gelingen dieser vorliegenden Dissertation beigetragen haben.

Herrn Prof. Dr. Heinz-Siegfried Kitzerow danke ich für die interessante Themenstellung und die Betreuung während meiner Zeit als Doktorand in seinem Arbeitskreis. Durch seine steten Ermunterungen, Ergebnisse kritisch zu hinterfragen und Hypothesen mit vielfältigen weiteren Experimenten zu bestätigen oder zu widerlegen, hat er nicht unerheblich zu den in dieser Arbeit beschriebenen neuen Erkenntnissen beigetragen.

Herrn Prof. Dr. Torsten Hegmann vom Liquid Crystals Institute der Kent State University (Kent, USA) gilt mein besonderer Dank zum einen für die fruchtbare Kooperation, die durch regen Ideenaustausch gekennzeichnet war und mir so immer neue Impulse für meine Arbeit gegeben hat. Insbesondere möchte ich mich an dieser Stelle bei seinen Mitarbeitern Brandy Kinkead und Javad Mirzaei bedanken, von denen ich viel über die Präparation von Flüssigkristalldispersionen lernen durfte und die mir eine Vielzahl an Proben zur weiteren Untersuchung zur Verfügung gestellt haben. Außerdem bedanke ich mich bei Prof. Hegmann für die Übernahme des Korreferates sowie die Bereitschaft, zu meiner Verteidigung die lange Anreise aus den Vereinigten Staaten auf sich zu nehmen.

Bei meinen Kolleginnen und Kollegen in der Physikalischen Chemie möchte ich mich ausdrücklich für die freundliche Atmosphäre und das angenehme Arbeitsklima bedanken. Die vielfältigen Diskussionen und Hilfestellungen im Labor sowie abwechslungsreiche Aktivitäten außerhalb werden mir sicher in guter Erinnerung bleiben.

Abschließend möchte ich mich auch bei meiner Familie und meinen Freunden bedanken, die mich während meines Studiums und der anschließenden Promotionszeit vielfältig unterstützt haben. Insbesondere Anna danke ich für die Unterstützung und Rücksichtnahme in den arbeitsreichen Monaten vor Abschluss der Promotion.

Contents

1 Introduction

Liquid crystals are a vivid example of the late success of a scientific discovery. Already in 1888, Friedrich Reinitzer [1] and Otto Lehmann [2] (excerpted from [3]) discovered this special state of matter appearing between the crystalline and the liquid phase, but not before the 1960s an interest in these materials for technological applications started. After cathode ray tubes had been already well established for display applications, research focused on new display technologies for smaller displays and perceived liquid crystals as versatile materials because of their special optical and dielectric properties. The first commercially successful liquid crystal display technology was patented by Helfrich and Schadt [4] in 1970 and utilized the field-induced reorientation of nematic liquid crystals between crossed polarizers as a switchable light shutter. Until nowadays, nematic liquid crystals still are one of the most frequently used materials in liquid crystal display technology.

During the last decades, manifold research has been carried out to overcome drawbacks of the first generations of LC-displays like small viewing angle or slow switching times. Improvements took place by the invention of new switching modes, new electronic technologies (e.g. thin film transistors) for addressing single pixels but also by tuning the physical properties of the liquid crystalline materials itself. Desired properties are low switching voltages for high energy efficiency and fast response times, which may be achieved by tuning the dielectric, elastic and viscous properties of the liquid crystalline material.

A relatively young research field of increasing interest to provide materials with unique physical properties is the doping of liquid crystals with nanoparticles. It is known that ferroelectric nanoparticles can enhance the dielectric anisotropy [5] and the orientational order [6] of nematic liquid crystals. Dispersions of ultra-small magnetic needles [7] or platelets [8] result in ferronematics, which can be reoriented by weak magnetic fields and allow thresholdless optical switching in electric fields [9]. Carbon nanotubes are found to be very well compatible with nematic hosts because of their anisometric shape [10]. Although the presence of carbon nanotubes strongly influences on the nematic properties of the host, a decreased light transmittance and increased switching voltages prohibit their use in display technology [11].

The examples mentioned so far utilize nanoparticles with additional special physical properties like ferroelectricity, magnetism or anisotropic shapes. For this reason it is difficult to distinguish between nanoparticle-induced effects due to these properties, or effects that are caused by the simple presence of nanoparticles in the nematic host. The influence of the latter effect on the liquid crystal can be revealed by investigating dispersions of spherical particles with no additional physical properties.

Recently, Hegmann and co-workers reported that doping a nematic liquid crystal with spherical nanoparticles with diameters smaller than 5 nm made of gold or semiconductors can significantly change the electro-optical properties of the host [12], [13]. While gold

nanoparticles also offer the possibility of obtaining metamaterials [14] and are therefore not only of interest for display applications, the luminescence of semiconducting quantum dots can be used as an analytical tracer to study the distribution of nanoparticles in a nematic dispersion [13].

Nanoparticles in this size regime are not particularly stable because of their high surface to volume ratio and tend to agglomerate. Therefore an organic ligand shell is necessary, which deactivates the surface and sterically prevents agglomeration. It is known that this organic coating plays a key role in the interaction of dopant and nematic host. Consequently, the coating has not only an important impact on the stability of dispersed particles within a nematic host, but also on the electro-optical behavior of the liquid crystalline material. Another key factor for the interaction between nanoparticles and host molecules is the diameter of the particle core. As recently reported by Kinkead et al. for CdSe nanoparticles of different core sizes, there seems to be a very specific relationship between particle size and changes in alignment and electro-optical properties [13]. However, a deep understanding of the impact of size on the interaction between nanoparticles and host is still missing. A third effect influencing the stability of nanoparticle dispersions is the nature of nematic liquid crystals themselves. Being an ordered liquid of rod-like molecules, the nematic liquid crystal shows a tendency to expel spherical dopants of certain size which disturb the nematic order, and therefore supports the agglomeration of particles [15].

The precise mechanisms of interplay between the properties of functionalized nanoparticles and the nematic host that lead to stable dispersions are not fully understood yet. For this reason, actual research needs to address compatibility and miscibility of the nanoscale materials in nematic liquid crystals prior to integration in electro-optic applications.

This work is intended to investigate the influence of particle size, core material and organic ligand shell of functionalized spherical nanoparticles in a size regime $d < 5\,\mathrm{nm}$ on the miscibility and stability of nanoparticle / liquid crystal dispersions. The goal is to identify important physical properties of functionalized particles and host molecules to give well dispersed systems, and pave the way for stable dispersions with improved electro-optical performance for display applications.

For this purpose, dispersions of differently functionalized gold and CdSe nanoparticles are prepared in two nematic hosts with different polarity, and investigated by optical microscopy and dielectric analysis. In particular, the influence of nanoparticles on the alignment of the liquid crystal at confining substrates as well as characteristic physical properties of a nematic liquid crystal like threshold voltage, dielectric properties and switching times are studied. By comparing effects on these quantities caused by different ligand shell functionalizations, core diameters or core materials, conclusions about the molecular interactions between nanoparticles and host molecules are drawn.

2 Background

2.1 Liquid crystals - The fourth state of matter

Depending on the thermodynamic conditions, atoms and molecules can arrange to different states of matter which are characterized by different degrees of orientational and positional order. The three classic states of matter are the crystal state, the liquid state and the gas state. The crystalline phase is the highest ordered state and shows a long-range positional order of its building blocks as well as a long-range orientational order for anisometrically shaped constituents. Each building block oscillates around a certain point in a three dimensional periodic lattice, which defines the crystal structure. Hence, the symmetry of the repetition unit corresponds to the symmetry of the whole crystal. Increasing the energy within the system leads to a melting of the crystal and the formation of a liquid phase. The liquid state is characterized by a complete absence of long-range order, and thereby appears fluid. Yet, depending on the constituents, attractive interactions between building blocks can lead to the formation of short-range order. The gas state is the classical high energy state of matter and characterized by a total absence of long-range or short-range order. The building blocks have a high translational energy and move randomly and with arbitrary orientation through a given volume, with a high rate of collisions with other building blocks.

The liquid crystal state is often referred as the fourth state of matter and features a long-range orientational order and a reduced or even absent positional order of molecules compared to a crystal phase. Thus, the liquid crystal state is classified to lay between the crystal state and the liquid state. Within the liquid crystal state, a general distinction is made between thermotropic, barotropic and lyotropic liquid crystals. The latter materials form liquid crystal phases as a result of their concentration within a solvent, while for barotropic materials the mesogenic phase is induced depending on the pressure. In ther-

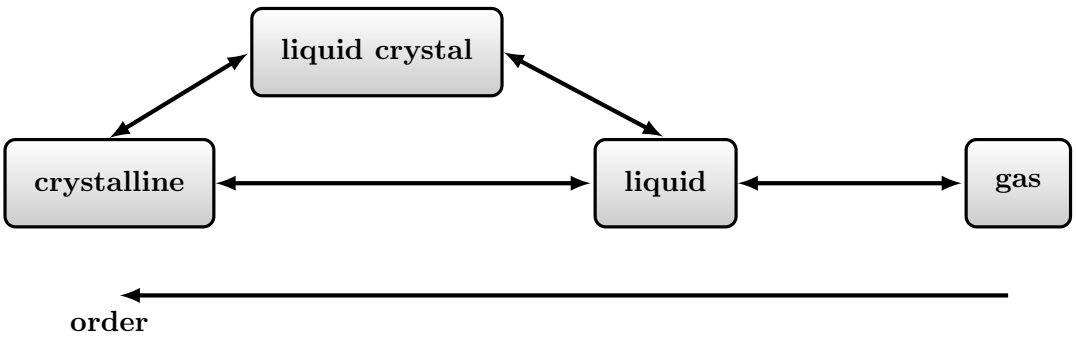

Figure 2.1: Liquid crystals as the fourth state of matter are located between the highly ordered crystalline phase and the isotropic liquid phase.

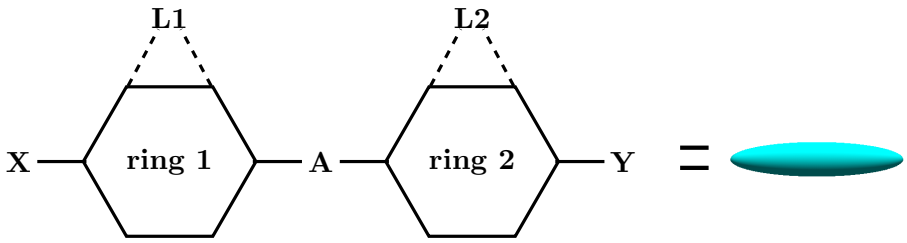

Figure 2.2: Schematic drawing of the general molecular structure of a rod-like liquid crystal molecule. In this work, the rod-like structure of a single molecule is depicted as elongated ellipsoid.

motropic liquid crystals, mesophases occur at different temperatures, the appearance of differently ordered states is a function of temperature. As in this work only thermotropic liquid crystals are used, a more detailed overview over these materials is given below.
Essential for all thermotropic liquid crystals is an anisometric molecule shape, which allows the formation of orientationally ordered phases. In general, one can observe calamitic (rod-like), discotic (disc-like), sanidic (board-like) and bent-core (banana-shaped) molecules to form thermotropic phases. As in this work only calamitic liquid crystals are used, discotic, sanidic and bent-core materials will not be discussed.

Calamitic molecules exhibit one long dimension and two short dimensions. In addition, their molecule structure shows a sophisticated interplay between rigidity and flexibility which allows the formation of mesophases. The rigidity maintains the rod-like structure of the molecules and thereby allows the formation of orientationally ordered mesophases by strong intermolecular interactions. However, a too high rigidity of molecules would energetically favor the formation of a crystalline phase. Hence, the simultaneous presence of flexible side chains supports the formation of fluid mesophases.

As a consequence of these requirements, calamitic liquid crystals often consist of molecules with a rigid core of two or more ring systems, and one or two flexible side chains **X** and **Y** (see figure 2.2). The core is often built by phenyl- or cyclohexane-rings, but also heterocycles as pyrimidine can serve as stabilizing core units. A linking group **A** can influence the electronic structure of the core system. The side chains are usually given by alkyl- or alkoxy chains of different length. By introducing functional groups to the side chains or the core, the physical properties of the molecules can be tuned. While for example a cyano-group replacing one side chain increases the polarizability α along the long axis of the molecules and therefore can lead to a high positive dielectric anisotropy of the material, fluorine groups in lateral ring positions can lead to negative dielectric anisotropies.

Rod-like molecules are found to form several mesophases with different degrees of positional and orientational order. Some common liquid crystalline mesophases for calamitic molecules are shown in figure 2.3. While smectic phases exhibit a layer structure with no translational freedom between the layers, the nematic phase is characterized by three-dimensional translational freedom. Both nematic and smectic phases show a long-range orientational order. As in this work only nematic liquid crystals are investigated, the following sections aim to give a short overview about the special properties of this phase.

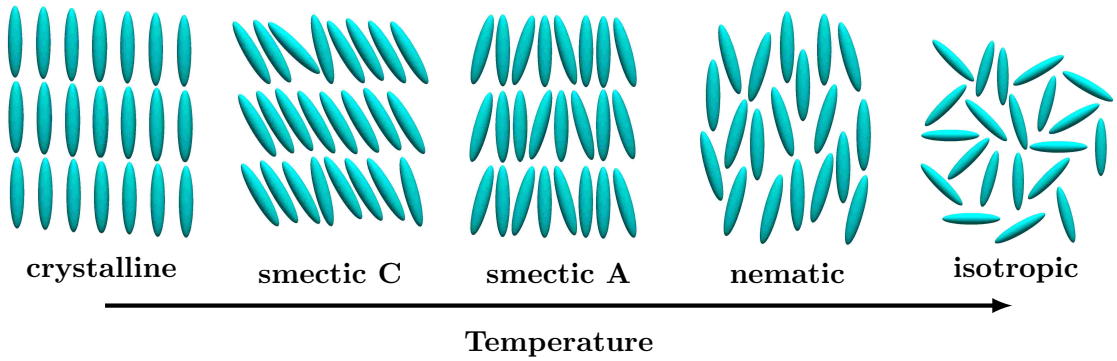

Figure 2.3: Schematic drawing of different liquid crystalline phases of a calamitic thermotropic liquid crystal.

2.2 The nematic phase

The nematic phase is the least ordered liquid crystalline phase and features a long-range orientational order only. This order is relatively weak, so the nematic phase is quite similar to the isotropic liquid phase with a small additional amount of order. For example, the latent heat for the phase transition of cholesteryl benzoate from crystalline to nematic is 272 J/g, but the latent heat for the transition from the nematic to the isotropic phase is only 29 J/g [16]. This shows that only comparable little energy is needed to overcome the nematic order, and stresses the similarity of the nematic phase with an isotropic fluid. The molecules in the nematic phase can freely rotate about all their axes. However, the relaxation times for the rotation about the short axes of the molecules is several magnitudes faster than for the rotation about the long axes ($10^{-11}\,\mathrm{s}^{-1}$ vs. $10^{-6}\,\mathrm{s}^{-1}$). As a result, all molecules in the nematic phase point on average in the same direction. This orientational order in the nematic phase can be characterized by a pseudo-vector **n**, which is called the director and depicts the local preferable direction of molecules.
The degree of orientational order in the nematic phase can be expressed by a scalar order parameter S, which is given by equation 2.1

$$S = \frac{1}{2}\left\langle 3\cos^2(\theta) - 1\right\rangle . \tag{2.1}$$

The angle θ is thereby given by the angle between the director **n** denoted for a given volume V and the long axis of the molecules within this volume. In the nematic phase the directions **n** and **-n** are physically equivalent, so the average over all angles θ vanishes. Equation 2.1 represents the quadrupole average, which is the lowest multipole giving a non-trivial solution [17].
The nematic order parameter S is a function of temperature, with increasing temperature the degree of orientational order decreases. In the approach by Maier and Saupe to describe $S(T)$, the average potential of every single molecule in a given volume with respect to the position and orientation of all other molecules is considered [18]. The Van-der-Waals-interactions between the molecules are replaced by a mean internal field, in which every

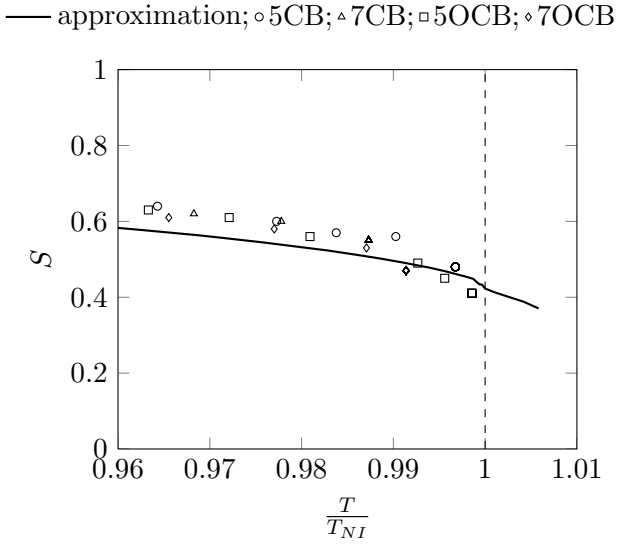

Figure 2.4: Temperature dependency of the order parameter S as calculated from equation 2.4. Experimental data are taken from reference [19].

molecule has a potential energy E_{pot} (equation 2.2) depending on its orientation in the field.

$$E_{pot}\left(S,\theta_i\right) = -\frac{1}{2}\cdot B\cdot S\left(3\cos^2\theta_i - 1\right) \tag{2.2}$$

The constant B in equation 2.2 is a factor depending on the molar volume of the molecules and S refers to the nematic order in the vicinity of the single molecule i. By applying Boltzmann statistics, the temperature dependency of the angular distribution can be estimated and the function $S\left(T\right)$ is given by

$$S\left(T\right) = \frac{3}{2}\cdot\frac{\int_0^{\pi/2} exp\left(-E_{pot}/k_BT\right)\cos^2\theta\sin\theta d\theta}{\int_0^{\pi/2} exp\left(-E_{pot}/k_BT\right)\sin\theta d\theta} - \frac{1}{2}. \tag{2.3}$$

This self-consistent integral equation can only be solved numerically. An analytic approximation is given by equation 2.4

$$S\left(T\right) = \left(1 - 0.98\frac{TV_m^2}{T_{NI}V_{m,NI}^2}\right)^{0.22}, \tag{2.4}$$

where T_{NI} represents the clearing temperature, V_m the molar volume of the respective nematic liquid crystal and $V_{m,NI}$ the molar volume at the clearing temperature T_{NI}. Equation 2.4 provides an universal temperature dependency of the nematic order parameter S, which is found to be valid for most nematic materials. Results for the order parameter calculated for the liquid crystal 5CB by equation 2.4 as well as experimental data for comparable nematogens are plotted in figure 2.4.

2.3 The Frank-Oseen energy

Although the nematic phase is characterized by a long range orientational order where all molecules point on average in the same direction, surface interactions as well as influences of external electric or magnetic fields can lead to strongly distorted director fields. However, the distance L, over which significant changes in the local director $\mathbf{n}$ occur, is usually much larger than the molecular dimension a of a single molecule. If the condition in equation 2.5 is fulfilled, the deformations in the director field can be mathematically described like a continuum.

$$\left|\frac{a}{L}\right| << 1. \tag{2.5}$$

According to Frank [20] and Oseen [21], the minimum in the free energy F_0 of a nematic liquid crystal is given by a uniform director field. Every distortion of this initial state leads to an increase of the total free energy. Considering surface interactions and external electrical fields as possible sources for director field distortions, the total free energy F of a nematic liquid crystal is given by equation 2.6

$$F = F_0 + \int_V (f_{elast} + f_{elec})\, dV + \int_A f_{sur} dA, \tag{2.6}$$

where f_{elast}, f_{elec} and f_{sur} represent the bulk elastic free energy density, the electric field energy density and the surface anchoring energy density, respectively.

2.3.1 The elastic free energy density

The bulk elastic free energy density in equation 2.6 is contributing to the elastic properties of the nematic phase. For calamitic molecules in a nematic phase, only three independent deformations of the director field (splay, twist and bend) influence the elastic energy density, as shown in figure 2.5. Therefore, the three first-order elastic moduli K_{11} (splay), K_{22} (twist) and K_{33} (bend) are needed to describe the elastic response of liquid crystals. Additionally, a chirality induced twist of the director field has to be considered for chiral nematics, by introducing the cholesteric pitch length q_0. If the nematic-nematic interactions in the bulk

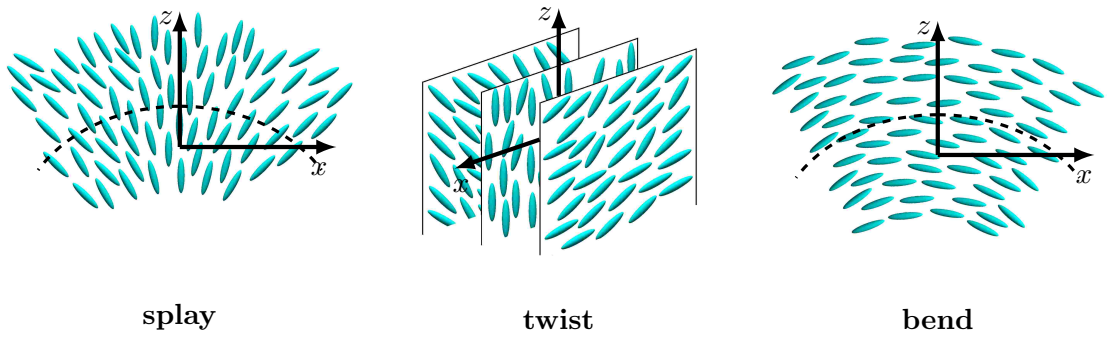

Figure 2.5: Schematic drawing of the three fundamental elastic deformations splay, twist and bend in a nematic liquid crystal.

are of comparable magnitude as the surface-bulk interactions, also the second-order saddle-splay elastic modulus K_{24} contributes to the elastic energy density. The total elastic free energy density is then given by equation 2.7

$$\begin{aligned} f_{elast} = f_0 + \frac{1}{2}K_{11}\left(\nabla \cdot n\right)^2 + \frac{1}{2}K_{22}\left(n \cdot \nabla \times n - q_0\right)^2 + \frac{1}{2}K_{33}\left(n \times \nabla \times n\right)^2 \\ + \frac{1}{2}\left(K_{24} - K_{22}\right)\nabla \cdot \left[n\left(\nabla \cdot n\right) + n \times \nabla \times n\right]. \end{aligned} \tag{2.7}$$

For a simplifying estimation of the elastic free energy density in a non-chiral nematic liquid crystal, the one-constant approximation can be used [17]. In this approach it is assumed that $K_{24} = 0$ and $K = K_{11} = K_{22} = K_{33}$, as all elastic moduli are in the same order of magnitude. Hence, the elastic free energy density can be approximated by equation 2.8

$$f_{elast} = f_0 + \frac{1}{2}K\left((\nabla n)^2 + (\nabla \times n)^2\right). \tag{2.8}$$

2.3.2 The electric free energy density

The electrostatic energy density within a dielectric medium is given by the electric field E and the induced displacement field D over the relation 2.9

$$f_{elec} = -\frac{1}{2}E \cdot D. \tag{2.9}$$

In a nematic liquid crystal, the magnitude of f_{elec} depends on the anisometric permittivity tensor ϵ, and therefore can change depending on the orientation of the liquid crystal molecules in an external electric field. Assuming that the liquid crystal is filled into a plate capacitor as liquid crystal test cell, which is connected to a power source with constant voltage, the reorientation of molecules results in work which has to be done by the power supply. Taking this energy into account, the electric field energy density f_{elec} in equation 2.6 can be described by

$$f_{elec} = -\frac{1}{2}\epsilon\epsilon_0 E^2 - \frac{1}{2}\epsilon_0 \Delta\epsilon \left(\vec{E}\vec{n}\right)^2. \tag{2.10}$$

The first term in equation 2.10 is independent from the director orientation and therefore considered as the isotropic contribution of the electric energy density. The second term of equation 2.10 depends on the director field distribution as well as on the dielectric anisotropy $\Delta\epsilon$ of the nematic liquid crystal. For materials with positive dielectric anisotropy ($\Delta\epsilon > 0$), the minimum in free energy density is given for a director orientation parallel to the external electric field, while for a material with negative dielectric anisotropy ($\Delta\epsilon < 0$) a director orientation perpendicular to the external field is energetically favored.

The equilibrium director field distribution in the absence of external fields is given by the boundary conditions and the elastic properties of the nematic liquid crystal only. An external electric field gives rise to an additional term in the total free energy and can change the

director field distribution with a minimum in the Frank-Oseen energy. As a nematic liquid crystal is a fluid medium, sufficiently large fields can induce a reorientation of the director field, which can be controlled by the external electric field. The equilibrium director field distributions under external fields as well as the dynamics of field-induced deformations are discussed in sections 2.5.1 and 2.5.2 of this chapter.

2.3.3 Surface interactions and alignment

Nematic liquid crystals can easily be aligned by specific interactions of molecules with the confining boundary surfaces of a given volume. The surface induced alignment is then transferred into the bulk of the liquid crystal by elastic forces, and the resulting director field distribution in the bulk represents the state with a minimum in the free energy F. In general, there are three possible alignment modes, as shown in figure 2.6. While homeotropic alignment is characterized by the director $\mathbf{n}$ perpendicular to the surface ($\theta_0 = 0$), planar alignment is given for $\mathbf{n}$ parallel to the surface ($\theta_0 = \pi/2$). An intermediate state between homeotropic and planar alignment is the tilted alignment mode, where the long axis of molecules orients in a defined angle to the substrate ($0 < \theta_0 < \pi/2$).

The actual alignment of nematic liquid crystals on a surface depends on several factors including intermolecular interactions, steric factors, surface topography and the elasticity of the liquid crystal molecules [22]. It is known that the spontaneous orientation of a nematic liquid crystal to a substrate depends on the relative magnitude of the surface energy of the surface and the surface tension of the liquid crystal [23]. If the surface tension of the liquid crystal is higher than the surface energy of the substrate, homeotropic alignment is energetically favored. For high surface energies and lower surface tension, planar alignment of the liquid crystal molecules is expected. Additionally, topographical structuring of the surface can influence on the alignment of molecules.

Homeotropic alignment on glass substrates is usually achieved by the use of surfactants [24]. Coating the glass substrates of a liquid crystal test cell with an amphiphilic surfactant like phospholipids (for example Lecithine) or fatty acids results in a monomolecular layer of surfactants on the surface, with the hydrophilic endgroups pointing to the glass substrate and the hydrophobic chains reaching into the volume of the test cell (see figure 2.7, (a)). The alignment of calamitic molecules is then given by steric interactions of the side chains of

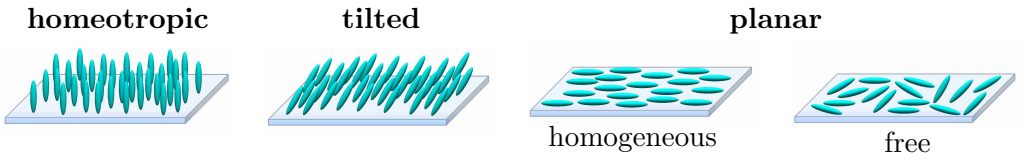

Figure 2.6: Schematic drawing of the three fundamental alignment modes of calamitic liquid crystals on an interface, with an additional distinction between free planar alignment and homogeneous planar alignment.

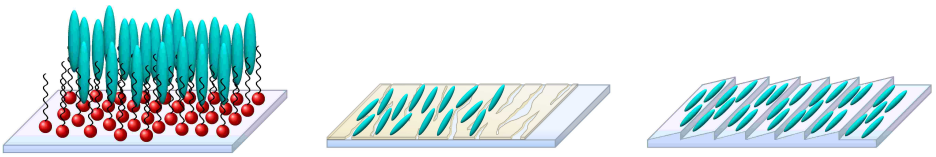

Figure 2.7: Schematic drawings of three different liquid crystal / surface interactions to induce homeotropic (a) or homogeneous planar ((b),(c)) alignment. (a) The amphiphil lecithine forms a monolayer on the surface, inducing homeotropic alignment due to topological interactions with the liquid crystal molecules. (b) Chatelain's method of rubbing a coating with high surface energy induces homogeneous planar alignment. (c) Oblique evaporation of metals or oxides leads to the formation of parallel topological stairs, which also induce homogeneous planar alignment.

molecules with the surfactant as well as by the reduction of surface energy in the hydrophobic part of the coating.

Tilted alignment modes can be achieved either by using surfactants [24] or by pure topological effects using oblique evaporation of thin Au or SiO films at very large angles (80-90°) [25].

Surface coatings with high surface energy can lead to the formation of strong planar anchoring of molecules to the substrates. However, an unstructured coating does not provide an easy direction for the orientation of molecules, so that the azimuthal angle φ is not defined and therefore arbitrary. A common method to achieve homogeneous planar alignment is the mechanical rubbing of the surface with paper or cloth, the so called Chatelain's method [24]. The mechanical rubbing results in parallel microscratches on the surface, which promote an orientation of molecules parallel to the scratches (see figure 2.7, (b)). Another method of inducing homogeneous planar alignment is the oblique evaporation of metals or oxides (e.g. SiO) under small angles onto the surface, which leads to the formation of parallel topological stairs along the crystal growth direction of the evaporated material (see figure 2.7, (c)).

For homogeneous planar alignment ($\theta_0 = \pi/2$, for definitions of angles see figure 2.8), Berreman showed that the alignment of molecules parallel to the rubbing direction of the surface minimizes the elastic free energy density f_{elast} of the liquid crystal [26]. This direction

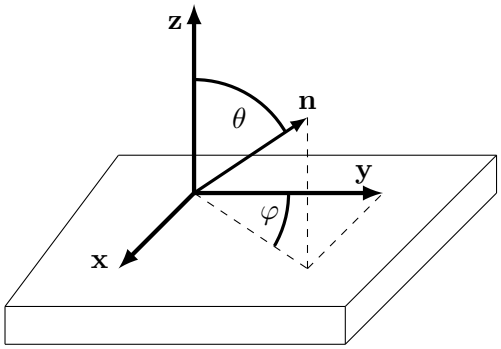

Figure 2.8: Definitions of the polar angle θ_0 and the azimuthal angle φ_0 describing the alignment of a nematic liquid crystal on a surface (sketch adapted from reference [24]).

is referred to as the easy direction of the surface, and denoted with the azimuthal angle φ_0. The minimum free surface energy F_{sur} is then given for an orientation along this easy direction ($\theta = \theta_0,\ \varphi = \varphi_0$), every deviation from this orientation increases the surface energy. The energy needed for a director deviation away from the easy direction is given by the anchoring energy W_{anchor}.

Rapini and Papoular introduced the two independent anchoring energies W^{θ}_{anchor} and W^{φ}_{anchor} [24] in order to estimate the free surface energy F_{sur} depending on the deviation from the easy direction, as shown in equation 2.11

$$\begin{aligned} F^{\theta}_{sur} &= \frac{1}{2} W^{\theta}_{anchor} \sin^2(\theta - \theta_0), \\ F^{\varphi}_{sur} &= \frac{1}{2} W^{\varphi}_{anchor} \sin^2(\varphi - \varphi_0). \end{aligned} \tag{2.11}$$

Hence, the increase in free energy is proportional to the anchoring energy and has its maximum for a deviation of $\pi/2$.
High anchoring energies lead to strong boundary conditions, where even large external fields lead to only small deviations from the easy direction. For $W_{anchor} = \infty$, the director cannot be deviated from the easy direction at the surface. Low (or finite) anchoring energies allow a field-dependent deviation from the easy direction. In order to describe the influence of the boundary conditions on the alignment in the bulk, the extrapolation length b can be used, which connects the anchoring energy with the elastic properties of the nematic material [17].

$$b = a^2 \frac{K_{ii}}{W_{anchor}} \propto a \frac{U_{bulk}}{W_{anchor}} \tag{2.12}$$

The quantity a represents the average molecular dimension of the nematic material, and U_{bulk} is a measure of the nematic-nematic interactions in the bulk.

For the case the anchoring energy W_{anchor} is comparable or even larger than U_{bulk}, the extrapolation length b is comparable to the molecular dimension a. As according to the continuum theory deformations of the director field are considered on a scale much larger than a, the extrapolation length can be neglected and the anchoring is strong. If $W_{anchor} << U_{bulk}$, the extrapolation length b can be considerably larger than the molecular dimension a. In this case, an external constraint can lead to a deformation of molecules in the surface region, and the anchoring is considered weak.

An experimental approach for the determination of the anchoring conditions is given by the analysis of angle distribution $\theta(z)$ during a field-induced reorientation of molecules. As discussed in detail in section 2.5, an external electric field can induce an orientation of molecules which contradicts the preferred alignment of molecules to the substrates. The degree of reorientation in the vicinity of the surfaces depends on the anchoring energy W_{anchor}. Considering opposite molecular orientations by surface forces and dielectric forces and solving the resulting equation of motion by applying Lagrangian mechanics yields the tilt angle distribution $\theta(z, E)$ given by

$$\theta(z, E) = 2 \arctan\left(e^{-\frac{z}{\xi_E}}\right), \tag{2.13}$$

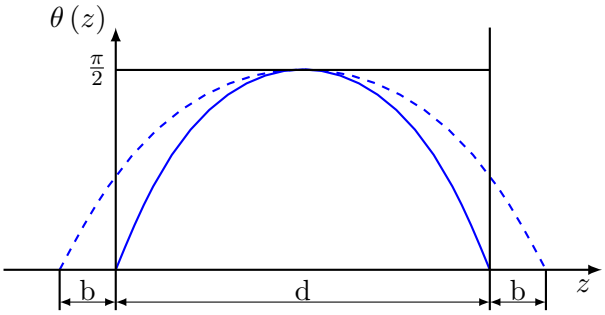

Figure 2.9: Director field distribution $\theta(z)$ of a Fréedericksz-transition for strong anchoring (solid line) and weak anchoring (dashed line). For weak anchoring conditions, the orientation of molecules at the boundaries is a function of the external field, thereby the cell thickness d appears larger. The difference between the solid line and the dashed line is a measure of the anchoring energy W_{anchor} [27].

with ξ_E being the field coherence length defined as

$$\xi_E = \frac{1}{E}\sqrt{\frac{K_{11}}{\epsilon\Delta\epsilon}}. \tag{2.14}$$

If the external field is sufficiently large, the field coherence length ξ_E becomes comparable to the surface extrapolation length b ($\xi_E \approx b$). This condition represents the second threshold of complete reorientation of molecules even in the vicinity of the surface, and allows b and consequently W_{anchor} to be calculated [27].

2.4 Physical properties of nematic liquid crystals

Nonionizing liquid crystals can show a very low intrinsic electrical conductivity (down to $10^{-19}\,\Omega^{-1}\mathrm{cm}^{-1}$, [24]) and therefore can be considered as dielectric media. Due to the partial order of the anisometric building blocks, liquid crystals can exhibit macroscopically anisotropic physical properties. For example, the effective refractive index n or the effective permittivity ϵ depend on the orientation of molecules to an external field. In consequence, n and ϵ of nematic materials are not scalar values, but need to be described as tensors of second order. This tensor differs for different ordered phases, the number of independent components is given by the symmetry of the liquid crystalline phase. As the symmetry of the thermotropic nematic phase is given by the point group $D_{h\infty}$, the permittivity tensor ϵ has only two independent components $\epsilon_\parallel$ and $\epsilon_\perp$, which correspond to the permittivity parallel and perpendicular to the director $\mathbf{n}$, respectively.

$$n = \begin{pmatrix} n_\perp & 0 & 0 \\ 0 & n_\perp & 0 \\ 0 & 0 & n_\parallel \end{pmatrix} \quad \epsilon = \begin{pmatrix} \epsilon_\perp & 0 & 0 \\ 0 & \epsilon_\perp & 0 \\ 0 & 0 & \epsilon_\parallel \end{pmatrix}$$

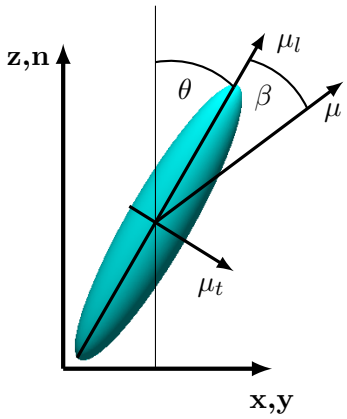

Figure 2.10: Schematic drawing of a calamitic molecule with the angle β between the total dipole moment μ and the long axis of molecule and the angle θ between the long axis and the director n. The quantities μ_l and μ_t depict the longitudinal and transversal part of μ, respectively.

2.4.1 Dielectric anisotropy

When a liquid crystal is placed between the plates of a capacitor, the capacitance of the capacitor increases. In vacuum, the capacitance C_0 of a plate-capacitor (plate area A, distance d) in vacuum is given by equation 2.15

$$C_0 = \frac{Q}{U} = \frac{Q}{E \cdot d} = \frac{Q}{\frac{Qd}{\epsilon_0 A}} = \frac{\epsilon_0 A}{d}. \tag{2.15}$$

As for any dielectric, the increase in capacitance is proportional to the factor ϵ, which represents the permittivity tensor of the dielectric material

$$C = \epsilon \cdot \epsilon_0 \frac{A}{d}. \tag{2.16}$$

The increase of capacitance is caused by electrical counter-fields, which arise in the dielectric material due to the presence of an external electric field E. This electric displacement field is denoted as D and given by the electric field E and the induced polarization P

$$D = \epsilon_0 \epsilon E = \epsilon_0 E + P. \tag{2.17}$$

The polarization P describes the electric dipole moment per volume. It is attributed by a permanent dipole moment μ and a field-induced dipole moment $\mu_{induced} = \alpha E_{local}$, which occurs due to a displacement of electrons and cores in an external field. A degree of this displacement is given by the molecular polarizability α.

$$P = \frac{N}{V} \left(\alpha E_{local} + \mu \right). \tag{2.18}$$

A connection between the microscopic properties polarizability α and permanent dipole moment μ of a single molecule with the macroscopic quantity ϵ is given by the Debye

equation 2.19

$$\frac{\epsilon - 1}{\epsilon + 2} = \frac{\rho N_A}{3M\epsilon_0}\left(\alpha + \frac{\mu^2}{3k_BT}\right). \tag{2.19}$$

As in polar liquids, the local electric field strength E_{local} depends on the dielectric surrounding and usually differs from the applied electric field E. Onsager developed the relation 2.20 [28]

$$\bar{\epsilon} = 1 + \frac{NFh}{V\epsilon_0}\left[\bar{\alpha} + \frac{F\mu^2}{3k_BT}\right] \tag{2.20}$$

with

$$h = \tfrac{3\epsilon}{2\epsilon+1}, \quad F = (1 - f\alpha)^{-1}, \quad \text{and } f = \tfrac{\epsilon-1}{2\pi\epsilon_0 a^3(2\epsilon+1)},$$

considering the interactions between dipoles in a condensed liquid phase as well as their volume. Equation 2.20 considers average values of ϵ and α and therefore is valid only for isotropic media. For the nematic phase, the dielectric tensor has to be used, whose elements $\epsilon_\parallel$ and $\epsilon_\perp$ are related to the molecular polarizabilities parallel $\alpha_\parallel$ and perpendicular $\alpha_\perp$ to the director, the angle β between the long axis of the calamitic molecules and a permanent dipole moment μ and to the scalar order parameter S. This relation is given by the Maier-Meier equations 2.21 and 2.22.

$$(\epsilon_\perp - 1) = \frac{NFh}{\epsilon_0}\left[\bar{\alpha} + \frac{1}{3}\Delta\alpha S + \frac{g_1^\perp \mu^2 F}{3k_BT}\left[1 + \frac{1}{2}\left(1 - 3\cos^2\beta\right)S\right]\right] \tag{2.21}$$

$$\left(\epsilon_\parallel - 1\right) = \frac{NFh}{\epsilon_0}\left[\bar{\alpha} + \frac{2}{3}\Delta\alpha S + \frac{g_1^\parallel \mu^2 F}{3k_BT}\left[1 + \frac{1}{2}\left(1 - 3\cos^2\beta\right)S\right]\right] \tag{2.22}$$

with $\Delta\alpha = \alpha_l - \alpha_t$ The dielectric anisotropy of the nematic liquid crystal is then given by equation 2.23

$$\Delta\epsilon = \epsilon_\parallel - \epsilon_\perp = \frac{NFh}{\epsilon_0}\left[(\alpha_l - \alpha_t) - \mu^2\frac{F}{2k_BT}\left(1 - 3\cos^2\beta\right)\right]S. \tag{2.23}$$

According to equation 2.23, the dielectric anisotropy $\Delta\epsilon$ scales linearly with the order parameter S. As S decreases with increasing temperature, $\Delta\epsilon\,(T)$ is a monotonously decreasing function with a vanishing dielectric anisotropy at $T = T_{NI}$.

The relation between the macroscopically observable values for $\epsilon_\perp$ and $\epsilon_\parallel$ and the molecular quantities α_t, α_l and μ_t, μ_l is given by the order parameter S. Considering an ordered phase with $S = 1$, the molecular polarizabilities α_t and α_l equal the macroscopic values for $\alpha_\perp$ and $\alpha_\parallel$. Hence, the order parameter S can be described as

$$S = \frac{\alpha_\parallel - \alpha_\perp}{\alpha_l - \alpha_t}. \tag{2.24}$$

2.4.2 Birefringence

For electromagnetic fields at optical frequencies, the polarization P reduces to

$$P = \frac{N}{V}\alpha E_{local}, \tag{2.25}$$

as the permanent dipole moments can not follow the fast switching of sign of the external field and do not contribute to the total polarization P. Connecting the Maxwell relation

$$\epsilon = n^2 \tag{2.26}$$

with the Debye equation for $\mu = 0$ gives the Lorentz-Lorenz equation 2.27, which connects the refractive index of the dielectric to the molecular polarizability α by

$$\frac{n^2 - 1}{n^2 + 2} = \frac{\rho N_A}{3M\epsilon_0}\alpha. \tag{2.27}$$

Taking into account the nematic order of calamitic building blocks and different polarizabilities $\alpha_\parallel$ and $\alpha_\perp$ parallel and perpendicular to the director, the Lorentz-Lorenz equation 2.27 leads to two observable refractive indices

$$\frac{n_\parallel^2 - 1}{\bar{n}^2 + 2} = \frac{\rho N_A}{3M\epsilon_0}\alpha_\parallel. \tag{2.28}$$

$$\frac{n_\perp^2 - 1}{\bar{n}^2 + 2} = \frac{\rho N_A}{3M\epsilon_0}\alpha_\perp. \tag{2.29}$$

with $\bar{n}^2 = \frac{n_\parallel^2 + 2n_\perp^2}{3}$.

Hence, a nematic liquid crystal is an uniaxial birefringent medium with the optical axis parallel to the director $\mathbf{n}$. The two principle refractive indices are given by $n_\parallel = n_e$ and $n_\perp = n_o$, the birefringence can be described by $\Delta n = n_e - n_o$. Typical values for Δn of nematic liquid crystals are 0.05-0.45.
The optical axis of the nematic phase is parallel to the director $\mathbf{n}$, whose distribution can be strongly distorted in a given volume V. Therefore the effective refractive index n_{eff} for linearly polarized light passing through the liquid crystal also depends on the director field distribution and can be described as

$$n_{eff} = \frac{1}{V}\int n\,(x, y, z)dV. \tag{2.30}$$

As shown in section 2.5, the director distribution $\mathbf{n}(x, y, z)$ can be manipulated by external electric fields, so that also the optical birefringence of the nematic liquid crystal can be electrically controlled. Considering the initial geometry given in section 2.5 (homogeneously planar alignment parallel to the y-axis, external electric field parallel to z) and assuming linearly polarized light of wavelength λ passing through the sample along the z-direction with the orientation of the electric field $\vec{E}$ under an angle of φ_0 to the y-axis gives rise to an

initial birefringence $\Delta n = n_e - n_o$. At sufficiently strong external fields, the initial alignment is distorted and the director describes a function $\theta(z)$.

This does not affect the ordinary refractive index n_o, as the director remains perpendicular to the x-axis. However, the extraordinary refractive index n_e decreases, tending towards n_o. The magnitude of n_e depends on the degree of deviation from the initial alignment and therefore depends on $\theta(z)$ by the equation

$$n_{e,eff}(z) = \frac{n_e n_o}{\sqrt{n_e^2 \cos^2\theta(z) + n_o^2 \sin^2\theta(z)}}. \tag{2.31}$$

In consequence, also the effective birefringence $\Delta n_{eff}(z) = n_{e,eff}(z) - n_o$ depends on the angle distribution $\theta(z)$ and decreases with increasing field strength. The total phase retardation between ordinary and extraordinary beam passing through the sample in this geometry is given by

$$\delta = \frac{2\pi d \Delta n_{eff}(z)}{\lambda}. \tag{2.32}$$

In order to detect the effective birefringence of the sample, a polarizer can be placed behind the sample under an angle of 90° with respect to the initial polarization state of the transmitting light. The detectable light intensity is then given by equation 2.33

$$I = \frac{1}{2} I_0 \sin^2(2\varphi_0) \sin^2\left(\frac{\delta}{2}\right), \tag{2.33}$$

where I_0 is the initial light intensity. According to equation 2.33, the maximum light transmission between crossed polarizers is given for $\varphi_0 = 45°$ and the field-dependent light transmission is an oscillating signal. The contrast ratio between I_{min} and I_{max} is not limited in theory, but usually restricted in experiment by the quality of the initial director orientation [24].

2.5 The Fréedericksz-transition

For a single calamitic molecule in free space the minimum electrostatic energy is given by an orientation of the long axis of the molecule parallel to the electric field for molecules with $\epsilon_l > \epsilon_t$, as this maximizes the electric displacement field D. However, the volume of the nematic phase is always confined by substrates, and hence the director field distribution is connected to the boundary conditions at the surfaces. In the equilibrium state, the director field distribution minimizes the free energy F of the volume, which in the absence of external fields is given by equation 2.34

$$F = \int_V f_{elast} dV + \int_s f_{sur} ds. \tag{2.34}$$

Any field-induced reorientation of molecules then creates additional distortions in the director field, which increase the elastic part of the free energy density f_{elast} and therefore give rise to an elastic restoring torque that tends to resist this reorientation. As a result, the equilibrium director field distribution under the influence of electric fields does not only

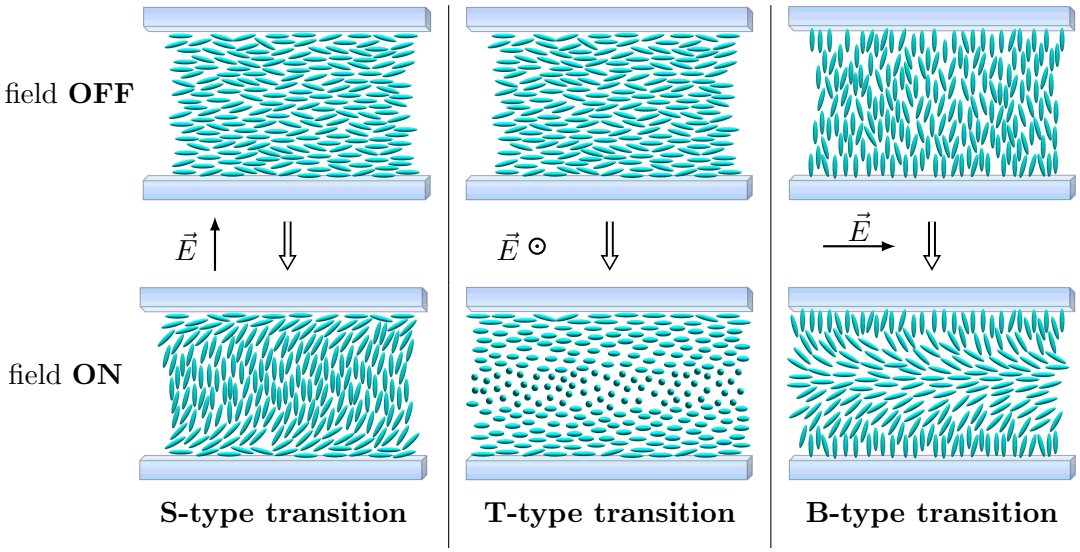

Figure 2.11: Schematic drawings of the three fundamental geometries for a Fréedericksz-transition for materials with positive dielectric anisotropy. The upper images show the undistorted initial alignment in the field OFF state, while the lower images show the distorted states, which correspond to a splay deformation (left), a pure twist deformation (middle) and a bend deformation (right).

depend on the applied electric field, but also on the elastic properties of the liquid crystal and the boundary conditions at the surfaces.

Hence, the analysis of field-induced distortions of the director field can reveal information as well on the boundary conditions and the elastic properties of the nematic material as on its dielectric properties. In a typical experiment, an external electric field is used to distort an uniformly aligned nematic liquid crystal, and changes in the director field distribution are detected by birefringence or capacitance measurements. However, this approach requires a well-defined initial director field. In this work, this is usually achieved by using liquid crystal test cells featuring strong parallel planar anchoring conditions, which lead to an homogeneously planar aligned liquid crystal.

This field-induced reorientation of the nematic director was at first investigated in detail by V. Fréedericksz and V. Zolina [29] and is therefore referred to as Fréedericksz-transition. There are three fundamental geometries for the Fréedericksz-transition which correspond to a splay deformation, a bend deformation and a pure twist deformation (see figure 2.11).

2.5.1 Static director field distribution under influence of an electric field

In order to simplify the theoretical derivations of the field-induced switching behavior and because of the close relation to the experiments performed in this work, only the splay-type Fréedericksz-transition is considered in the following section. Therefore the initial equilibrium director field is assumed to be given by an homogeneously planar aligned nematic phase parallel to the y-axis of the sample. Applying electric fields parallel to the z-direction then creates distortions in the director field, but reduces the director distribution to a one-dimensional function depending on z only. A similar approach is possible for any initial director configuration and for any geometry of the Fréedericksz-transition. Using the initial

geometry described above, the elastic part of the free energy density simplifies from equation 2.7 to equation 2.35, as only bend and splay deformations of the director field can occur

$$f_{elast} = f_0 + \frac{1}{2}\left(K_{11}\cos^2\Theta + K_{33}\sin^2\Theta\right)\left(\frac{d\Theta}{dz}\right)^2. \tag{2.35}$$

For the undistorted liquid crystal, the slope of the tilt angle Θ/dz is zero and hence f_{elast} equals the minimum energy f_0. Any deformation of the director field increases the elastic free energy density proportional to the square of the slope of the tilt angle. As shown in reference [22], the elastic torque density originating from such deformations is connected to the elastic free energy density by equation 2.36

$$\tau_{elast} = -\frac{\partial}{\partial\Theta}\Delta f_{elast} + \frac{d}{dz}\frac{\partial}{\left(\frac{d\Theta}{dz}\right)}\Delta f_{elast}. \tag{2.36}$$

By combining equations 2.35 and 2.36, the resulting elastic restoring torque density is given by equation 2.37

$$\tau_{elast} = (K_{33} - K_{11})\sin\Theta\cos\Theta\left(\frac{d\Theta}{dz}\right)^2 + \left(K_{11}\cos^2\Theta + K_{33}\sin^2\Theta\right)\frac{d^2\Theta}{dz^2}. \tag{2.37}$$

On the other hand, the presence of an external electric field tends to minimize the electric part of the free energy density f_{elec} by reorienting the molecules with their long axis parallel to the z-direction. The resulting electrostatic torque density acting on the liquid crystal molecules is given by equation 2.38

$$\tau_{elec} = -\frac{\partial}{\partial\Theta}\Delta f_{elec} + \frac{d}{dz}\frac{\partial}{\left(\frac{d\Theta}{dz}\right)}\Delta f_{elec}, \tag{2.38}$$

with the change in the electric field energy density Δf_{elec} given by the expression

$$\Delta f_{elec} = \frac{1}{2}\frac{D_z^2}{\left(\epsilon_\parallel\sin^2\Theta + \epsilon_\perp\cos^2\Theta\right)} - \frac{1}{2}\frac{D_z^2}{\epsilon_\perp}. \tag{2.39}$$

With the initially chosen uniform alignment in the xy-plane, the dielectric tensor ϵ reduces to a function of z only. As the the electric field within the liquid crystal correlates to the local distribution of ϵ, it also becomes a function of z. In consequence, the z-component of the displacement field vector D is constant, and hence the second term is independent of the director orientation $\Theta(z)$. Using only the left part of equation 2.39 for the differentiation of equation 2.38 yields the expression 2.40

$$\tau_{elec} = \frac{D_z^2\left(\epsilon_\parallel - \epsilon_\perp\right)}{\left(\epsilon_\parallel\sin^2\Theta + \epsilon_\perp\cos^2\Theta\right)^2}\sin\Theta\cos\Theta, \tag{2.40}$$

which can be simplified to equation 2.41

$$\tau_{elec} = \left(\epsilon_\parallel - \epsilon_\perp\right)E^2\sin\Theta\cos\Theta. \tag{2.41}$$

The equilibrium director field distribution under the influence of electric fields is given by an orientation $\Theta(z)$ where electric and elastic torque sum up and the total torque vanishes

$$\tau_{elec} + \tau_{elast} = 0. \tag{2.42}$$

In the simplified geometry treated here, this equilibrium condition is given by equation

$$\begin{aligned}\left(\epsilon_{\parallel} - \epsilon_{\perp}\right) E^2 \sin\Theta\cos\Theta + (K_{33} - K_{11}) \sin\Theta\cos\Theta \left(\frac{d\Theta}{dz}\right)^2 \\ + \left(K_{11}\cos^2\Theta + K_{33}\sin^2\Theta\right) \frac{d^2\Theta}{dz^2} = 0.\end{aligned} \tag{2.43}$$

This nonlinear differential equation gives the static equilibrium director distribution $\Theta(z)$ in the liquid crystal cell. Even in this simple geometry, analytical solutions are not available and the equation can only be solved numerically.

Assuming only very small distortions of the director field ($\Theta << 1$) leads to a pure splay deformation of the director field, while larger displacements are dominated by a splay deformation with an admixture of bend deformations. Thus, the restriction to $\Theta << 1$ omits the bend deformation and equation 2.43 can be approximated by the linear differential equation

$$K_{11}\frac{d^2\Theta}{dz^2} + \epsilon_0 \Delta\epsilon E^2 \Theta = 0. \tag{2.44}$$

One solution of equation 2.44 is given by

$$\Theta(z) = \Theta_0 \sin\left((\frac{\pi z}{d})\right), \tag{2.45}$$

where Θ_0 is a constant ($\Theta_0 << 1$) and d is the cell gap. Substitution of this solution in equation 2.43 and considering only first-order terms yields

$$\epsilon_0 \Delta\epsilon E^2 \sin\Theta\cos\Theta - K_{11}\left((\frac{\pi}{d})\right)^2 \Theta = 0, \tag{2.46}$$

For sufficiently small distortions $\sin\Theta\cos\Theta < \Theta$, so that nontrivial solutions of equation 2.46 require

$$E^2 > \frac{\pi^2 K_{11}}{d^2 \epsilon_0 \Delta\epsilon} \equiv E_{Th}^2. \tag{2.47}$$

With the relation $E = V/d$, the threshold voltage of the deformation of a uniformly aligned nematic liquid crystal is given by

$$V_{Th} = \pi\sqrt{\frac{K_{11}}{\epsilon_0 \Delta\epsilon}}. \tag{2.48}$$

Only above this threshold voltage V_{Th} the destabilizing electric torque τ_{elec} overcomes the stabilizing restoring elastic torque τ_{elast} and a deformation of the director field occurs. This field-induced rotation is degenerate, clockwise and anticlockwise rotation are equally probable [27]. In order to avoid domain walls separating regions with different rotation directions within the bulk, rubbed alignment layers which induce small, well-defined pretilt angles to

the molecules at the interface can be used. This leads favorable direction of rotation, as the displacement field D degenerates.

The threshold voltage V_{Th} for the Fréedericksz-transition of a nematic material is a simply accessible physical property which allows the determination of the elastic constants the liquid crystal. A larger elastic constant K_{ii} corresponds to a stiffer medium that requires higher electric torques to distort the liquid crystal. On the other hand a large difference between ϵ_l and ϵ_t goes along with a large dielectric anisotropy $\Delta\epsilon$ and therefore increases the electric torque on the molecules. By measuring the threshold voltage V_{Th}, information on the ratio between elastic torque and electric torque is obtained, and for known values of $\Delta\epsilon$ the elastic constant K_{ii} of the respective director deformation can be determined.

Although the relation for the threshold voltage V_{Th} given by equation 2.48 is widely used, it should be noted that it is connected to several restrictions:

- **Restriction to small distortions**
  The simplifying assumptions made for the electric part of the free energy density given by equation 2.39 are only valid for homogeneously aligned molecules and small distortions. In a strongly deformed director field, the displacement field D is no longer parallel to the applied external field, but non-uniformly distributed over the cell gap. This gives rise to additional electric torques, which can induce a rotation of molecules out of the (y, z)-plane in the geometry stated above. Because of the large anisotropy between $\epsilon_{\parallel}$ and $\epsilon_{\perp}$ compared to the magnetic anisotropy of typical nematic materials, this effect has to be taken into account for a reorientation in electric fields, while it can be neglected for a reorientation in magnetic fields.

- **Conductivity**
  For conducting samples an additional contribution to the electric torque due to an anisotropy of conductivity has to be considered [30]. Additionally, samples with sufficient amounts of charged dopants can build electric double layers at the interfaces, which can reduce the local field strength E_{loc} and therefore influence on the displacement field D [31]. In consequence, higher external voltages have to be applied to overcome the restoring elastic torque of the liquid crystal, which simulates higher appearing threshold voltages.

- **Boundary conditions**
  The derivation of threshold voltage V_{Th} assumes strong boundary conditions with infinite anchoring energy, which is denoted by a director orientation of

$$n = (z = 0) = n\,(z = d) = n\,(0,\ 1,\ 0) \tag{2.49}$$

  for any given field strength E. As discussed in section 2.3.3 (see figure 2.9), a finite anchoring energy ($W_{anchor} < \infty$) results in an increase in the apparent thickness of the cell, what influences on the critical field strength for the Fréedericksz-transition

$$E_{Th,weak} = \frac{E_{Th,strong}}{d + 2b}. \tag{2.50}$$

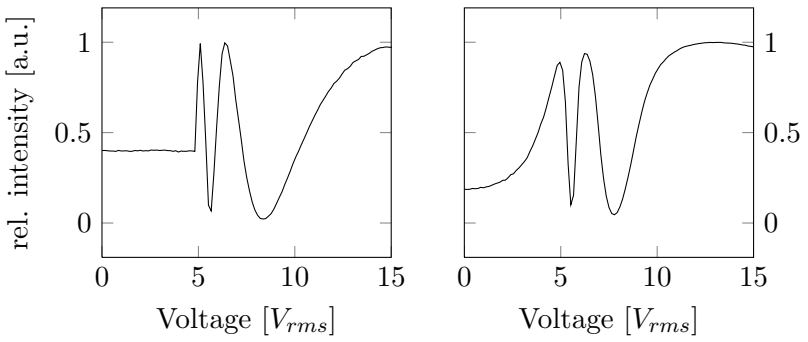

Figure 2.12: Field-dependent light transmission characteristics of an homogeneously planar aligned nematic liquid crystal without pretilt angle (left) and with pretilt angle (right) to the substrates.

Hence, weak anchoring conditions decrease the critical field strength E_{Th}, but do not influence on the elastic properties of the liquid crystal. This has to be considered when using equation 2.48 to estimated changes in elastic properties due to observed changes of threshold.

It should also be noted that a threshold V_{Th} is only defined for zero pretilt angle of the director at the limiting boundaries [32]. Only an initial director orientation perpendicular to the external field requires a critical electric torque to overcome the restoring elastic torque of the nematic material. For any finite pretilt angle, even small electric torques are sufficient for a reorientation of molecules, thus a continuous distortion of director field instead of a Fréedericksz-transition occurs as shown in the right diagram of figure 2.12.

According to equation 2.45, the function $\Theta(z)$ in the regime of small distortions is given by a sinusoidal increase of Θ. The maximum tilt angle $\Theta_0 = \Theta_{max}$ in the midlayer of the liquid crystal test cell depends on the applied field, and reaches a saturation value of $\pi/2$ for very large electric fields.

In order to obtain the z-dependent director distribution over the cell gap, equation 2.43 is integrated to

$$\left(K_{11}\cos^2\Theta + K_{33}\sin^2\Theta\right)\left(\frac{d\Theta}{dz}\right)^2 = \frac{D_z^2}{\left(\epsilon_\parallel \sin^2\Theta + \epsilon_\perp\cos^2\Theta\right)} - \frac{D_z^2}{\left(\epsilon_\parallel \sin^2\Theta_{max} + \epsilon_\perp\cos^2\Theta_{max}\right)}. \tag{2.51}$$

A numerical integration of equation 2.51 yields the function $\Theta(z)$ for different applied voltages, some tilt angle distributions are plotted in figure 2.13.

2.5.2 Dynamic of field-induced director deformations

The dynamic of field-induced director deformations is given by the solution of the equation of motion which considers besides elastic and electric torques also viscous forces. In a general

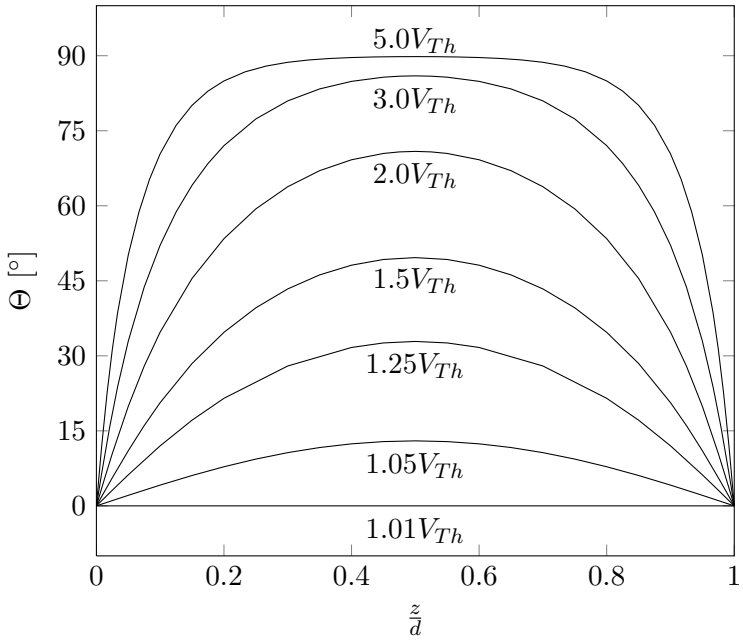

Figure 2.13: Diagram showing director tilt angle distributions for the nematic liquid crystal 5CB at different applied voltages. The distortion of the initially parallel planar director field by an electric field parallel to the z-axis sets in above the threshold voltage, a maximum tilt angle of $\pi/2$ is reached for $V = 5V_{Th}$.

approach, this equation of motion is given by the expression 2.52

$$\tau_{elec} + \tau_{elast} = \gamma_1 \frac{d\Theta}{dt}, \tag{2.52}$$

where γ_1 represents the rotational viscosity of the nematic material.

The viscosity is an internal resistance to flow, which rises from intermolecular forces in a fluid. The rotational viscosity γ_1 describes the resistance to the rotational motion of the molecules under the influence of external fields. For the experimental determination of γ_1 usually a pure twist-deformation is investigated, as the reorientation of molecules in a twist-deformation is not connected to changes in the position of the centers of gravity of molecules and therefore free of convection [33]. For the two fundamental other deformations splay and bend, the boundary conditions to the substrates induce a velocity profile along the cell gap, so that molecules rotate at different angular velocities. While molecules in the bulk can freely rotate, the angular velocity vanishes at the restricting surfaces. This gradient in angular velocity leads to an inhomogeneous rotation of the director and causes back-flow effects of molecules, which attribute to additional friction. Therefore, the rotational viscosity γ_1 obtained from measurements of splay or bend deformations is smaller than the rotational viscosity obtained for a pure twist deformation [34], and is depicted as effective rotational viscosity γ_1^{eff}. Detailed studies on the reorientation behavior of nematic liquid crystals in magnetic fields show that the effective rotational viscosity γ_1^{eff} can be as small as 25 % of γ_1[35].

For the case discussed above, substituting equations 2.41 and 2.37 for the torques yields equation 2.53

$$\gamma_1 \frac{d\Theta}{dt} = \epsilon_0 \Delta\epsilon E^2 \sin\Theta\cos\Theta + (K_{33} - K_{11}) \sin\Theta\cos\Theta \left(\frac{d\Theta}{dz}\right)^2 + \left(K_{11}\cos^2\Theta + K_{33}\sin^2\Theta\right) \frac{d^2\Theta}{dz^2}. \tag{2.53}$$

This equation of motion is a nonlinear differential equation of $\Theta(z,t)$ and can only be solved numerically using some simplifying assumptions.

For the case of a relaxation process from a distorted director field to the field-off distribution, the dielectric part of equation 2.53 can be omitted and the time evolution of the relaxation is given by equation 2.54

$$\gamma_1 \frac{d}{dt}\Theta(z,t) = (K_{33} - K_{11}) \sin\Theta\cos\Theta \left(\frac{d\Theta}{dz}\right)^2 + \left(K_{11}\cos^2\Theta + K_{33}\sin^2\Theta\right) \frac{d^2\Theta}{dz^2}. \tag{2.54}$$

Assuming that the electric field only induced a small distortion in the director field, the equation for the director relaxation can be approximated to equation 2.55

$$\gamma_1 \frac{d\Theta}{dt} = -K_{11} \left(\frac{\pi}{d}\right)^2 \Theta. \tag{2.55}$$

The solution of this differential equation gives an exponential decay of the director field distortion (equation 2.56)

$$\Theta(t) = \Theta(t=0)\, exp\left(\frac{-t}{\tau_{decay}}\right) \tag{2.56}$$

with the time constant τ_{decay}

$$\tau_{decay} = \frac{\gamma_1}{K_{11}} \left(\frac{d}{\pi}\right)^2. \tag{2.57}$$

For the analysis of rise time τ_{rise}, an initially undistorted director field is assumed, so that

$$\Theta(z, t=0) \approx 0. \tag{2.58}$$

Assuming only small field induced deformations, the angle distribution after a time t can be approximated by the relation 2.59

$$\Theta(z,t) = \Theta_0(t) \sin\left(\frac{\pi z}{d}\right) \tag{2.59}$$

and the equation of motion simplifies to 2.60

$$\gamma_1 \frac{d\theta}{dt} = \epsilon_0 \Delta\epsilon E^2 \Theta - K_{11} \left(\frac{\pi}{d}\right)^2 \Theta. \tag{2.60}$$

Again, a solution of this differential equation is given by an exponential function 2.61 describing an exponential increase of the director distortion over time.

$$\Theta_0(t) = \Theta(0)\, exp\left(\frac{-t}{\tau_{rise}}\right) \tag{2.61}$$

The time constant τ_{rise} of this evolution is given by equation 2.62

$$\tau_{rise} = \frac{d^2\gamma_1}{K_{11}\pi^2}\left[\left(\frac{E}{E_{Th}}\right)^2 - 1\right]^{-1}. \tag{2.62}$$

The equations 2.57 and 2.62 are, similar to equation 2.48 for the threshold voltage V_{Th}, connected to several restrictions.

The derivation of switching times is only valid for small deviations from the initial director field distribution. At first, large displacements represent a combination of splay and bend deformation and can not be treated with one single elastic constant only. More striking is that for large distortions in the director field the electric torque is not strictly parallel to the z-direction, which influences on the direction of rotation. In this case, all three fundamental director field distortions as well as all components of the displacement field vector D have to be considered for the calculation of switching times.

As noted above by equation 2.50, weak anchoring conditions result in an increase of the apparent thickness of the cell. As the switching times τ_{rise} and τ_{decay} depend on the square of the cell thickness, weak boundary conditions increase the switching times of the liquid crystal.

2.6 Nematic liquid crystals and doping

The effect of doping a nematic liquid crystal with spherical dopants strongly depends on the dimensions of the dopant. This section aims to give a short overview over different mechanisms of interactions between spherical dopants and a nematic host for different size regimes.

2.6.1 Size effects of dopants in the nematic phase

Colloidal particles with diameters of several μm induce topological defects to the director field of a nematic liquid crystal [36]. This is caused by surface interactions of liquid crystal molecules on the spherical particles, which constraint the formation of defects in an homogeneous initial director field. The particles then carry a radial hedgehog defect of charge 1 in their interior, which requires the additional formation of defects in the nematic surrounding to give a configuration with total charge zero. For particles with homeotropic boundary conditions, theoretical calculations predict three different possible director distortions [37], [36]. They are given by an hyperbolic hedgehog (figure 2.14,(a)), a hyperbolic disclination ring (figure 2.14,(b)) or a quadrupolar Saturn-ring defect (figure 2.14,(c)). As shown by Fukuda and co-workers [38], the particle radius r influences on the energy of the Saturn-ring effect only, while the energy of the hyperbolic disclination ring is not affected by particle size. For decreasing r the energy of the Saturn-ring defect decreases logarithmically, so for small particle this defect type gives a minimum in the free energy F. Detailed experimental investigations on these defects by confocal fluorescence polarizing microscopy are given by Matthias et al. in reference [39]. Colloidal particles with strong degenerate planar anchoring conditions induce a pair of point defects called boojums [40]. In recent own work, a comparable director field distribution around microdisc resonators with planar boundary

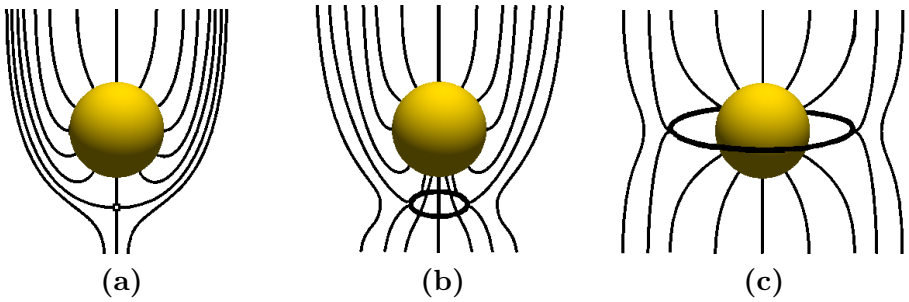

Figure 2.14: Schematic drawings of the three possible particle induced distortions in the director field around a spherical colloidal particle with strong homeotropic anchoring conditions. (a) Hyperbolic hedgehog, (a) hyperbolic disclination ring and (c) Saturn-ring configuration. Drawings adapted from reference [36].

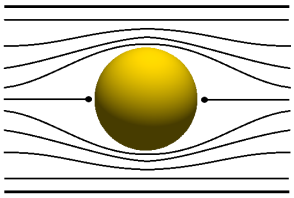

Figure 2.15: Schematic drawing of the particle induced distortion in the director field around a spherical colloidal particle with strong planar anchoring conditions.

conditions has been verified experimentally by fluorescence confocal polarizing microscopy [41].

Poulin et al. showed that colloidal particles in this size regime can arrange to one-dimensional arrays by sharing topological defects [37]. The driving force for this self-assembly of particles is the minimization of the elastic part of free energy density, as topological defects represent a highly distorted director field. As shown by Ravnik et al. in reference [42], this tendency to minimize the elastic free energy density can be used to entangle colloidal particles and to obtain one-, two- or even three-dimensional arrays of entangled particles.

Comparing the surface alignment energy given by the Rapini-Papoular energy multiplied by the surface of a single particle with the elastic free energy density of the bulk reveals that the surface energy scales as a^2, while the bulk energy scales as a only. In consequence, the influence of surface energy decreases with decreasing particle size, and the director orientation on the surface is more and more dominated by the bulk properties. Lubensky et al. estimated a critical particle radius $r_{c,1}$ above which strong anchoring conditions can be assumed to be $\approx 300\,\mathrm{nm}$ [36]. Below this value, the above mentioned formation of topological defects is less likely to occur, and for significantly smaller particles an influence of the boundary conditions of the particles on the director field is not expected.

However, also particles with smaller diameters than $d = 2 \cdot r_{c,1}$ show an attraction towards topological defects and areas of high elastic energy density in nematic liquid crystals,

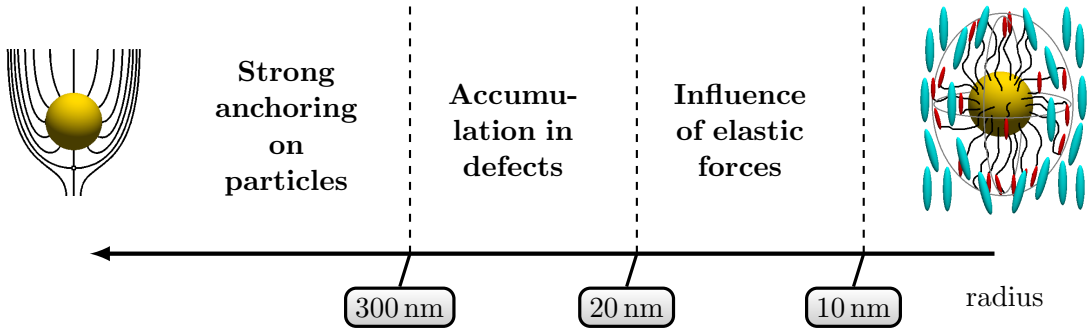

Figure 2.16: Schematic drawing illustrating size effects of dopants in a nematic liquid crystalline host. With decreasing radius dimension, at first the formation of defects due to strong anchoring conditions vanishes. Secondly, no accumulation of particles in defect free regions of the director field is observed, while particles smaller than 10 nm even cannot be dragged by the nematic to isotropic phase front. The radii of all particles investigated in this work are smaller than 10 nm, and therefore located at the very right end of this scheme.

as shown by Voloschenko et al. in reference [43]. Driving force for this mechanism is the elimination of nematic order within the volume of the particle. The authors estimate the energy gain of placing a particle at a location with highly distorted director field and find a sufficient reduction of elastic free energy density in the excluded volume in order to trap particles. This mechanism holds down to a critical particle radius of $r_{c,2} \approx 20\,\text{nm}$ at room temperature to occupy regions with high elastic energy. For smaller particles the gain in free energy is not sufficient to overcome the Brownian motion of molecules, and the particles are expected be randomly dispersed in the liquid crystalline host.

A third critical radius of $r_{c,3} \approx 10\,\text{nm}$ is given by West and co-workers in reference [44] for the drag of particles along an nematic-isotropic interface. In the isotropic phase, elastic forces due to orientational ordering of molecules are absent, while the nematic order can induce these elastic forces on a dispersed particle. West et al. showed that the onset of elastic forces at a moving interface between the nematic and isotropic phase can drag particles along the interface. While the elastic force scales as a^2, the opposing viscous drag scales as a. The authors showed that in consequence only for particles larger than $r_{c,3}$ the elastic forces can overcome the viscous drag and move the particles. Smaller particles are not affected by the moving phase interface.

In conclusion, spherical nanoparticles in a size regime smaller than 10 nm should neither induce topological defects, nor be attracted by regions of high elastic energy. However, the reduction of dimension also gives rise to new interactions which can prevent the homogeneous dispersion in a nematic host. Therefore, some special physical properties of nanoscopic particles are presented in the following subsection.

2.6.2 Nanoparticles

While the physical properties of macroscopic objects are mainly determined by the bulk atoms, the ratio of surface atoms increases for very small objects and the physical properties can dramatically change. The ratio $\frac{N_S}{N_V}$ between surface atoms and bulk atoms can roughly be estimated for transition metals by the empirical law

$$\frac{N_S}{N_V} \approx \frac{1}{2R}, \tag{2.63}$$

where R is the radius of a single nanoparticle in nm [45]. As can be seen from equation 2.63, the number of surface atoms scales with the diameter and for small particles a high ratio of particles is located at the surface. This leads to a strong influence of the surface atoms on the physical properties of the nanoparticles, which are dominated by the tendency to minimize the surface tension by changing shape and size or by agglomeration.

In the synthesis of nanoparticles, the shape and the size distribution of particles depends on the growth conditions. Below the melting temperature of a material the formation of a crystalline structure from solution gains the melting enthalpy ΔG_m of the crystal, which is the driving force of crystal growth. However, for very small nuclei the increase in surface energy by the formation of clusters requires energy. The following derivation follows the classical nucleation theory, a detailed overview is, for example, given in reference [31].

The gain in enthalpy ΔG_V by the crystallization of atoms to a cluster depends on the size of particles and therefore scales as r^3

$$\Delta G_V = -\frac{4}{3}\pi r^3 \left|\Delta G_m\right|. \tag{2.64}$$

On the other side, the formation of particles increases the surface enthalpy $\Delta G_A = \gamma \Delta A$, which therefore scales as r^2

$$\Delta G_A = 4\pi r^2 \gamma. \tag{2.65}$$

Combining equations 2.64 and 2.65 yields the total enthalpy change ΔG_{tot}, which is shown by equation 2.66

$$\Delta G_{tot} = \Delta G_V + \Delta G_A = \frac{4}{3}\pi r^2 \Delta G_m + 4\pi r^2 \gamma. \tag{2.66}$$

As can be seen from figure 2.17, the different scaling of ΔG_V and ΔG_A with the radius r results in a critical radius r_c, above which the growth of particles reduces the total free enthalpy ΔG_{tot}. This radius is given by equation 2.67

$$r_c = -\frac{2\gamma}{\Delta G_m} \tag{2.67}$$

and depends on the ratio of surface tension γ and the melting enthalpy ΔG_m. The formation of a small nuclei requires energy and therefore at first increases the total free enthalpy ΔG_{tot}. Only above a certain critical radius r_c of particles the gain in ΔG_m dominates and thermodynamically stable nanoparticles are formed. This influence of size on the stability of particles leads to a growth process called Ostwald-ripening, where after an initial nucleation step small particles below the critical radius r_c can resolve in order to release atoms

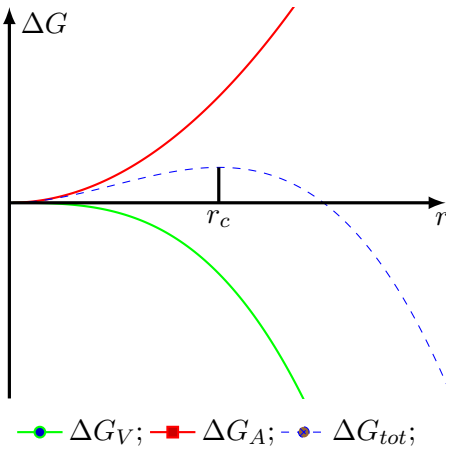

Figure 2.17: Qualitative size dependence of ΔG_V, ΔG_A and ΔG_{tot} from the particle radius r. Only above a critical radius r_c a stable nucleus is formed, which can grow to a macroscopic crystal.

which then assemble to larger clusters. Assuming this mechanism of particle growth, the number of particles growing above the critical radius is smaller than the number of initial nuclei. Additionally, the size distribution is not monodisperse, as Ostwald-ripening leads to a broadening of size distribution.
Under conditions of thermodynamic equilibrium, the shape of a crystal is determined by a minimum in the total surface energy E_S

$$E_S = \sum_i \gamma_i A_i = \ min, \tag{2.68}$$

where the index i addresses different crystal surfaces A_i with the specific surface energies γ_i [45]. While for liquids this condition of minimizing the total surface energy E_S leads to the formation of spherical droplets, a nanometric crystal cannot be fully spherical. The stability of nanoparticles then depends on the number of particles at the surface with missing neighbors. This number is minimized for particles building a periodically layered polyhedron. Such particles are in particular stable, the number of atoms required for such particles are referred to as magic numbers. An overview over the series of magic numbers associated with different polyhedra is given in table 2.1.

Table 2.1: Magic numbers of different polyhedra.

Polyhedron	**magic numbers**							
Icosa-/cubo-octahedron	13	55	147	309	561	923	561	923
Truncated decahedron	75	100	146	192	238	247	268	318
Truncated octahedron	38	116	201	225	314	405	807	1289

In order to stabilize nanoparticles with small diameters and prevent agglomeration or Ostwald-ripening, an organic ligand shell can be used to deactivate the surface. The choice

of ligands has a significant influence on the chemical compatibility with solvents or liquid crystalline hosts. While hydrophobic ligands increase the solubility in organic solvents, ionic ligands can be used to obtain charged particles dissoluble in water [46]. The use of laterally [47] or terminally [48] bound mesogenic units in the ligand shell can lead to a liquid crystalline behavior of nanoparticles themselves, and also improve the intermolecular interactions between liquid crystalline host molecules and the ligand shell [49].

The nanoparticles used in this work feature core diameters between 1.6 nm and 5.4 nm and are all coated with an hydrophobic organic ligand shell. The dimensions of the functionalized particles can be therefore estimated to be slightly larger than the core diameters. For comparison, the molecular size of the host 5CB is given by ≈ 2.5 nm in length and ≈ 0.5 nm in width.

2.7 Microscopy on liquid crystals

Optical microscopy is a very versatile tool for investigations on liquid crystals. In the frame of this work, polarizing optical microscopy as well as confocal microscopy techniques are used to investigate the influence of nanoparticles on nematic liquid crystals. Therefore the following section aims to give a brief overview over these techniques and their benefits in investigating nematic liquid crystals.

2.7.1 Polarizing optical microscopy

Polarizing optical microscopy is a standard tool in the identification of liquid crystalline phases, phase transition temperatures or alignment and defect studies in liquid crystalline materials. It consists of a conventional light microscope with additional polarizers, which allow to study the birefringence of samples placed between them. By rotating or tilting the liquid crystalline sample between crossed polarizers, the optical axes of the material can be identified.

One fundamental drawback of polarizing optical microscopy in the investigation of director fields is the lack of resolution along the axis of observation. The intensity at any lateral point in the observation plane represents only the integrated birefringence over the complete sample thickness. Information about the birefringence at different axial positions is not accessible with conventional microscopy.

2.7.2 Confocal microscopy techniques

Since the 1950s, other microscope techniques allow to overcome the restriction in axial resolution in conventional microscopes. For example, in 1955 Marvin Minsky invented the confocal microscope technique that allows to resolve images not only laterally, but also axially [50] (patented 1957, [51]). Since then, the basic principle of confocal microscopy remained unchanged: Light of a point-like light source or a laser is focused onto the sample using a high aperture objective. The reflected or re-emitted light is then collected by the same objective and focused on a pinhole, which is located in front of the light detector. With this setup, only light from the focal plane can pass the pinhole and be registered in

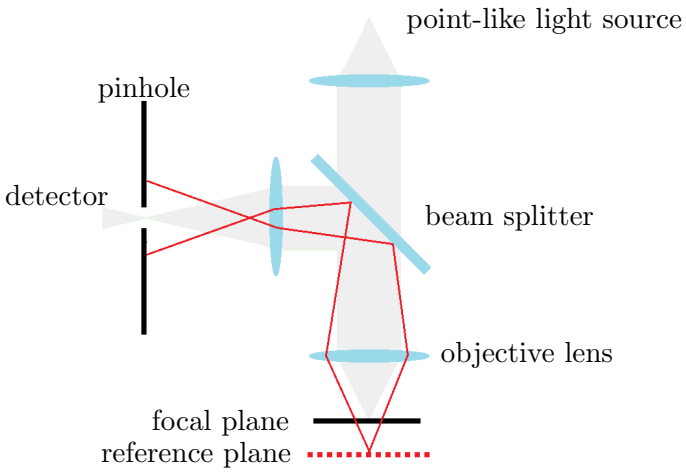

Figure 2.18: Schematic working principle of a confocal microscope: Only light from the focal plane can pass the pinhole in front of the detector, light from other planes is blocked and can not reach the detector.

the detector, light coming from other planes will be filtered by the pinhole. The principle setup of this microscope technique is shown in figure 2.18. This technique is named confocal microscopy, since the focal points of excitation light and reflected light coincide. Being a scanning probe microscope technique, the confocal microscopy does not give a direct image of the sample, but requires a point-by-point measurement. Unlike other scanning probe microscope techniques such as atomic force microscopy, the scanning probe in confocal microscopy is a small volume of highly focused light, the so-called voxel. For at least partially transparent samples, this offers the opportunity of arbitrary scans through the material without being restricted by the samples surface.

Fluorescence confocal microscopy

When samples show fluorescence by themselves or if they can be doped with small amounts of fluorescent dyes, fluorescence confocal microscopy is a powerful tool for three- dimensional imaging. Especially biologists use this technique for investigations on bacteria, living cells or in-situ measurements in living organisms [52]. In the research field of liquid crystals, fluorescence confocal microscopy can be used to image the spatial distribution of fluorescent species dispersed in a liquid crystal, for example of luminescent quantum dots in a nematic nanoparticle dispersion.

Fluorescence confocal microscopy requires an additional filter in front of the detector to extract the excitation wavelength, so that only re-emitted fluorescence light is detected. Considering that fluorescent light usually consists of a broad energy distribution, for practical applications only the fluorescence wavelength with highest intensity is used to estimate the maximum resolution in a fluorescence confocal microscope measurement. The theoretical

resolution is then given by

$$\begin{aligned} \Delta z_{conf} &= \frac{1.26 \cdot n \cdot \lambda_{gm}}{NA^2} \\ \Delta r_{conf} &= \frac{0.32 \cdot \lambda_{gm}}{NA} \end{aligned} \tag{2.69}$$

with $\lambda_{gm} = \sqrt{\lambda_{ex} \cdot \lambda_{em}}$ [53].

The resolutions given by equations 2.69 assume an arbitrary small pinhole diameter, which allows highly selective detection of light of the focal plane only. In practice, only finite pinhole diameters can be used, and the choice of diameter influences on the resolution of the confocal measurement. In order to quantify this effect, the normalized pinhole diameter v_p can be used, which is given by relation 2.70

$$v_p = \frac{2\pi \cdot d}{\lambda_{ex} \cdot m} \cdot NA, \tag{2.70}$$

with d being the physical diameter of the pinhole, m the magnification of the Objective and NA the numerical aperture of the objective. High resolution measurements are possible for normalized diameters $v_p \leq 2.5$, above $v_p \geq 4$ only the axial resolution of a conventional bright field microscope is obtained [54].

Fluorescence confocal polarizing microscopy

By adding polarizers to a fluorescence confocal microscope, the benefits of optical polarizing microscopy and fluorescence confocal microscopy are combined. This technique is a powerful method to visualize the director field distribution in three-dimensions, as in contrast to normal polarizing microscopy the confocal setup allows to detect birefringence not only laterally, but also along the axis of observation. As liquid crystals usually show no suitable fluorescence, a small amount of an anisometric dichroic dye is added to the nematic phase. According to the guest-host mechanism, the dye molecules orient along the local director of the nematic phase [24]. If the orientation of the transition dipole moment $\vec{M}$ of the dye to the long axis of the dye molecule is known, the detection of fluorescence intensity between crossed polarizers allows the three-dimensional imaging of the director field distribution for an homogeneous distribution of dye.
Assuming the transition dipole moments for absorption $\vec{M}_{abs}$ and emission $\vec{M}_{em}$ are parallel to the long axis of dye molecules and the excitation light $\vec{E}_0$ is linearly polarized, the absorbed light intensity is given by

$$I_{abs} \propto \left(\vec{M}_{abs}\vec{E}_0\right)^2 = \left(\left|\vec{M}_{abs}\right| \left|\vec{E}_0\right| cos\left(\zeta\right)\right)^2. \tag{2.71}$$

Assuming further that the rotational relaxation time τ_{rot} of the dye is slow compared to the lifetime τ_{excite} of the excited state, the orientation ζ' of dye during re-emittance of light can be considered identical to the orientation ζ during absorption. For the dichroic dye BTBP (n,n'-bis(2,5-di-tert-butylphenyl)-3,4,9,10-perylendicaboximid) used in this work, Lavrentovich showed that this is a reasonable assumption [55], so that the rotation of dye

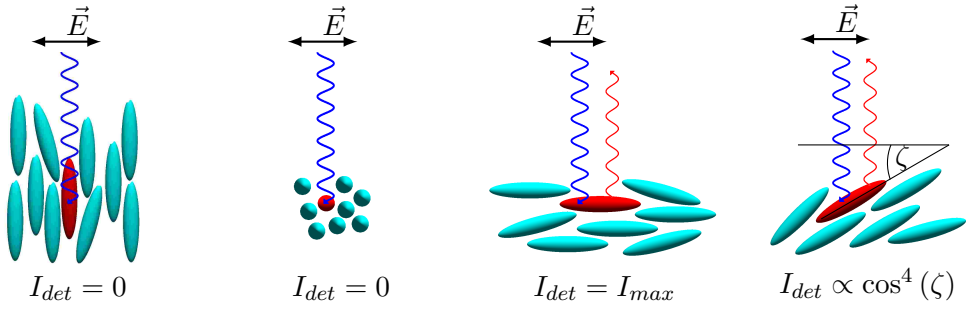

Figure 2.19: Schematic drawings of detectable fluorescence intensity I_{det} for different orientations of fluorescent dye in a nematic host. If the transition dipole moment of the dye $\vec{M}$ and the polarization of the incoming excitation beam $\vec{E}$ are perpendicular to each other, no fluorescence intensity is detected. For a parallel orientation of $\vec{M}$ and $\vec{E}$ the highest intensity is detected, in the general case the intensity depends on $I_{det} \propto \cos^4(\zeta)$.

can be neglected. The detectable light intensity is then given by

$$I_{det} = I_{abs}\left(\vec{M}_{em}P\right)^2 = I_{abs}\left(\left|\vec{M}_{abs}\right|\left|\vec{E}\right|\cos^2(\zeta')\right). \tag{2.72}$$

With $\zeta = \zeta'$ follows

$$I_{det} = \left(\left|\vec{M}_{abs}\right|\left|\vec{M}_{em}\right|\left|\vec{E}_0\right|\left|\vec{E}\right|\right)^2 \cdot \cos^4(\zeta). \tag{2.73}$$

In consequence, the detectable light intensity scales with the angle ζ between the excitation light and the transition dipole moment $\vec{M}$ over the relation 2.74

$$I_{det} \propto \cos^4(\zeta). \tag{2.74}$$

The high sensitivity of I_{det} to the angle α allows the detection of even very small director field fluctuations. Four fundamental orientations of dye and excitation field are shown in figure 2.19. In cases where $\vec{M}$ is perpendicular to the plane of polarization of the exciting light, no fluorescence intensity can be detected. For parallel alignment of $\vec{M}$ and $\vec{E}$, the maximum fluorescence intensity can be detected. In the general case of arbitrary orientation of $\vec{M}$ and $\vec{E}$, the intensity scales by $\cos^4(\zeta)$ as given by equation 2.74.

The spatial resolution of fluorescence confocal polarizing microscopy is given by equation 2.69. However, as liquid crystals can form optically anisotropic phases birefringence has to be considered, which reduces the spatial resolution. This effect increases with increasing scanning depth d, and can roughly be estimated by equation 2.75

$$\Delta x = \frac{\Delta n}{\bar{n}} d. \tag{2.75}$$

Additionally, nematic liquid crystals strongly scatter light, which reduces the detectable fluorescence intensity. This effect also scales with the scanning depth d and can only partially be compensated by an increase of excitation light intensity. A high spatial resolution with good contrast is obtained for materials with low birefringence and for measurements using small scanning depths only.

3 Experimentals

3.1 Materials

In this work, nanoparticles made of gold or CdSe with different core sizes, dispersity and functionalization are dispersed in two different nematic hosts. The synthesis of these particles is not part of this work. They are either purchased from Sigma Aldrich or kindly provided by Prof. Hegmann's group[1] and Prof. Goodby's group[2]. Details on synthesis and characterization are reported in the respective citations given below. The following section provides a short overview of the materials used.

3.1.1 Nanoparticles

Gold nanoparticles

Nanoparticles with gold cores are found to be promising candidates for metamaterials if arranged regularly in a liquid crystalline host [14]. Spherical gold particles with core diameters $< 10\,\text{nm}$ are easily accessible via the Brust-Schiffrin method [56], and a variety of functionalization methods have been reported recently [49], [57], [58]. In this work, alkylthiol capped gold particles with different core sizes are investigated (particles AuSH6, AuSH12, see table 3.1), based on earlier work by Prof. Hegmann. As a comparison, mesogenic coated particles with very similar core diameters (AuCB) are investigated to compare the effect of mesogenic or non-mesogenic coating of particles on the properties of nanoparticle / liquid crystal dispersions. Finally, hydrophobic silanized gold particles (AuSi) are studied, which exhibit a more stable ligand binding compared to the aliphatic or mesogenic coated particles. This allows to draw conclusions about the role of ligand stability on dispersion properties. The nanoparticles with gold cores used in this work are listed in table 3.1.

Table 3.1: Investigated gold nanoparticles

Particles	Functionalization	Diameter [nm]	Source
AuSH6	hexanethiol	1.6	Hegmann et al. [59]
AuSH12$_{(s)}$	dodecanethiol	1.93 ± 0.47	Hegmann et al. [60]
AuSH12$_{(m)}$	dodecanethiol	3.82	Sigma Aldrich
AuSH12$_{(l)}$	dodecanethiol	5.4	Hegmann et al. [59]
AuCB	5OCB-undecylthiol	2.36	Goodby et al. [14]
AuSi	octadecyl-silane	4.2 ± 0.58	Hegmann et al. [61]

[1] Prof. Dr. Torsten Hegmann, Department of Chemistry, University of Manitoba, Winnipeg, Canada and Liquid Crystal Institute, Kent State University, Kent, USA

[2] Prof. Dr. John W. Goodby, Department of Chemistry, University of York, York, England

The hexanethiol capped particles AuSH6, the small diameters dodecanethiol functionalized particles AuSH12$_{(s)}$ and the large diameter dodecanethiol capped particles AuSH12$_{(l)}$ were synthesized in Prof. Hegmann's group by Dr. Hao Qi, following a Brust-Schiffrin approach [56]. Characterization data can be found in reference [62]. The dodecanethiol capped particles AuSH12$_{(m)}$ with medium core diameter were purchased from Sigma Aldrich as a 2 % (w/v) solution in toluene. Mesogenic functionalized particles capped with 11-(4′-cyanobiphenyl-4-yloxy)undecylthiol (AuCB) were synthesized by Dr. Michael Draper following the Hutchinson ligand exchange method [63] and were kindly provided by Prof. Goodby's group. The characterization of these particles can be found in references [49] and [14]. Gold particles conjugated by octadecyl-silane (AuSi) were synthesized by Javad Mirzaei in Prof. Hegmanns group. A detailed characterization of the latter is given in reference [61].

CdSe nanoparticles

Semiconductor nanoparticles are promising candidates for use in medical or photonic applications because of their interesting electronic and photonic properties. Dispersions of semiconductor nanoparticles in liquid crystalline materials have been studied over the last years. A recent review is given in reference [64]. For the experimental investigation of nanoparticle / liquid crystal dispersions, one benefit of the use of fluorescent CdSe particles is the possibility to perform fluorescence confocal microscopy studies to investigate the distribution of particles within the dispersion. Particles of the Lumidot^{TM}- series from Sigma-Aldrich with a maximum emission wavelength of 590 nm (CdSe590) have been shown to exhibit distinct effects on alignment and electro-optic properties [13]. In this work, these particles are dispersed in two different nematic hosts to investigate host effects. In addition, slightly larger CdSe particles with a maximum emission wavelength of 610 nm (CdSe610) are dispersed in the same two hosts as well, to study effects of different core sizes in different hosts. The influence of polydispersity is investigated by the use of magic sized CdSe nanoparticles with very narrow size distributions (msCdSe). A slight modification of core composition reveals additional information about the influence of core material (msCdSe:Zn). The investigated nanoparticles with semiconducting CdSe or CdSe:Zn cores are shown in table 3.2.

Table 3.2: Investigated CdSe nanoparticles

Particles	**Functionalization**	**Diameter** $[nm]$	**Source**
CdSe590	hexadecylamine	$4.0 - 4.3$	Sigma Aldrich
CdSe610	hexadecylamine	$4.7 - 5.2$	Sigma Aldrich
msCdSe	myristic acid	2.0 ± 0.1	Hegmann et al. [65]
msCdSe:Zn	myristic acid / trioctylphosphine	2.0 ± 0.1	Hegmann et al.[65]

The hexadecylamine capped quantum dots CdSe590 and CdSe610 were purchased from Sigma-Aldrich as a 5 % (w) solution in toluene. They belong to the Lumidot^{TM}- series and exhibit a maximum in fluorescence emission at 590 nm or 610 nm, respectively. The

monodisperse magic size quantum dots msCdSe and msCdSe:Zn were synthesized by Javad Mirzaei in Prof. Hegmann's group, the characterization of these particles can be found in reference [65].

3.1.2 Liquid crystalline hosts

The liquid crystalline materials 4-cyano-4'-pentylbiphenyl (5CB, Synthon Chemicals) and 5-n-heptyl-2-(octyloxy-phenyl)pyrimidine (FELIX-2900-03, Synthon Chemicals) are used as nematic hosts for dispersing the nanoparticles. The liquid crystal 5CB is one of the workhorses in liquid crystal research and therefore numerous physical properties for the pure compound as well as studies on several nanoparticle dispersions with this host are available in literature. Thus, this host material is well suited to compare physical properties of the pure liquid crystal with nanoparticle doped samples and to classify the results in comparative studies on other nanoparticle / 5CB dispersions.

The host material FELIX-2900-03 provides superior solubility of different hydrophobic nanoparticles compared to 5CB ([12], [13], [61], [65]). Although literature does not provide a complete characterization of physical properties, this material is a promising candidate for stable dispersions. An overview of important physical properties of these two host materials is given in table 3.3.

Table 3.3: Nematic LC hosts

LC host	Phase sequence	Δn	$\Delta\epsilon$
5CB	Cr 22,5 N 35 Iso	0.19	+11.76
FELIX-2900-03	Cr 52 (SmA 45) N 72 Iso	0.14	+0.55

3.2 Dispersion preparation

For investigating the effects of nanoparticle doping on nematic liquid crystals, the nanoparticles need to be homogeneously dispersed in the nematic host material. The dispersions of AuSi-particles in FELIX-2900-03 as well as msCdSe and msCdSe:Zn particles in FELIX-2900-03 were prepared by Javad Mirzaei in Prof. Hegmann's group and provided already filled in liquid crystal test cells (LC Vision, USA). The dispersion of $AuSH12_{(s)}$ in FELIX-2900-03 was prepared by Brandy Kinkead in Prof. Hegmann's group and provided filled in test cells from Instec, Inc (USA). Dispersions of AuSH6 and $AuSH12_{(l)}$ in FELIX-2900-03 were prepared in our laboratory in collaboration with and under guidance of Brandy Kinkead. Dispersions of the remaining gold ($AuSH12_{(m)}$, AuCB) and CdSe (CdSe590, CdSe610) nanoparticles are prepared in own work by dispersing the particles in the nematic hosts 5CB and FELIX-2900-03. An overview over the dispersions investigated in this work is given in table 3.4.

To ensure that only property changes due to nanoparticle doping are investigated in microscopic and electro-optical studies, a complete removal of organic solvents has to be ensured. Thus, the liquid crystal 5CB is solved in a small amount of dichloromethane and the liquid

Table 3.4: Overview of the nanoparticle / liquid crystal dispersions and the respective concentrations investigated in this work.

Particles	**Host**	
	FELIX-2900-03 [%(w/w)]	**5CB** [%(w/w)]
AuSH6	3.0	
AuSH12$_{(s)}$	5.0	
AuSH12$_{(m)}$		0 - 2.5
AuSH12$_{(l)}$	3.0	
AuCB		0 - 5.0
AuSi	0 - 7.5	
CdSe590	0 - 2.5	0 - 2.5
CdSe610	0 - 5.0	0 - 2.5
msCdSe	0 - 5.0	
msCdSe:Zn	0 - 5.0	

crystal FELIX-2900-03 is dissolved in toluene, followed by subsequently removal of solvent under varying conditions. A method that restores the initial phase transition temperatures compared to the undissolved liquid crystals is then considered to completely remove all solvent. However, due to the reactive properties of small nanoparticles, special requirements have to be fulfilled.

As it is known that the treatment of functionalized nanoparticles under high temperatures in the presence of other ligand molecules may lead to ligand exchange reactions [58], high temperatures were avoided. Although ligand exchange reactions are very useful and utilized in the synthesis of different kinds of functionalized particles, they are not desired in the preparation of dispersions. Furthermore, high temperatures enhance the rate of Oswald ripening, thereby changing the core parameters of the nanoparticles. It is shown in literature that boiling dodecanethiol capped gold particles with small cores in toluene for several hours leads to gold particles with larger core diameters (see references [61], [66]).

In consequence, high temperatures are avoided where possible in the preparation of dispersions to prevent ligand exchange reactions and Oswald ripening. It is found that stirring the solution of liquid crystal and solvent at a temperature just below the boiling point of the solvent for 24-36 hours in a steady flow of argon (Method A) does not completely remove the solvent (see figure 3.1). Only an additional treatment under reduced pressure ($p < 5.0 \cdot 10^{-3}$ Pa, Method B) leads to the complete removal of solvent. This is confirmed by identical phase transition temperatures and electro-optical switching parameters of the solvent treated sample compared to the pure 5CB. It should be noted that the use of vacuum in the preparation of solvents might change the composition of nematic host, when the host material is not a pure compound but a mixture of different liquid crystals. In this work only pure compounds are used for dissolving nanoparticles. Thus, the use of vacuum can not affect the solvent-free liquid crystal composition.

In a first step of preparation, the particles are dissolved to a homogeneous, agglomerate free solution. As the particles AuSH12$_{(m)}$, CdSe590 and CdSe610 purchased from Sigma-Aldrich

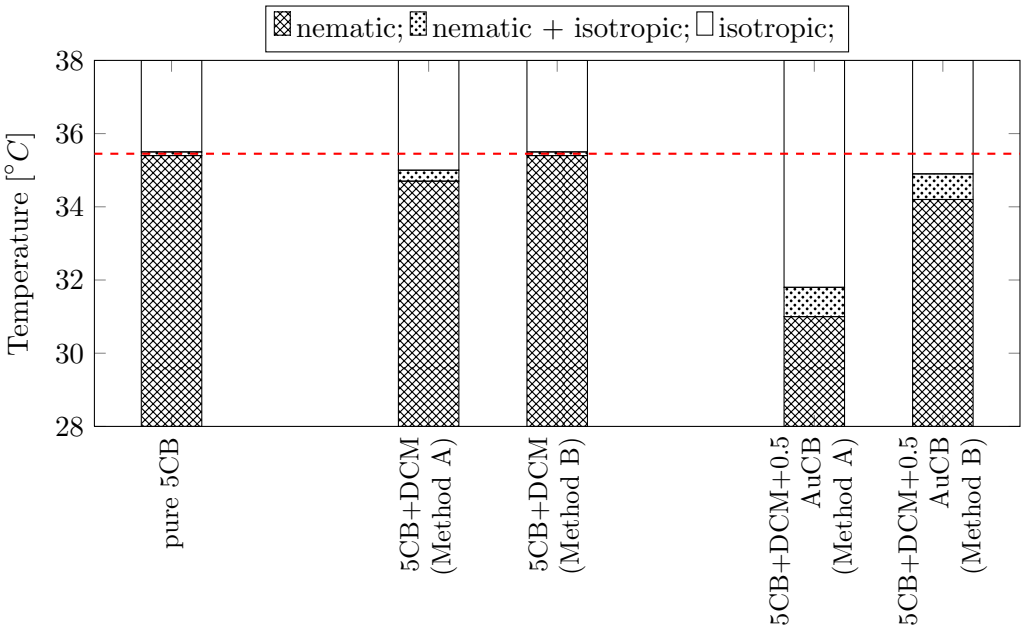

Figure 3.1: Study of the influence of solvent on the clearing temperature T_{NI}. The clearing temperature is investigated optically for pure 5CB (left column), solvent treated 5CB (center columns) and nanoparticle doped 5CB (right columns). It is found that temperature treatment only (Method A) does not completely remove the solvent, as the phase transition temperature remains lowered. Only additional removal of solvent under low pressure ($p < 5.0 \cdot 10^{-3}$ Pa, Method B) restores the initial phase transition temperatures. It is then assumed that the decrease and broadening of phase transition in the nanoparticle doped sample after treatment with Method B is not an effect of solvent, but caused by the presence of nanoparticles.

are already solved in toluene, only the particles AuCB have to be solved in our laboratory. The solvent dichloromethane is reported to exhibit a good solubility for these particles [14]. Thus, a small amount of particles (typically 3-5 mg) was dissolved in $\sim$ 500-1000 µL solvent under mechanical stirring and mild temperatures (max 40 °C). In addition, ultra-sonication is used to promote the solution process by applying short pulses (Bandelin Sonorex RK 255, 160 W, 35 kHz, 15 s every 60 min). As ultra-sonication leads to a mechanical rubbing of particles and therefore might lead to a loss of ligands, it is considered not suitable for long term use in the preparation of dispersions.

Subsequently, the nanoparticle / liquid crystal dispersions are prepared by mixing the nanoparticle solution and a solution of dissolved liquid crystal in the desired ratio and removing the solvent under mechanical stirring at moderate temperatures and low pressure treatment (Method B). The resulting dispersions are found to differ in stability, even under identical treatment. The same particle / host dispersion can sometimes show severe agglomeration, while another preparation attempt gives a optically homogeneous dispersion with no signs of agglomeration. Only dispersions with no signs of agglomeration were filled into test cells and used for further experiments. It should be noted that once a homogeneous dispersion has been filled in a test cell without visible agglomeration, agglomeration is not found to occur within the test cell even after long time and the sample can be considered stable.

Test cells

For investigating the alignment and electro-optical properties of dispersions, different home made or commercially available test cells are filled with the liquid crystalline dispersion by capillary forces. For this purpose, the dispersions are heated to the isotropic phase and a small droplet of the mixture is placed by a glass capillary next to the cover glass of the test cell, in a way that the liquid floats into the cell gap. It is found that filling the test cells in the isotropic phase gives less agglomeration than filling in the nematic phase, due to a higher solubility of particles in the isotropic phase.

For alignment studies on uncoated glass substrates, cleaned standard microscope glass slides (Carl Roth, 76x76 mm, cut edges) covered by microscopy cover slips (Menzel Cover Slips, 18x18 mm) are used. The substrates are successively cleaned with demineralized water and aceton, followed by treatment in O_2-plasma (Harrick Plasma Cleaner/Sterilizer model PDC-32G, 150-300 s excitation time) to completely remove organic residues. After the cleaning procedure, the glass slide and cover slip are mounted to a cell using 10 µm mylar spacer foil, clamped with inverse metal tweezers and fixed with epoxy glue (Pattex 2K). The homemade test cells usually yield cell gaps typically between 11 and 20 µm. The larger cell gap compared to the spacer thickness is explained by glue floating between substrate and cover slip before hardening, and therefore slightly lifting the cover slip.

Cell gaps are measured by placing the sample perpendicular in the beam path of a Lambda 19 UV/VIS spectrometer and measuring the transmission intensity while scanning the wavelength range between 400-800 nm. This gives an oscillating transmission spectrum due to wavelength dependent constructive or destructive interference of transmitted and on the glass / air interface reflected waves (see, for example, physics of Fabry-Pérot-Etalon,

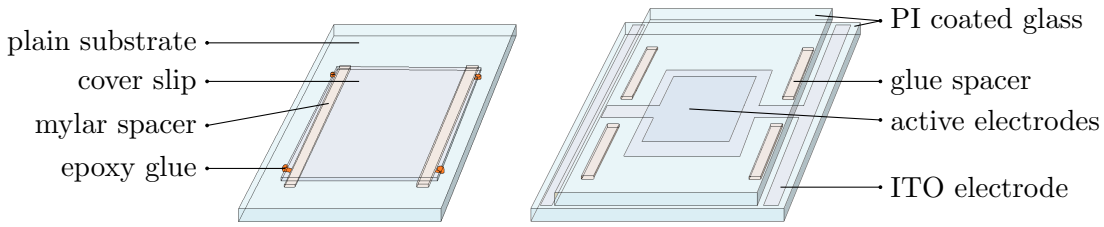

Figure 3.2: Left: Sketch of a self-made test cell with untreated glass for alignment studies. Right: Sketch of a commercially available electro-optic test cell (EHC).

[67]). For perpendicular light incidence as given here, the cell gap can be calculated from the wavelength difference between two adjacent transmittance minima or maxima, using the equation

$$d_{gap} = \frac{1}{2} \cdot \left(\frac{1}{\lambda_2} - \frac{1}{\lambda_1} \right). \tag{3.1}$$

In practice, the gap thickness d_{gap} is calculated for at least ten adjacent maxima in the spectrum and the arithmetic mean is considered as cell thickness, typically giving standard deviations smaller than 5 %. This value is mainly determined by the wavelength resolution of the spectrometer ($\Delta\lambda = 0.4\,\mathrm{nm}$).

The cell gap is measured twice for each test cell at different positions of the sample, and only those test cells are used for experiments where the mean gap thickness of the two measurements differ less than the standard deviation of both measurements. This ensures a constant cell thickness over the complete cell area.

Electro-optic experiments on samples prepared in our laboratory are performed using commercially available liquid crystal test cells from E.H.C Co.,Ltd (Tokyo, Japan). The test cells are coated with anti-parallel rubbed polyimide alignment layers for strong planar anchoring conditions (KSRP-XX/A111P1NSS05, XX = 04, 10 or 25, indicating cell gaps of 4, 10, or 25 µm, respectively). The pretilt angle of these cells is smaller than 1° [68]. The active ITO-electrode area is 10x10 mm with a resistivity of 100 Ω.

Before filling the test cells, the capacitance of the empty cell is measured on a LCR bridge (HP4274A or HP4284A, see section 3.5.1) at room temperature and a test frequency of 1 kHz with an amplitude of 0.3 V_{rms}. The cell gap is determined by the interference method described above using a Lambda 19 UV/VIS spectrometer. As shown by Wu et al. in reference [69], cell gap and capacitance of the empty cell are insensitive to temperature within the temperature range of experiments (25-75 °C) and therefore can be measured at room temperature.

Dispersions prepared in Prof. Hegmann's group are filled in commercially available electro-optic test cells either from Instec Inc, USA, or LC Vision, USA. Both test cell types exhibit cell gaps of 4 µm and parallel or anti-parallel rubbed polyimide layers for strong anchoring conditions. The pretilt angle is stated to be between 1-3° [13]. As these cells were sent to our laboratory already filled with liquid crystal / nanoparticle dispersions, data for capacitance and cell thickness of the empty cells were measured in an LCAS 1 automated liquid crystal analyzer (LC vision, USA) in Prof. Hegmann's laboratory and then provided for own measurements.

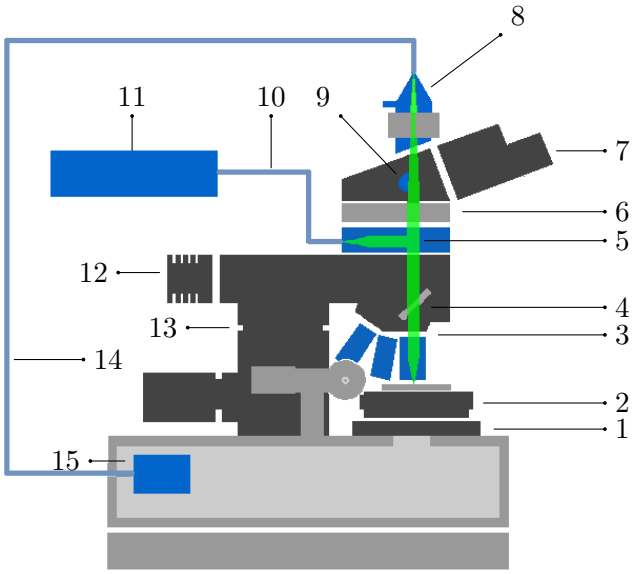

Figure 3.3: Schematic structure and beam path of the ALPHA300 in the configuration for confocal measurements (adapted from [54]). 1) xy-positioning unit 2) scanning table 3) objective revolver 4) LED-light beam splitter 5) laser-light beam splitter 6) edge filter 7) camera 8) adjusting unit for pinhole fiber 9) switch camera / fiber 10) polarization state remaining mono-mode optical fiber 11) argon ion laser 12) white LED 13) axial height control unit of microscope 14) multi-mode optical fiber 15) avalanche photo diode

3.3 Microscopy

3.3.1 Polarizing optical microscopy

Polarizing optical microscopy was carried out either on a Leitz Ortholux II Pol-BK microscope with sodium-gas lamp or on a Leica DM4500P microscope with halogen lamp and daylight filter. Macroscopic studies were performed on a Leica S6D macroscope with halogen lamp illumination. Images were captured either with a Nikon D90 consumer camera with self made microscope mount or a Leica DFC295 microscopy camera in combination with Leica Application Suite software.

3.3.2 Fluorescence confocal microscopy techniques

For fluorescence confocal measurements, the scanning microscope ALPHA300 (WITec GmbH, Germany) is used. This modular microscope combines several scanning microscope techniques like atomic force microscopy, scanning optical near field microscopy or confocal microscopy. The configuration for confocal fluorescence measurements is shown in figure 3.3. The ALPHA300 microscope does not exhibit a separate pinhole in front of the detector for confocal imaging, as the multi-mode optical fiber with a diameter of 25 µm serves as pinhole. This simplifies adjustment and ensures confocal measurements, as only light from the focal plane is focused on the fiber and therefore registered in the detector. However, the fixed diameter of the fiber allows no adjustment of pinhole diameter and therefore no resolution

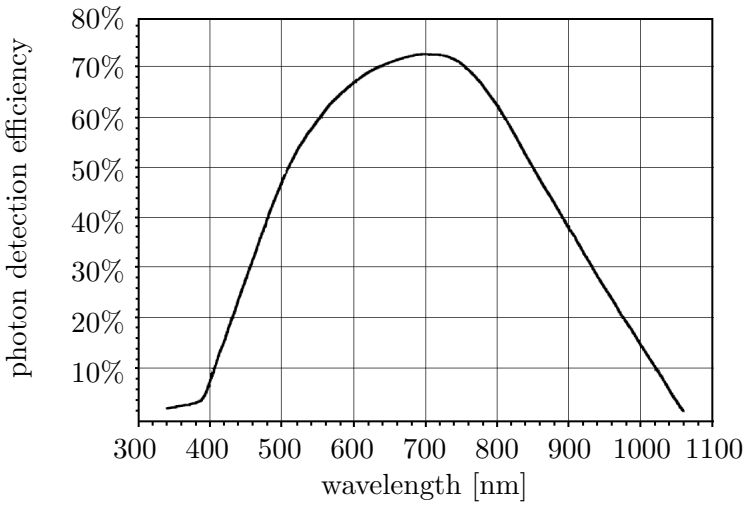

Figure 3.4: Spectral sensitivity of the avalanche photo diode [54].

maximization in combination with different microscope objectives can be carried out. An argon-ion laser ($\lambda_{ex} = 488\,\text{nm}$) is used for excitation of fluorescent species and an edge filter transmitting light only for $\lambda > 520\,\text{nm}$ is used to separate the excitation wavelength from re-emitted fluorescent light before light detection.

The detector for total fluorescence intensity measurements is an avalanche photo diode (Hamamatsu H6240-01). Its spectral sensitivity is shown in figure 3.4. For wavelength resolved measurements, a SpectraPro-2300i spectrograph (Princeton Instruments / Acton, $f = 300\,\text{mm}, f/3.9$ imaging, grating: 600 lines/mm^{-1}) with a Peltier-cooled Andor CCD detector (model DV-401-BV) is available. In order to enable the ALPHA300 for fluorescence confocal polarizing microscopic measurements, the confocal setup has to be equipped with a polarization control unit. Therefore, the beam splitter cube is replaced by an interference beam splitter for $\lambda = 488\,\text{nm}$ that preserves the state of polarization. In addition, a quarter wave plate for the excitation wavelength of 488 nm is placed between beam splitter and objective. By adjusting the angle between the optical axis of the wave plate and the plane of polarization of the exciting laser to an angle of 45°, the linearly polarized laser light is transformed into a circular polarization state. By adding a rotating linear polarizer between beam splitter and pinhole fiber, any plane of polarization of re-emitted light can be selected to be detected in the photo-diode or spectrograph. The result of experimental verification of circular polarization is shown in figure 3.5.

In a first step, the φ-angle dependent light transmission of the excitation laser through a linear polarizer is measured without retardation plate. The resulting data is then fitted to a simple model of light transmission of linear polarized light through a linear polarizer. This measurement indicates a deviation of the plane of laser light polarization of 2.8° from the x-axis of the microscope. In a second step, the same measurement is repeated with the retardation plate in the beam path under an angle of 47.8° to the x-axis of the microscope. For circular polarized light, theory predicts $I(\varphi)$ to be 50 % for any given angle φ. Although the experimental data show small deviations from this ideal behavior, the quality of polarization state is seen to be sufficient for confocal polarizing microscope imaging, as the

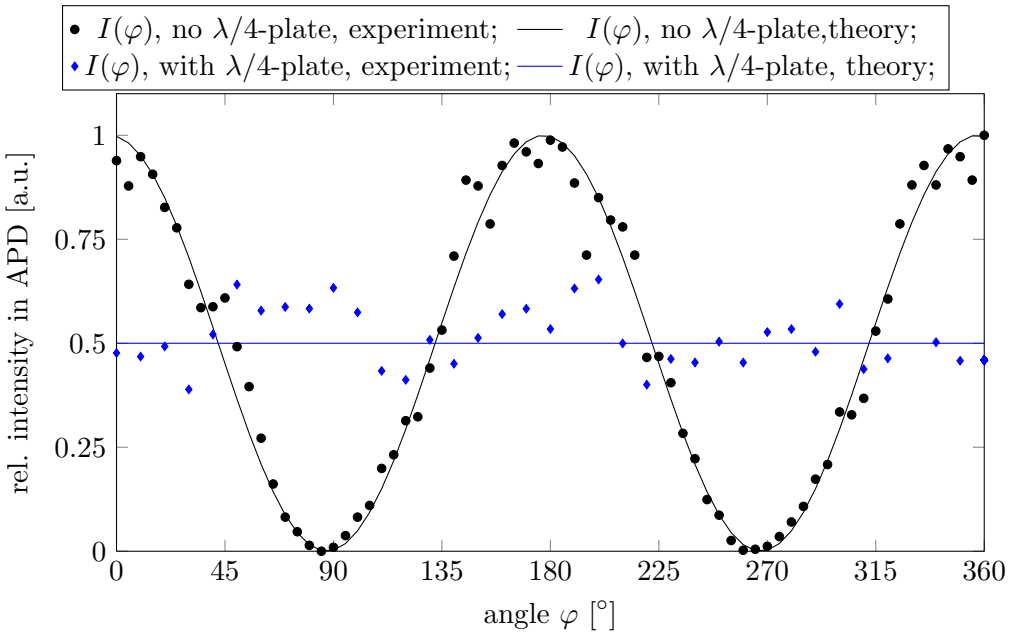

Figure 3.5: Experimental verification of circularly polarized excitation beam. By fitting the experimental transmittance data of laser light passing through a linear polarizer (black dots) to the theoretical model (black line), a deviation of the plane of laser light polarization of 2.8° from the x-axis of the microscope is found. By placing a $\lambda/4$ retardation plate in the beam path, the linearly polarized light is transformed to circularly polarized light (blue dots), whose transmission intensity is predicted to be independent of polarizer orientation (blue line).

light intensity is higher than 40 % for any plane of polarization. However, these deviations do not allow a direct comparison of measured fluorescence intensities for different states of polarization.

The resolution of confocal fluorescence measurements depends also on the proper choice of microscope objective and pinhole diameter. As mentioned above, the pinhole diameter of the experimental setup is given by the diameter of the optical fiber and therefore fixed at 25 µm. In table 3.5, the available objectives and their reachable theoretical lateral and axial resolutions ($\Delta\ r$, $\Delta\ z$) are listed.

Table 3.5: Summary of calculated objective parameters

Objective	**Cover slip correction**	v_p	Δr $[nm]$	Δz $[nm]$
Nikon 40x/0.60	yes (variable)	2.42	273	1882
Nikon 60x/0.80	yes (0.17 mm)	2.15	205	1058
Nikon 100x/0.90	no	1.45	182	836
Nikon 100x/1.25 oil	yes (0.17 mm)	2.01	131	433

As in confocal measurements the actual depth resolution of the microscope is of particular interest, Δz is determined experimentally for all four objectives by moving a silver mirror along the axial z-direction of the microscope and measuring the reflected light intensity with respect to the mirror position. The reflecting surface of the mirror represents an optical δ-

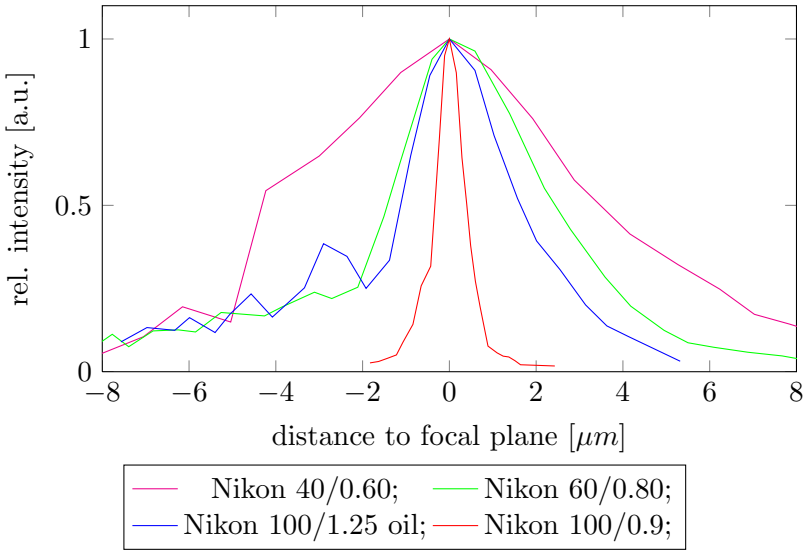

Figure 3.6: Experimental determination of depth resolution for different objectives in confocal measurements by detecting light reflected from a mirror from different axial positions. A narrow peak width indicates a high depth resolution. This is found for the Nikon 100/0.9 objective.

function in z-direction, that is blurred by the point spread function of the microscope and therefore depicted as broadened peak. The shape and peak width depend on the shape of point spread function and allow to draw conclusions on the axial resolution. A narrow peak width indicates a high axial resolution. The results of this study are shown in figure 3.6. In general, a high depth resolution is achieved using objectives with high numerical aperture. However, the choice of objective is also restricted by other factors. As the investigation of liquid crystalline materials often requires the use of a microscope cover slip, high resolution images can only be obtained with objectives that feature a cover slip correction. In addition, the use of oil immersion objectives is not suitable at high temperatures, as the viscosity and surface tension of the immersion oil changes with temperature. Consequently, the oil does not sufficiently wet the objective, but spreads on the sample surface at high temperatures. In conclusion, the Nikon 60/0.8 objective is found to be most suitable for confocal measurements on liquid crystalline samples.

3.4 Phase transition temperatures

For the determination of phase transition temperatures, polarizing optical microscopy is used. The dispersions are filled in polyimide coated electro-optic test cells by capillary forces and then rapidly heated into the isotropic phase, followed by a slow cooling to room temperature. This ensures an equilibrium state of dispersion defined by the boundary conditions of the test cell, and overcomes a possible ordered state due to filling effects. Afterwards, the samples are slowly heated in a heating stage with a controlled heating rate of 1 °C/min. Phase transition temperatures are obtained by observing changes in the microscopic textures between crossed polarizers.

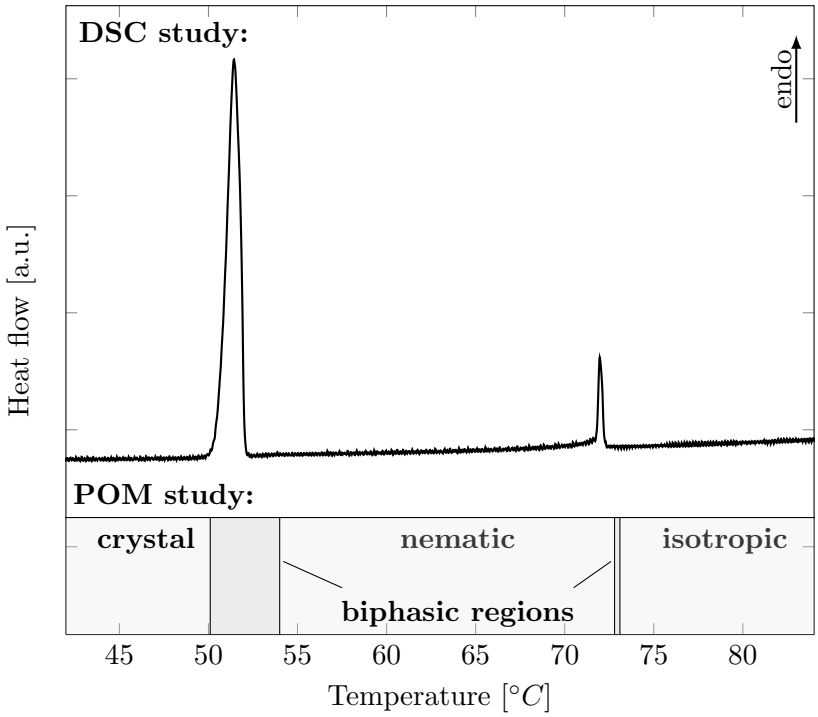

Figure 3.7: Comparison of phase transition temperatures of the pure compound FELIX-2900-03, measured by differential scanning calorimetry and optical polarizing microscopy. In general, both methods give similar transition temperatures. The optical method allows the detection of biphasic regions and thus is preferred in this work.

The use of polarizing optical microscopy over differential scanning calorimetry for measuring phase transition temperatures is justified by possible influences of local alignment changes or particle agglomerations on the phase transition temperature. These cannot be detected by DSC measurement, but are accessible by the spatial resolution of an optical method. In addition, DSC does not register the appearance of biphasic regions, while the optical detection thereof is very simple. To prove the equivalence of DSC and optical techniques, the pure compound FELIX-2900-03 characterized by DSC as well as by microscopic investigations. DSC measurements are performed on a Perkin Elmer Pyris 1 DSC at a heating rate of 1 °C/min. The resulting phase transition temperatures from DSC measurements and optical detection are found to be comparable, the results are shown in figure 3.7.

3.5 Electro-optic characterization

By means of electro-optic characterization, the physical quantities threshold voltage V_{Th}, permittivity perpendicular and parallel to the director ($\epsilon_\perp$, $\epsilon_\parallel$), dielectric anisotropy ($\Delta\epsilon$) and rise and decay times (τ_{rise}, τ_{decay}) of liquid crystals and their dispersions with nanoparticles are measured.

For this purpose, two different experimental approaches are described in the literature, the Single-Cell-method [69] and the Two-Cell-Method [70]. In the latter method, two different test cells are prepared with rubbed planar and homeotropic alignment and characterized by

dielectric measurements. The benefits of this approach are measurements of true planar and homeotropic alignment. Consequently, data for dielectric anisotropy can be very precise. Furthermore, the preparation of samples with positive and negative dielectric is identical, switching experiments can either be performed with the planar alignment cell ($\Delta\epsilon > 0$) or the homeotropic sample ($\Delta\epsilon < 0$). A drawback of this technique is that the accuracy depends on the quality of alignment layers of two samples. Thus, for a given material to be analyzed, both a high quality planar alignment layer as well as a high quality homeotropic alignment layer are needed.

The Single-Cell methods uses only one test cell with either rubbed planar ($\Delta\epsilon > 0$) or homeotropic ($\Delta\epsilon < 0$) alignment layer. By applying strong external fields, the initial director alignment is reoriented from planar to homeotropic or vice versa, and thus dielectric measurements parallel and perpendicular to the director are possible. This methods benefits from the use of one cell only. Only one high quality alignment layer is needed and errors due to the comparison of different test cells do not occur. The drawback of incomplete reorientation of director under external fields can be overcome by extrapolation to infinite field strength. Even at high field strengths, the director in the vicinity of the strong boundary surface, represented by an interfacial layer ξ_E (see equation 2.14), remains untilted, and lower values for $\Delta\epsilon$ are measured. In order to obtain true values for $\Delta\epsilon$, a linear extrapolation of capacitance at infinite field is performed. It has been shown experimentally [69],[71] and theoretically [72] that results using the Single-Cell-Method are comparable to results obtained from the Two-Cell-Method. However, the use of test cells with large cell gap ($d > 20\,\mu m$) is recommended to keep the influence of the surface induced orientation small and to obtain high quality data for linear extrapolation.

In this work, electro-optic test cells are characterized by the Single-Cell-Method as described by Wu et al. [69], with additional simultaneous measurement of light transmittance in a polarizing microscope. As is it known that dispersed nanoparticles can move to and reside on the substrate / liquid crystal interface, changing the properties of the initial alignment layer [62], it is virtually impossible to prepare two different test cells with identical surface coverage of particles, as it would be required for the Two-Cell-Method. Furthermore, dielectric measurements for both methods require homogeneous, strong alignment over the complete electrode area. As this condition can also not be guaranteed for all dispersions, additional optical measurements of local birefringence are necessary.

All investigated nematic liquid crystalline materials exhibit positive dielectric anisotropy. Thus, samples are prepared with anti-parallel rubbed polyimide alignment layers for strong planar anchoring conditions. Applying an external electric field perpendicular to the substrates then leads to an reorientation of the liquid crystal molecules to homeotropic alignment, causing a field dependent increase of capacitance and decrease of birefringence. As only test cells with smaller cell gap ($4\,\mu m$ or $10\,\mu m$) than recommended are used, the measured values for $\epsilon_{\parallel}$ and $\Delta\epsilon$ are expected to be up to 2 % smaller than actual values [69].

The experimental setup used for electro-optical characterization consists of a test cell holder with fixed connectors for electrical contacting, which is connected to a high precision LCR bridge (HP4274A or HP4284A) and placed within a heating stage. For temperature

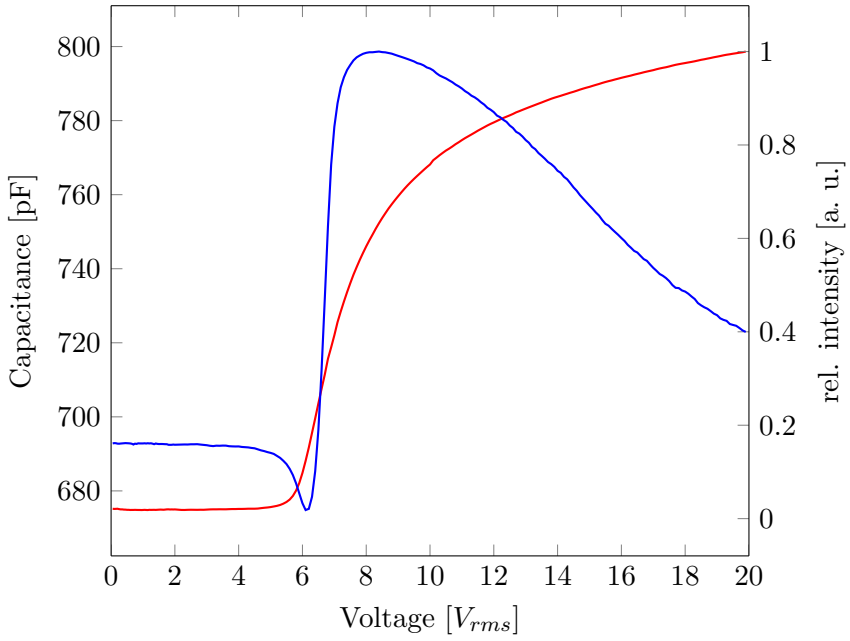

Figure 3.8: Example of data recorded in a combined capacitance / transmittance measurement for a 4 µm sample with pure FELIX-2900-03 at $T = 58\,°C$.

control, a Linkam LTS 350 heating stage with TMS 94 controller or a Mettler FP 5 heating stage are used. To perform simultaneous transmission measurements, the sample is positioned under an azimuthal angle of 45° between crossed polarizers in the beam path of a Leitz Ortholux II Pol-BK microscope, which is equipped with an Oriel photomultiplier tube for light detection. A Rhode & Schwarz AFS arbitrary function generator with Krohn & Hite amplifier model 7500 serves as additional bias supply for switching experiments. More detailed information about capacitance and transmission measurements are given in the following sections 3.5.1 and 3.5.2. A typical example of data obtained in a combined field dependent capacitance-transmission measurement is shown in figure 3.8.

3.5.1 Capacitance measurements

Capacitance measurements were either performed on a HP4274A LCR bridge or on a HP4284A LCR bridge, each at a test frequency of 1 kHz. The HP4274A LCR bridge is capable of a maximum test signal level of $5\,V_{rms}$ only, which is not sufficient to completely reorient the liquid crystal within the test cell. Thus, for measurements of the quantity $\epsilon_{\parallel}$ an external DC bias of up to 35 V was used for reorientation. For this purpose, a Rhode & Schwarz AFS arbitrary function generator in combination with a Krohn & Hite model 7500 amplifier were connected to the external bias port of the LCR bridge. All measurements on the HP4274A LCR bridge were performed using an AC test level amplitude of $0.3\,V_{rms}$ and a stepwise increasing DC bias from 0 to 35 V. The AC test level amplitude is small with respect to the threshold voltage for the Fréedericksz transition and therefore neglectable. For the analysis of data, the measured capacitance values are plotted versus the applied DC bias.

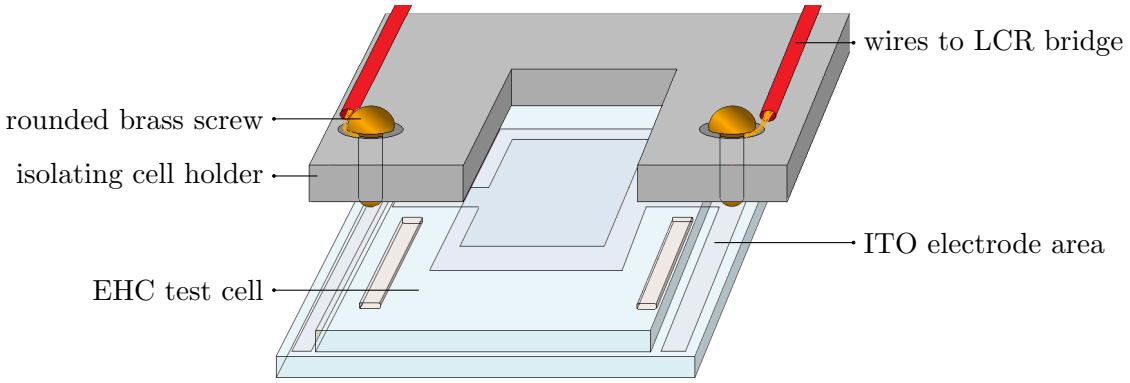

Figure 3.9: The use of a fixed connector to electrically contact the EHC test cells allows to overcome parasitic capacitance effects. The connector contacts the ITO-electrodes of the sample by rounded brass screws, that are connected to the LCR bridge using always the same wires.

The HP4284A LCR bridge with built-in power amplification (option HP4284A-001) is capable of a maximum test signal level of 20 V_{rms}. No external DC bias for reorientation of the liquid crystal is needed in this case. Measurements are performed by stepwise increasing the AC test level amplitude from 0.05 V_{rms} to 19.95 V_{rms}.

When performing capacitance measurements to determine the capacitance of the liquid crystal, a parasitic capacitance of the measuring circuit has to be taken into account. The precision LCR bridges offer an internal compensation, which considers the parasitic capacitances on the bridge side of the connector port. Thus, when connecting a sample to this interface, only the parasitic capacitance of the wires and contacts to the test cell have to be estimated. Assuming that the area, resistance and capacitance of the electrode material of the EHC test cells is identical on all samples, using a fixed connector (see figure 3.9) allows the determination of the parasitic capacitance of the experimental setup. Considering the parallel-plate-model for a capacitor, the capacitance of a test cell with infinite cell gap should be zero (see equation 3.2) in absence of a parasitic capacitance.

$$C = \epsilon_r \cdot \epsilon_0 \cdot \frac{A}{d} \tag{3.2}$$

By measuring the cell gap thickness as well as the cell capacitance of several empty test cells and performing a linear extrapolation of these data to infinite cell gap gives a residual capacitance, which can be considered as the parasitic capacitance of the measuring circuit.

While the standard deviation in capacitance measurements is usually smaller than 0.1 % and therefore neglectable, the standard deviation in cell gap measurements has to be considered for the linear extrapolation calculations. Therefore, a weighted linear regression calculation with uncertainty in x-direction is performed to obtain the residual capacitances for both LCR bridges. The results are shown in figure 3.10. The parasitic capacitances for measurements with the LCR bridges HP4274A and HP4284A are determined to be 2.6 pF and 8.2 pF, respectively.

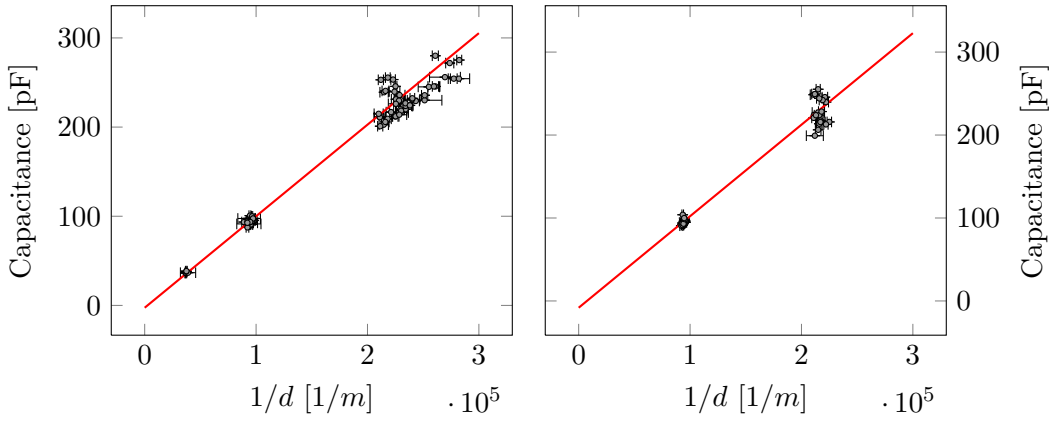

Figure 3.10: Determination of parasitic capacitances in the experimental setup for the HP4274A (left) and HP4284A (right) LCR bridges. The parasitic capacitance of dielectric measurements with the HP4274A LCR bridge was found to be 2.6 pF. For measurements with the HP4284A LCR bridge the parasitic capacitance was found to be 8.2 pF.

The improvement in accuracy of calculated permittivities when considering the parasitic capacitance leads to changes by +0.02 for the HP4274A LCR bridge and +0.08 for the HP4284A LCR bridge. Thus considering parasitic capacitances does slightly increase $\epsilon_\perp$ and $\epsilon_\parallel$, but does not significantly change their values [73].

To obtain the permittivity perpendicular to the long axis of the molecules, the average value of the capacitance plateau at small voltages is used in the equation

$$\epsilon_\perp = \frac{C_{filled} - C_{parasitic}}{C_{empty} - C_{parasitic}}. \tag{3.3}$$

To define the initial capacitance plateau and obtain its average value, all data points from $V_{rms} = 0\,\mathrm{V}$ till $V_{rms} = 0.8 \cdot V_{Th}$ are considered.

The permittivity $\epsilon_\parallel$ parallel to the long axis is obtained by extrapolation of capacitance for infinite field strength. This is done by plotting the capacitance versus normalized inverse voltage (see figure 3.11), followed by linear regression and determination of axis intercept. The permittivity can then be calculated using the equation

$$\epsilon_\parallel = \frac{C_{filled,V\to\infty} - C_{parasitic}}{C_{empty} - C_{parasitic}}. \tag{3.4}$$

In a plot shown in figure 3.11, a linear correlation is predicted for small $\frac{V_{Th}}{V}$ [72]. In practice, the best line fit changes value depending on the amount of data points considered for fitting calculation. A different choice of considered data results in different intersections of line fit with the ordinate and therefore yields different extrapolated capacitances for infinite field strength. To overcome this problem, a detailed correlation analysis is performed. Therefore, the Pearson correlation coefficient r is calculated for each linear fit with an increasing number of considered data points, starting with the value obtained for the highest applied

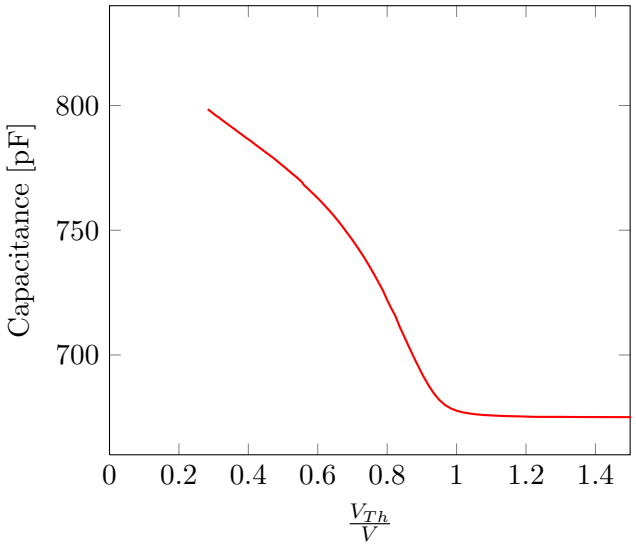

Figure 3.11: Capacitance data shown in figure 3.8 replotted as a function of $\frac{V_{Th}}{V}$. This plot allows the extrapolation of capacitance at infinite field strength and hence the calculation of the permittivity parallel to the the liquid crystal molecules, $\epsilon_{\parallel}$.

voltage (i.e. the lowest values for $\frac{V_{Th}}{V}$) (see figure 3.12). In the same manner also the resulting ordinate intersections with the linear fit and their standard deviations are determined (figure 3.13). A combination of these data allows to chose a rational dataset for extrapolation calculus: As the Pearson coefficient should be close to -1 for a good linear correlation and the standard deviation of ordinate intersection decreases with increasing number of considered data points, the best choice for linear fit in the given example is to consider all data with $\frac{V_{Th}}{V_{max}} < 0.5$. This choice is confirmed by the calculated ordinate intersections, as $\frac{V_{Th}}{V_{max}} = 0.5$ represents the upper limit of a capacitance plateau.

In general, capacitance data can also be used to determine the threshold voltage V_{Th} of the Fréedericksz transition. For this purpose, the threshold V_{Th} is defined by a deviation of 5 % of the normalized capacitance

$$C_{norm} = \frac{C_{measured} - C_{min}}{C_{max} - C_{min}}. \tag{3.5}$$

Yet, dielectric measurements require a homogeneous, planar initial alignment with strong boundary conditions over the complete electrode area, which could not be fulfilled for all samples investigated in this work. Therefore, an additional method to determine V_{Th} is realized by transmission measurements (see chapter 3.5.2). Where necessary, additional indices D and T are used to distinguish between values obtained by Dielectric ($V_{Th,D}$) or Transmittance ($V_{Th,T}$) measurements.

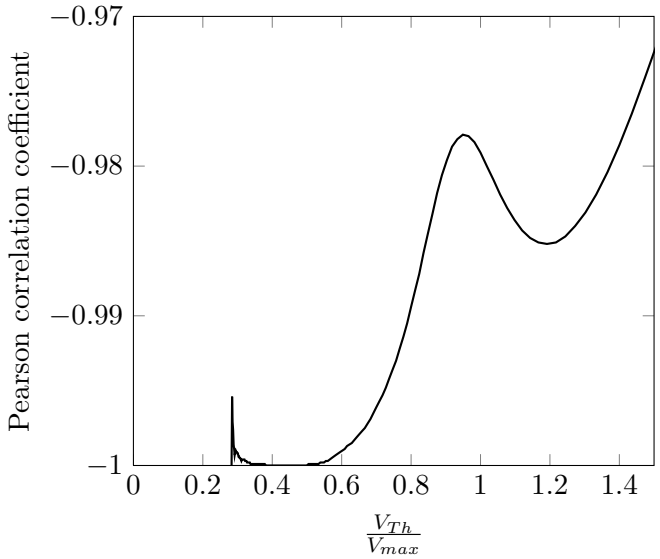

Figure 3.12: Calculated Pearson coefficients r for linear regression calculus with different number of data points. In general, a good linear correlation can be confirmed as predicted in theory [72]. However, the best linear correlation in this example is found for considering values from the highest applied voltage to $0.4 < \frac{V_{Th}}{V_{max}} < 0.5$.

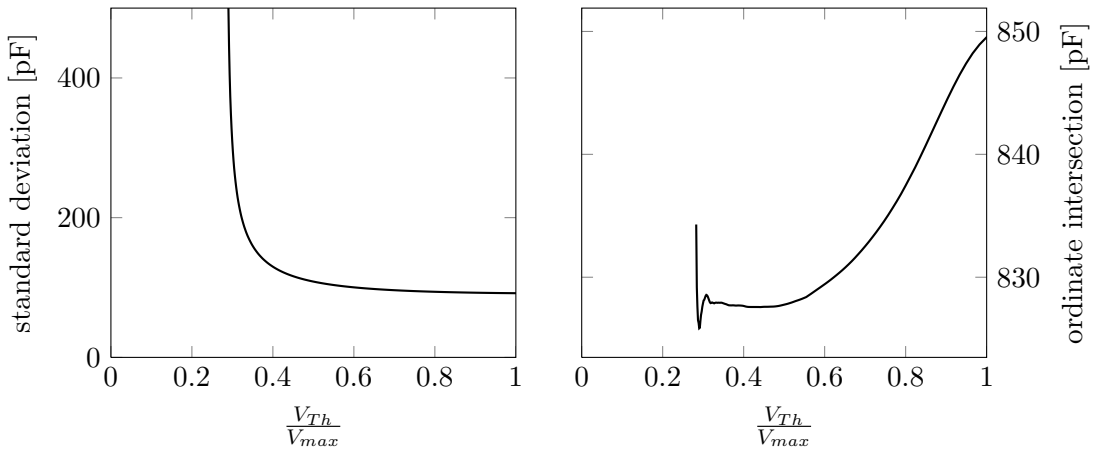

Figure 3.13: Calculated ordinate intersections (right) and corresponding standard deviations for linear regression calculus with different number of data points. As the standard deviation decreases with increasing number of data points, the best choice for linear extrapolation is considering all data points that fulfill $\frac{V_{Th}}{V_{max}} < 0.5$.

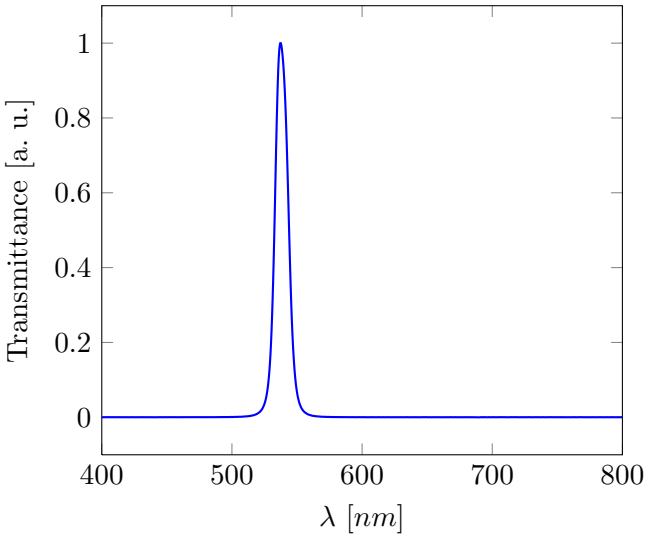

Figure 3.14: Transmission spectrum of the interference filter used for monochromatic illumination. The maximum of the transmittance peak is at 542 nm, the FWHM is 10.8 nm.

3.5.2 Transmittance measurements

Light transmission measurements were performed on a Leitz Ortholux II Pol-BK microscope with the easy axis oriented at an azimuthal angle of 45° between crossed polarizers. For illumination, a halogen lamp (XENOPHOT, Osram) with interference filter for transmission at 542 nm (FWHM 10.8 nm, see figure 3.14) was used. The use of white light and interference filter is preferred over the use of a monochromatic illumination and legitimated by the requirements for dynamic measurements (see section 3.5.3): The sodium gas-lamps with monochromatic light at a wavelength of 589 nm that were available for this work, are not sufficiently DC stabilized, so that measurements of the dynamics of Fréedericksz transition in the millisecond regime are not possible. Thus, to obtain comparability of data, not only dynamic measurements but also the field-dependent transmittance measurements were performed using the DC stabilized halogen lamp with interference filter. For light detection, a photomultiplier (Oriel) was used. To ensure a birefringence detection from the liquid crystals thermodynamic equilibrium state, a latency period of 250-500 ms is used for each applied voltage before data acquisition. This latency is one magnitude higher than the switching times of the nematic liquid crystals 5CB and Felix-2900-03, therefore a completion of director reorientation can be expected after this period. No hysteresis between signals on increasing and decreasing voltage is found, which proves that transmittance is measured under equilibrium conditions.

The number of intensity oscillations in the recorded transmittance characteristics is directly related to the total phase retardation δ of the sample. With given material properties (e.g. $\Delta\, n_{eff}$) and illumination wavelength λ, the phase retardation and thus the number of oscillations increases with the cell thickness d. As for this work only test cells with 4 µm or 10 µm were used, the number of intensity extrema typically varies between two and six,

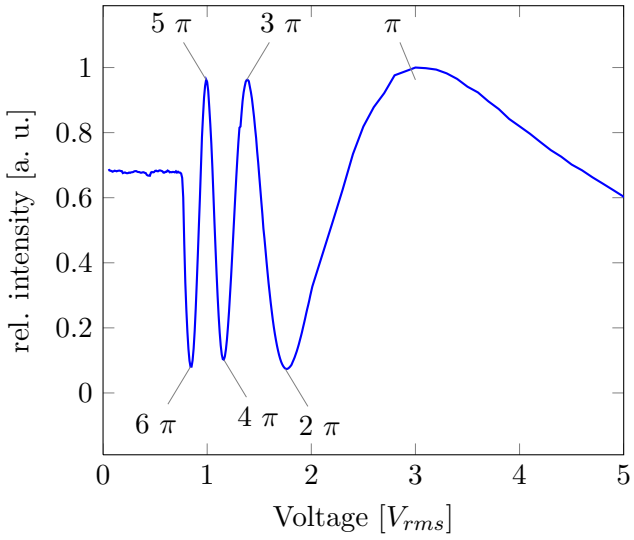

Figure 3.15: Measured transmission intensity for a 10 µm cell. Each extreme value represents an additional phase retardation of π.

respectively. Each extreme value represents an additional phase retardation of π, as can be seen in figure 3.15. For the calculation of threshold voltage from transmittance data, $V_{Th,T}$, it is necessary to convert the oscillating intensity data to the phase retardation δ

$$\delta = 2 \cdot \arcsin\left(\sqrt{\frac{I}{I_{max}}}\right), \tag{3.6}$$

which is a monotonically decreasing function of the applied voltage. The threshold $V_{Th,T}$ is then defined by a decrease of phase retardation by 5 %.

In contrast to the ideal predictions of theory, the relative light intensity found at the extreme value deviates from the predicted values 0 and 1. The contrast ratio between I_{max} and I_{min} is restricted to the quality of the initial director orientation [24] and therefore connected to the quality of the polyimide alignment layers of the electro-optic test cells. This deviation has to be considered when performing the previously mentioned conversion of light intensity to phase retardation, as in the interval [0,1] the $\arcsin(x)$-function can be considered linear only for small arguments close to 0, but not for arguments close to 1. Thus it is crucial to correctly scale the intensity data over the complete range between [0,1] as predicted by theory. Otherwise, the calculated values for phase retardation would be considered to be too small.

To obtain correct values for phase retardation, the extreme values of the intensity oscillations are determined and a stepwise scaling of intensity is performed for every interval between two extreme values. The result can be seen in figure 3.16. Scaling the intensity data correctly also allows the determination of the effective birefringence of the test cell, using the equation

$$\Delta n = \int_{\infty}^{V} \frac{\lambda}{\pi \cdot d} \cdot \arcsin\left(\sqrt{\frac{2 \cdot I}{I_0}}\right) \, dV. \tag{3.7}$$

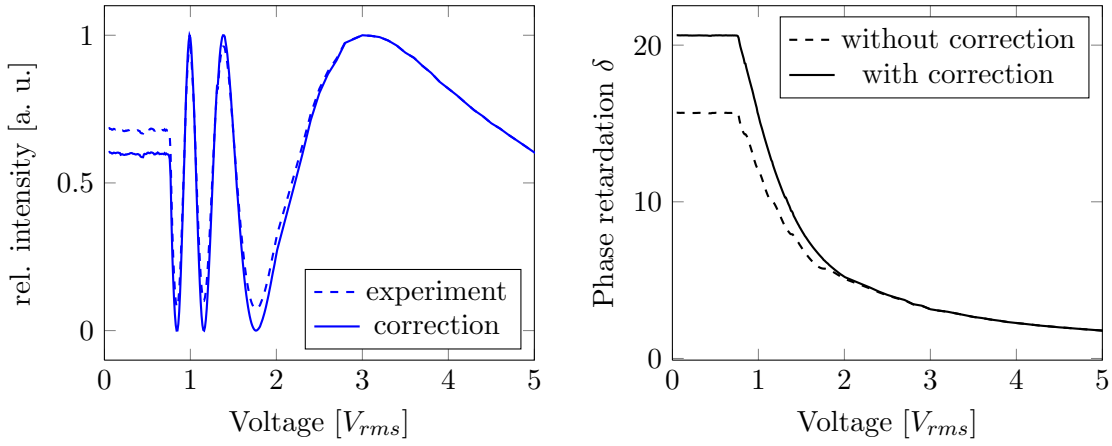

Figure 3.16: Left: Measured transmission intensity and correctly scaled transmission intensity. Right: Total phase retardation calculated from experimental data and correctly scaled data.

The initial birefringence of the 5CB test cell investigated in figure 3.16 ($d = 10.55\,\mu m$,25 °C) is then found to be $\Delta n_{eff} = 0.17$, which is in good agreement with literature (see reference [19]).

3.5.3 Dynamic measurements

The dynamics of the Fréedericksz transition is investigated by transmission measurements only, since the data acquisition rates of the HP4274A and HP4284A LCR bridges are too slow for measurements in the millisecond regime. The applied switching voltages were delivered by a Rhode & Schwarz AFS arbitrary function generator with Krohn & Hite amplifier model 7500. Intensity data is recorded using a Picoscope 3206 A USB oscilloscope with 100 Ms/s sampling rate. According to the theoretical derivation of rise and decay times of nematic liquid crystals [22], the commonly used formulas 3.8 and 3.9 are only valid for small distortions in the director field and negligible backflow effects (see chapter 2.5.2).

$$\tau_{rise} = \frac{\gamma \cdot d^2}{\pi^2 \cdot K} \cdot \left[\left(\frac{V}{V_{Th}} \right)^2 - 1 \right]^{-1} \tag{3.8}$$

$$\tau_{decay} = \frac{\gamma \cdot d^2}{\pi^2 \cdot K} \tag{3.9}$$

In practice, these restrictions are usually considered by measuring the switching times between a voltage V_a just below the threshold voltage $V_{Th,T}$, and a voltage V_b corresponding to the first extreme value in the field dependent transmission oscillation([70]). The transmission intensity at the voltage V_a corresponds to the initial director field distribution without distortions due to external fields and depends on the total phase retardation in the sample. This is, for a certain wavelength, given by the cell thickness and the effective index of refraction Δn_{eff}. In case the combination of cell gap and birefringence leads to an initial transmission close to transmission at the first extreme value, no sufficient contrast between

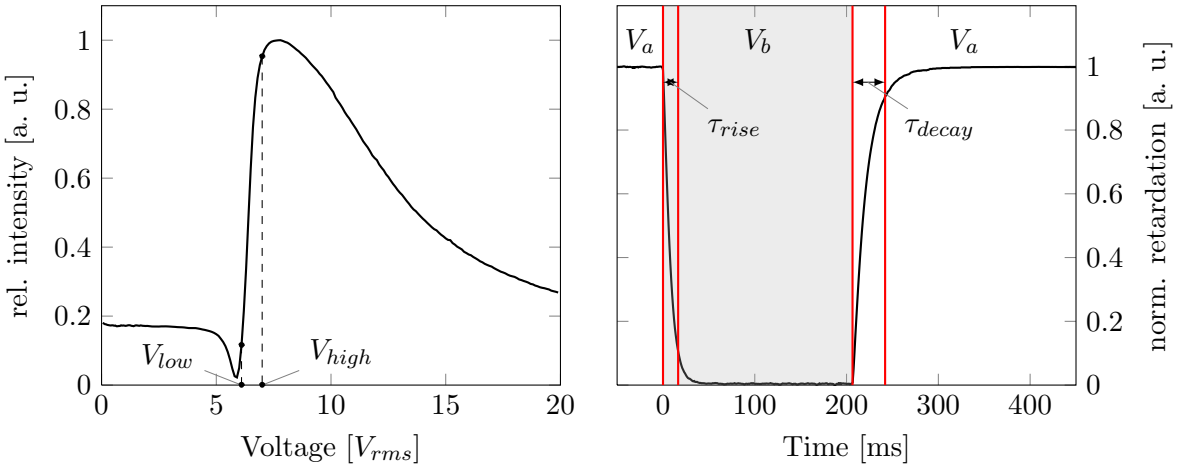

Figure 3.17: Left: Example of determination of V_a and V_b in the transmission characteristic of a 4 µm EHC cell with pure FELIX-2900-03 at 58 °C. The choice close to the extreme values of oscillation ensures good contrast, but requires proper scaling of data. Right: Example of switching characteristics. By switching between V_a and V_b, a good contrast is observed that allows determination of rise and fall times.

the director field distribution at V_a and V_b can be observed. In reference [70] this problem is overcome by a modification of cell thickness until sufficient contrast is achieved. However, due to the choice of EHC test cells with fixed cell gaps of 4 µm or 10 µm, this is not applicable for the characterization of nanoparticle dispersions in this work.

Thus, switching experiments are performed between a voltage V_a just above the voltage of the first minimum in intensity and a voltage V_b below the following maximum. As with increasing temperature the birefringence and thus the number of oscillations decreases, V_a and V_b are chosen on an oscillation that remains over the complete temperature interval of interest. The frequency of switching voltage is 10 kHz and therefore light modulations caused by the AC field are at least one magnitude faster than the switching times. To obtain a smooth signal, a low band filter was used, filtering all oscillations at frequencies of 10 kHz and higher.

The choice of V_a and V_b close to the extreme values gives a good contrast for the determination of switching times. However, the measured intensities have to be properly scaled as described above to prevent errors in the calculation of normalized phase retardation due to the non-linear behavior of the arcsin function. For this purpose, a field-dependent transmittance characteristic is measured at least twice before every switching experiment to ensure proper choice of V_a and V_b and to be able to scale the intensity data in switching experiments.

Switching times are defined as the time between a change in voltage between V_a to V_b or vice versa and a change of normalized phase retardation of 90 %. Figure 3.17 gives an overview of the determination of switching times for a 4 µm cell with pure FELIX-2900-03 at 58 °C.

As seen in equation 3.9, at a given cell thickness the decay time τ_{decay} depends on the ratio of rotational viscosity γ_1 and an effective elastic constant K_{eff}. It is independent of applied voltages V_a and V_b. Thus, the ratios $\frac{\gamma_1}{K_{eff}}$ of different samples can directly be

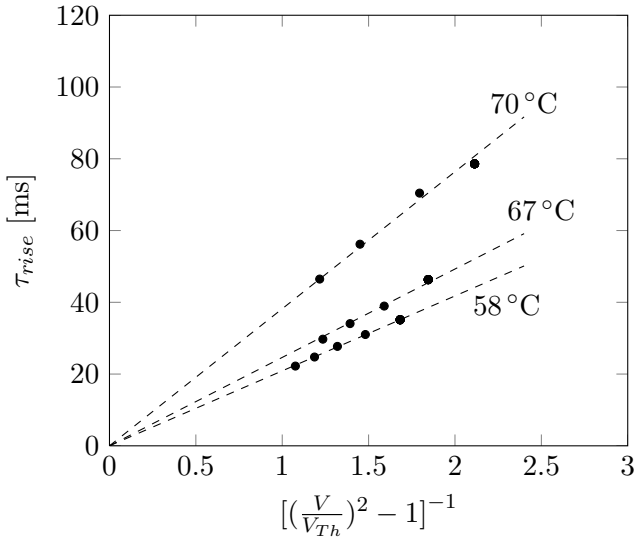

Figure 3.18: The field dependent rise times are characterized by measuring switching times between V_a and V_b for at least four values V_b, followed by a linear regression calculus.

compared by dividing the measured decay times by the square of sample thickness d^2. All decay time data given in this work represent average values of at least four measurements.

In contrast to τ_{decay}, the rise time τ_{rise} does depend on the applied voltages V_a and V_b and their amplitude compared to the threshold voltage V_{Th}. Therefore, the rise time is characterized by plotting τ_{rise} versus $\left[\left(\frac{V}{V_{Th}}\right)^2 - 1\right]^{-1}$. This results in a linear correlation. The slope divided by $\frac{\pi^2}{d^2}$ represents the ratio $\frac{\gamma_1}{K_{eff}}$. For calculating the slope by linear regression, at least four data pairs of different voltages V_b are used.

4 Results and discussion

4.1 General observations

Doping a liquid crystalline material with nanoparticles can cover a wide range of doping concentrations. Podgornov et al. utilized only 0.1 % (w) of gold nanorods to significantly increase the internal electric field within ferroelectric liquid crystals [74]. On the other end of the doping spectrum, Vardanyan et al. recently reported defect-free nanocomposites containing up to 90 % (w) gold nanoparticles in 6CB [75]. In this work, dispersions with a nanoparticle amount between 0.25 % (w) and 7.5 % (w) are investigated.

In comparison to the weight percentage of particles in a dispersion, the molar fraction of particles is several magnitudes smaller. This is due to the high molar mass of functionalized metal or semiconductor particles. For example, the molar mass of the mesogenic functionalized AuCB particles was determined by Draper et al. to be 164727 g/mol [14], while the molar mass of the nematic host 5CB is only 249.35 g/mol [19]. This gives a molar mass ratio between nanoparticle and host molecule of over 660:1. The high ratio of molar masses leads to mole fractions of particles in the range of $10^{-4} - 10^{-6}$ when preparing dispersions between 0.25 % (w) and 7.5 % (w) of nanoparticles.

Considering the mole fractions and the volume of a single host molecule and a nanoparticle, the mean distance r of particles in the dispersion can be estimated by using a simple hard sphere model. In this model, the particle's diameter is given by the solid core's diameter d_{core} plus an additional length due to the organic capping d_{shell}. The effective volume of the organic shell around the particle varies with the amount of interdigitation of ligands and host molecules. In a simple model, d_{shell} is assumed to be only 50 % of the length of a single ligand molecule, taking into account a certain degree of interdigitation. The average volume of one particle is then given by

$$V_{NP} = \frac{1}{6} \cdot \pi \cdot (d_{core} + d_{shell})^3 \,. \tag{4.1}$$

The average volume of a single host molecule can be estimated by

$$V_{LC} = \left(\frac{\delta_{LC}}{M_{LC}} \cdot N_A \right)^{-1}, \tag{4.2}$$

where δ_{LC} is the density of the liquid crystal, M_{LC} the molar mass and N_A Avogadro's constant. With M_{NP} being the molar mass of the nanoparticles and x being the mass fraction of particles in the dispersion, the mean distance r between two nanoparticles in a

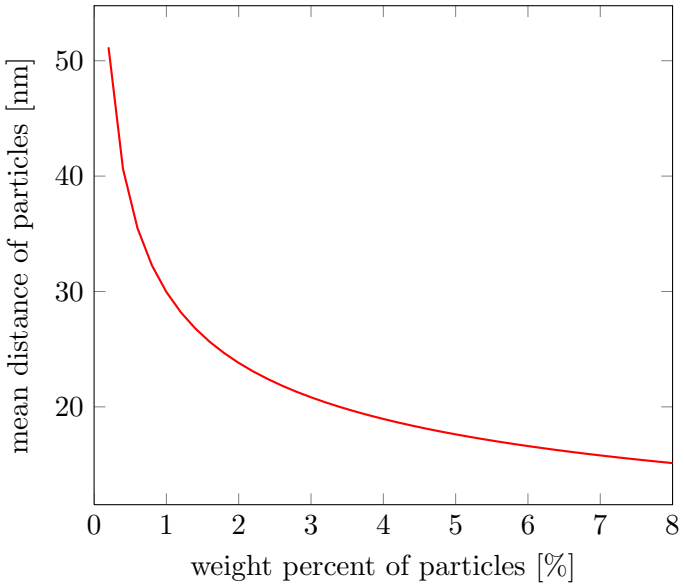

Figure 4.1: Diagram showing the average mean distance between two nanoparticles in a homogeneous dispersion for different mass fractions of particles. The results shown here are based on a simple model of hard spheres in a nematic host. For the calculation, physical properties of AuCB given in reference [14] and date for the host 5CB found in reference [19] are used for the calculation.

homogeneous dispersion is given by the equation

$$r = \sqrt[3]{V_{NP} + \left[\frac{M_{LC} \cdot x}{1-x} \cdot \frac{1}{M_{NP}}\right]^{-1} \cdot V_{LC}}. \tag{4.3}$$

One precondition for treating the nematic phase as a continuum is that significant changes in the nematic director take place on a length scale L much larger than the molecular dimension a (see equation 2.5). As it is shown in figure 4.1, the mean distance for all concentrations investigated in this work is smaller than 50 nm. In consequence, the mean distance between single particles can be assumed to be smaller than the length L for any concentration investigated in this work. Therefore it can be expected that the presence of particles can have a direct influence on the order parameter S or the elastic constants of deformation K_{ii} of the nematic phase. Equation 4.3 can also be used to estimate the minimum concentration of particles required to give a mean particle distance lower than the length scale L with significant changes in the director field. Assuming a length L of ≈ 300 nm, a mean distance between single particles is given by 0.001 % (w) of homogeneously dispersed particles. This is well below the typical doping concentrations used in this work, but as shown below in this section the actual particle concentration in the bulk can be dramatically reduced by agglomeration or particle interactions with the surface.

In accordance with thermodynamical considerations, mixtures of nematogens and isotropic solutes show a higher concentration of solute in the isotropic phase than in the nematic phase ([76], [77]). As a result, a higher miscibility of nanoparticle solution in a liquid crystalline host is observed for temperatures where the liquid crystal is in the isotropic state,

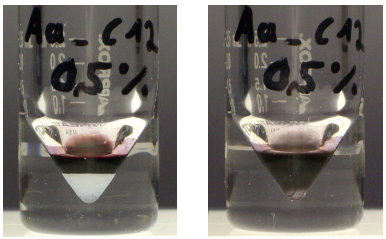

(a) **(b)**

Figure 4.2: Photographs of a mixture of AuSH12$_{(m)}$ particles dissolved in toluene and added to 5CB in a V-vial during the preparation process. (a) At room temperature the host 5CB is in the nematic phase and does not mix with the toluene solution with nanoparticles. (b) After heating the mixture to the isotropic phase, mixing of 5CB and the toluene / particle solution occurs, even without additional mechanical stirring.

rather than in the nematic phase. In figure 4.2, two photographs of a mixture of 5CB and a solution of AuSH12$_{(m)}$ particles in toluene are shown. While the liquid crystal is in the nematic phase (figure 4.2 (a)), a phase separation occurs and the liquid crystal does not dissolve in the dispersion. Only after heating the sample slightly over the phase transition temperature of 5CB, a homogeneous mixture is obtained (figure 4.2 (b)).

For this reason, dispersions are prepared and filled into the test cells at temperatures above the clearing temperature of the nematic host. However, agglomeration of nanoparticles is occasionally observed to occur during the evaporation process of solvent, resulting in a solid precipitate on the ground of the V-vial. This effect has been observed for all nanoparticle / liquid crystal combinations prepared in this work, only with differences in the aggregation rate during preparation. As the experimental parameters like temperature, stirring rate and low pressure treatment are kept constant, the agglomeration seems to occur randomly. Even the use of steady argon flow over the V-vial, to keep away reactive gases like oxygen from the mixtures, does not increase the rate of stable dispersions.

This indicates a general lack of experimental control over the formation of homogeneous dispersions. In consequence, only dispersions with no visible signs of agglomeration were filled into test cells and investigated in this work, dispersions with visible signs of agglomeration are discarded. However, under a microscope with high magnification objective almost every test cell reveals areas with small particle agglomerates. As visible agglomerates represent areas with a very high particle density, their appearance decreases the average particle concentration of homogeneously dispersed nanoparticles in the liquid crystal.

Additionally, even with no visible agglomeration, a small ratio of particles resides at the surface of the V-vial during the preparation process. For the strongly luminescent CdSe particles CdSe590 and CdSe610, this effect can even be seen with the naked eye by a thin orange layer residing on the glass after removing the dispersion from the V-vial (see figure 4.4 (a)). This residue leads to an additional decrease of particle concentration in the dispersion. Consequently, the precise concentration of particles in a test cell is unknown, but

certainly smaller than the concentration expected from the weighted quantities.

To reveal the magnitude of this depletion effect, two stable dispersions of 0.5 % (w) $AuSH12_{(m)}$ particles in 5CB are prepared and filled into two untreated glass cells and two EO-test cells each. For comparison of their properties, textures between crossed polarizers are studied for the untreated glass cells, and the threshold voltage of the EO-test cells is measured (see figure 4.3). It is found that test cells filled with a dispersion from the same batch show similar textures and comparable threshold voltages. Test cells filled with a dispersion prepared in another batch, however, slightly differ in textures and threshold voltages. This indicates that during the evaporation process of solvent different degrees of particle depletion occur in different batches. As samples filled with dispersions from the same batch show comparable results, depletion effects during the filling process seem to be negligible.

Depletion effects have to be taken into account when comparing changes in the liquid crystalline properties due to the presence of different concentrations of dispersed nanoparticles. In order to allow proper data interpretation, several assumptions are made:

- The actual particle concentration of the dispersion in a test cell is unknown, but lower than expected by the weighted quantities of liquid crystal and dopant.
- For stable dispersions, the depletion of particles is considered proportional to the initial concentration, assuming constant ratios of particles residing on the V-vial or forming small agglomerates. The particle concentration of dispersions showing visible agglomeration in the bulk even before being filled in a test cell cannot be estimated, as the degree of agglomeration cannot be determined. Hence, dispersion with visible agglomeration in the bulk cannot be used for further experiments and are discarded.
- As a consequence of the first two assumptions, higher weighted quantities of dopant should lead to a higher particle concentration in the dispersion. Hence, comparability of concentration dependent changes of dispersion properties is remained.

4.2 Stability and solubility of nanoparticles in dispersions

The miscibility and compatibility of nanoparticles in a nematic host and the stability of the dispersions are determined from the bulk dispersion in a V-vial. Visible agglomeration of particles or the visible settling of particles on the glass interface indicates incompatibility, while the formation of a homogeneous mixture with no visible particles indicates the formation of a stable dispersion.

Dispersions of $AuSH12_{(m)}$ and AuCB in 5CB show a dark red or black color with slight opaque glint. This has also been reported by Qi et al. (see reference [78]) recently and is put down to the surface plasmon resonance of the gold nanoparticles. These particles give homogeneous dispersions for concentrations up to 2.5 % (w) or 5 % (w), respectively. At higher concentrations, the formation of agglomerates is observed during the preparation process.

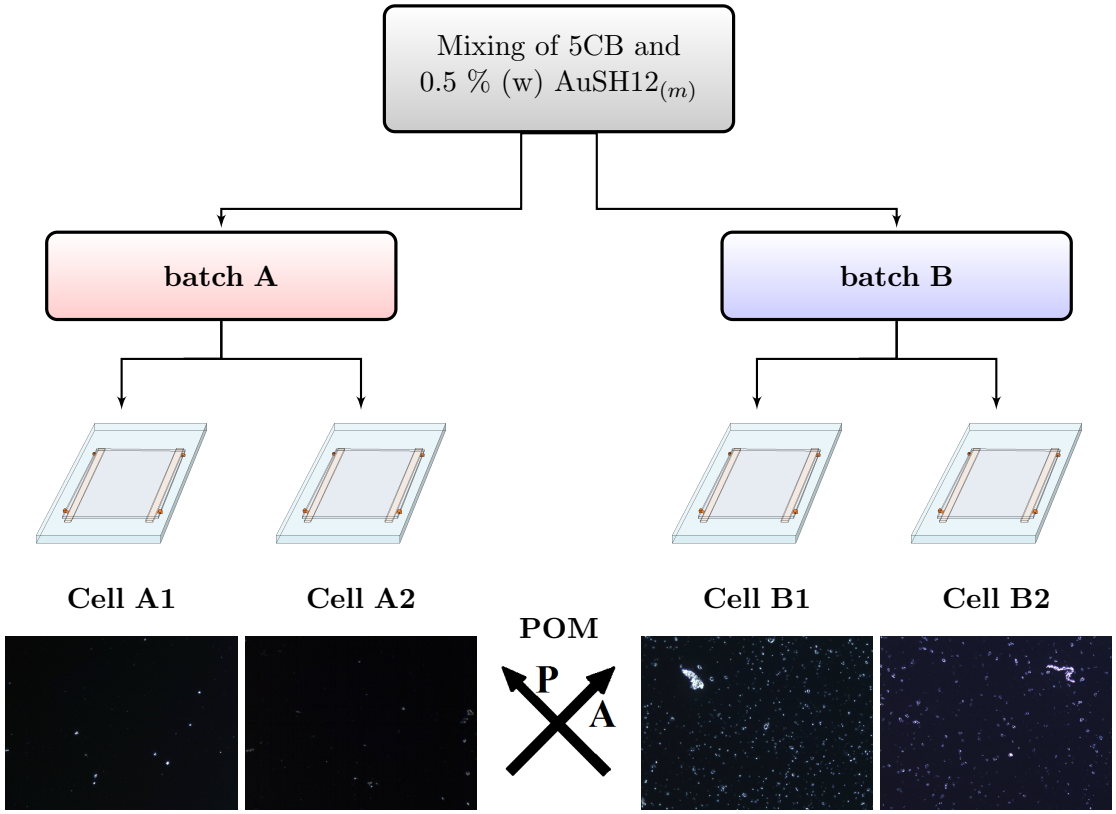

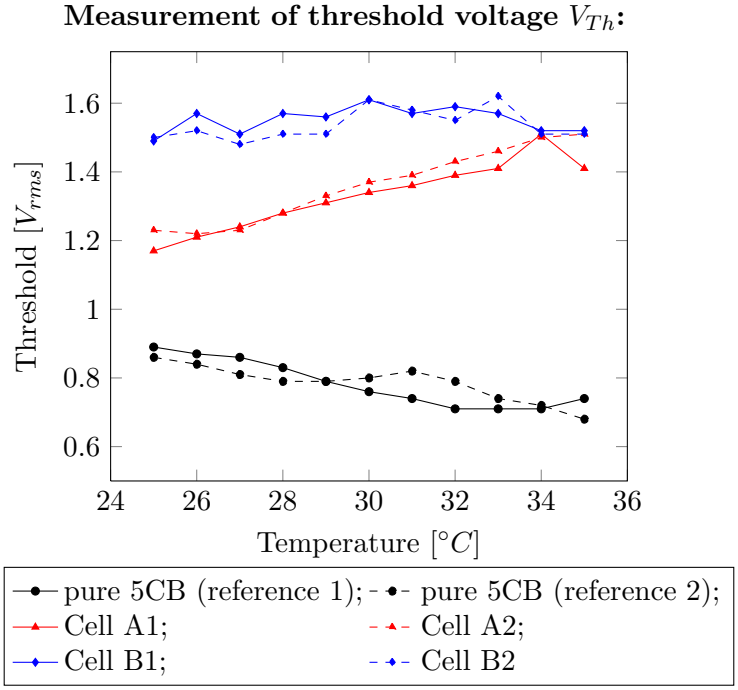

Figure 4.3: Comparison of polarizing optical microscopy (POM) textures and threshold voltages of two batches of 0.5 % (w) AuSH12$_{(m)}$ in 5CB. While the results obtained for different test cells filled with dispersion from the same batch are well comparable, results obtained from dispersion prepared in another batch slightly differ. This effect is ascribed to different degrees of particle depletion during the preparation process of the dispersions.

The dispersions are stable in the range of a few hours only, as after one night (14 hours) all dispersions show severe agglomeration and settling of particles on the bottom of the V-vial. Similar observations are reported by Kinkead et al. (see reference [13]), who found comparably low solubility of alkylthiol capped gold particles in polar nematics like 5CB or 8CB compared to more apolar mesogens like FELIX-2900-03. A possible explanation for lower solubility of alkylthiol capped particles could be polar interactions of the cyanobiphenyl units of the host molecules, which prevent strong interaction to the apolar alkylchains of AuSH particles. For the mesogenic capped particles AuCB, a strong interaction between the ligands and the mesogenic host 5CB could be expected due to a high chemical similarity. An experimental verification has been given by Draper et al. recently, who report a high miscibility and stability of the mesogenic capped gold particles AuCB in the host 5CB (see reference [14]). In own experiments, the dispersions of AuCB in 5CB indeed show a good miscibility, but no superior stability compared to aliphatic capped particles.

Interestingly it is found that the stability of dispersions in the bulk can differ from the stability of dispersions filled into test cells. Although the mixtures of $AuSH12_{(m)}$ and AuCB in 5CB show no good long term stability in the bulk, once a stable dispersion is filled into test cells without signs of agglomeration, the dispersion remains stable and does not show signs of agglomeration within the cell even for years. This could be caused by a lower mobility of particles in a test cell, as convection is reduced within the test cell and the diffusion of particles presumably is not sufficient to lead to high local particle concentrations and agglomeration.

Mixtures of CdSe590 and CdSe610 nanoparticles in the hosts 5CB and FELIX-2900-03 result in homogeneous orange or reddish dispersions up to 2.5 % (w). Again, higher concentrations lead to the formation of visible agglomerations during the preparation process, what is in accordance with results found by Kinkead et al. (see reference [13]) before. The authors report extensive aggregation of hexadecylamine capped particles with different core diameters in the host FELIX-2900-03 at a concentration of 5 % (w).

Dispersions of CdSe590 and CdSe610 in 5CB are found to be stable for several days, while dispersions in FELIX-2900-03 show agglomeration within a few hours. This is again in accordance with the earlier work of Kinkead et al. [13], as inferior miscibility and aggregation behavior in the host FELIX-2900-03 is reported for hexadecylamine capped CdSe590 quantum dots compared to similar particles with different core diameters. However, this reference reports good stability for the CdSe610 particles in FELIX-2900-03, which could not be confirmed in own experiments. In this work, the difference of core diameter between the smaller CdSe590 particles and the larger CdSe610 is found to have no influence on the stability of nanoparticle / liquid crystal dispersions.

4.3 Phase transition temperatures

Solute impurities in nematic liquid crystals depress the nematic to isotropic phase transition temperature and lead to the formation of a two-phase region ([76], [79]). Hence, also commercially available pure compounds exhibit a small temperature range of coexisting phases

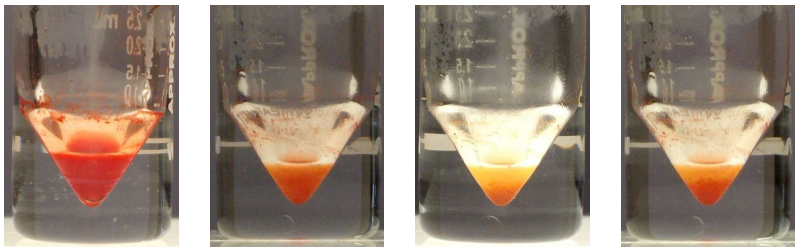

(a) (b) (c) (d)

Figure 4.4: Photographs of a dispersion of 2.5 % (w) CdSe590 in FELIX-2900-03 in a V-vial. (a) After removing of all solvent and with the dispersion in the isotropic phase, (b) at $T_{NI} - T = 12\,\mathrm{K}$, directly after cooling to the nematic phase, (c) at $T_{NI} - T = 12\,\mathrm{K}$, 4 hours after cooling to the nematic phase and (d) at $T_{NI} - T = 12\,\mathrm{K}$, 6 hours after cooling to the nematic phase.

due to small amounts of impurities or chemical decomposition [77]. For the nematic hosts FELIX-2900-03 and 5CB, this biphasic region is found to be in the range of 0.2 °C at a heating rate of 1 °C/min.

Applying the thermodynamic model derived in references [76] and [79], doping these hosts with spherical nanoparticles in the size regime of a few nanometers would lead to a further decrease of clearing temperature, and a broadening of the biphasic region.

This effect is experimentally observed for most of the nanoparticle dispersions investigated in this work. In general, the onset temperatures of phase transition in the nematic host 5CB decrease as well for gold nanoparticles as for CdSe particles, results are shown in figures 4.5 and 4.6. For the mesogenic coated gold particles AuCB, the most distinct decrease is observed for the lowest concentration of 0.5 % (w) nanoparticles. The dispersions with higher concentrations also show a decrease of onset temperature, but it is only half as pronounced as for the lowest concentration. For comparison with data from literature, only phase transition temperatures of the AuCB particles in the nematic host 8CB are reported by Draper in reference [49]. Assuming that the general behavior between 5CB and 8CB is comparable due to the similar chemical structure of the molecules, a very similar behavior is reported here: The doping of small amounts of nanoparticles leads to a decrease of phase transition temperature. With increasing concentration this effect is reversed and even higher phase transition temperatures than for the pure host can be observed at concentrations higher than 10 % [49]. Draper explains this concentration dependence by a knock-on effect, where the nanoparticles can stabilize the liquid crystalline host in the vicinity of the particle above a certain particle concentration [49]. If the particles are well-dispersed and distributed homogeneously over the sample, this stabilization process superimposes the decrease of clearing temperature, and sufficiently high particle concentrations lead to higher phase transition temperatures.

The biphasic temperature range increases for all AuCB dispersions to the same amount compared to the pure host. It is found to be between 0.3-0.4 °C at a heating rate of 1 °C/min. For the given mole fractions of particles, this temperature range is large compared to the theoretical predictions for spherical particles in a nematic host. Assuming that the theo-

retical model for small spherical molecules like Bu_4Sn or Pr_4Sn reported by Oweimreen in references [76] and [79] can also be applied to nanoparticles with diameters 10 to 15 times larger, a biphasic temperature range of only 0.02-0.03 K would be expected. The over one magnitude larger temperature interval of 0.3-0.4 °C found in experiments could indicate a higher mole fraction of solute impurities in the nematic host than the sole mole fraction of particles. This could be caused by external impurities as well as by chemical deposition and ligand loss of the mesogenic functionalized particles. It is known that ligand exchange takes place even at low temperatures, as this method is used for the synthesis of functionalized gold nanoparticles with prescribed compositions of different ligands [57]. In consequence it can be assumed that dissolving AuCB particles in dichloromethane and mixing with the nematic host 5CB also leads to an uncertain amount of free ligands in the dispersion.

The aliphatic coated gold particles $AuSH12_{(m)}$ are found to decrease the onset of clearing temperature and exhibit a pronounced broadening of the biphasic region. However, also under consideration of data from literature given by Qi et al. in reference [12], a concentration dependent trend of increase or decrease cannot be found in the investigated concentration range. It might be possible that the same knock-on of stabilization effect as observed for AuCB particles would occur at higher particle concentrations. But due to agglomeration effects and solubility problems in dispersions of AuSH in 5CB, data for higher concentrations than 2.5 % are not available.

The hexadecylamine capped CdSe particles CdSe590 and CdSe610 do not show a very pronounced effect on the phase transition temperatures in 5CB, but the effects are of comparable magnitude for the two systems: Both slightly decrease the onset temperature with increasing concentration, and exhibit biphasic regions of a magnitude comparable to the dispersions with gold particles in 5CB. As the CdSe590 and CdSe610 particles are chemically identical, and no difference can be observed between the smaller CdSe590 particles and the CdSe610 particles with larger diameters, the size of particles seems to have no considerable influence on the phase transition temperatures of nanoparticle dispersions in the nematic host 5CB.

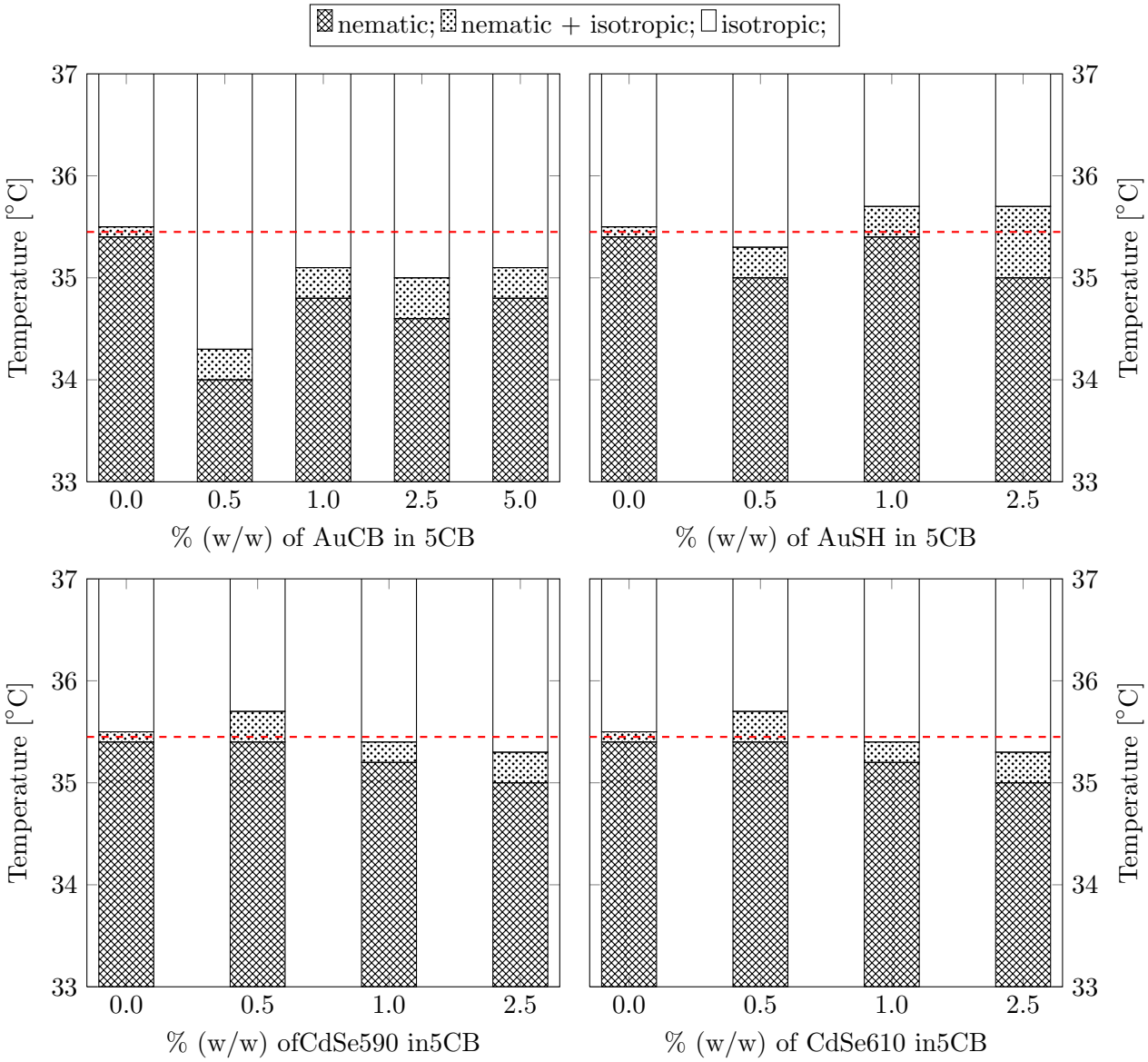

Figure 4.5: Phase transition diagrams of dispersions of AuCB, AuSH12$_{(m)}$, CdSe590 and CdSe610 particles in 5CB, respectively. The dashed red line indicates the clearing temperature of the pure liquid crystalline host, biphasic regions are shown as dotted bars.

In contrast, the different diameters of hexadecylamine functionalized CdSe particles seem to have an influence on the phase transition behavior in the nematic host FELIX-2900-03. The smaller CdSe590 particles show a slight decrease of onset temperature with increasing concentration and only slight broadening of biphasic region, their behavior is comparable to the dispersions in 5CB. This is also the case for the magnitude of the biphasic region for CdSe610 / FELIX-2900-03 dispersions, however, the latter particles induce a very distinct decrease of the onset temperature of phase transition of more than 1.5 °C. While the sample with 1 % (w) CdSe610 particles shows the lowest onset of phase transition, the sample with 2.5 % (w) has the highest onset temperature of all dispersions investigated. It is not clear if these observations are connected to the stability of the dispersions, or represent artefacts from the preparation of samples. As shown in figure 4.55 later in this work, samples with CdSe610 quantum dots dispersed in FELIX-2900-03 show an ambiguous effect of nanoparticle doping on the threshold voltage V_{Th}, while other electro-optical data are not accessible due to a lack of stability of dispersion. In conclusion, my own data for CdSe610 in FELIX-2900-03 seem to be unreliable. However, Kinkead et al. published data about the same particle / host combination in reference [13], which will be considered to draw conclusions where necessary.

The decrease of phase transition onset of the magic sized CdSe in FELIX-2900-03 is more pronounced than for the CdSe590 and CdSe610 particles, but the range of biphasic region is comparable. The Zn doped magic sized CdSe particles however do show a completely different behavior than all other CdSe particles. An increase of onset temperature up to 1 °C is found for a particle concentration of 2.5 % (w), while the sample containing 5.0 % (w) of particles still has a slightly higher onset of phase transition temperature. As for CdSe610 particles in FELIX-2900-03, it is not clear if this is connected to an influence of nanoparticles on the stability of the dispersion. Similar samples have been investigated by Mirzaei et al. before and the results are published in reference [65], but the authors do not report a stabilization effect of Zn doped CdSe particles on the nematic host.

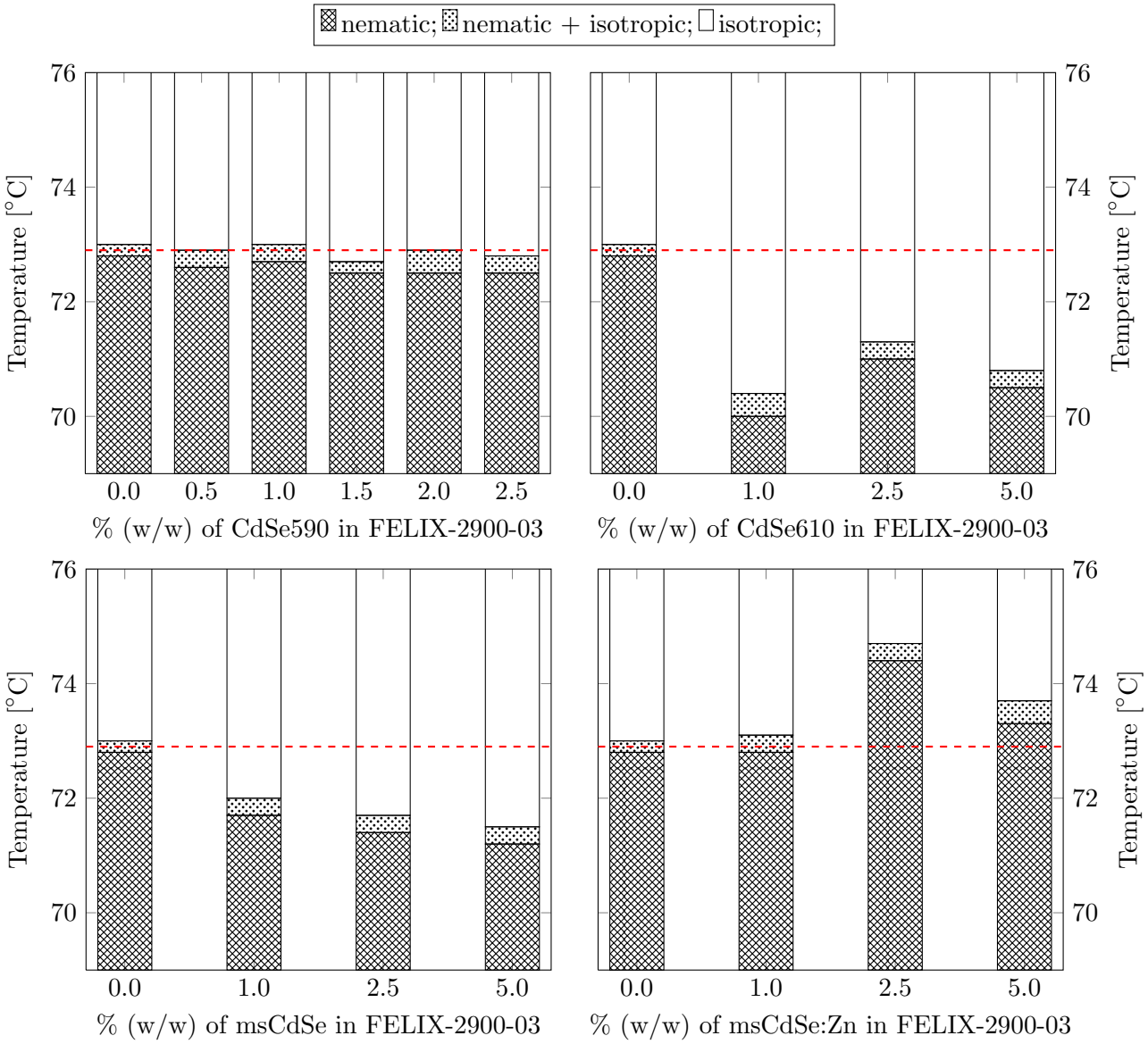

Figure 4.6: Phase transition diagrams of dispersions of CdSe590, CdSe610, msCdSe and msCdSe:Zn particles in FELIX-2900-03, respectively. The dashed red line indicates the clearing temperature of the pure liquid crystalline host, biphasic regions are shown as dotted bars.

Dispersions of silanized gold particles AuSi in FELIX-2900-03 are found to stabilize the nematic phase to higher temperatures in a concentration range of 0.5-1.0 %(w), while lower or higher concentrations lead to decreasing onset temperatures for the phase transition. The magnitude of the biphasic temperature region is found to increase with increasing particle concentration, as predicted by theory [76]. The stabilization effect of the mesogenic phase at medium particle concentrations has been experimentally confirmed by DSC measurements recently reported by Mirzaei et al., and it is found to occur as well on heating as on cooling. In addition, DSC measurements also reveal a stabilization of the smectic A phase at lower temperatures (see reference [61]).

Comparable stabilizing effects due to particle doping have been reported for anisometrically shaped dopants like carbon nanotubes [80], polar ferroelectric nanoparticles [81], and mesogenic functionalized spherical gold particles [49]. For latter particles, a model is presented by Draper et al., wherein the spherical particles can transform to anisometrically shaped particles due to anisotropic interactions of the mesogenic capped ligands with the surrounding [14]. The electric dipole moment of spherical ferroelectric nanoparticles investigated by Lopatina et al. in reference [81] is assumed to cause an anisometrically shaped electric field within the surrounding nematic phase of the particle, which leads also to anisometric interactions between particles and host. The shape of carbon nanotubes as investigated by Duran et al. in reference [80] is anisometric by itself, so that all three systems reported to feature comparable stabilizing effects comprise anisometric particle / host interactions. Therefore, it could be concluded that also the silanized gold particles AuSi show anisometric interaction with the FELIX-2900-03 host molecules. This could be caused by a deformation of the spherical ligand shell to an ellipsoid, similar to the model proposed by Draper et al. for mesogenic coated particles AuCB [14]. While the authors assume a specific interaction of the mesogenic end-groups with the polar core of the host molecules 5CB that leads to a deformation of the spherical particles, a similar mechanism is possible for the interaction of the aliphatic endgroups of AuSi particles with the hydrocarbon sidechains of the non-polar host FELIX-2900-03.

In all aforementioned cases, the stabilization of mesophases due to doping requires homogeneously and well-dispersed particles in the respective host. In general, a high compatibility and high stability of particles in the liquid crystalline host is required to obtain stabilizing effects, as discussed by Khatua et al. in reference [82]. Taking this into account, one can conclude that the silanized gold nanoparticles AuSi in FELIX-2900-03 are well miscible in this nematic host and form a homogeneous dispersion. At 0.25 % (w) of particles, the mean distance between the dispersed particles is around 50 nm (see figure 4.1) and obviously too large for a stabilization of the nematic mesophase. In consequence, the phase destabilization due to the presence of particles still dominates. At higher concentrations the mean distance decreases, and a concentration regime of mesophase stabilization occurs. The decrease of onset temperature of phases transition observed for concentrations higher than 2.5 % (w) could be caused by the formation of particle aggregates at high concentrations, which would reduce the mean distance between particles again. This model would be in agreement with the general observation, that only small fractions of gold nanoparticles up to 5 % (w) can

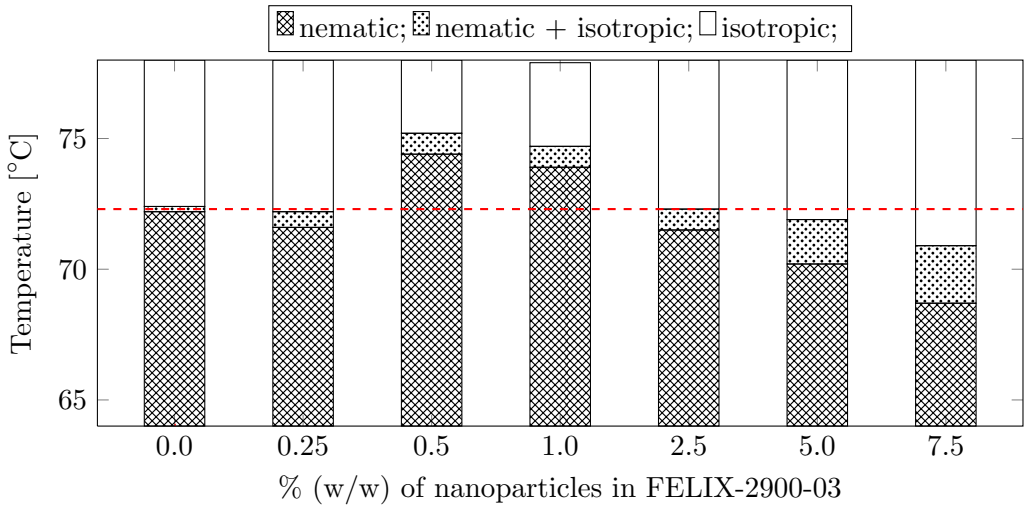

Figure 4.7: Phase transition temperatures of dispersions of AuSi in FELIX-2900-03 at different particle concentrations. The dashed red line indicates the clearing temperature of the pure liquid crystalline host, biphasic regions are shown as dotted bars.

be homogeneously dispersed in a nematic liquid crystal [57].

Another approach to explain the phase stabilization by the presence of nanoparticles is given by Vardanyan et al. in reference [75]. The authors of latter study propose a stabilization mechanism of the nematic phase by the formation of gold-gold aggregates at medium concentrations. The formation of clusters leads to a parallel packing of molecules within the clusters, which increases the nematic order of the dispersion. This ordering process gets distorted by a further increase of particle concentration, so that higher concentrations again show a decrease of clearing temperature. According to this model, it could also be possible that the formation of aggregates in the investigated AuSi dispersions occurs at particle concentrations blow 1 % (w), and a further increase of particle density disturbs the formation of gold-gold clusters. However, although the experimental observations by Vardanyan et al. concerning a concentration dependent increase and decrease of phase transition are similar to the results for AuSi particles in FELIX-2900-03, their effects occur at concentrations one magnitude higher than investigated in this work. At particle concentrations up to 7.5 % (w) and therefore comparable to the AuSi dispersions, the authors report no stabilization of the mesogenic phases [83].

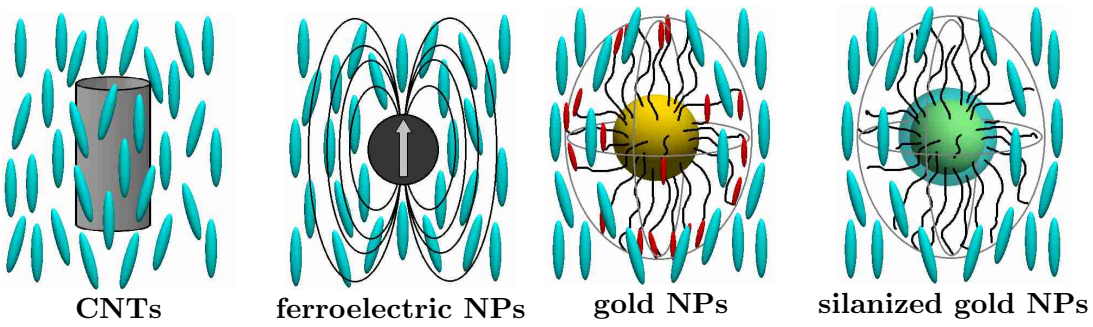

Figure 4.8: Schematic drawings of nanoparticles dispersed in a nematic host. The examples shown here are examples for particles with assumed anisometric particle / host interactions that stabilize the nematic phase and increase the onset temperature of the nematic to isotropic phase transition. (a) Carbon nanotubes as reported by Duran et al. in reference [80], (b) Ferroelectric particles as presented by Lopatina et al. in reference [81], (c) Mesogenic capped gold nanoparticles as reported by Draper et al. in reference [14] and (d) Silanized gold nanoparticles AuSi investigated in this work. Due to similar phase stabilization effects, anisometric interactions between latter particles and the nematic host are assumed.

4.4 Textures and alignment studies

Microscopic textures of nanoparticle / liquid crystal dispersions between crossed polarizers are investigated to reveal information about the distribution of particles in the dispersion. Between confining substrates, the interactions of liquid crystal molecules with the interface define the director distribution of the nematic phase in the bulk. If the presence of nanoparticles influences on these boundary conditions, this is a clear sign for interactions of particles with the substrate's surface. For this reason, the pure hosts and the nanoparticle dispersions are investigated by polarizing optical microscopy and results are compared to obtain information about the localization of nanoparticles in the samples.

4.4.1 Alignment on untreated glass

Between untreated glass slides, the pure nematic hosts 5CB and FELIX-2900-03 show unordered textures as shown in figure 4.9. The polar host 5CB shows a bright texture which is rich of inhomogeneities (see figure 4.9, (a)). However, classic defect lines like typically found in a nematic schlieren texture are not found. By rotating the sample between crossed polarizers, the observable colors change between purple and green, but the observable light intensity remains unchanged. This indicates a random planar orientation of molecules on the substrates with no preferred easy direction of alignment.

The apolar liquid crystal FELIX-2900-03 shows a similar texture, however the image appears dark with gray defects (see figure 4.9, (b)). By rotating the sample between crossed polarizers dark and bright domains change, but there is no complete dark or homogeneous bright state. This indicates a general homeotropic alignment of molecules on the substrates, again with many defects and no preferred easy direction of alignment.

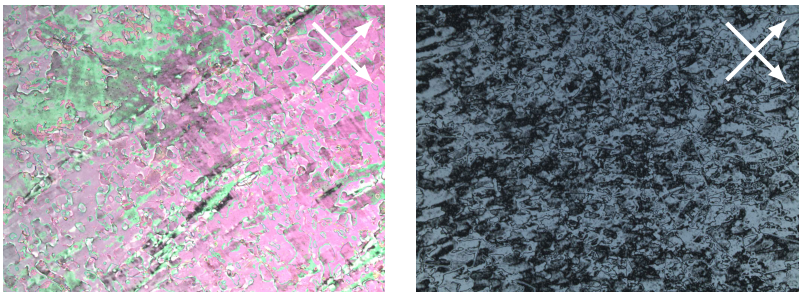

pure 5CB **pure FELIX-2900-03**

Figure 4.9: Macroscopic images of the nematic hosts 5CB (left) and FELIX-2900-03 (right) in self-built plain glass cells between crossed polarizers. Images are obtained at $T_{NI} - T = 8\,\mathrm{K}$ for white light illumination.

For the nematic host 5CB, the concentration dependent alignment and texture changes on plain glass are investigated for dispersions of AuCB, AuSH12$_{(m)}$, CdSe590 and CdSe610 nanoparticles. Dispersions of silanized gold particles AuSi and the magic size quantum dots msCdSe and msCdSe:Zn in the host FELIX-2900-03 are investigated in collaboration with Javad Mirzaei from Prof. Hegmann's group. The respective results for these dispersions have been published in references [65] and [61]. Textures of CdSe590 and CdSe610 particles in the host FELIX-2900-03 are not studied in this work, as a detailed texture study on these dispersions is given in reference [13] by Kinkead et al..

All textures are investigated after cooling the samples from the isotropic into the nematic phase. It is found that the cooling rate plays a crucial role in the formation of different textures. While fast cooling rates (e.g. 5 °C/min or faster) often lead to several domains with different alignment, homogeneous alignment can be achieved by slow cooling (typically 1 °C/min or lower). The importance of cooling rate has also been reported earlier by Qi et al., who found that the formation of birefringent stripe patterns in dispersions of alkylthiol capped gold nanoparticles is only observed for sufficiently slow cooling rates, while larger cooling rates lead to homeotropic domains or areas with schlieren textures [12].

Dispersions of the mesogenic capped gold particles AuCB in 5CB show homeotropic alignment on plain glass between crossed polarizers for the complete range of investigated concentrations (see figure 4.10). While at a low concentration of 0.5 % (w) almost no agglomeration is observed between parallel polarizers, increasing the particle concentration also increases the number of visible agglomerates in the sample.

This result is an example of an general observation made for nanoparticle / liquid crystal dispersions. On the one hand, it has been reported earlier by Qi et al. [78] that usually low particle concentrations below 1 % (w) give well dispersed nanoparticle dispersions with no significant textural effects, while agglomeration and unusual textural features appear only at higher concentrations. On the other hand, the appearance of homeotropic alignment due to nanoparticle doping has also been reported by different groups for different nanoparticle / liquid crystal systems before. For mesogenic coated gold particles similar to the inves-

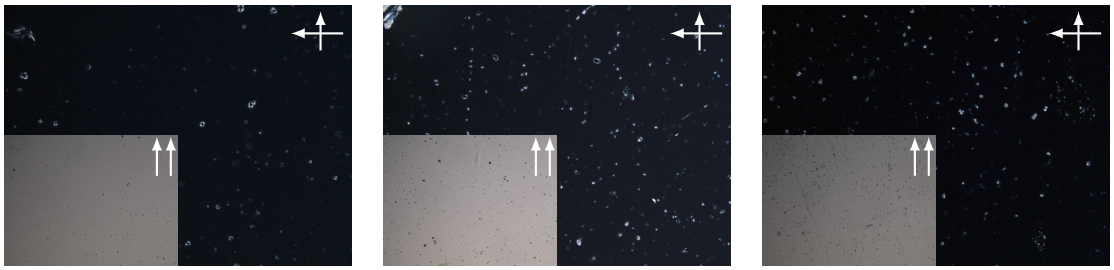

0.5 % AuCB in 5CB **1.0 % AuCB in 5CB** **2.5 % AuCB in 5CB**

Figure 4.10: Polarizing optical microscopy images of dispersions of AuCB particles in the host 5CB. The images were obtained at room temperature between crossed polarizers (large images) and parallel polarizers (small images). The white arrows indicate the position of polarizer and analyzer, respectively.

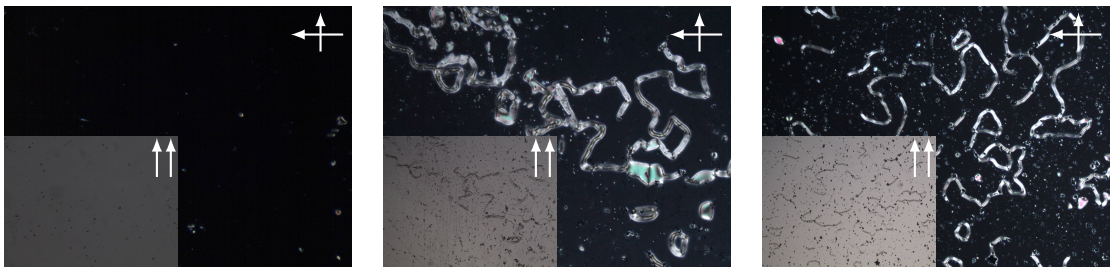

0.5 % AuSH in 5CB **1.0 % AuSH in 5CB** **2.5 % AuSH in 5CB**

Figure 4.11: Polarizing optical microscopy images of dispersions of AuSH particles in the host 5CB. The image were obtained at room temperature between crossed polarizers (large images) and parallel polarizers (small images). The white arrows indicate the position of polarizer and analyzer, respectively.

tigated AuCB, Draper et al. reported homeotropic alignment due to nanoparticle doping in the nematic host 8CB (references [49] and [14]). Bezrodna et al. reported partially homeotropic domains due to the doping of 5CB with functionalized montmorillonite clay in reference [84]. Qi et al. found homeotropic alignment in various experiments for dispersions of alkylthiol capped gold particles in the nematic hosts 5CB, 8CB or FELIX-2900-03 (references [12], [62]). The origin of the homeotropic alignment is presumably the deposition of particles on the substrate interface. Qi et al. showed in reference [78] that preloading the substrate surface with nanoparticles and filling the cell with a pure liquid crystal also induces homeotropic alignment.

Dispersions of AuSH12$_{(m)}$ in 5CB also show homeotropic alignment on plain glass (figure 4.11). In addition, the appearance of birefringent stripes is observed with increasing concentration of particles. This confirms that also in the host 5CB the appearance of birefringent stripes depends on the particle concentration, as suggested by Qi et al. [12] for the host FELIX-2900-03. These birefringent stripes form during the phase transition from the isotropic to the nematic phase, and have been reported by Qi et al. in several publications before ([12], [62], [78]). A detailed study on the origin and the director field topology of

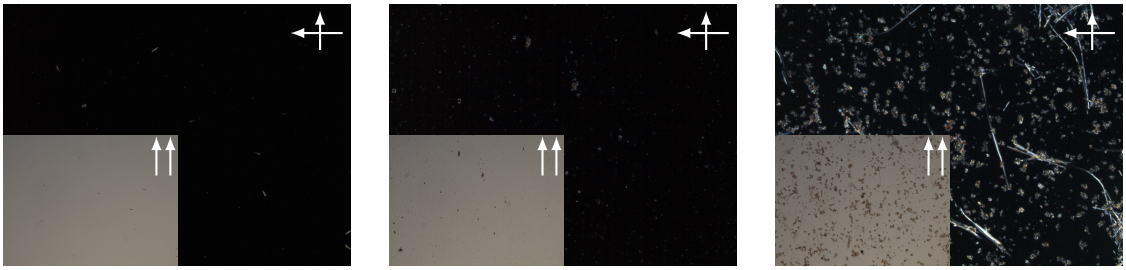

0.5 % CdSe610 in 5CB **1.0 % CdSe610 in 5CB** **2.5 % CdSe610 in 5CB**

Figure 4.12: Polarizing optical microscopy images of dispersions of CdSe610 particles in the host 5CB. The image were obtained at room temperature between crossed polarizers (large images) and parallel polarizers (small images). The white arrows indicate the position of polarizer and analyzer, respectively.

these birefringent stripes is given in section 4.4.2.

In contrast to the observations by Qi et al., a temperature dependent alignment change from planar to homeotropic as reported for dodecanethiol capped particles in the host FELIX-2900-03 [78] could not be observed in 5CB. The $AuSH12_{(m)}$ doped samples show homeotropic alignment immediately after the phase transition from isotropic to nematic. An explanation could be given by the different phase transition temperatures of 5CB and FELIX-2900-03. As the clearing temperature of 5CB is almost 40 °C lower compared to FELIX-2900-03, the particle / substrate interaction during the phase transition takes place at significant lower temperatures in 5CB. This might simplify the separation of particles onto the substrates in 5CB, as the particles carry less thermal energy and are more likely to precipitate. Studying the samples between parallel polarizers shows that at a concentration of 0.5 % (w) almost no visible agglomerates of particles appears, while the samples with concentrations of 1.0 % (w) and 2.5 % (w) show numerous black agglomerates.

The particles CdSe610 induce homogeneous homeotropic alignment and show almost no visible signs of agglomeration for low particle concentrations (figure 4.12). Only at the highest concentration of 2.5 % (w), severe agglomeration is observed. At this high concentration, the texture also shows homeotropic alignment in general, but the alignment is disturbed by the presence of macroscopic agglomerates of nanoparticles. These results in birefringent regions on the sample between crossed polarizers, which, however, show a different texture than the birefringent stripes observed for alkylthiol capped gold particles.

Dispersions of CdSe590 particles with identical capping but smaller core diameter than the CdSe610 particles show inferior solubility in the host 5CB, as even for the lowest concentration of 0.5 % (w) agglomerates of particles can be observed (figure 4.13). It is found that the amount of agglomerates increases with concentration. These observations are in accordance with results reported by Kinkead et al. in reference [13]. The authors report an inferior miscibility of CdSe590 particles in the nematic host FELIX-2900-03, while CdSe610 particles are better soluble and form homogeneous dispersions. Being identically capped with hexadecylamine, the only difference between both particles is the core diameter, which

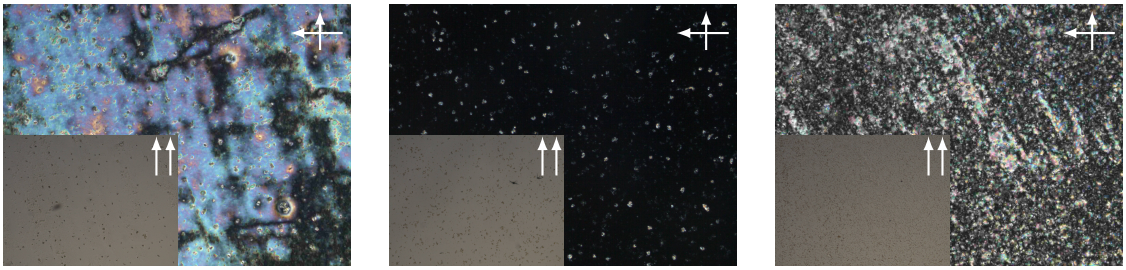

0.5 % CdSe590 in 5CB **1.0 % CdSe590 in 5CB** **2.5 % CdSe590 in 5CB**

Figure 4.13: Polarizing optical microscopy images of dispersions of CdSe590 particles in the host 5CB. The images were obtained at room temperature between crossed polarizers (large images) and parallel polarizers (small images). The white arrows indicate the position of polarizer and analyzer, respectively.

is slightly larger for the CdSe610 particles. This indicates that even slight changes of the core diameter can have a dramatic influence on the miscibility and stability of a nanoparticle / liquid crystal dispersion.

As reported in [13], also the alignment between dispersions of CdSe590 and CdSe610 differs dramatically. As seen in figure 4.12, CdSe610 particles induce almost defect free homeotropic alignment at low concentrations. For dispersions with CdSe590 particles, this is found only for the dispersion with 1.0 % (w) of particles, the samples with 0.5 % (w) and 2.5 % (w) nanoparticles show an inhomogeneous texture with large birefringent areas. The appearance of birefringent stripes is not observed for any cooling rate between 0.2 °C/min and 2 °C/min.

A texture analysis for msCdSe and msCdSe:Zn particles in the host FELIX-2900-03 can not be given here, as the dispersions have been prepared by Javad Mirzaei in Prof. Hegmann's group and have been directly filled into polyimide coated electro-optic test cells. However, a detailed texture analysis is given in reference [65]. While the particles msCdSe induce a schlieren texture between untreated glass slides, the Zn doped msCdSe:Zn particles induce homeotropic alignment with an increasing number of birefringent stripes with increasing particle concentration. This shows how specific the interactions between dopants and substrate's interface react on slight changes on the composition of the ligand shell. While the msCdSe particles are capped with myristic acid only, msCdSe:Zn feature an additional small percentage of trioctylphosphine ligands. This obviously decreases the miscibility within the nematic host or facilitates the interaction with the surface, so that latter particles reside on the interface and induce homeotropic alignment, while msCdSe particles do not show this effect.

4.4.2 Birefringent stripe textures

As shown in figure 4.11, the presence of nanoparticles in a nematic liquid crystal can lead to the formation of birefringent stripe patterns in an homeotropic environment. Their appearance depends on the particle concentration, it is found that higher concentrations

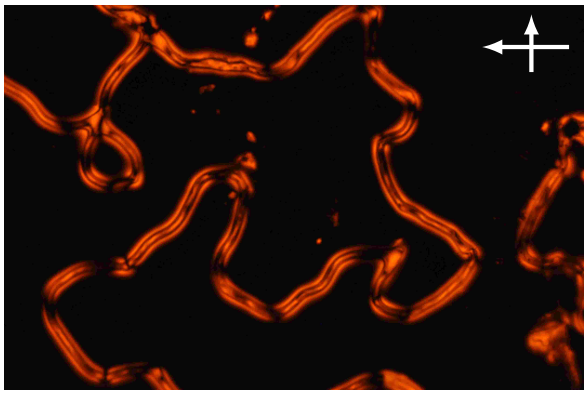

Figure 4.14: POM image of a dispersion of 3% AuSH12$_{(l)}$ in FELIX-2900-03. The image was obtained using monochromatic light ($\lambda = 589\,\text{nm}$) between crossed polarizers.

facilitate the formation of disclination lines. The formation of birefringent stripes is usually observed connected to a phase transition under a slow heating or cooling rate. In FELIX-2900-03, they appear as well on cooling from the isotropic phase as, but less pronounced, on heating from the smectic A phase. All these phenomena have been reported firstly by Qi et al. in reference [12]. The authors not only found these birefringent textures on plain glass samples, but also in polyimide coated electro-optic test cells. This requires a strong tendency of the dispersion to form homeotropic alignment with birefringent stripes, as the strong boundary conditions of the rubbed polyimide alignment layers have to be overcome during this process.

In order to clarify the origin and the director field topology of these birefringent stripes as well as their stabilization process, detailed studies by means of polarizing optical microscopy and fluorescence confocal polarizing microscopy are performed. The results of this study have been published in reference [59] already.

In a representative experiment, a dispersion of 3 % (w) of AuSH12$_{(l)}$ in FELIX-2900-03 is prepared and filled into a 10 µm self-made cell, consisting of an untreated microscope slide and a glued cover slip. The sample is then heated to the isotropic phase and slowly (2 °C/min) cooled down to $T_{NI} - T = 3\,\text{K}$.

After preparation, the sample appears dark between crossed polarizers and exhibits several bright stripes. Under rotation of the sample between polarizers, the dark areas remain dark. This indicates a homeotropic alignment, where the director is aligned perpendicular to the glass substrates. In contrast, the intensity profile of the bright stripes changes during rotation, depending on the angle φ between the stripe axis and the plane of polarization of the incident light. The stripes appear dark if the angle is 0° or 90°, and they exhibit a varying, but always symmetric, intensity profile for $0° < \varphi < 90°$, with maximum brightness at $|\varphi| = 45°$. This typical birefringent behavior indicates a planar, or at least partially planar alignment in the center of the stripes. So the stripes represent a change of the director field from homeotropic in the surrounding to at least partially planar in the center of the stripe.

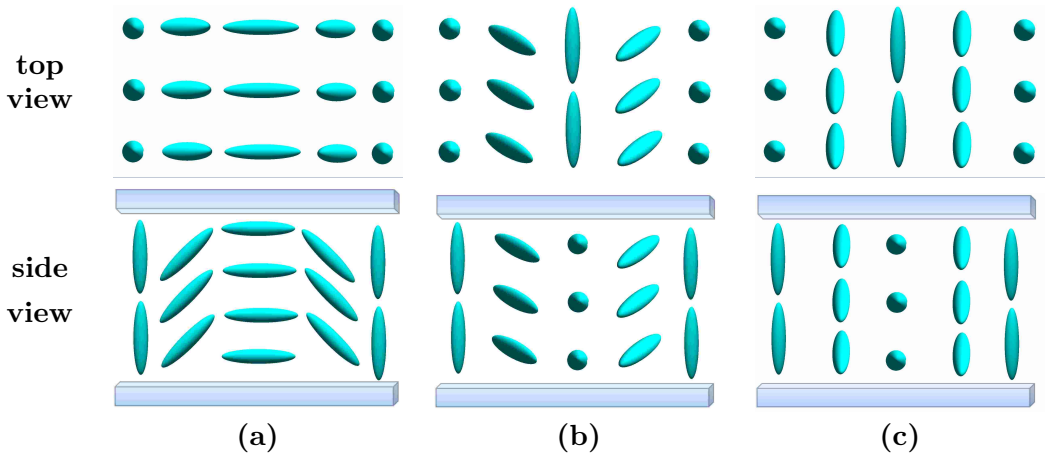

Figure 4.15: Schematic drawing of the three possible director deformations that can lead to birefringent stripes appearing in a homeotropic alignment. **(a)** Director field with bend deformation; **(b)** A combination of splay, twist and bend deformation; and **(c)** Twist deformation, respectively.

In general, there are three different kinds of director deformations that can lead to this transition from homeotropic to planar. The director may bend (figure 4.15, (a)), twist (figure 4.15, (c)), or show a combination of splay, twist and bend (see figure 4.15, (b)). By polarizing optical microscopy, the latter case can be excluded, as it would result in a non-symmetrical intensity distribution between crossed polarizers. In addition, the complete extinction of the transmitted light along the transverse direction observed for $\varphi = 0°$ and $\varphi = 90°$ indicates that either the director component along the stripe axis or the component perpendicular to the stripe axis remains zero while the director changes gradually from homeotropic to planar. In order to reveal the director deformation and distinguish between a bend or twist deformation, a three-dimensional imaging of the director distribution is required. Therefore, fluorescence confocal polarizing microscopy (FCPM) measurements are performed with different states of excitation polarization.

The FCPM image obtained with circular polarized excitation light shows two intersecting vertical and horizontal bright stripes on a dark background with few bright spots (figure 4.16, (a)). These bright spots are caused by agglomerations of undissolved fluorescence dye and not of interest for further investigations. The overall intensity profile confirms the homeotropic alignment in the uniform-appearing areas of the cell, while the orientation of the director within the stripes has planar components. By performing two additional measurements with linearly polarized light, additional information about the director information is obtained. While using excitation light polarized parallel to the x-axis of the (x,y)-scan leads to fluorescence signal only from the horizontal parts of the stripes (figure 4.16, (b)), using excitation light that is polarized parallel to the y-axis shows only the vertical parts thereof (figure 4.16, (c)). This strongly indicates that the director within the stripes is oriented parallel to the wall of stripe. Hence, the birefringent stripes most likely correspond to twist disclinations.

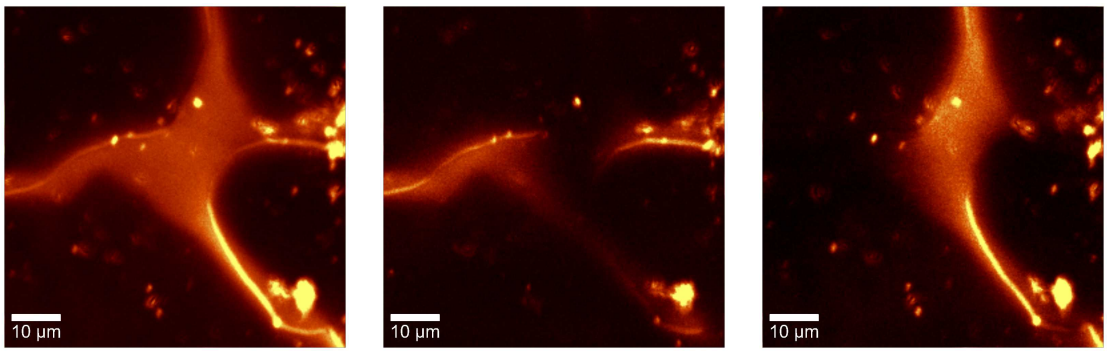

(a) **(b)** **(c)**

Figure 4.16: Fluorescence confocal polarizing microscopy images of a sample containing 3% (w) $AuSH12_{(l)}$ nanoparticles and 0.01% (w) of the dichroic fluorescent dye BTBP in FELIX-2900-03. Excitation illumation exhibits (a) circularly polarized light, (b) linearly polarized light (**E** horizontal) and (c) polarized light (**E** vertical), respectively.

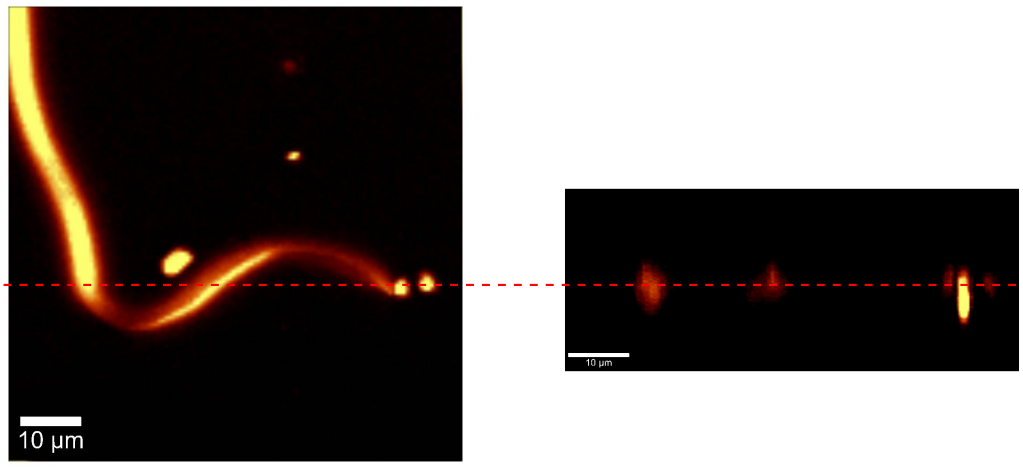

(a) **(b)**

Figure 4.17: (a) Fluorescence confocal polarizing microscopy (FCPM) top view [(x,y) plane] and (b) FCPM side view [(x,z) plane] of a gold nanoparticle dispersion containing 3% (w) AuSH6 nanoparticles and 0.01% (w) of the dichroic fluorescent dye BTBP in Felix-2900-03. The dashed line indicates a shared cross-section between both images.

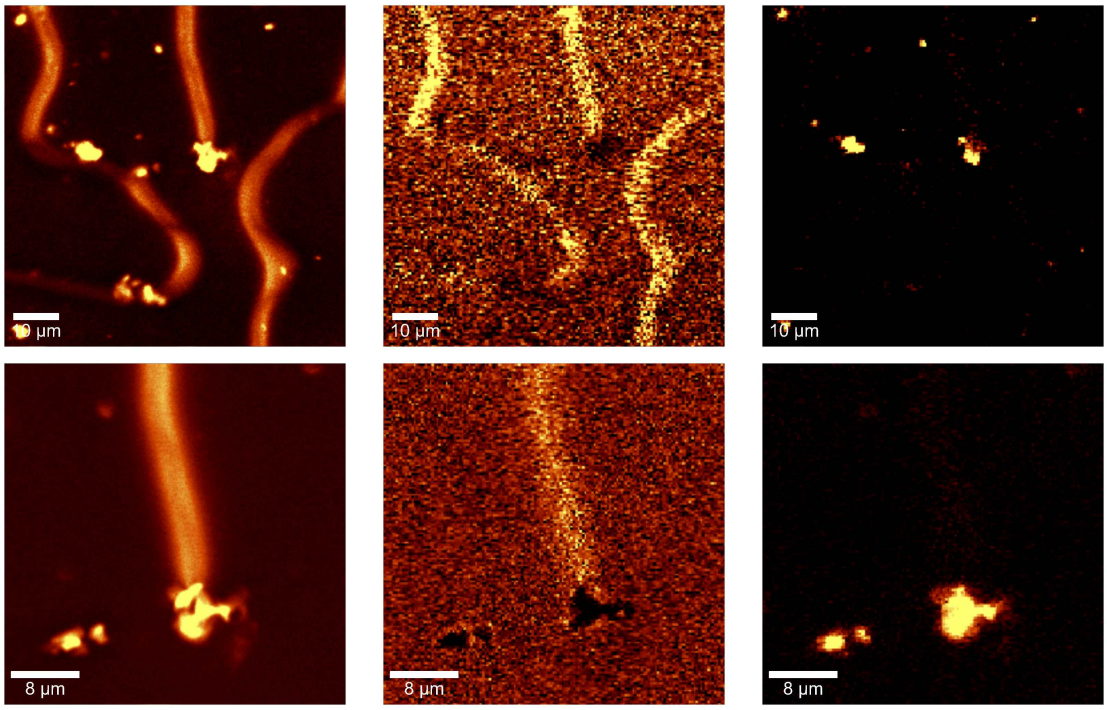

Figure 4.18: Fluorescence confocal polarizing microscopy image of a sample containing 1% (w) CdSe610 nanoparticles and 0.01% (w) of the dichroic fluorescent dye BTBP in FELIX-2900-03. (a)Total fluorescence intensity, (b) fluorescence intensity in the spectral range of 542-552 nm, representing the emission of the dichroic dye BTBP and (c) fluorescence intensity in the spectral range of 605-615 nm, originating from CdSe nanoparticles only.

In order to obtain information about the axial depth of the birefringent regions within the cell gap, additional (x,z)-scans are performed in a FELIX-2900-03 sample doped with 3 % (w) of hexanethiol capped AuSH6 particles. The bright spherical signal spot in the right side of the (x,y)-scan in figure 4.17 is caused by an agglomeration of undissolved BTBP dye. Its size along the z-direction is roughly 10 µm and therefore corresponds approximately to the thickness of the cell. In contrast, the two left signals in the (x,z)-scan are caused by a birefringent stripe, and their deepness is noticeably smaller than the cell gap. Although the position of the glass substrates cannot be seen due to the homeotropic alignment of the liquid crystal, it is striking that the upper limits of all signals share the same altitude in the (x,z)-scan. This can be seen as a strong hint that the upper substrate is located at this height. In conclusion, this experiment indicates that the birefringent stripes do not fill the cell gap completely, but seem to be fixed at only one substrate of the cell. This interaction of the birefringent stripes with the substrate might even lead to a stabilization of the disclination line.

In order to get more information about stabilization processes of the birefringent stripes, wavelength resolved FCPM measurements are performed. With this technique, a distinction between fluorescence emission from the dichroic dye BTBP and from the luminescent

quantum dots can be made. This allows not only to reveal the local director orientation by analyzing the dye signal, but also to map the particle density of quantum dots.

In general, it is found that closed loops of defect lines are more stable than open-ended stripes. The latter ones are usually unstable and disappear several seconds or minutes after the phase transition from the isotropic phase. However, very few open-ended stripes show a very high stability, even higher than usually observed for closed loops. Their stabilization process is investigated in a sample of FELIX-2900-03 doped with 0.001 % (w) of the dichroic dye BTBP and 1 % (w) of CdSe610 nanoparticles. Using a SpectraPro-2300i spectrograph, the fluorescence intensities from the dye ($\lambda_{max} = 540\,\text{nm}$) and the luminescent particles ($\lambda_{max} = 610\,\text{nm}$) are separated. The resulting wavelength-resolved FCPM images reveal that these very stable open-ended stripes are stabilized by agglomerations of nanoparticles.

While images obtained by measuring the total fluorescence intensity show both the bright disclination lines and bright spots at their end (figure 4.18, (a)), the wavelength-resolved images show either the stripes (for $\lambda = 540\,\text{nm}$) (figure 4.18, (b)) or the bright spots at their end ($\lambda = 610\,\text{nm}$) (figure 4.18, (c)). In addition, the bright areas at $\lambda = 610\,\text{nm}$ appear dark at $\lambda = 540\,\text{nm}$, indicating a lack of dichroic dye at these positions. In conclusion, the bright spots at 610 nm appear to be agglomerations of CdSe nanoparticles, stabilizing the ends of open disclination lines pinned to them.

Qi et al. suggest an enhancement of the nanoparticles concentration within the twist disclination lines (see reference [12]). The authors argue that the separation into particle-poor, homeotropic domains and particle-rich, birefringent domains could initially be driven by a drag of gold clusters along the phase separation lines during cooling from the isotropic phase. As a result, a lower concentration of particles leads to a lower stripe density in the nematic phase. The authors also refer to a work by West et al. published in reference [44], where West and his co-workers report such a drag for silica nanoparticles. However, the authors of latter study also predict a critical particle radius $r_{c,3}$, which is required for a drag of particles along the nematic / isotropic interface. Only for larger particles the elastic forces of the nematic phase are large enough to overcome the viscous drag of particles. For the host 5CB, the authors calculate this critical radius to be $r_{c,3} \approx 10\,\text{nm}$, and therefore larger than the radius of nanoparticles used in this study. Additionally, Voloschenko et al. showed that although strong distortions of the director field can attract small particles, a critical radius of more than 20 nm is necessary to overcome thermal fluctuations of Brownian motion [43]. Hence, a drag of particles due to the elastic forces of the ordered nematic phase can presumably be excluded due to the small diameters of the particles used in this work.

However, Soulé and co-workers report the formation of nanoparticle networks as a consequence of different solubility of particles in the nematic and the isotropic phase [85]. When slowly cooling from the isotropic phase, dispersed droplets of a nematic phase nucleate and coalesce coming into contact. This leads to isotropic domains being confined between nematic droplets, and a higher particle concentration due to higher solubility within the isotropic phase. The formation of birefringent stripes follows a similar mechanism, the stripes represent coalescence lines of former nematic droplets in an isotropic surrounding. Hence, the assumption of higher particle concentration within the stripes is not unreasonable. Sim-

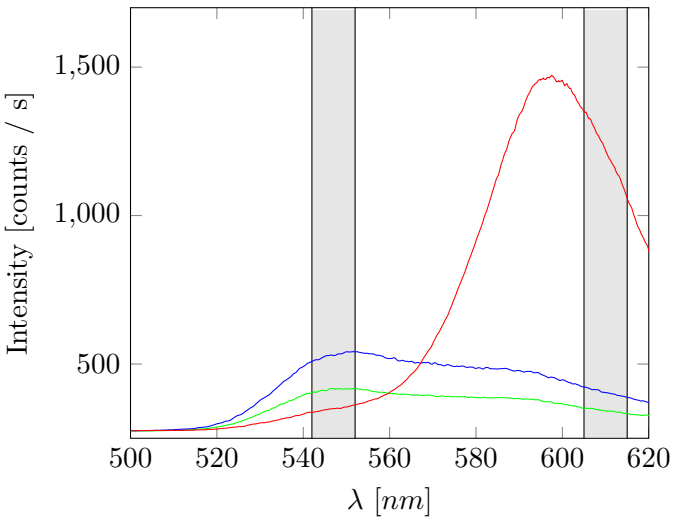

Figure 4.19: Spatially resolved fluorescence intensity spectra obtained from the sample shown in figure 4.18. The fluorescence emission is measured in the homeotropically aligned area (green plot), at the position of a birefringent stripe (blue plot) and at the position of a CdSe610 agglomerate (red plot), respectively. The gray areas indicate the wavelength intervals considered for the calculation of intensities in figure 4.18.

ilar observations are reported by da Cruz et al. in reference [86], where the authors report the formation of particle-rich and particle-poor domains in a dispersion of γ-Fe_2O_3 in the host 5CB. The size of particles used in this study is comparable to the particle size in this work, but in contrast to gold or CdSe particles the detection of γ-Fe_2O_3 particles within a nematic or isotropic domain is possible via the magnetic properties of these domains. A linear self-assembly of gold nanoparticles comparable to $AuSH12_{(l)}$ in smectic 8CB on structured MoS_2 surfaces have recently reported by Coursault and co-workers in reference [87], indicating that a selective ordering of very small particles is possible at the substrate's interface. A recent example of a self-organization of octanethiol functionalized gold nanoparticles with 3 nm diameter in a cholesteric template is given by Bitar et al. in reference [88]. In conclusion, the self-organization of nanoparticles in a nematic host has been proven in literature, although the driving force for this process differs from the mechanism for colloidal particles. The minimization of elastic free energy by a particle drag to locations with high distortions in the director field requires a certain size of particles ($d > 40\,\text{nm}$, [43]). Smaller particles obviously follow another mechanism of ordering, presumably connected to specific interactions of their functionalization and the host molecules.

Admittedly, on the basis of confocal fluorescence polarizing microscopy measurements performed here, the question if an enhancement of the nanoparticle concentration within the twist deformation occurs cannot be answered. With proper contrast settings, a slight accumulation of fluorescence signal at $\lambda = 610\,\text{nm}$ within the region of the birefringent stripe can be found. However, these signals might also be caused by the dichroic dye BTBP, which features a very broad fluorescence spectrum and therefore also contributes to the fluorescence intensity at $\lambda = 610\,\text{nm}$, as shown in figure 4.19.

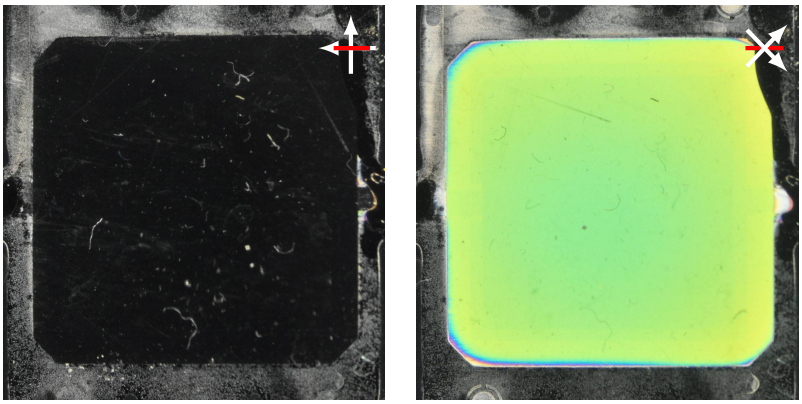

$\varphi = 0°$ $\varphi = 45°$

Figure 4.20: Macroscopic images from the nematic host 5CB in an electro-optic test cell between crossed polarizers obtained at room temperature. The angle φ represents the angle between the rubbing direction of the cell and the plane of polarization of the incident light. The white arrows represent the orientation of polarizer and analyzer, the red bar represents the easy direction of the test cell.

4.4.3 Alignment in electro-optic test cells

The electro-optic test cells used in this work are coated with a rubbed polyimide layer, which induces a homogeneous, strong planar anchoring of the liquid crystal molecules on the surface. Between crossed polarizers this results in a complete dark state for an angle φ between the rubbing direction of the sample and the plane of polarization of the incident light of $\varphi = 0°$ or $\varphi = 90°$ (see figure 4.20, left) and a homogeneous bright state with maximum light transmission for an angel of $\varphi = 45°$ (see figure 4.20, right).

The dispersions of AuCB, AuSH12$_{(m)}$, CdSe590 and CdSe610 in the nematic host 5CB are found not to alter this behavior. After preparing the dispersions, they are filled into the test cell by capillary forces, being in the isotropic state. After filling, the samples are cooled down to room temperature, heated to the isotropic phase again, and then investigated by polarizing optical microscopy in the nematic phase at room temperature. This temperature treatment should allow the liquid crystal to overcome the initial alignment caused by the filling procedure, and align in accordance to the thermodynamical equilibrium state defined by the boundary conditions of the alignment layers. As a result, a homogeneous planar alignment is obtained over the complete cell area for all particle dispersions mentioned above and for all concentrations investigated. The appearance of birefringent stripes after slow cooling from the isotropic phase, as observed for uncoated glass cells (see section 4.4.1) or reported also in FELIX-2900-03 for polyimide coated test-cells [12] could not be observed.

Dispersions with different concentration of CdSe590 in the nematic host FELIX-2900-03 show striking effects on the polyimide alignment layer of the electro-optic test cells. In addition, a filtering effect occurs, especially for samples with 4 µm cell gap. For these samples, macroscopic images taken without polarizers (see figure 4.21, bottom) show a

homogeneous filling of the cells without visible agglomerations. However, textures obtained between crossed polarizers (see figure 4.21, top) reveal homeotropic alignment close to the filling point and an alignment change to planar more far away of the filling point. The size of the homeotropic area seems to be correlated to the amount of particles in the respective dispersion.

In contrast to 4 µm cells, images taken from dispersions of CdSe590 in FELIX-2900-03 in 10 µm cells without polarizers (figure 4.22, bottom) reveal precipitation of reddish particles from the filling point along the floating direction of the dispersion. The area covered by particles is found to be larger for higher particle concentrations. Images obtained between crossed polarizers (figure 4.22, top) show homeotropic alignment in these areas with visible surface coverage, and inhomogeneous planar alignment in the rest of the cells. A homogeneous planar alignment as expected from the polyimide alignment layer of the test cell does not occur with this cell thickness at any concentration.

The semicircular spreading of particles which cover the surface along the floating direction during filling indicates that the dispersions of CdSe590 particles in the host FELIX-2900-03 are not stable. In consequence, a movement of particles from the liquid crystal to the interface occurs while the liquid crystal floats into the cell gap. Assuming this depletion of particles is proportional to the amount of particles in the bulk, the surface coverage of the polyimide alignment layer with nanoparticles should decrease with increasing distance from the filling point. This is also indicated by the textures obtained between crossed polarizers, as the alignment of the liquid crystal is more likely to be homogeneous planar far away from the filling point, and homeotropic in areas with a visible surface coverage with particles. This indicates that a precipitation of nanoparticles on the substrates can superimpose the effect of the polyimide alignment layer and induces homeotropic alignment. Only in areas far away from the filling point, the particle concentration is not sufficiently high to induce homeotropic alignment.

A filtering effect on the cell gap is observed especially for 4 µm cells and indicates that most visible agglomerates are larger than 4 µm. Consequently, they cannot enter the cell gap and hence accumulate at the substrate on the filling side of the sample. This effect is very striking for dispersions of CdSe610 in FELIX-2900-03. Images obtained without polarizers from samples with 4 µm cell gap (figure 4.23, bottom) all show a homogeneous filling of the test cells without visible agglomerations in the cell gap. But especially the samples with 2.5 % (w) and 5.0 % (w) CdSe610 exhibit a very strong accumulation of particles on the left side of the substrate, which is the filling side of the test cells.

This strong accumulation of particles outside of the cell gap makes it impossible to predict the concentration of particles in the center of the sample. Although under a microscope the cells appear homogeneously filled and agglomerate free within the electrode area, this additional depletion due to agglomerates has to be considered for the electro-optical analysis of the samples. As mentioned in section 4.1, it is assumed that the amount of precipitation is proportional to the particle concentration. This is in fairly good accordance with the visible amounts of agglomerates seen in the bottom images of figure 4.23. Hence, electro-optical data obtained from these samples can only give a general trend of concentration dependent

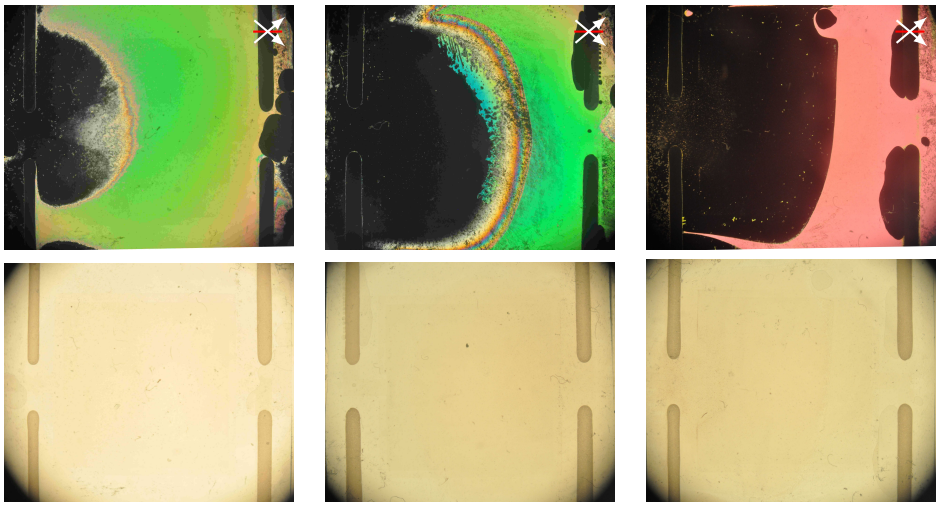

Figure 4.21: Macroscopic images of 4 µm electro-optic test cells filled with dispersions of CdSe590 in FELIX-2900-03. The test cells were filled from the left side. Images were obtained without polarizers (bottom) or between crossed polarizers (top) at a temperature $T_{NI} - T = 7\,\mathrm{K}$. The white arrows represent the orientation of polarizer and analyzer, the red bar represents the easy direction of the test cell.

changes of physical properties, a comparison to other nanoparticle / liquid crystal systems is difficult as the actual concentration range is unknown.

However, Kinkead et al. report the successful preparation of stable dispersions of CdSe590 and CdSe610 particles in FELIX-2900-03 and also provide electro-optical data in reference [13]. The difference between samples reported in reference [13] and own samples is the use of different electro-optic test cells. While Kinkead et al. use antiparallel rubbed polyimide coated test cells from LC Vision, USA, own samples are prepared in antiparallel rubbed polyimide coated test cells from E.H.C Co., Ltd, Japan. Without having further details from the manufacturers, the polyimide layer of both types of test cells differs: The pretilt angle for LC Vision cells is given by 1-3° [13], the pretilt angle for E.H.C cells is below 1° [68]. It can be concluded that the different textures of CdSe590 / FELIX-2900-03 are caused by different interactions between the nanoparticles and the polyimide alignment layer.

Images of CdSe610 in FELIX-2900-03 in 4 µm cells obtained between crossed polarizers (figure 4.23, top) show a similar influence of the nanoparticles on the alignment layer as found for CdSe590 particles. The influence of the polyimide alignment layer is not visible, and with increasing particle concentration, the size of areas with homeotropic alignment also increases. At the highest concentration investigated for CdSe610 (5 % (w)), only homeotropic alignment occurs. Similar results concerning filtering effects and textures between crossed polarizers are found for dispersions of CdSe610 in FELIX-2900-03 in 10 µm cells (see figure 4.23).

From our observations made for dispersions of CdSe590 and CdSe610 in FELIX-2900-03, a model is developed to explain the changes in alignment. In general, the textures observed

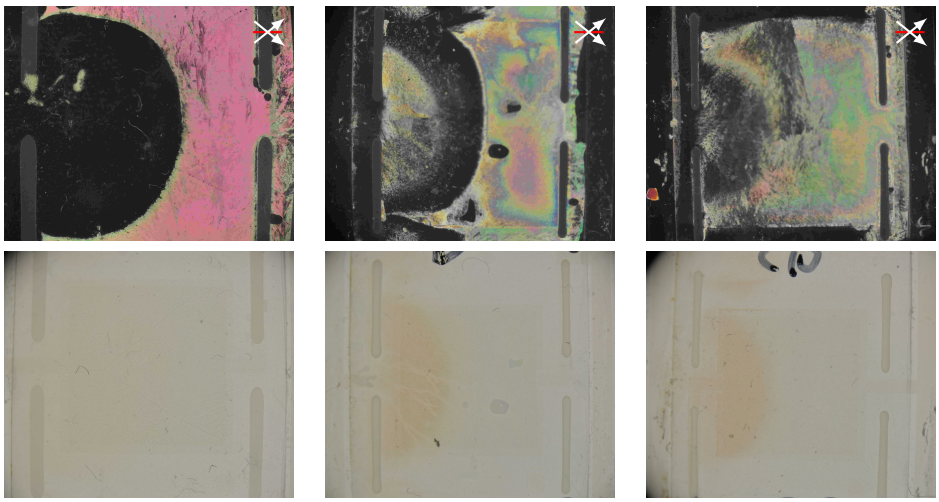

0.5 % CdSe590 **1.5 % CdSe590** **2.5 % CdSe590**

Figure 4.22: Macroscopic images of 10 µm electro-optic test cells filled from the left side with dispersions of CdSe590 in FELIX-2900-03. Images were obtained without polarizers (bottom) or between crossed polarizers (top) at a temperature $T_{NI} - T = 7\,\mathrm{K}$. The white arrows represent the orientation of polarizer and analyzer, the red bar represents the easy direction of the test cell.

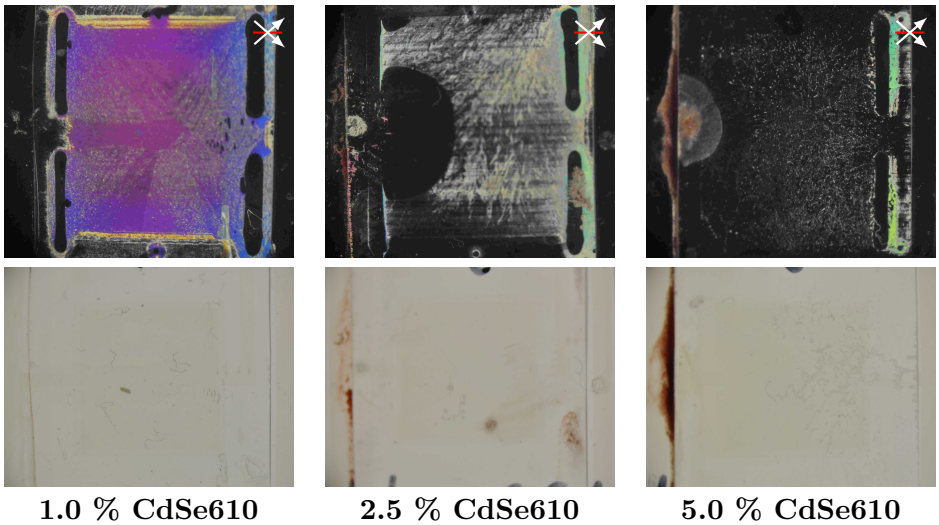

1.0 % CdSe610 **2.5 % CdSe610** **5.0 % CdSe610**

Figure 4.23: Macroscopic images of 4 µm electro-optic test cells filled from the left side with dispersions of CdSe610 in FELIX-2900-03. Images were obtained without polarizers (bottom) or between crossed polarizers (top) at a temperature $T_{NI} - T = 7\,\mathrm{K}$. The white arrows represent the orientation of polarizer and analyzer, the red bar represents the easy direction of the test cell.

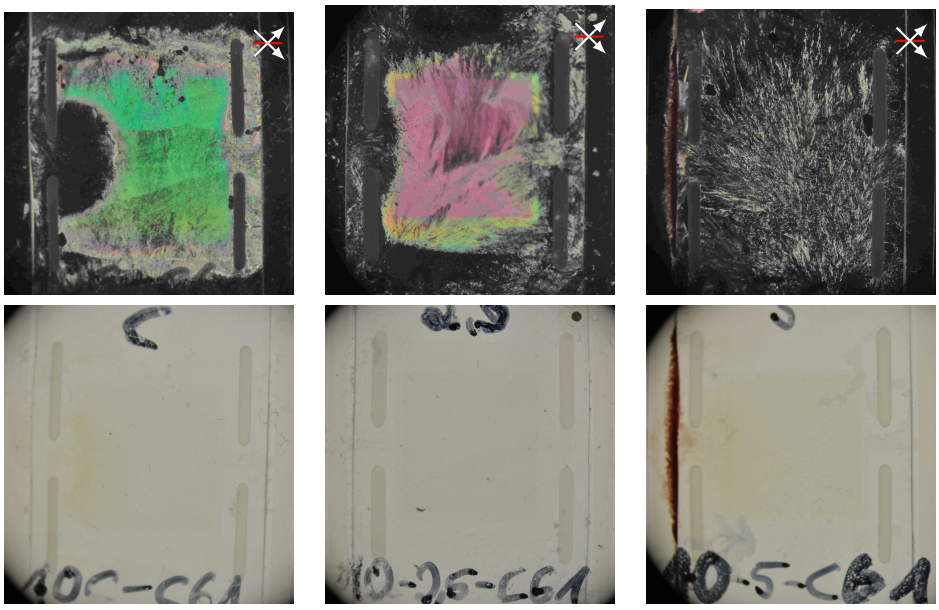

Figure 4.24: Macroscopic images of 10 µm electro-optic test cells filled from the left side with dispersions of CdSe610 in FELIX-2900-03. Images were obtained without polarizers (bottom) or between crossed polarizers (top) at a temperature $T_{NI} - T = 7\,\mathrm{K}$. The white arrows represent the orientation of polarizer and analyzer, the red bar represents the easy direction of the test cell.

between crossed polarizers can be divided into three regions (see figure 4.25). In the area very close to the filling point, usually homeotropic alignment is observed (region **(A)**). This region covers a semicircular area around the filling point, the diameter of this field varies from cell to cell. The neighboring region **(B)** is an intermediate region with partially planar alignment. In this region, the molecules are mostly aligned parallel to the substrates, but by rotating the sample between crossed polarizers it can be shown that the alignment differs from the polyimide induced homogeneous planar alignment in region **(C)**. It is found that the size of these three regions and their ratio vary for different cells and different concentrations, a clear concentration dependent trend could not be confirmed. For example, cells filled with a dispersion of 5 % (w) CdSe610 in FELIX-2900-03 only exhibit region **(A)**, while the 4 µm cell filled with 1 % (w) CdSe610 in FELIX-2900-03 does not show a region **(A)** at all. This is connected to different amounts of particles residing on the surface during the filling process and cannot be controlled experimentally.

By measuring the electrical field-dependent light transmission between crossed polarizers in the regions **(A)**, **(B)** and **(C)**, additional information about the alignment of the liquid crystal and the position of nanoparticles within the test cell can be obtained (see figure 4.26). In region **(A)**, the light transmission remains zero under external electrical fields, which is proof for the homeotropic alignment of the liquid crystal molecules in this area. In region **(B)**, a Fréedericksz transition from planar to homeotropic alignment occurs with increasing external field. However, the Fréedericksz transition does not exhibit a well-defined threshold voltage V_{Th}, where the deformation of the initial director field begins. This is

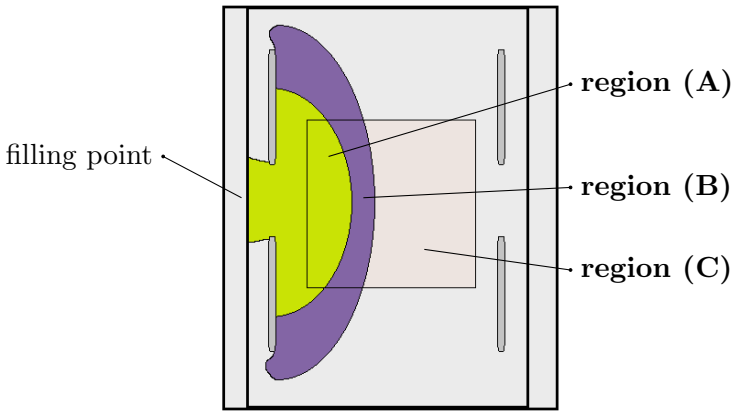

Figure 4.25: Schematic drawing of an electro-optical test cell with different regions of alignment as found for dispersions of CdSe590 and CdSe610 in FELIX-2900-03. Although the size of the different regions varies for different cells, in general the three regions **(A)** with homeotropic alignment, an intermediate region **(B)** and an area with planar alignment **(C)** are found to occur.

usually found only for samples featuring a tilted alignment of molecules to the substrates, which is most likely caused by partial coverage of particles on the surface. This partial coverage then reduces the surface energy of the interface and, together with topological effects, induces tilted alignment. Transmission characteristics obtained from region **(C)** show a Fréedericksz transition with well defined threshold voltage. In addition to an observation of planar alignment parallel to the easy axis of the cell by rotating the sample between crossed polarizers, this indicates strong boundary conditions caused by the initial polyimide alignment layer.

An experimental proof of CdSe particles residing at the liquid crystal / glass interface is given by confocal fluorescence microscopy analysis (figure 4.27). The (x,z)-scan shown here is obtained from a sample of 1 % (w) CdSe610 in FELIX-2900-03 between untreated glass plates. The polarizing optical microscopy image of this sample shows homeotropic alignment comparable to the image given in figure 4.13. The bright intensity signals are caused by small agglomerates of particles, while the signals with lower intensity are probably caused by single quantum dots. The asymmetric shape of the fluorescence signals is caused by the point spread function of the confocal microscope, which is always elongated along the axial direction. The fluorescence signals form two lines of equal height, which are separated by a distance of roughly 10 µm. This corresponds to the cell gap of the sample, what strongly indicates that the particles reside on the interface in areas with homeotropic alignment.

To summarize the statement of the model developed here, the different textures for CdSe590 and CdSe610 particles in FELIX-2900-03 observed between crossed polarizers are caused by different amounts of nanoparticles residing on the liquid crystal / substrate interface. When the particle coverage is sufficiently high, homeotropic alignment is induced, while only partial coverage of particles leads to tilted alignment. The surface coverage decreases with increasing distance to the filling point. Only at very low or no particle coverage,

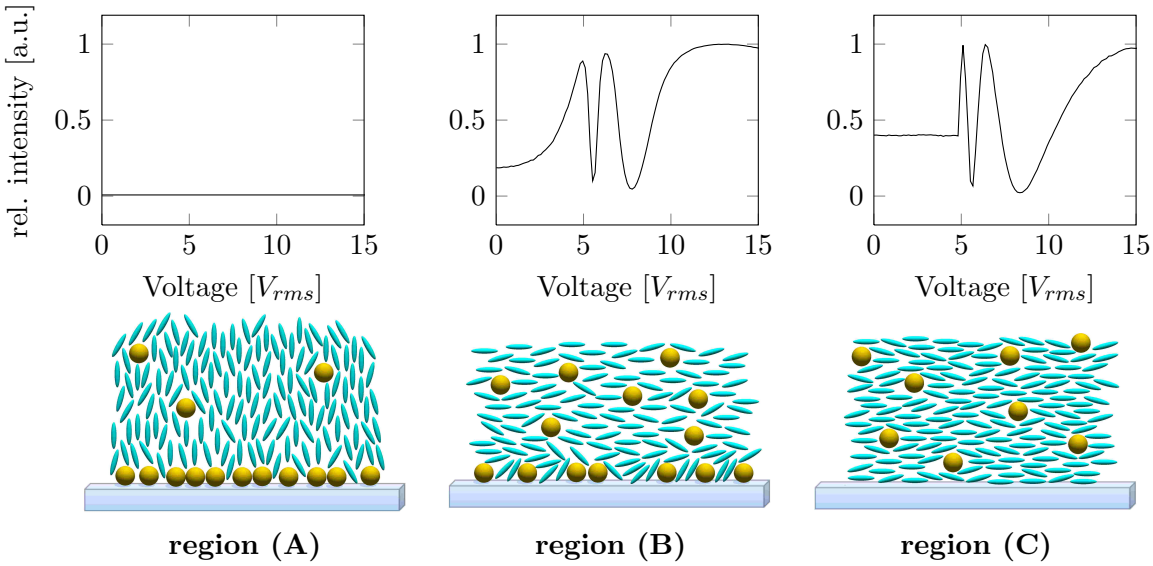

Figure 4.26: Electro-optical response of a dispersion of 1 % CdSe610 in FELIX-2900-03. The light transmission is measured in the three predefined regions **(A)**, **(B)** and **(C)**, respectively (top), and a model about surface / liquid crystal interactions is derived from these observations (bottom).

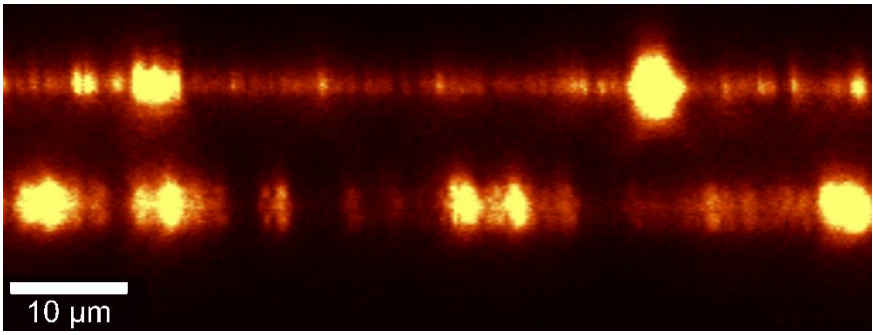

Figure 4.27: Confocal fluorescence microscopy image obtained from a sample of 1 % (w) CdSe610 in FELIX-2900-03. The intensity distribution in the (x,z)-plane strongly indicates that the luminescent nanopatricles are residing on the liquid crystal / glass interface.

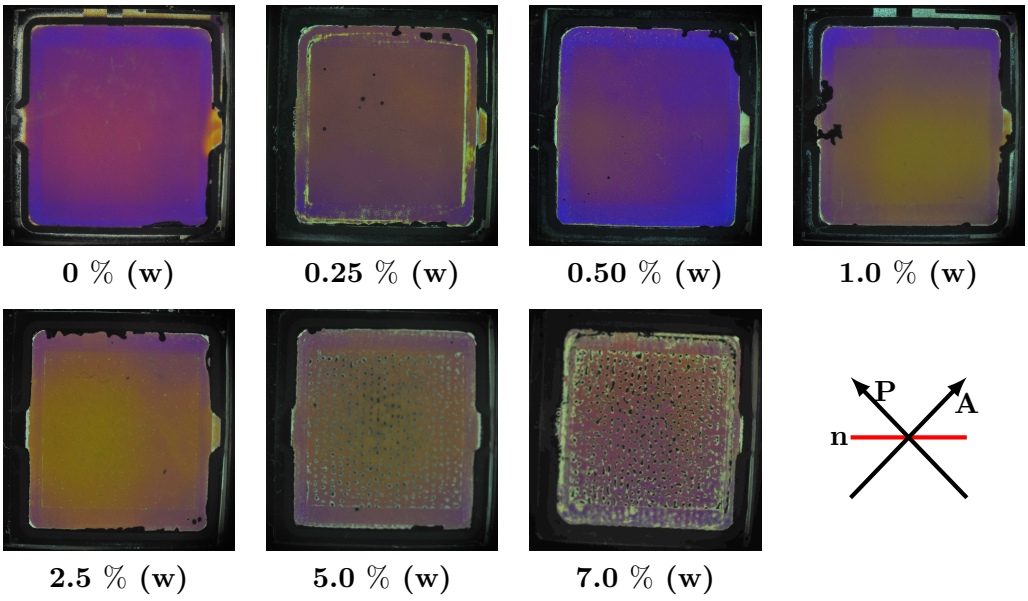

Figure 4.28: Macroscopic images of 4 µm electro-optic test cells filled dispersions of AuSi in FELIX-2900-03. Images were obtained between crossed polarizers at a temperature $T_{NI} - T = 7\,\mathrm{K}$. The black arrows on the lower right represent the orientation of polarizer and analyzer, the red bar represents the easy direction of the test cell.

the alignment induced by the initial polyimide alignment layer is retained.

Mixtures of silanized AuSi particles in FELIX-2900-03 show an homogeneous planar alignment over the complete concentration range from 0.25 % (w) to 7.5 % (w) (figure 4.28). However, at particle concentrations higher than 2.5 % (w), an increasing number of black domains is observed, which remain after cooling from the isotropic phase. As these dark domains also remain dark when tilting the samples between crossed polarizers to polar angles up to 60°, homeotropic alignment can be excluded. Hence, these domains are identified to be isotropic domains. In addition, fluorescence confocal polarizing microscopic studies performed by Javad Mirzaei in Prof. Hegmann's group revealed a higher solubility of the dichroic dye BTBP in these dark domains than in the nematic surrounding [61]. It is known that the dichroic dye shows a higher solubility in the isotropic phase than in the nematic phase, which allows to conclude that for particle concentrations higher than 2.5 % (w), a coexistence of nematic and isotropic phase occurs even for temperatures far below the clearing temperature of the dispersions. Another observation reported by Prof. Hegmann's group is the enrichment of particles in these isotropic domains [61]. This indicates that the well-known depletion effect of particles from the nematic into the isotropic phase also occurs at high concentrations in dispersions of silanized gold particles in the host FELIX-2900-03. However, these instabilities only occur at concentrations of 5 % (w) or higher, which is higher than the typical solubility limit of nanoparticles in a nematic host [57].

Dispersions of magic sized quantum dots msCdSe and msCdSe:Zn in FELIX-2900-03 are filled in 4 µm LC Vision electro-optic test cells and do not show precipitation effects as seen

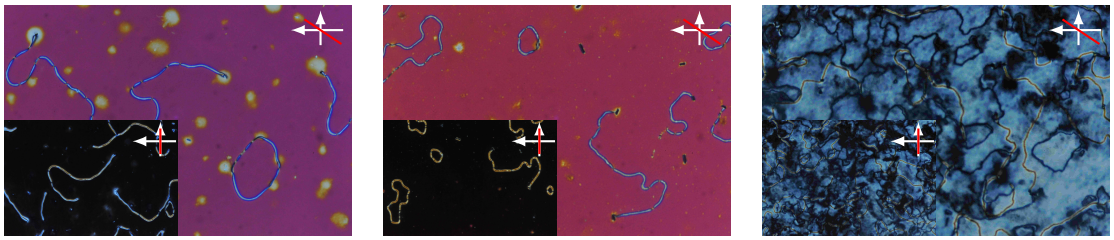

1.0 % msCdSe **2.5 % msCdSe** **5.0 % msCdSe**

Figure 4.29: Polarizing optical microscopy images of dispersions of msCdSe particles in FELIX-2900-03 at $T_{NI} - T = 4\,\mathrm{K}$. Images are obtained between crossed polarizers, with the easy direction of the test cell under an angle $\varphi = 45°$ to the the plane of polarization of the incident light (large images) or parallel to the plane of polarization of the incident light (small images). The magnification is $M = 5x$.

for CdSe590 and CdSe610 particles in E.H.C test cells before. Dispersions of msCdSe show homogeneous planar alignment for 1 % (w) and 2.5 % (w), and a schlieren texture for 5 % (w) of particles (see figure 4.29)). In contrast to all other nanoparticle / liquid crystal dispersions investigated in this work, the birefringent stripes investigated in section 4.4.2 are found to occur also in electro-optic test cells after slowly cooling down from the isotropic phase. But in contrast to the birefringent stripes observed for $\mathrm{AuSH12}_{(m)}$ particles between plain glass, these stripes appear in an homogeneous planar alignment, as clearly can be seen by rotating the samples between crossed polarizers. While the background appears bright under an angle $\varphi = 45°$ to the the plane of polarization of the incident light for 1 % (w) and 2.5 % (w) of msCdSe particles, the background is dark for $\varphi = 0°$ or $\varphi = 90°$. At the highest concentration of 5 % (w) msCdSe particles, the effect of the polyimide alignment layer is superimposed by the nanoparticles, and the birefringent stripes appear in an inhomogeneous schlieren texture surrounding.

Polarizing optical microscopy images from dispersions of msCdSe:Zn particles in FELIX-2900-03 show similar textures as obtained for msCdSe dispersions. At 1.0 % (w) and 2.5 % (w) of particles, the uniform alignment of the rubbed polyimide layer remains. At 5.0 % (w) of nanoparticles numerous planar aligned areas occur, probably caused by particles residing on the interface. The test cells filled with msCdSe:Zn / FELIX-2900-03 dispersions show numerous visible agglomerates at all three concentrations investigated. This indicates that the miscibility or stability of the Zn doped msCdSe:Zn particles in the liquid crystalline host is inferior to the msCdSe particles. As the interaction between particle and host mainly takes place over the ligand shell, this can most likely be attributed to the additional trioctylphosphine ligands on the Zn doped particles. These are sterically more demanding than the aliphatic amine and therefore seem to reduce the degree of interdigitation between ligand shell and host molecules.

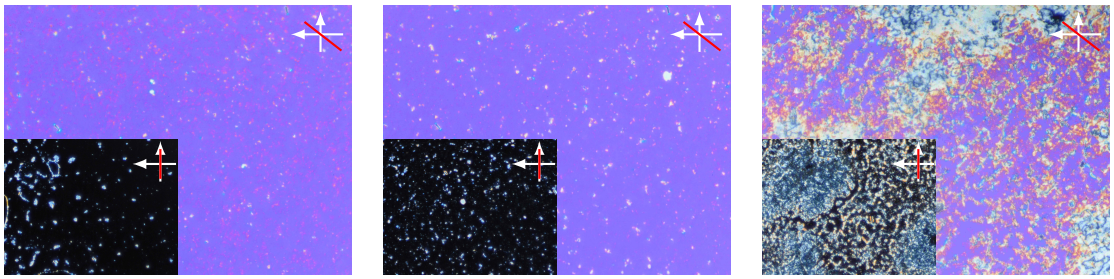

1.0 % msCdSe:Zn **2.5 % msCdSe:Zn** **5.0 % msCdSe:Zn**

Figure 4.30: Polarizing optical microscopy images of dispersions of msCdSe:Zn particles in FELIX-2900-03 at $T_{NI} - T = 7\,\mathrm{K}$. Images are obtained between crossed polarizers, with the easy direction of the test cell under an angle $\varphi = 45°$ to the the plane of polarization of the incident light (large images) or parallel to the plane of polarization of the incident light (small images). The magnification is $M = 10x$.

4.5 Behavior under the influence of electric fields

4.5.1 Field-induced alignment changes

Besides studying the alignment of nanoparticle / liquid crystal dispersions in polyimide coated electro-optical test cells directly after filling, an influence of nanoparticles on the initial alignment layers under external electric fields is investigated. Of particular interest are changes of alignment that remain after the electric field is switched off again, as this indicates a change of boundary conditions due to the presence of nanoparticles.

Applying an electric field to a nematic liquid crystal filled in an electro-optic test cell usually leads to a reorientation of the liquid crystalline material only, but does not alter the alignment layer of the test cell. The boundary conditions remain unchanged, and after removing the external field the liquid crystal shows the same alignment again as before the switching experiment. Applying an electric field to a nanoparticle / liquid crystal dispersion, however, can modify the surface anchoring of the liquid crystals on the substrate interface of the test cell. As noted in section 4.4.3, dispersions of AuCB, AuSH12$_{(m)}$, CdSe590 or CdSe610 in 5CB show a homogeneous planar alignment induced by a rubbed polyimide alignment layer after filling into electro-optic test cells by E.H.C Co., Ltd (Tokyo, Japan). Dispersions of AuSi and low concentrations of the magic sized quantum dots msCdSe and msCdSe:Zn in FELIX-2900-03 filled in test cells by LC Vision in general also exhibit a homogeneous planar alignment, besides the appearance of birefringent stripes in dispersions with msCdSe particles. As a consequence of the homogeneous planar alignment, all these samples appear bright between crossed polarizers with the easy axis of the test cells oriented under an azimuthal angle of $\varphi = 45°$ to the plane of polarization of incident light. However, after one electro-optic measurement cycle it is found that dispersions of AuCB and AuSH12$_{(m)}$ in 5CB show gradual color changes within the electrode area between crossed polarizers. Dispersions containing AuCB particles even change to a non-birefringent black state after up to 10 cycles (see figure 4.32). An electro-optic measurement cycle is given by a sine voltage of 1 kHz whose amplitude is stepwise increased from $0.05\,\mathrm{V}_{rms}$ to $19.85\,\mathrm{V}_{rms}$

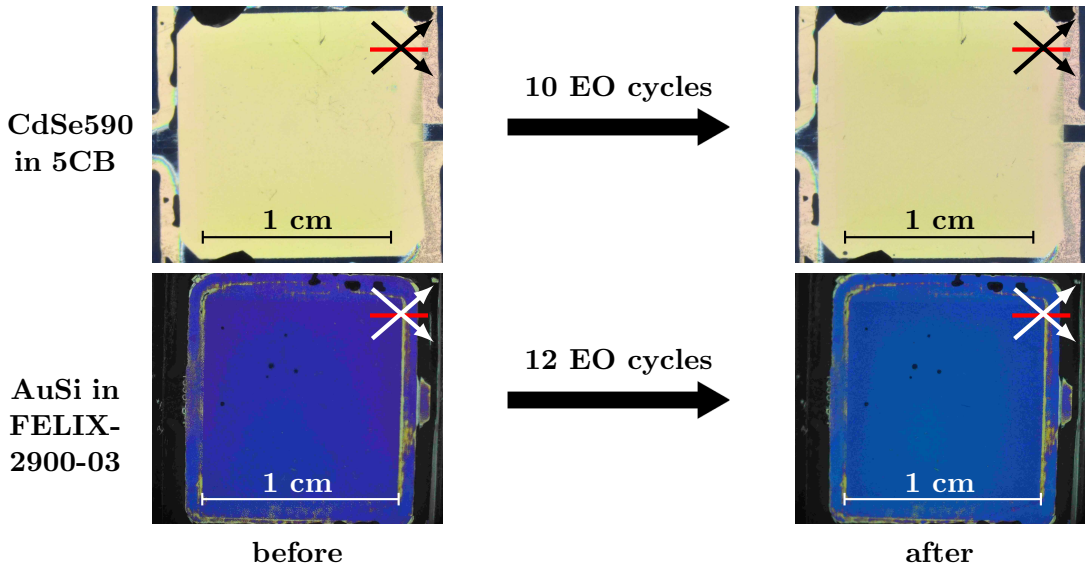

Figure 4.31: Macroscopic photographs of electro-optic test cells filled with dispersions of 0.5 % (w) CdSe590 in 5CB (top) and 0.5 % (w) AuSi in FELIX-2900-03 (bottom) before and after treatment in electric field. The images are taken at $T_{NI} - T = 8\,\mathrm{K}$ using a white light source between crossed polarizers. The orientation of the cell's rubbing direction with respect to the crossed polarizers is indicated by the bars and arrows, respectively.

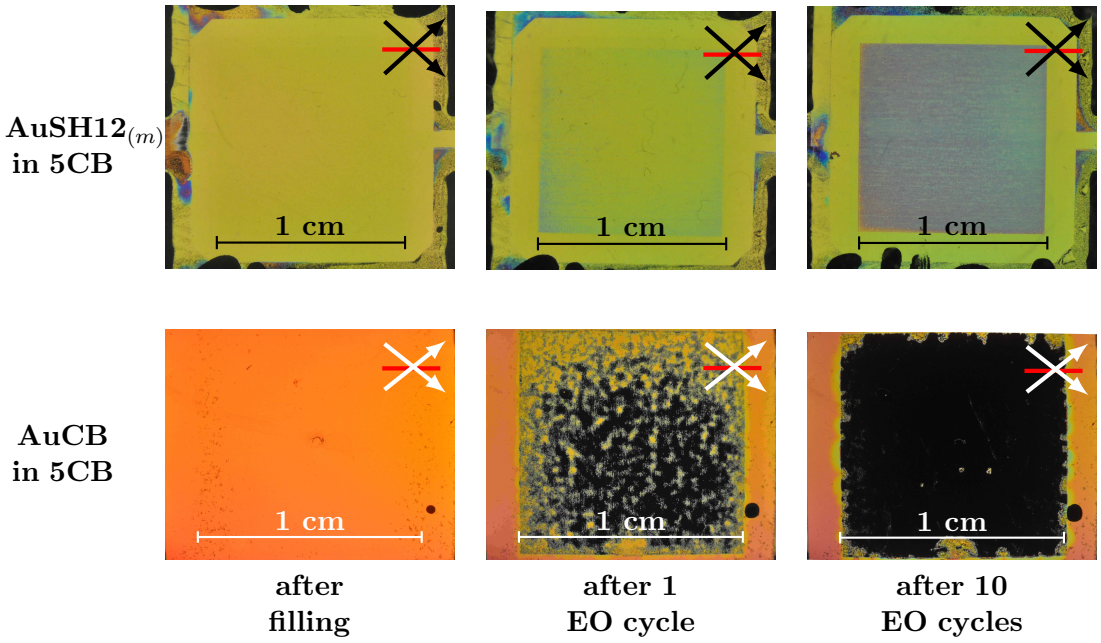

Figure 4.32: Macroscopic photographs of electro-optic test cells filled with dispersions of 0.5 % (w) AuSH12$_{(m)}$ particles (top) and 1.0 % (w) AuCB particles (bottom) in the nematic host 5CB. The images are taken at $T_{NI} - T = 8\,\mathrm{K}$ using a white light source between crossed polarizers. The orientation of the cell's rubbing direction with respect to the crossed polarizers is indicated by the bars and arrows, respectively.

(see section 3.5.1, measurement of threshold voltage V_{Th} and dielectric anisotropy $\Delta\epsilon$). In contrast, dispersions of the semiconductor particles CdSe590 and CdSe610 in 5CB as well as dispersions of msCdSe and msCdSe:Zn in FELIX-2900-03 do not show field induced alignment changes (see figure 4.31). Dispersions of the gold particles AuSi in FELIX-2900-03 are also found to be stable under the influence of an electric field, and do not change the properties of the polyimide alignment layer.

These field-induced alignment changes occur only within the active ITO-electrode areas of the electro-optic test cells, and exhibit a sharp boundary line to the unaltered planar alignment in the surrounding. In figure 4.33, microscopic photographs of one edge of a sample of 2.5 % AuCB in the nematic mixture EN18 (Chisso Corporation, $\Delta\epsilon$ = -6 at $T = 25\,^{\circ}\mathrm{C}$, [89]) after treatment in electric fields are shown. The nematic mixture EN18 is used as a host material for the analysis of phase gratings (see section 4.5.1), and features a negative dielectric anisotropy $\Delta\epsilon$. However, similar alignment changes are obtained in the host 5CB. By rotating the sample by 45° between crossed polarizers (figure 4.33 (a) and (b)), it can clearly be seen that the homogeneous planar alignment outside of the electrodes remains unaltered, while the area within the electrodes is optically isotropic and remains dark. Without polarizers, a yellowish to brownish precipitate is found to reside on the electrodes. Small birefringent domains within the electrodes occur only on positions where this precipitate is absent (compare figures 4.33 (b) and (c)). As in electro-optic test cells used for these investigations (E.H.C Co., Ltd Tokyo, Japan) the upper and lower transparent electrode areas have different dimensions, a small frame of the larger electrode has no directly opposing counter electrode, and the electric field strength in this area is significantly lower than between both electrodes. As shown in figure 4.33 (c), this ITO-frame is visible under a microscope, but features no alignment changes of the liquid crystal molecules. This strongly indicates that the alignment changes are caused under influence of an applied electric field, and are not related to an initially different surface anchoring of molecules on the polyimide coated ITO electrode compared to the polyimide coated glass without electrode material.

The appearance of a yellowish to brownish precipitate on the active ITO electrodes after applying electrical fields indicates a drag of particles to the surfaces. However, an electrophoresis requires a charged interface between the nanoparticles and the nematic host, which allows the particles to move under the influence of an external electric field. The direction of movement would then depend of the sign of charges. By applying a DC voltage of 30 V for 1 hour on a sample containing 5 % (w) of AuCB particles in 5CB, a yellowish precipitate on the active electrode area of the test cell is observed. Breaking the test cell open reveals that this precipitation covers both substrates, what is somewhat unexpected: Charged particles with only positive or negative charges would move into one direction under the influence of a DC bias only. Interestingly, this precipitation also occurs under the influence of an AC field of 1 kHz, which should not lead to a directed drag of particles onto the surface at all. Because of these surprising observations, a closer look on possible origins of charges within the nanoparticle / liquid crystal dispersions appears necessary.

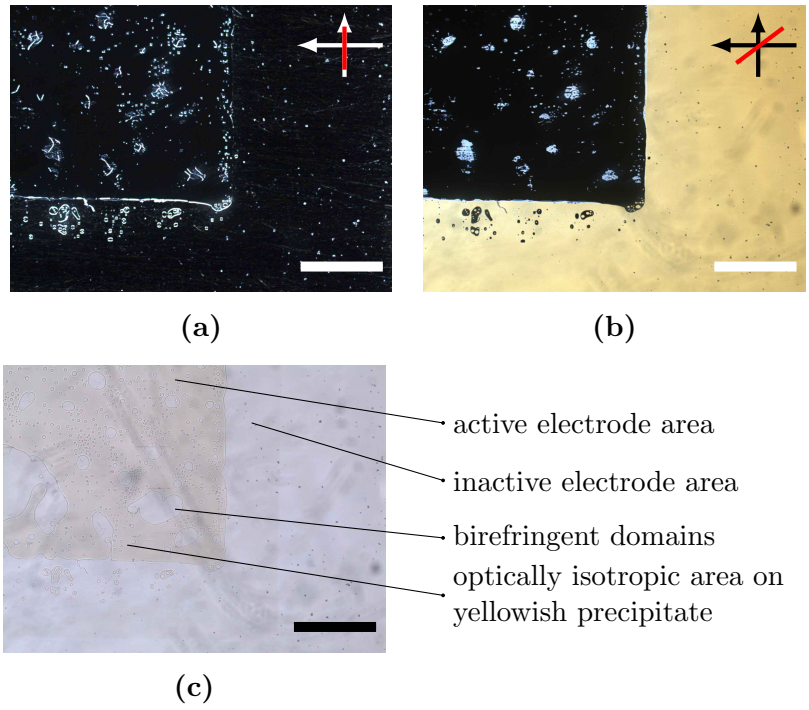

Figure 4.33: Polarizing optical micrographs of a sample containing 2.5 % (w) AuCB particles in the nematic host EN18 after applying a sinusoidal AC field of 1 kHz at 25 V_{rms} for 30 min. Images are obtained under white light illumation at room temperature, arrows and red bars indicate the orientation of polarizers and the cell's rubbing direction, respectively, the bars on the bottom of each picture represent 100 µm.

It is striking that these precipitation effects are only observed for metallic gold nanoparticles, while all semiconductor nanoparticles investigated in this work do not show an altering of alignment layers under the influence of electric fields. However, the metallic core of a functionalized gold nanoparticle is initially uncharged, and a resulting net charge of the functionalized particle can only be caused by the adsorption of ions on the particle surface or the desorption of charged ligands, as stated by Turkevich et al. in reference [90]. The authors of this study suggest that the chemically bound organic ligands are sources for positive or negative charges, which form a Stern layer on the particle's surface. This Stern layer is then surrounded by a diffuse Debye atmosphere of counter ions, whose Debye length κ^{-1} depends on the total ion concentration in the nematic host. In consequence, the core material has no direct influence on the charge of particles, but can only promote or hinder the adsorption, chemisorption or desorption of charged ligands. For all gold particles investigated in this work, thiol-groups are used to anchor ligands onto the core. It is well-known that sulfur has a high affinity to gold, and the resulting Au-S bond has a homolytic bond strength of ca 210 kJ/mol [91]. Compared to a typical S-S homolytic bond strength of a dialkyl disulfides of ca. 240 kJ/mol [92], the Au-S bond can be considered a strong covalent bond. In comparison, the functionalization of CdSe590 and CdSe610 particles with hexadecylamine results in a highly uniform distribution of amino groups that are strongly hydrogen-bonded to Cd and Se atoms of the core [93]. The typical hydrogen bonding energy on a Cd or Se surface is in the order of 10-100 kJ/mol [94], and therefore significantly smaller than the bonding energy between Au and S. However, as the altering of alignment layers only occurs for thiol-capped particles, the ligand exchange for these particles is expected to be more vivid than for the semiconducting CdSe particles.

As a drag of particles in only observed for gold species, charges on CdSe particles in dispersion seem to be neglectable. Hence, the different synthesis routes for AuSi, AuCB and $\mathrm{AuSH12}_{(m)}$ particles are analyzed for possible sources of ionic impurities and charges on the particles, which cause a drag of latter in external electric fields.

Dodecanethiol functionalized nanoparticles $\mathrm{AuSH12}_{(m)}$ are synthesized following a Brust-Schiffrin approach [56]. In this procedure, an aqueous solution of chloroauric acid $\mathrm{HAuCl_4}$ is reduced by sodium borhydride $\mathrm{NaBH_4}$ in the presence of tetraoctly-ammoniumbromide as phase transfer agent, yielding small nanoparticles in an apolar solvent like toluene. At first, the nanoparticles are stabilized by tetraoctly-ammoniumbromide ligands, which are only loosely bound and can easily be replaced by thiol ligands. However, latter phase transfer agent is in general a problematic impurity and can barely be completely removed from the reaction product [49]. An insufficient cleaning procedure of the nanoparticles gives rise to a ionic contamination by tetraoctly-ammoniumbromide.

The AuCB particles are synthesized via the Hutchinson-method as reported in reference [63], which utilizes triphenylphosphine capped particles as an intermediate species. Therefore the Hutchinson method is a two-step method, which is still closely related to the well-known Brust approach. Again, the first step is the reduction of chloroauric acid $\mathrm{HAuCl_4}$ by sodium borhydride $\mathrm{NaBH_4}$ in the presence of tetraoctly-ammoniumbromide as phase transfer agent, so the aforementioned impurity problem also occurs in this approach. In addition, Weare et al. showed that the average empiric molecular formula of nanoparti-

cles synthesized via this method is $Au_{101}(PPh_3)_{21}Cl_5$, giving rise to 3.7 % (w) of not fully reduced gold species [63].

The synthesis of AuSi particles requires several additional steps for the silanization of silane-ligand shell as described in reference [95]. However, the initial functionalization of gold nanoparticles is again carried out with silanized thiol-ligands in a one-phase synthesis as described in reference [96], and uses tetrabutylammonium borohydride as reducing reagent. So also in this approach ionic impurities could be expected, but the silanized AuSi particles show a high stability under the influence of electric fields.

In conclusion, the origin of electrophoresis in dispersions containing AuCB and $AuSH12_{(m)}$ particles is presumably less connected to additional ionic impurities by contaminants, but more to charges on the particles itself. These could be caused a loss of thiol ligands for latter particles, while the desorption of ligands is prevented by the silanization of AuSi particles. As shown above, the Au-S in general is relatively strong. However, vivid ligand exchange reactions of thiol-ligands on gold particles occur and can be used for the synthesis of particles with prescribed compositions of different ligands [57]. It can be assumed that the breaking of the Au-S bond during the desorption of thiol-ligands is heterolytic, yielding negatively charged thiol-endgroups instead of thiol radicals. This could be one source of charges in the dispersion, leading to positively charged gold cores and negatively charged ions in the host. The different degree of electrophoresis then depends on the Debye length κ^{-1} around the single particles, which correlates with the total amount of ionic impurities.

Another observation that supports the hypothesis of ligand loss as source for charged species is the change from birefringent to non-birefringent behavior in areas with high agglomerate density. As shown before, the field induced altering of the polyimide alignment layer can lead to an optically isotropic alignment of molecules on the substrates, where the resulting dark state within the electrode area remains dark under rotation of the sample between crossed polarizers. Hence, either the alignment is changed to homeotropic alignment, or the liquid crystalline order vanishes and the isotropic phase occurs. By tilting the sample between crossed polarizers to polar angles up to $\theta = 45°$, a coexistence of both states can be confirmed: While some domains clearly show birefringence at large polar angles, other areas remain dark for every orientation between crossed polarizers.

The appearance of isotropic domains is found to be associated to high particle concentrations. In a 10 µm test cell filled with a dispersion of 2.5 % (w) AuCB in the nematic mixture EN18, a semicircular circlet of agglomerated particles at constant distance to the filling point appears. This observation is strongly related to the semicircular precipitation of CdSe590 and CdSe610 particles in the host FELIX-2900-03 as reported in section 4.4.3. The semicircular shape can be explained by the filling procedure, where single droplets of dispersion are stepwise placed near the cell gap between the glue spacers of the test cell. Due to a depletion effect, agglomerates of particles are not dispersed in the nematic liquid crystal, but reside on the liquid crystal / air interface that floats through the cell gap by capillary forces. After the first droplet of dispersion has completely entered the cell, but before the second droplet is placed near the cell gap, the agglomerates are expelled from the nematic phase and reside on the interface, forming a semicircular circlet on the surface. After the second droplet is placed near the cell gap, the filling continues with no or less

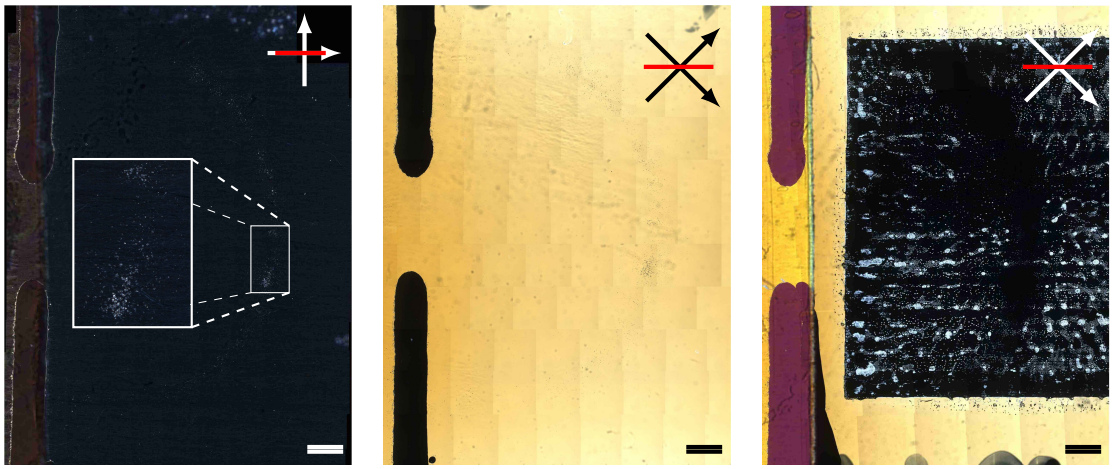

(a) **(b)** **(c)**

Figure 4.34: Mosaic pictures of a dispersion of 2.5 % (w) AuCB particles in the nematic host EN18, assembled of 130 single polarizing optical microscopy images obtained with a M=5 objective under white light illumination at room temperature. Arrows and red bars indicate the orientation of polarizers and the cell's rubbing direction, respectively, the bars on the bottom of each picture represent 1 mm. The white framed inlay in the left picture (a) is a magnification of the marked area, visualizing the presence of agglomerates of particles in a semicircular circlet from the filling point. Image (b) is obtained by rotating the sample shown in image (a) by an azimuthal angle of 45°, image (c) shows the same sample after applying a sinusoidal AC field of 1 kHz at 25 V_{rms} to the sample for 30 min.

agglomerates residing at the liquid crystal / air interface.

Mosaic pictures of this sample are shown in figure 4.34, depicting a large part of the polyimide coated test cell. These images are obtained by assembling 130 single polarizing optical microscopy photographs each, and allow a very high resolution for details within the test cell. The aforementioned circlet of particles can easily be spotted between crossed polarizers, with an angle φ between the easy direction of the cell and the plane of polarization of the incident light of 0° or 90° (see figure 4.34, (a)). By rotating the polarizers to an azimuthal angle of $\varphi = 45°$ to the easy direction of the sample (figure 4.34, (b)), the agglomerates are harder to spot, but the initial homogeneous planar alignment of the molecules due to the rubbed polyimide alignment layer gets clearly visible. After applying an sinusoidal AC field of 1 kHz at 25 V_{rms} to the sample for 30 min, the alignment within the active electrode area changes to an optically isotropic state, with only few birefringent domains left. Conspicuously, no birefringent domains appear in the area of the semicircular agglomeration circlet. In this area, the sample appears completely dark and the dispersion exhibits isotropic phase behavior only, as proved by tilting the sample between crossed polarizers. Hence, it is found that under the influence of external electric AC fields, a locally high particle concentration of AuCB particles leads to a loss of nematic order, while lower particle concentrations of AuCB induce homeotropic alignment.

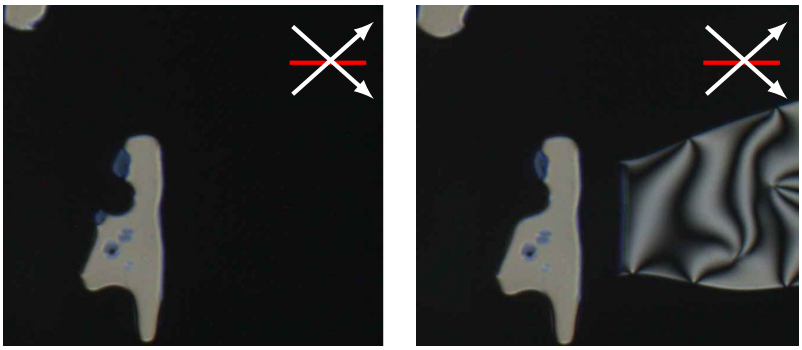

field **OFF** field **ON**

Figure 4.35: Polarizing optical microscopy images of an field-induced Fréedericksz transition of EN18 molecules from homeotropic (left, field OFF) to planar (right, field ON) alignment. Images are obtained under white light illumination at room temperature, arrows and red bars indicate the orientation of polarizers and the cell's rubbing direction, respectively.

Considering the observations made for AuCB and AuSH12$_{(m)}$ particles in 5CB, a model is developed that explains the behavior of these dispersions under influence of an electric field. The particles carry positive charges, due to the desorption of anionic thiol ligands. Under the influence of an electric field, the particles and ligands move along a field gradient within the cell to the liquid crystal / substrate interface. By residing on the substrates, they superimpose the effect of the polyimide alignment layer and induce homeotropic alignment. After exposure to high field strengths or after long exposure to the electric field, a large amount of ligands moves from the particles into the liquid crystalline host. Above a certain concentration of dissolved ligands, this process leads to a loss of liquid crystalline properties. Taking into account the number of ligands per nanoparticle as determined by Draper et al. in reference [14], a particle concentration of 5 % (w) AuCB in 5CB can lead to a maximum molar fraction of ligands of 1.71×10^{-2} in the dispersion.

The field induced deposition of nanoparticles or ligand molecules onto the surface can be used to intentionally superimpose the effect of the polyimide alignment layer of the electro-optical test cell and induce homeotropic alignment. In nematic hosts with negative dielectric anisotropy $\Delta\epsilon$, this offers the possibility to achieve an electrical switching of molecules also in polyimide coated and therefore planar aligned cells. An experimental proof of principle is given in figure 4.35, where optical polarizing microscopy images of a dispersion of 2.5 % (w) AuCB in EN18 in a polyimide coated electro-optical test-cell are shown. By applying electrical AC fields, the polyimide alignment layer has been superimposed by nanoparticles and ligands, and homeotropic alignment is obtained (figure 4.35, left). By applying an AC field (1 kHz, 20 V_{rms}), a Fréedericksz transition is induced in the right part of the sample, which leads to a birefringent schlieren texture (figure 4.35, right). Obviously the switching does not take place over the whole sample, which is presumably attributed to a loss of liquid crystalline properties in the non-switching areas shown in figure 4.35.

Possible applications: Switchable phase gratings

As shown in the previous section 4.5, the nanoparticles $AuSH12_{(m)}$ and AuCB can be intentionally precipitated from the dispersion onto the substrate's surface by applying electric fields to the test cell. This feature of nanoparticle / liquid crystal dispersions can be used for the preparation of two-dimensional phase gratings. The following section aims to give a short overview over different approaches for the utilization of liquid crystals in phase gratings, and presents first experimental results with nanoparticle / liquid crystal dispersions.

Phase gratings are optical devices that manipulate the phase of transmitting light by adding a phase retardation to the propagating wave. By adjusting the spatial distribution and the magnitude of phase retardation added, complex diffraction phenomena can be generated. These devices find applications in projection displays, beam steering, slitting or filtering devices as well as in light shutters [97].

In order to obtain gratings with a tunable phase retardation, the use of liquid crystalline materials is a common tool. Liquid crystals can offer a high birefringence, which allows applications with thin film gratings, and their birefringence is electrically adjustable.

The first types of liquid crystalline phase gratings make use of a sinusoidal director distribution in electrohydrodynamic instabilities. In 1973, Kashnow and Bigelow reported that weakly conducting nematic liquid crystal can be used as a phase grating material [98]. The authors utilize convection rolls in the Williams regime or two-dimensional patterns in the chevron regime of electrohydrodynamic instabilities in nematic materials with negative dielectric anisotropy (see reference [99]).

Another approach for tunable phase gratings and more commonly used in technology is a Fréedericksz-type reorientation of a nematic liquid crystal in an electric field to adjust the optical phase retardation. In reference [100], Resler et al. present an one-dimensional beam steerer for infrared wavelengths. A planar aligned nematic liquid crystal is used as active medium, and deliberately reoriented by a one-dimensional array of electrodes. The resulting one-dimensional phase grating allows the deflection of an incident plane wave perpendicular to the electrode grating. A two-dimensional phase grating for the visible range is reported by Sakata et al. in reference [101]. The authors utilize one-dimensional groove gratings to homogeneously orient a nematic liquid crystal, and present a two-stack device with crossed grating directions that works as a light shutter without additional polarizers.

The approach followed in this work utilizes a two-dimensional array of homeotropically and planar aligned surfaces, that are prepared by the selective deposition of AuCB nanoparticles on the dispersion / substrate interface. The use of a structured alignment layer for a two-dimensional phase grating is also reported in references [102] and [97]. However, the authors of these studies use photoalignment techniques to obtain structured alignment layers, while this work aims to utilize the special properties of nanoparticle doped liquid crystals.

The deposition of particles onto the surface is caused by electric fields, thus structured electrodes are needed for the selective deposition of particles. Therefore, a comb like structure of ITO-on-glass electrodes is used. Assembling the substrates by an angle of 90° gives a cell with a regularly arranged pattern of squared pixels that can be used for a Fréedericksz-type

reorientation of molecules. The general idea of this phase grating with patterned electrodes is shown on top of figure 4.36. For a nematic liquid crystal with negative dielectric anisotropy as the mixture EN18 (Chisso Corporation, $\Delta\epsilon$ = -6 at 25 °C, [89]), the substrates are prepared with lecithine to obtain homeotropic alignment. By applying an external electric field above the threshold voltage of the Fréedericksz transition, a reorientation of the liquid crystal molecules perpendicular to the field direction occurs, and between crossed polarizers the pixel appears bright due to a birefringent schlieren texture. A schematic model of the molecular reorientation is shown on bottom of figure 4.36 below the experimental results.

The structured electrodes are prepared by photo-lithography using a photoresist (POSITIV 20) and ink-jetted photo masks for selective UV-light exposure. For the preparation, ITO-substrates are coated with the photoresist and dried at 70 °C for 60 min. Then the photo-masks are placed onto the substrates, and the substrates are exposed to UV-light for 150 s. The unexposed photoresist is removed by washing the substrates in 1 molar NaOH solution. In order to selectively remove ITO via etching, the substrates are etched with 3 molar hydrochloric acid and zinc powder. Due to very high etching rates, etching times of more than 3-5 s lead to a strong underetching of the photoresist. A buffered $NaHCO_3$ aqueous solution is used to immediately stop the etching process. Finally, the photoresist is removed by acetone, and the substrates are cleaned as described in the experimental section.

The use of ink-jetted photo masks gives rise to a minimum lattice constant of the ITO electrodes to ca. 500 µm. This is at least one magnitude too large for control over plane waves in the visible range, as reported in reference [103]. In addition, the patterned electrodes give rise to fringing-fields, which do not allow a precise control of the spatial phase retardation distribution of the cell (see reference [104]). In conclusion, the experiments shown here can only be a proof of principle that the intentional spatial deposition of nanoparticles is a suitable method for obtaining structured alignment layers.

When using a sample with initial planar alignment, a similar switching effect can be achieved for liquid crystalline materials with a positive dielectric anisotropy. However, the use of materials with a negative dielectric anisotropy offers the utilization of the special properties of nanoparticle / liquid crystal dispersions with AuCB particles: In a sample with initial planar alignment, high electric fields can be used to deposit the nanoparticles onto the active electrode pixels. This results in a regularly array of pixels with homeotropic alignment in a planar surrounding. After deposition, the liquid crystal material can be electrically switched as schematically shown in figure 4.37. In contrast to the grating shown in figure 4.36, such a grating would be active with no applied electric field, and the contrast of spatial phase retardation can be decreased by applying voltages above the threshold voltage of the Fréedericksz transition.

However, the implementation of this idea in experiment has not been successful. For this experiment, a dispersion of 1 % (w) AuCB in EN 18 is used and filled in a self-made test cell with structured electrodes and a polyvinylalcohol alignment layer for initial planar alignment. The lower concentration of particles compared to the results shown in section 4.5 above is justified to avoid a decomposition of particles and a loss of nematic order. However, the targeted deposition of nanoparticles onto the active pixels after applying as well AC and

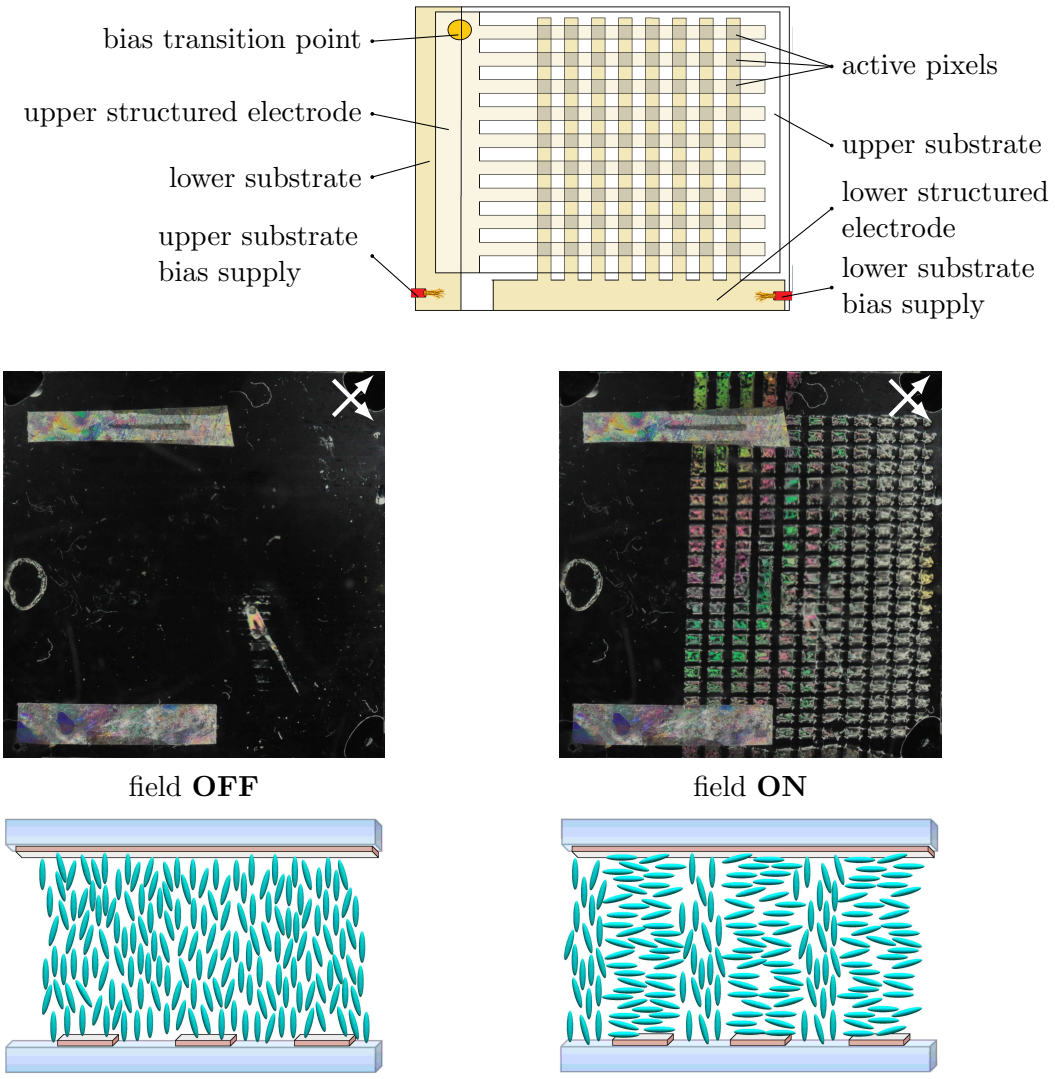

Figure 4.36: Scheme of the general idea of a phase grating using nematic liquid crystals and patterned electrodes. Top: Schematic drawing of a self-built test cell. Two comb like electrodes are placed under an angle of 90° to give a regularly array of square pixels. Middle: Experimental realization of this concept for a cell with homeotropic alignment, filled with the liquid crystal mixture EN18 featuring a negative dielectric anisotropy. Bottom: Schematic model of the field-induced molecular reorientation.

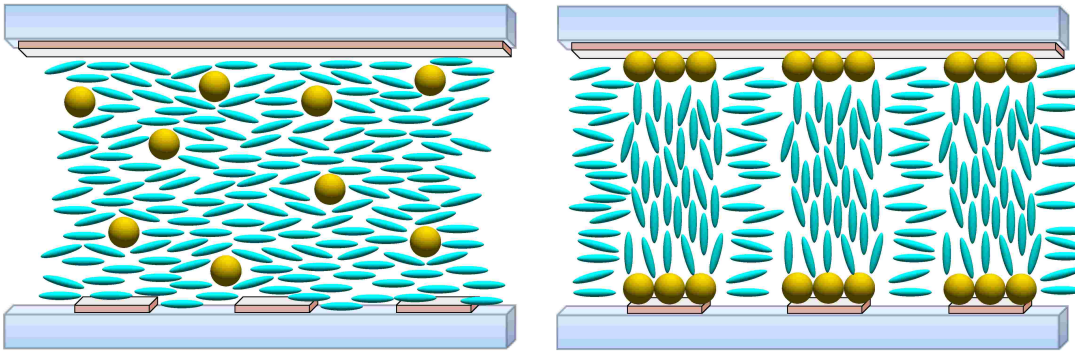

before deposition **after deposition**

Figure 4.37: Schematic model of a targeted deposition of AuCB nanoparticles onto the active ITO electrodes, which induces an alignment change of the nematic host from initially planar alignment to homeotropic alignment.

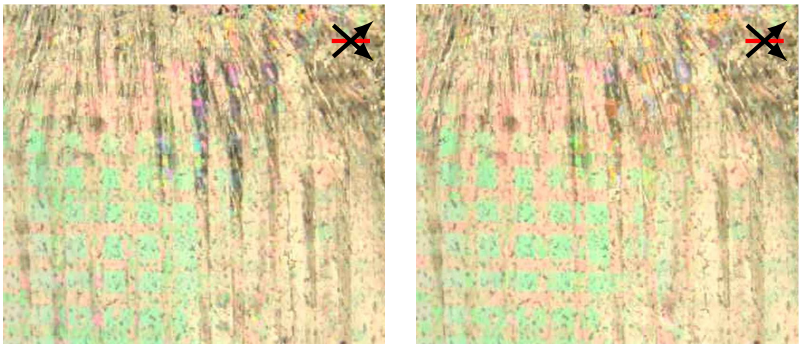

field **OFF** field **ON**

Figure 4.38: Polarizing optical micrographs of a phase grating after targeted deposition of particles from a dispersion of 1.0 % (w) AuCB particles in EN18. Images are obtained under white light illumation at room temperature, arrows and red bars indicate the orientation of polarizers and the cell's rubbing direction, respectively. The lack of switching contrast between the field OFF state (left) and the field ON state (right) indicates an insufficient deposition of nanoparticles onto the surface.

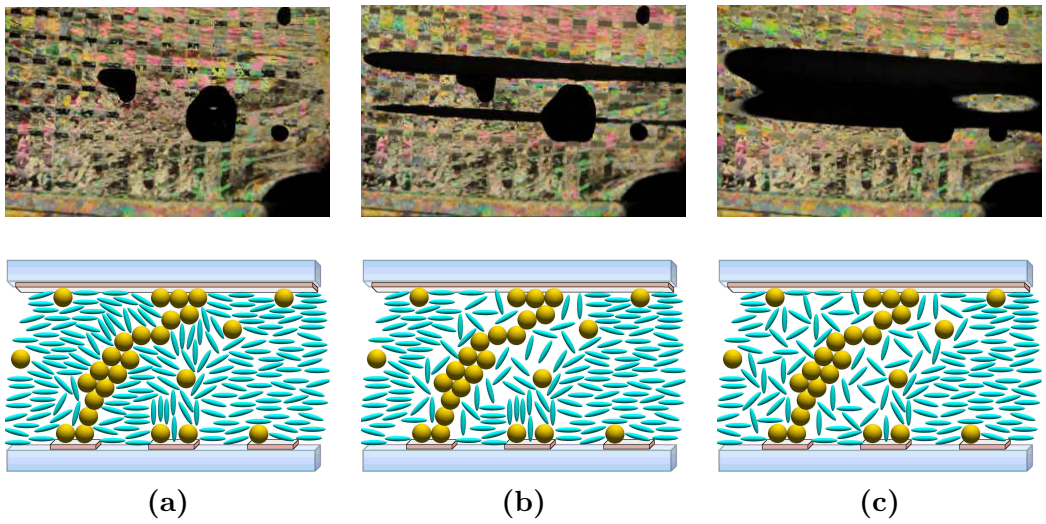

Figure 4.39: Top: Polarizing optical micrographs of a short-circuited phase grating containing a dispersion of 1.0 % (w) AuCB particles in the host EN18, before (a), immediately after (b) and a few seconds after switching on an external electric field (c). Arrows and red bars indicate the orientation of polarizers and the cell's rubbing direction, respectively. Bottom: Schematic drawing of the loss of nematic order due short-circuiting heat.

DC fields up to 30 V is not sufficient to superimpose the initial planar alignment layer and induce homeotropic alignment. As can be seen in figure 4.38, polarizing microscopy images obtained between crossed polarizers only show slight color changes on the active pixels instead of an array of black squares. This indicates that the deposition of particles has only induced a slight change in alignment, but the planar alignment layer still dominates the overall orientation of the liquid crystal molecules.

Another problematic effect is illustrated in figure 4.39, which shows the short-circuiting of a test cell. The gold nanoparticles AuCB do not exhibit a very good solubility and miscibility in the host EN18, which leads to the formation of agglomerates. These agglomerates are not filtered by the cell gap, which is estimated to be ca. 15 µm in this case, and therefore can enter the cell gap. Here they form a conductive connection between the electrodes on the upper and lower substrate, and applying a voltage causes a short-circuit current. In consequence, the gold agglomerates as well as the ITO electrodes serve as heating resistors, which get heated by the current flow. In consequence, an electrical switching of the phase grating is not possible, and the increasing temperature in the surrounding of the agglomerate heats the liquid crystalline host into the isotropic phase. This can clearly be seen in polarizing optical microscopy images shown in figure 4.39 (top). A molecular model of the spatial spreading of the isotropic phase is shown in below the experimental results in figure 4.39. As Schnabel et al. argue that coated gold nanoparticles act as non-conductive particles because of their dense insulating organic ligand shell [105], the conductive properties observed here can be seen as additional indication of a strong desorption of ligands from the particles.

4.5.2 Reverse switching - Electroconvection via nanoparticle doping

As firstly reported by Qi et al. in reference [62], doping the nematic host FELIX-2900-03 with alkylthiol capped gold nanoparticles can completely reverse the electro-optic response of the dispersion compared to the pure host. The authors found that AuSH6 or $AuSH12_{(s)}$ gold particles in FELIX-2900-03 can induce homeotropic alignment in an electro-optic test cell, when the mixture is slowly (1 °C/min) cooled down from the isotropic phase. When applying external electric fields to the sample, the dispersion switches from homeotropic to a birefringent alignment. This is usually only found for nematic liquid crystalline materials with a negative dielectric anisotropy, although experiments clearly prove a positive dielectric anisotropy of the nanoparticle / liquid crystal dispersion. However, when the mixture is cooled down from the isotropic to the nematic phase under the influence of an external electric field and the field is switched off after cooling, the dispersion shows planar alignment comparable to an undoped sample. Being in this state, an external electric field switches the alignment from planar to homeotropic, as expected for a nematic material with positive dielectric anisotropy. In order to reveal the origin of this unusual switching behavior, detailed electro-optical studies on dispersions of $AuSH12_{(s)}$ in FELIX-2900-03 are performed. The results of this study have been published in reference [60] already.

The electro-optic test cells (LC vision, USA) were prepared and filled with by Brandy Kinkead in Prof. Hegmann's group, electro-optic experiments were performed in own work. Before measurement, the test cells are heated up to the isotropic phase and then slowly (1 °C/min) cooled down. All electro-optical measurements shown here are performed at $T_{NI} - T = 3\,\mathrm{K}$. While the undoped FELIX-2900-03 shows a homogeneous planar alignment induced by the rubbed polyimide alignment layer of the electro-optic test cell, the mixture doped with 5 % (w) of $AuSH12_{(s)}$ shows mainly homeotropic alignment, in agreement with the observations by Qi et al. cited above (see figure 4.40 for POM images).

The electrical switching behavior of both samples changes fundamentally with the frequency of the applied external AC bias. At a test frequency of 1 kHz, the pure FELIX-2900-03 shows a typical Fréedericksz transition from planar to homeotropic alignment, while the nanoparticle dispersion shows almost no response to the external field. This can simply be explained by the initial homeotropic alignment of liquid crystal molecules in the dispersion, which is stabilized by the external field perpendicular to the substrates. However, at test frequencies below 1 Hz, only the field-dependent light transmission of the undoped sample remains unaltered, while the doped sample shows a clear switching of alignment to a birefringent state.

The switching characteristic for both samples in this low frequency regime is shown in figure 4.41. The pure liquid crystal switches from a birefringent bright state, caused by parallel alignment of the molecules to the substrates, through some intensity oscillations to a non-birefringent or homeotropic dark state. This represents a typical field-dependent light transmission characteristic of a Fréedericksz transition for nematic materials with positive dielectric anisotropy and initial planar alignment. The critical voltage $V_{Th,T}$ for this transition is calculated to be $4.3\,\mathrm{V}_{rms}$. The nanoparticle dispersion, however, shows a reversed switching behavior. While the director is homeotropically aligned in the field-off state, the

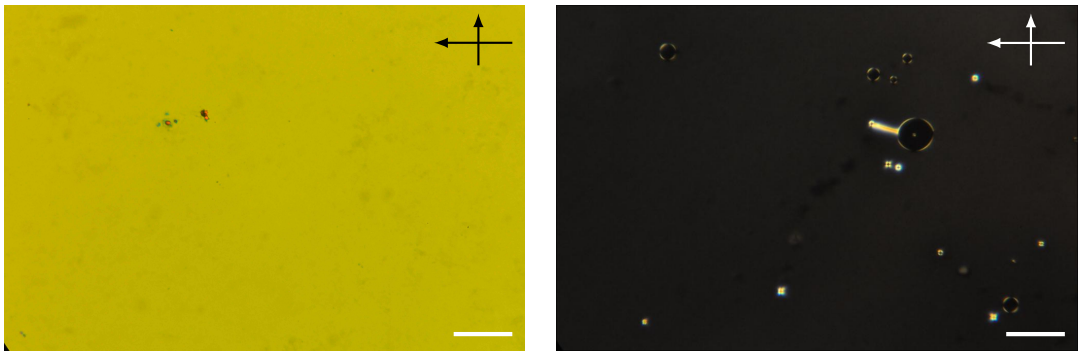

(a) (b)

Figure 4.40: Polarizing optical microscopy images of (a) the pure liquid crystal FELIX-2900-03 and (b) a mixture of 5% (w) of $AuSH12_{(s)}$ in FELIX-2900-03. The white bar represents 100 µm, the arrows the position of polarizer and analyzer, respectively. The rubbing direction of the cells was adjusted at an azimuthal angle of $\varphi = 45°$ between crossed polarizers. Both samples were heated up to the isotropic phase and then cooled at a rate of 1 °C/min to $T = T_{NI} - 3\,\mathrm{K}$, a white light source was used for illumination.

director distribution changes to a birefringent state above a threshold voltage of roughly $10\,V_{rms}$, without undergoing intensity oscillations. As reported by Qi et al. in reference [62], this threshold for the inverse switching is independent from the particle concentration in the dispersion. The observed switching from homeotropic to seemingly planar alignment for the doped sample is very surprising, as the liquid crystal host FELIX-2900-03 exhibits a positive dielectric anisotropy, so that external electric fields perpendicular to the substrates should lead to a stabilization of homeotropic alignment, and not to switching to a birefringent state. The switching is completely reversible, as the director reorients back to homeotropic alignment when the applied voltage drops below the threshold voltage or when the external field is turned off.

The homeotropic alignment in the doped mixture presumably is caused by gold particles residing at the liquid crystal / substrate interface, forming a monolayer and superimposing the orientational effects of the polyimide alignment layer (see section 4.4.3). In the birefringent bright state, polarizing microscopy images show parallel stripes perpendicular to the rubbing direction of the cell, as depicted in figure 4.42 at different magnifications. The distance between two parallel stripes is determined to be 8-9 µm, and therefore in the range of the cell gap. These regular patterns are identified to be electrohydrodynamic instabilities, which can emerge at sufficiently low AC frequencies and above a certain threshold amplitude [98].

The transition from the dark state shown in figure 4.40 (b) to a bright state as shown in figure 4.42 indicates that the homeotropic alignment induced by the nanoparticles becomes unstable when applying an external field perpendicular to the substrates, which leads to a rotation of the long axes of the molecules away from the direction of the external electric field. Finally, this instability leads to the formation of convection rolls. These convection

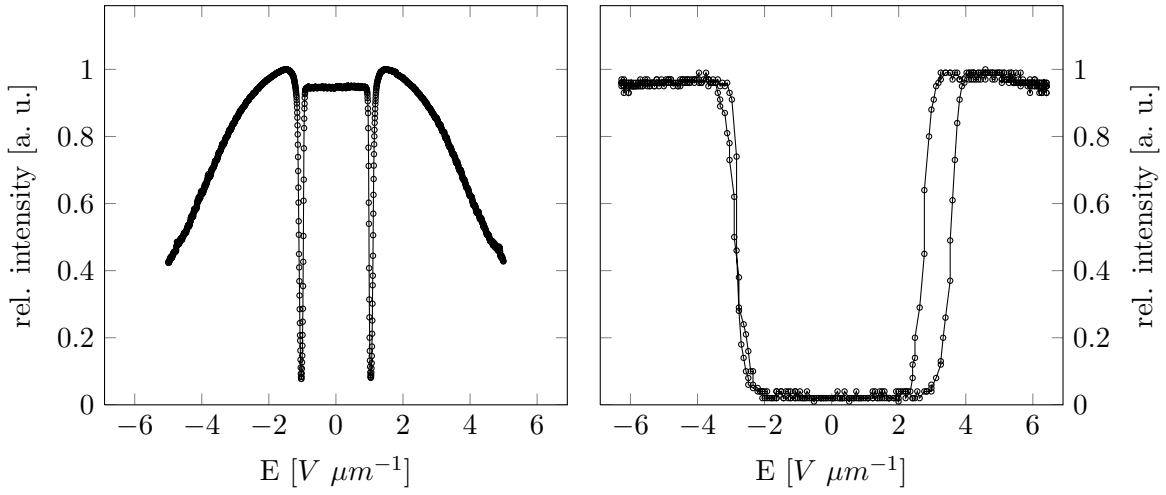

Figure 4.41: Electro-optic characteristic of (left) the undoped FELIX-2900-03 and (right) FELIX-2900-03 doped with 5% (w) of $AuSH12_{(s)}$ at an AC frequency of 0.01 Hz. The measurement is performed with an interference filter for monochromatic light ($\lambda = 579\,\mathrm{nm}$).

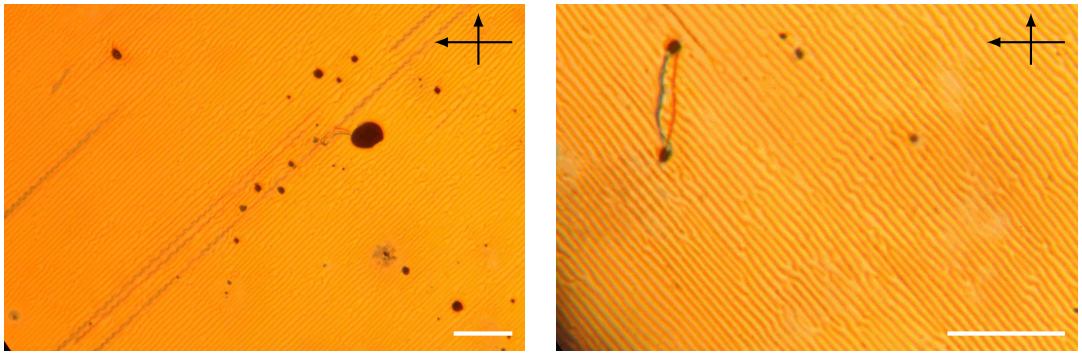

Figure 4.42: Parallel convection rolls due to electrohydrodynamic instabilities in FELIX-2900-03 doped with 5% (w) of $AuSH12_{(s)}$ at an applied DC bias of 30 V. The white bar represents 100 µm, the arrows the position of polarizer and analyzer, respectively.(a) Magnification 10x, (b) magnification 32x. The convection rolls have a spacing of 8-9 µm.

rolls reproducibly form parallel stripes, what indicates that the polyimide alignment layer still has an effect on the liquid crystal alignment, in spite of the homeotropic alignment induced by the nanoparticles.

The reverse switching behavior and the appearance of electrohydrodynamic instabilities are similar to recent experimental observations made on electroconvection by Buka et al. as reported in references [106], [107] and [108]. In all three cases, the authors report the appearance of electroconvection in a nematic liquid crystal with positive dielectric anisotropy, negative conductivity anisotropy and initial homeotropic alignment. Convection rolls similar to results shown in figure 4.42 are reported to appear at low frequencies, while higher frequencies lead to the formation of square patterns, which could not be observed in the nanoparticle dispersions investigated here.

To test whether the present nanoparticle/liquid crystal dispersion is indeed an example for a (+, -) nematic system according to [107], the dielectric anisotropy in the temperature range near the phase transition temperature is measured. The dielectric permittivities parallel $\epsilon_{\parallel}$ and perpendicular $\epsilon_{\perp}$ to the director are shown in figure 4.43 for the temperature range from $T = T_{NI} - 14\,\mathrm{K}$ to the isotropic phase for the pure liquid crystal FELIX-2900-03. At the temperature of the electro-optic measurements, the dielectric anisotropy is found to be positive with an absolute value of about $\Delta\epsilon = +0.55$. A reliable measurement of the conductivity anisotropy $\Delta\sigma$ has not been successful, as conductivity measurements with the LCR bridge HP4284A did not give reproducible data. In consequence, only two preconditions (homeotropic alignment and positive dielectric anisotropy $\Delta\epsilon$) for electroconvection in a (+, -) nematic system are obviously fulfilled, while the negative conductivity anisotropy remains to be proven. A simplified schematic model of the nanoparticle induced formation of convection rolls is shown in figure 4.44.

In order to point out the dual alignment modes of the nanoparticle dispersion reported by Qi et al. in reference [62], measurements at a more typical frequency for electro-optical experiments of 1 kHz instead of 0.01 Hz are performed. At this frequency, the pure FELIX-2900-03 shows again the characteristic of a typical Fréedericksz transition from planar to homeotropic alignment. This indicates that the DC behavior of the liquid crystalline host does not generally differ from its AC behavior. However, the reverse switching of the doped samples does not appear at high AC frequencies. As the director is homeotropically aligned in the initially field-free state, this orientation is even stabilized by the applied field, resulting in a completely dark characteristic.

A different switching characteristic is observed when the doped liquid crystal is rapidly cooled from the isotropic phase (10 °C/min). In this case, the homeotropic alignment does not appear, but the liquid crystal orients parallel to the substrates due to the polyimide alignment layer of the cell. For this initial alignment, the doped liquid crystal shows also the typical characteristics of a usual Fréedericksz transition similar to the undoped liquid crystal. The behavior shown in figure 4.45 confirms that the nanoparticle / liquid crystal dispersion exhibits a positive dielectric anisotropy as the undoped compound. In both cases, the positive dielectric anisotropy drives the molecules to orient parallel to the electric field.

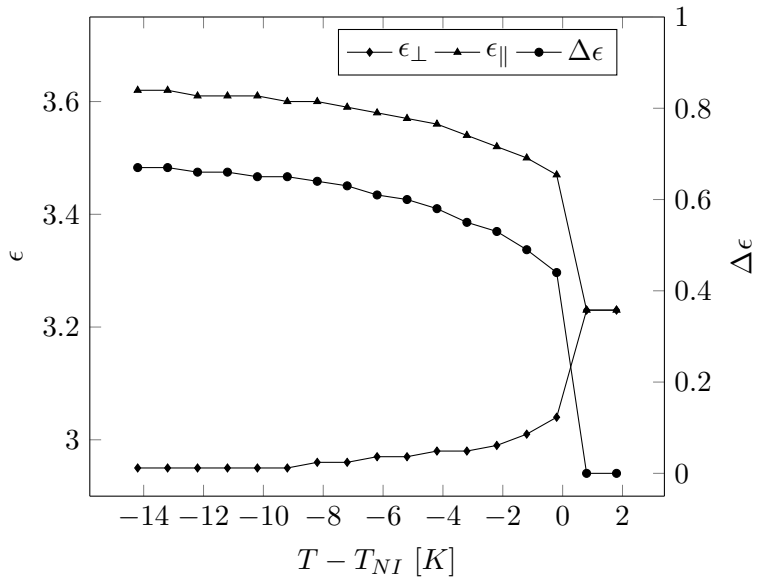

Figure 4.43: Measurement of the permittivities parallel $\epsilon_\parallel$ and perpendicular $\epsilon_\perp$ to the director in a sample filled with the host FELIX-2900-03. The dielectric anisotropy $\Delta\epsilon$ is proved to be comparable small, but positive for this host.

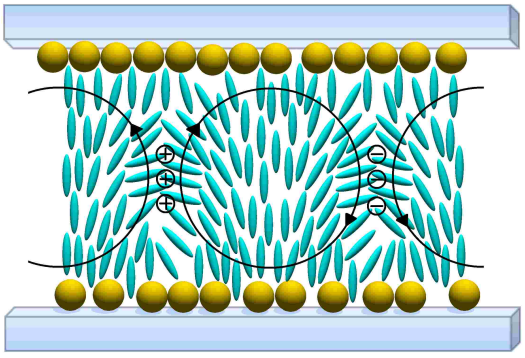

Figure 4.44: Simplified model of electroconvection rolls in a gold nanoparticle dispersion with nanoparticle induced homeotropic alignment.

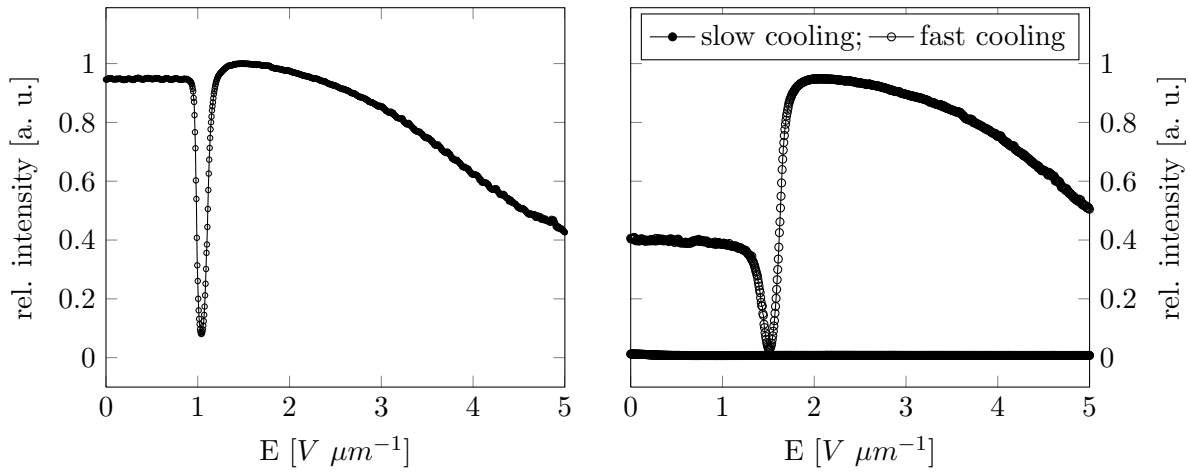

Figure 4.45: Electro-optic characteristic of (left) the undoped FELIX-2900-03 and (right) FELIX-2900-03 doped with 5% (w) of $AuSH12_{(s)}$ at an AC frequency of 1 kHz. While the cooling rate has no influence on the switching characteristic of the undoped sample, the doped sample shows a clear difference in the field dependent light transmission. All measurements are performed with an interference filter for monochromatic light ($\lambda = 579\,\mathrm{nm}$).

As stated by Qi et al. in reference [62], nanoparticle induced homeotropic alignment and the formation of convection rolls are more likely to be observed in thinner cells. The authors contribute this to a more advantageous interface to bulk ratio, as a certain amount of particles is required to reside on the interface in order to induce homeotropic alignment. However, the formation of convection rolls is also a bulk property, as nanoparticles influence on the conductivity properties of the bulk. As demonstrated by Kashnow and Bigelow in reference [98], a sufficiently conducting nematic liquid crystal is required for the formation of electrohydrodynamic instabilities. Hence, the role of nanoparticles in the bulk of the dispersion is presumably connected to an increase of charges, as discussed in section 4.5.1. Additionally, an homogeneous charge carrier distribution is required for the formation of convection rolls, which is confirmed again by observations of Qi and co-workers in reference [62]. The authors point out the crucial role of a high miscibility of nanoparticles in the respective host, as reverse switching has only be observed for well dispersible alkylthiol-capped gold particles in the apolar host FELIX-2900-03, while in the more polar hosts 5CB or 8CB with less miscibility of aliphatic capped particles reverse switching has barely been observed. In another work of these authors (see reference [78]), the authors report that the reverse switching mode has not only been observed for functionalized gold particles, but also for silver or CdSe particles of a similar size regime. This underlines that the choice of core material is less crucial for the appearance of convection rolls, but presumably the ability of nanoparticles to induce homeotropic alignment and increase the conductivity of the host material. Assuming the nanoparticle dispersion to be a (+, -) nematic system, a negative $\Delta\sigma = \sigma_{\parallel} - \sigma_{\perp}$ is required. According to Blinov and Chigrinov, the anisotropy of the conductivity $\Delta\sigma$ depends on the type of dopant [24]. As the conductivity of a material is connected to the charge carrier mobility, it is directly related to the diffusion coefficients of charge carriers. Therefore for the nematic phase, a negative $\Delta\sigma$ requires a larger diffusion

coefficient perpendicular to the director **n** than parallel to **n**. This seems unlikely for comparable large nanoparticles, so presumably the anisotropy of conductivity is not caused by the particles themselves, but only mediated by the generation of charged molecular dopants like charged thiol-ligands or other impurities.

4.6 Discussion of electro-optic properties

This section gives an overview over the electro-optical data threshold voltage V_{Th}, dielectric anisotropy $\Delta\epsilon$ and switching times τ_{rise} and τ_{decay} of the nanoparticle / liquid crystal dispersions investigated in this work. As shown in section 4.3, nanoparticle doping can induce a shift of phase transition temperatures. Therefore all data is plotted versus $T - T_{NI}$, as according to results by Kurochkin et al. the change in nematic properties depends on the reduced temperatures only, and not on the absolute values [109]. Taking into account the results about alignment and behavior in electric fields presented in the previous sections as well as data from literature, conclusions about the correlation between particle or host properties and the resulting electro-optical properties of the dispersions are drawn.

The electro-optic results for AuCB particles in the host 5CB are shown in figure 4.46. For this nanoparticle / liquid crystal combination, doping of the nematic host clearly increases the threshold voltage of the Fréedericksz transition. In the concentration regime investigated, this increase in threshold is found to be proportional to the particle concentration. In addition, the temperature dependence of V_{Th} is reversed due to the presence of nanoparticles. While the pure host shows a slight decrease of threshold voltage with increasing temperature, all dispersions show an increase of threshold with increasing temperature. This is presumably connected to the electric properties of the dopant, an explanation model for these observations is given later in this section.

The observations on the threshold of the Fréedericksz transition presented here are in clear contradiction to results reported for the same nanoparticle / host combination by Draper et al.. In reference [14], the authors report a large reduction of V_{Th} for dispersions containing AuCB particles, or similar mesogenic functionalized gold nanoparticles.

However, although the composition of the nanoparticle/ liquid crystal dispersion is identical in both studies, the methodical approach in the determination of threshold differs. Draper et al. use the analysis of field dependent capacitance change for the determination of threshold ($V_{Th,D}$), while the data shown here are calculated from transmittance measurements ($V_{Th,T}$). As presented in section 4.5, dispersions of AuCB particles in 5CB are not stable under the influence of an external electric field, but nanoparticles tend to precipitate onto the substrates. The surface coverage of particles on top of the initial polyimide alignment layer reduces its surface energy, and can even act as an additional alignment layer for homeotropic alignment. This effect is pronounced differently in different areas of the active electrode area. While transmission measurements can now selectively choose small regions without noticeable surface coverage for data acquisition, the capacitance is measured always over the complete electrode area and cannot consider local changes in alignment. As an in-

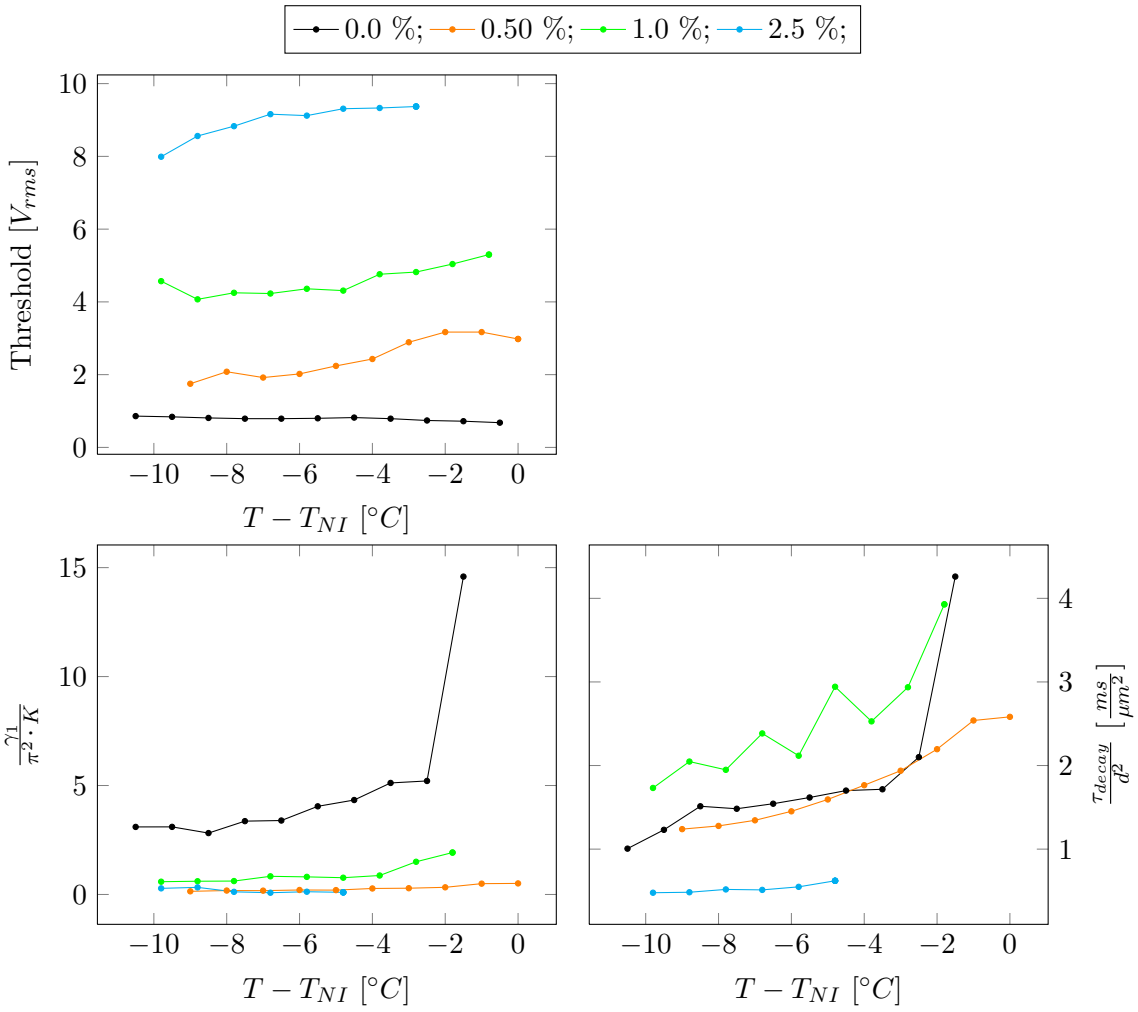

Figure 4.46: Plots of electro-optic data (V_{Th}, τ_{rise} and τ_{decay}) vs. $T - T_{NI}$ for dispersions of AuCB particles in 5CB at different particle concentrations. The plot of $\Delta\epsilon$ vs. $T - T_{NI}$ is missing, as dielectric data are not available due to field-induced alignment changes.

dicator for the absence of surface coverage in transmission measurements, a well-defined threshold in the field-dependent light transmission characteristics is used. In conclusion, threshold voltages $V_{Th,T}$ obtained from transmission measurements are more reliable in these AuCB / 5CB dispersions with instable alignment properties.

As a consequence of these instabilities, reliable capacitance data are only accessible for small test signal amplitudes clearly below the threshold voltage of the Fréedericksz transition. Hence, only the permittivity perpendicular to the molecules can be measured, while the analysis of $\epsilon_{\parallel}$ and the dielectric anisotropy $\Delta\epsilon$ is not possible in these dispersions. The temperature dependent permittivities for a 1 % (w) doped AuCB sample and the pure host 5CB are shown in figure 4.47.

For capacitance measurements perpendicular to the molecules, Draper et al. report a large reduction in capacitance up to negative capacitances of -4 nF when gold nanoparticles

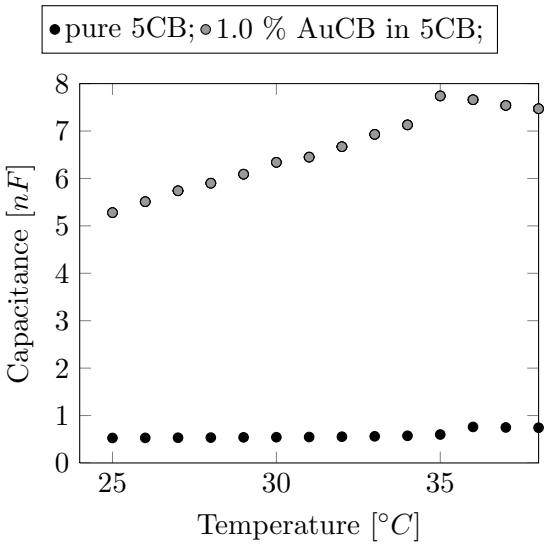

Figure 4.47: Results of temperature dependent capacitance measurements for 10 µm test cells filled with the pure host 5CB and a dispersion of 1 % (w) AuCB in 5CB.

are present in the mixture (see reference [49]). The authors attribute this observation to the plasmon properties of the gold particles being coupled to the applied field. However, own measurements cannot confirm the appearance of negative capacitances perpendicular to the molecules. Instead, positive values in the range between 5-7 nF are obtained (see figure 4.47), which roughly correspond to the absolute values of the capacitances given by Draper et al. in reference [49]. This pronounced increase of measured permittivity for the doped sample compared to the pure host in general does not match physical models about the influence of dopants on the effective permittivity. As reported by Barbero et al. in reference [110], the effective dielectric constant of a dispersion with small concentrations of dopant is independent of the doping. This could be confirmed by own measurements of the silanized particles AuSi in FELIX-2900-03, as discussed later in this section (see figure 4.61).

The analysis of switching times via light transmission measurement reveals a clear decrease in rise times τ_{rise} for doped samples. A particle concentration dependent trend for decay times τ_{decay} is hardly given. While the decay time of the dispersion with 0.5 % (w) AuCB is comparable to the pure host 5CB, the dispersion with 1.0 % (w) shows slower decay times and the dispersion with 2.5 % significantly faster decay times than the pure host. The general decrease of rise times τ_{rise} could either be related to a decrease of the rotational viscosity γ_1, an increase of the effective elastic constant K or a combination thereof. However, decay times τ_{decay} do not confirm a clear trend for γ_1 or K. Additionally, the strong increase of $V_{Th,T}$ and missing data for $\Delta\epsilon$ prevent a reliable interpretation of switching times.

Doping the host 5CB with dodecanethiol capped particles AuSH12$_m$ also increases the threshold voltage V_{Th}, as can be seen in the upper left plot of figure 4.48. The magnitude of increase depends on the amount of added nanoparticles, a higher concentration leads to higher threshold voltages. However, the increase is less pronounced than for the mesogenic

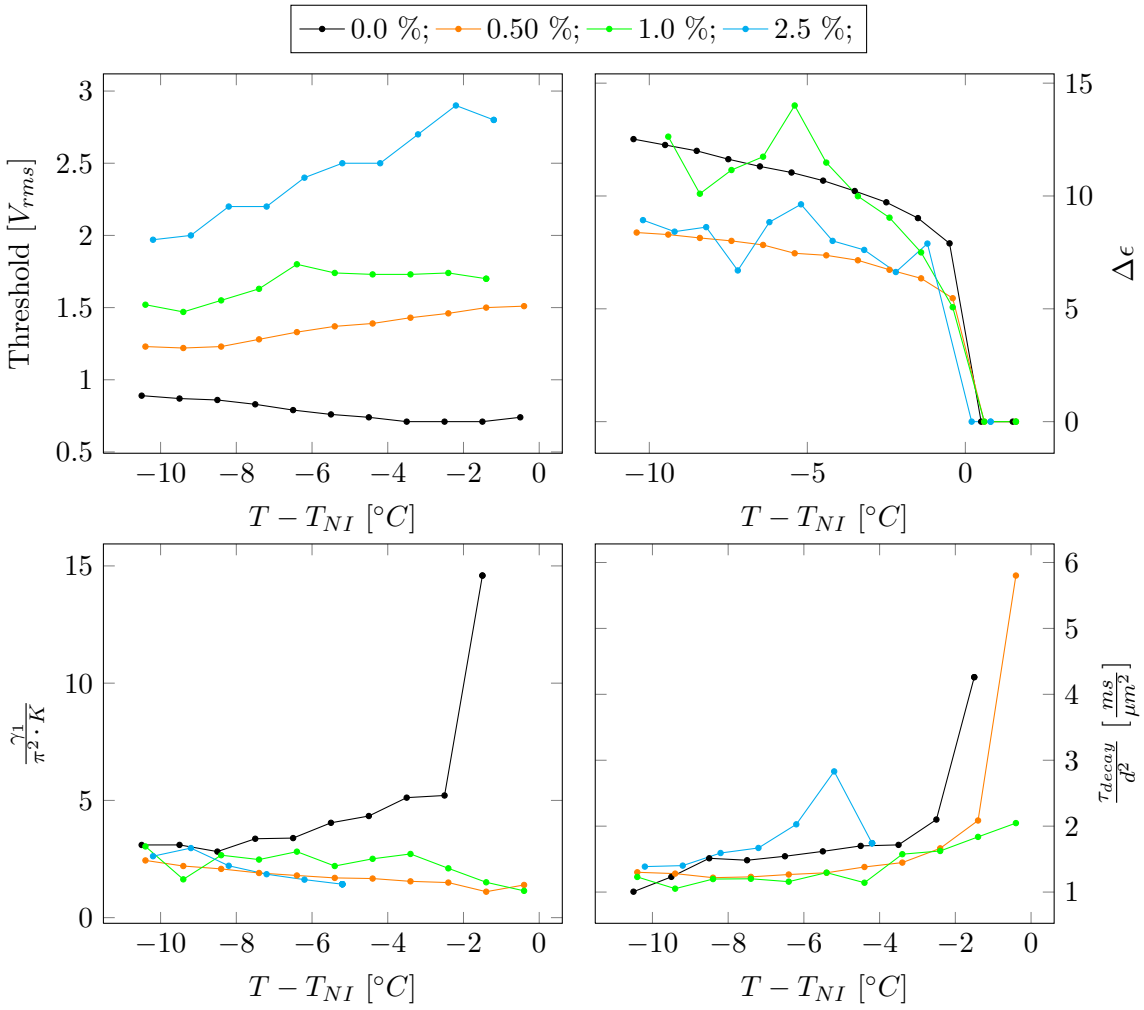

Figure 4.48: Plots of electro-optic data (V_{Th}, $\Delta\epsilon$, τ_{rise} and τ_{decay}) vs. $T - T_{NI}$ for dispersions of AuSH12$_m$ particles in 5CB at different particle concentrations.

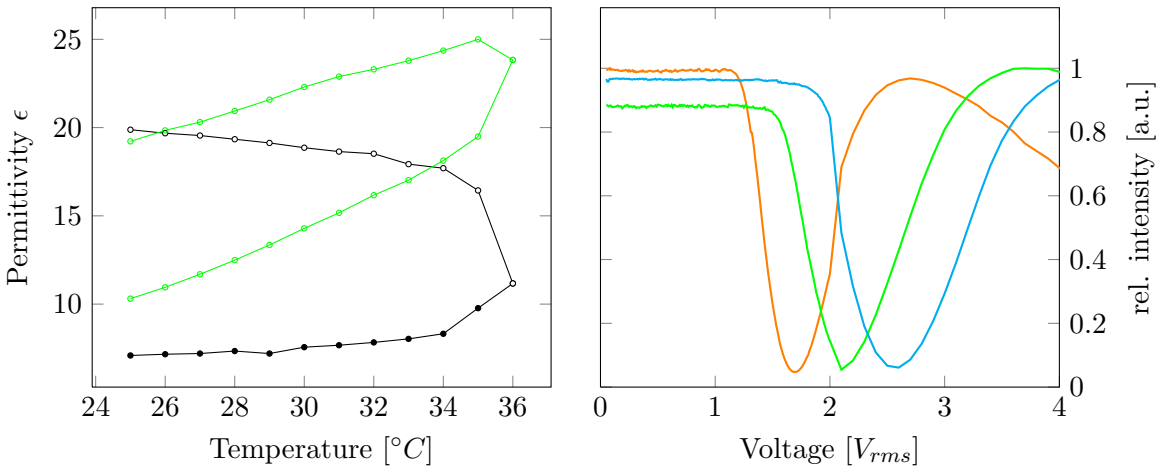

Figure 4.49: Left: Comparison of temperature dependent permittivity of the pure host 5CB (black plot) and a dispersion of 1 % (w) AuSH12$_m$ particles in 5CB. Right: Field dependent light transmission characteristics for AuSH12$_m$ doped 5CB at different particle concentrations. The colors correspond to the concentrations shown in figure 4.48, measurements are performed at $T_{NI} - T = 3\,\mathrm{K}$ with an interference filter for monochromatic light ($\lambda = 542\,\mathrm{nm}$).

doped particles AuCB: While a concentration of 2.5 % (w) AuCB increases the threshold of the mixture by the factor 10-12, 2.5 % (w) of AuSH12$_m$ particles lead only to an increase by the factor 2-3. The temperature dependency of threshold is again reversed, so that the effect of nanoparticle doping on the threshold voltage V_{Th} is more pronounced at high temperatures.

Measurements of the dielectric anisotropy of mixtures doped with AuSH12$_m$ particles indicate that $\Delta\epsilon$ is decreased by the presence of nanoparticles in the dispersion. However, it should be noted that also the gold particles AuSH12$_m$ at least partially cover the surface of the alignment layer (see figure 4.32, section 4.5). Especially at higher doping concentrations, this effect leads to incorrect measurements, which manifests in a discontinuous decrease of $\Delta\epsilon$. Only for samples with 0.5 % (w) AuSH12$_m$ a smooth decay of $\Delta\epsilon$ is obtained. For the interpretation of data, the focus is put on this curve, but also the two noisy measurements for 1.0 % (w) and 2.5 % (w) of particles confirm the general trend of a decrease of $\Delta\epsilon$ by doping with AuSH12$_m$ particles.

As shown in the left diagram of figure 4.49, the presence of 1 % (w) AuSH12$_m$ nanoparticles increases both $\epsilon_\perp$ and $\epsilon_\parallel$. However, a stronger increase for $\epsilon_\perp$ leads to the decrease in $\Delta\epsilon$. This influence of nanoparticles on $\epsilon_\perp$ can only partially be explained by an effect of nanoparticles on the alignment layer. Increasing the pretilt angle of the molecules leads to a proportion of ϵ_l to the capacitance measured perpendicular to the molecules, and therefore increases the resulting value for $\epsilon_\perp$. The general increase of both permittivities parallel and perpendicular to the molecules, however, cannot be explained by surface effects: The maximum value of $\epsilon_\parallel$ for the host is given by ϵ_l for a nematic order parameter of $S = 1$, which corresponds to perfectly parallel aligned molecules. In this case, only ϵ_l contributes to the measurement of $\epsilon_\parallel$. Under these conditions, resulting values for $\epsilon_\parallel$ larger than ϵ_l are

physically impossible, which indicates that other effects are present.

The results shown here for alkylthiol capped gold particles in 5CB partially differ from results published for alkylthiol capped particles dispersed in the host FELIX-2900-03 by Prof. Hegmann's group before. Qi et al. report no distinct differences for the dielectric anisotropy compared to the pure LC, as well as very similar threshold voltages for the Fréedericksz transition [62]. This shows the importance of the nematic host for changes in electro-optical properties, as the results shown here for the host 5CB clearly indicate a strong influence of particles on the electro-optical properties of the mixture. Considering aliphatic and mesogenic capped gold particles in the hosts 5CB and 8CB, the authors only note a small influence on the electro-optical response [78]. However, the idea of nanoparticles residing on the initial alignment layer and therefore changing the pretilt angle of the molecules is also discussed in this reference as possible source of changes of electro-optic properties. The authors then conclude that the slight changes in electro-optic behavior are caused by nanoparticles altering the alignment layer, and that the nanoparticles dispersed in the bulk of the mixture do not influence on the electro-optic properties. The own analysis of field-dependent light transmission characteristics reveals the presence of a well-defined threshold for the Fréedericksz transition (see figure 4.49), which indicates strong boundary conditions and very small pretilt angles. In conclusion, an influence of nanoparticles on the alignment layers of the electro-optical test cells during measurement can be neglected for AuSH12$_m$ particles in 5CB.

The analysis of switching times again shows a decrease of rise times for doped samples, while the obtained data for decay times show no clear trend due to nanoparticle doping. As the increase in threshold is presumably not directly connected to changes in the elastic properties of the dispersion, but to charge effects on the interface (see discussion below), a reliable interpretation of switching times appears not feasible.

A possible explanation model for the increase of threshold voltages and permittivity values for AuCB and AuSH12$_m$ particles is given by the formation of electric double layers at the interfaces between the active electrode areas and the bulk dispersion. As shown in section 4.5.1 by analyzing field-induced alignment changes, these particles presumably give rise to high charge carrier concentrations when dispersed in 5CB. Assuming these charge carriers form electric double layers as proposed by Stern [111] at the electrode interfaces explains the increase in threshold as well as high capacitances in these samples.

The Stern layer model combines the ideas of an immobile Helmholtz layer of adsorbed ions at the interface and a diffuse Gouy-Chapman layer of mobile ions in the bulk [112]. In consequence, a Stern double layer within an electro-optic test cell can be described as two capacitors in series (equation 4.4)

$$\frac{1}{C_{DL}} = \frac{1}{C_{HH}} + \frac{1}{C_{GC}}. \tag{4.4}$$

The capacitance C_{HH} of the immobile Helmholtz layer can be estimated by the simple equation 2.15 for a plate capacitor. The two plates are given by the electrode interface and

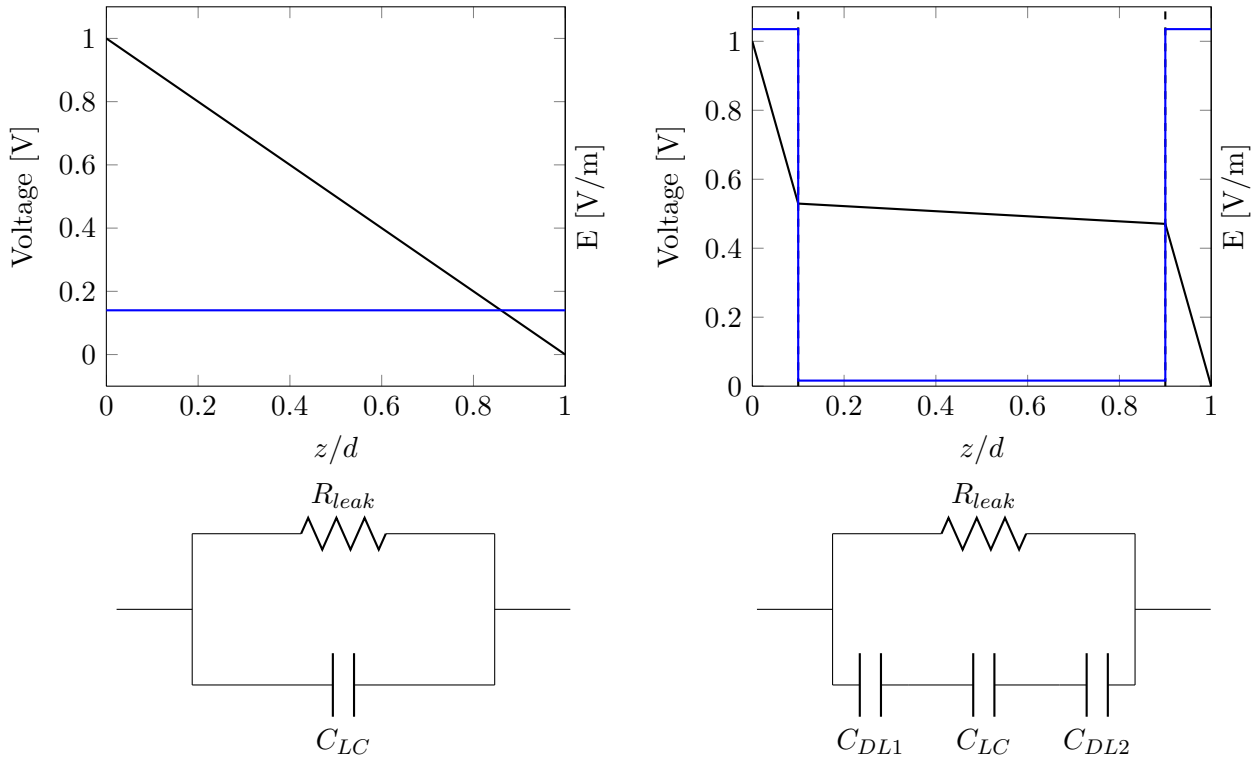

Figure 4.50: Schematic representation of a liquid crystal test cell as capacitor without (left) and with (right) electric double layer at the interfaces. In the diagrams on the top the voltage drop (black lines) and the respective field strength E (blue lines) within a test cell of thickness d are shown, the lower images represent the equivalent circuits of the test cells. The presence of electric double layers causes a voltage drop at the two interfaces, which leads to a lower electric field strength E in the bulk of the liquid crystal.

the layer of adsorbed ions, so the gap between the two plates can be estimated to be in the range of a few nm only. According to equation 2.15, this very thin gap gives rise to a very high capacitance of the Helmholtz layer.

The capacitance C_{GC} of the diffuse Gouy-Chapman layer depends on the spatial distribution of ions $\rho_{ion}(x,y,z)$ in the electric potential $\psi(x,y,z)$ within the cell gap, which can be estimated by the Poisson-Boltzmann equation 4.5

$$\nabla^2\psi = \frac{c_0 e}{\epsilon\epsilon_0}\left(\exp\left(\frac{e\psi(x,y,z)}{k_B T}\right) - \exp\left(-\frac{e\psi(x,y,z)}{k_B T}\right)\right), \tag{4.5}$$

using c_0 as the bulk concentration of charged particles. For the simple geometry of an electro-optic test cell, the Poisson-Boltzmann equation reduces to an one-dimensional problem along the z-axis, whose solution is given by

$$\psi = \psi_0 \cdot \exp(-\kappa z). \tag{4.6}$$

The decay length of the exponential decrease of ψ is given by the Debye length $\lambda_D = \kappa^{-1}$ with

$$\kappa = \sqrt{\frac{e^2}{\epsilon\epsilon_0 k_B T}\sum c_i Z_i^2}. \tag{4.7}$$

Here, c_i denotes the concentration of ion sort i and Z_i denotes its valency. The capacitance C_{GC} of the diffuse Gouy-Chapman layer can then be estimated by equation 4.8 [112]

$$C_{GC} = \frac{\epsilon\epsilon_0}{\lambda_D}. \tag{4.8}$$

Hence, the capacitance C_{GC} depends on the temperature as well as on the concentration of ions in the bulk. The observed increase of capacitance with increasing temperature (see figure 4.47 and figure 4.49, left) indicates that the concentration of ions in the bulk is strongly temperature dependent. At higher temperatures, more charged species contribute to the total capacitance of the test cell.

The temperature-dependent increase of capacitance also explains the increase of threshold voltage as well as the inversion of temperature dependency, as observed for dispersions of AuCB and AuSH12$_m$ particles in 5CB. It is known that the presence of electric double layers within a capacitor as discussed above leads to a potential drop at the electrode / electrolyte interface [113]. Thereby, the electric field strength E in the bulk of the nanoparticle dispersion is significantly reduced, as can be seen in the upper plots in figure 4.50. This explains the apparent increase of threshold voltage, as higher external voltages are needed to achieve the critical field strength within the bulk, which is necessary to overcome the elastic repulsion force of the nematic order and to reorient the liquid crystal molecules along the field direction. As the extent of this reduction is not known, conclusions about the influence of nanoparticles of the elastic properties of the host should not be drawn from the threshold data obtained for AuCB and AuSH12$_m$ dispersions. Presumably the concentration of ions and thereby also the influence of the Gouy-Chapman layer on the total capacitance increase with increasing temperature. As a result, the local field strength is lowered further and

higher external voltages are needed to overcome the elastic restoring torque of the nematic liquid crystal. This presumably causes the inversion of temperature dependency of V_{Th} compared to the pure compound 5CB.

The model of a Stern double layer on the active electrodes explains the higher capacitance values for the AuCB and AuSH12$_m$ doped samples compared to the pure host as well as higher threshold voltages. Hence, the nanoparticle induced changes of nematic properties V_{Th} and $\Delta\epsilon$ are presumably not caused by the presence of particles in the bulk, but dominated by the presence of ions at the interfaces. Besides altering the liquid crystal alignment by surface coverage, the formation of electric double layers is an additional influence of nanoparticle doping on the properties of the resulting dispersions.

Presumably, also the observed reversed switching of dispersions containing AuSH12$_s$ in FELIX-2900-03 (see section 4.5.2) is connected to unusual electric properties of the nanoparticle dispersion. The reverse switching is identified to correspond to the formation of electroconvection rolls in a (+,-) material. Hence, the dispersion is expected to exhibit a negative anisotropy of conductivity, which is caused by the presence of gold nanoparticles. Although also the negative anisotropy of conductivity could not be confirmed by experiment, the reverse switching is an example of a bulk property of charged nanoparticles in a nematic host.

In conclusion, it is found that charged nanoparticles can influence on the dielectric response of a nematic liquid crystal by altering the bulk properties as well as influencing on the alignment layers. Effects by charged dopants are more pronounced in the polar host 5CB, but can also occur in the apolar host FELIX-2900-03.

Comparing the results for dispersions of AuCB and AuSH12$_m$ in 5CB, the experimental data shown here do not reveal an advantage of mesogenic capped particles over the use of aliphatic functionalized particles, as stated in reference [14] by Draper et al.. The general idea proclaimed in latter reference is that mesogenic capped particles are chemically more similar to the nematic host, and therefore promise a better solubility and stability.

It has been shown in several publications that the interaction between the surface functionalization of nanoparticles and the respective host molecules requires a more sophisticated fine tuning. As shown in a theoretical study by Soulé et al. [85], mixed monolayers of mesogenic and aliphatic ligands on nanoparticles are expected to show the highest miscibility in a nematic host. When the nanoparticles are in a size regime comparable to the size of single host molecules, the authors consider entropic effects like mixing entropy and entropy-driven self-assembly to be relevant for the formation of homogeneous dispersions. Hence, their model does not consider the nanoparticles as hard spheres, but as particles with a soft shell that can be partially penetrated by the host molecules. By fine adjusting the ratio of shorter aliphatic ligands and longer mesogenic ligands to the core diameter, an optimal overlap of ligand molecules and host molecules is enabled. This maximizes the mixing entropy of the binary mixture of particles and host, and thus leads to the formation of stable dispersions. A schematic drawing of this soft-shell-model is shown in figure 4.51.

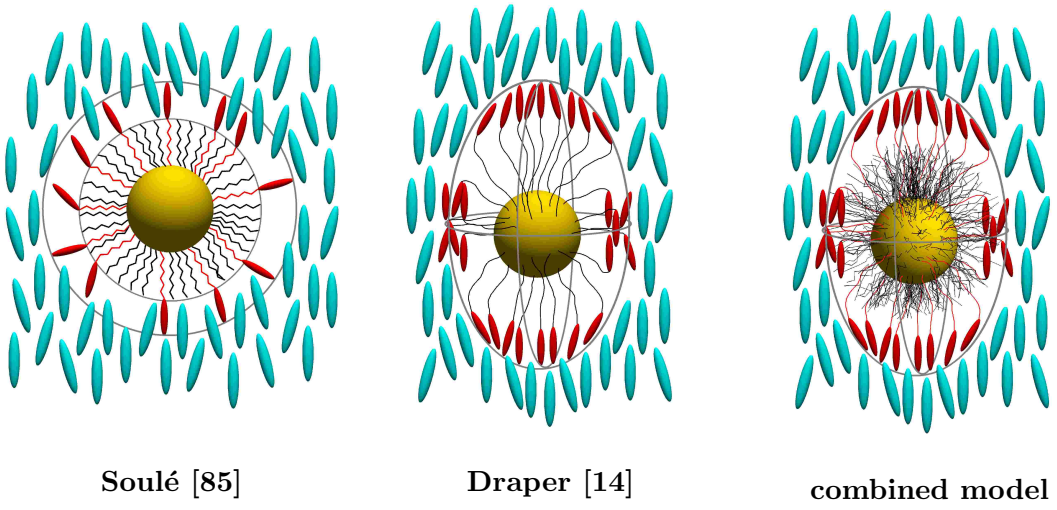

Figure 4.51: Schematic drawings of interaction models between the particle's ligand shell and the nematic host molecules. Left: Soft sphere model for mixed monolayers of mesogenic and aliphatic capped gold particles, adapted from Soulé et al. from reference [85]. Middle: Tactoidal deformation of spherical gold nanoparticles with purely mesogenic capping, adapted from Draper et al. from reference [14]. Right: New model combining the tactoidal deformation and the soft ligand shell.

This soft-shell model has been experimentally proven by Milette et al., the respective data is given in reference [57]. The results presented in this study confirm that a proper combination of core diameter, ligand chain length and ligand shell composition leads to a high miscibility of functionalized particles in a nematic host. However, a spherical ligand shell is less compatible with the unidirectional order of the nematic host than an anisometric soft shell. As shown by Draper et al. in reference [14], the fully mesogenic functionalized nanoparticles AuCB can form tactoidal ligand shells, which promise a better miscibility in an anisometric host (see figure 4.51, middle). Additionally, Wojcik et al. showed that an anisometric mesogenic ligand shell around spherical particles supports the formation of mesophases by particles and is therefore energetically favored over an isometric spherical ligand shell (see reference [48]). This process of nanoparticles forming anisometric ligand shells and forming mesophases has recently been optimized by Mang and co-workers, who report the formation of regular nanoparticle arrays for different combinations of mesogenic ligand and co-ligands in reference [114]. Hence, two setscrews of optimizing the interaction of nanoparticles with the nematic host have been identified, namely a penetrable soft ligand shell of long mesogenic ligand and shorter co-ligand and the possibility to deform the spherical ligand shell to a tactoidal shape. Combining the soft-shell model by Soulé and the tactoidal deformation model by Draper and Wojcik, an advanced model is obtained, which is believed to show the best miscibility and stability in a nematic phase (see figure 4.51, right).

Besides utilizing a mixed ligand shell with shorter aliphatic ligands and longer mesogenic capped ligands to promote the interaction between nanoparticles and host molecules, also the curvature of the nanoparticles has an influence on the possible degree of interdigitation. Following the argumentation of Milette et al. [57], the high surface curvature of 2 nm

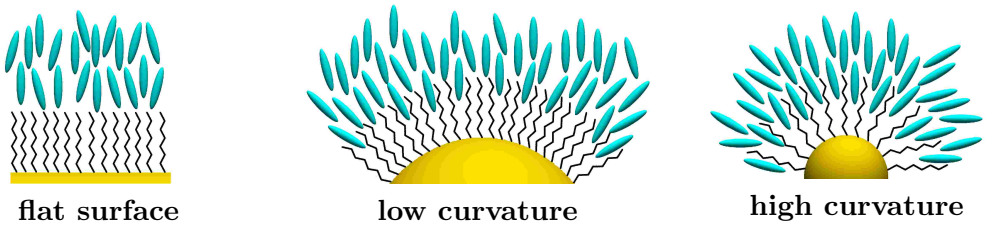

Figure 4.52: Schematic drawings illustrating the influence of radius curvature on the possible degree of interdigitation between ligand shell and host molecules (adapted from Coursault et al. [87]).

AuSH12$_s$ particles provides sufficient free space between the ligands for interactions with the hydrocarbon chain of 5CB, or both side chains of FELIX-2900-03. Larger particles show a denser packing of ligands, and hence lower miscibility in a nematic host. As illustrated by Coursault et al., a flat surface (radius of curvature ∞) results in a very dense monolayer packing of ligands and prevents an interdigitation with ligand molecules. With decreasing curvature, the packing gets less dense and allows more interaction between ligand shell and host molecules. This principle is shown in figure 4.52, adapted from reference [87].

Hence, this model indeed gives an explanation for the higher miscibility of alkylthiol-capped particles in FELIX-2900-03 compared to 5CB, as reported by Qi. et al. in reference [78]. Milette et al. also report a miscibility of dodecanethiol functionalized gold particles in the size regime of AuSH12$_m$ in 5CB only for low concentrations, while higher concentrations lead to the formation of agglomerates. The authors show by surface plasmon resonance analysis that at low concentrations the dodecanethiol capping features a higher mobility and hence allows the penetration of hydrocarbon chains. At high concentrations, a red shift of the surface plasmon resonance frequency indicates a closer packing of ligands, which prevents interdigitation of ligands and host molecules and finally leads to a phase separation. As shown by Khathua et al. in reference [82], dodecanethiol functionalized gold particles with even larger core diameters ($d > 6\,\mathrm{nm}$) have a too densely packed ligand shell and therefore do not show a distinct surface plasmon resonance band due to precipitation.

As the curvature of nanoparticles has been identified to play an important role for the degree of possible interdigitation of ligands and host molecules, this influence should be observable in a comparison of CdSe590 and CdSe610 particles, which are chemically identical but only differ in the diameter of the CdSe core. The electro-optical results for dispersions of CdSe610 particles in the host 5CB are shown in figure 4.53. The presence of CdSe610 nanoparticles leads only to very slight decreases in threshold voltage V_{Th} and dielectric anisotropy $\Delta\epsilon$ of the mixture compared to the pure host. The decrease of V_{Th} is more pronounced at lower temperatures, but in contrast to dispersions of AuCB and AuSH12$_m$ in 5CB, nanoparticle doping with CdSe610 does not alter the temperature dependency of V_{Th}. For all doping concentrations the threshold decreases with increasing temperature. The magnitude of decrease is not correlated to the particle concentration, however mixtures with higher amounts of particles show a less smooth decrease of V_{Th} and $\Delta\epsilon$.

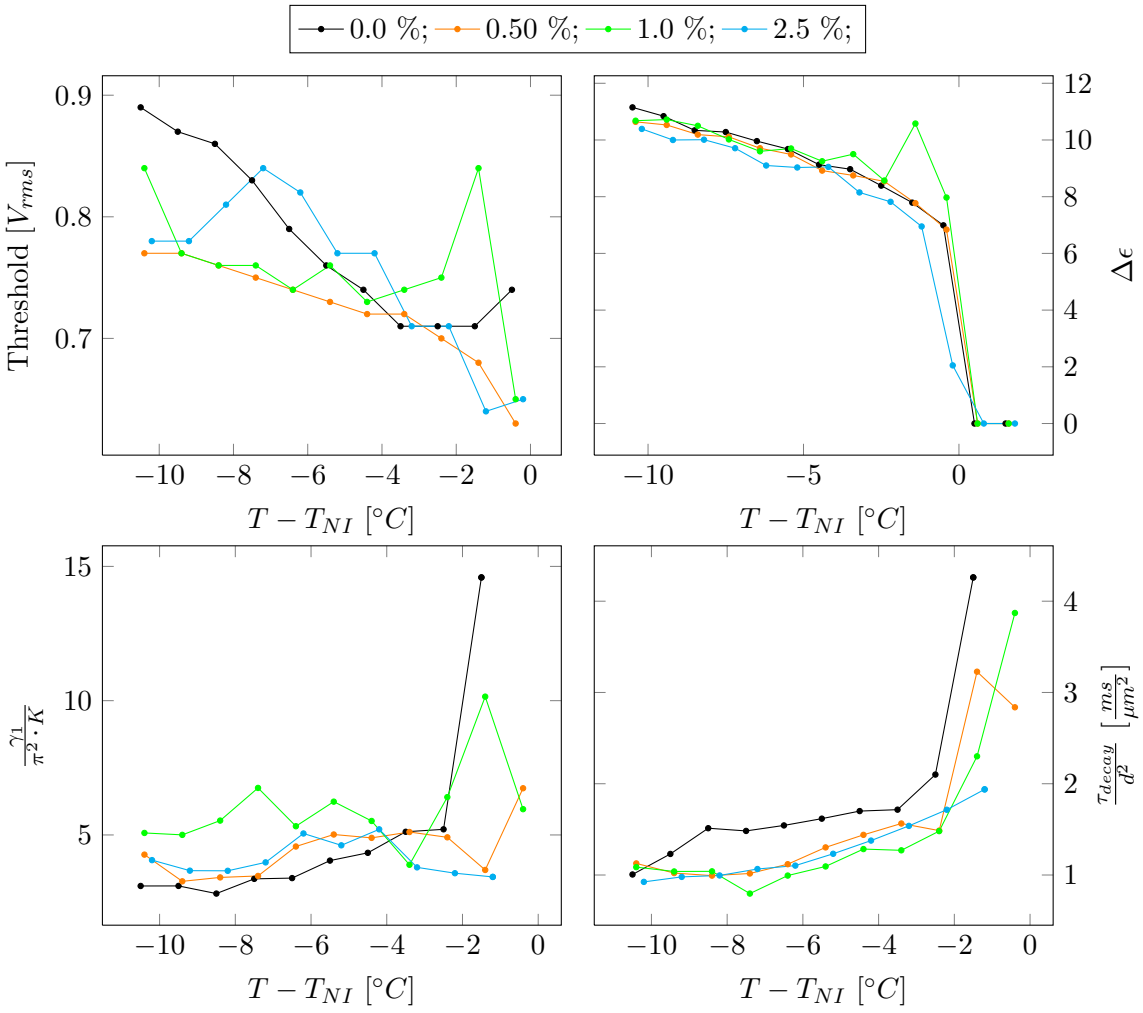

Figure 4.53: Plots of electro-optic data (V_{Th}, $\Delta\epsilon$, τ_{rise} and τ_{decay}) vs. $T - T_{NI}$ for dispersions of CdSe610 particles in 5CB at different particle concentrations.

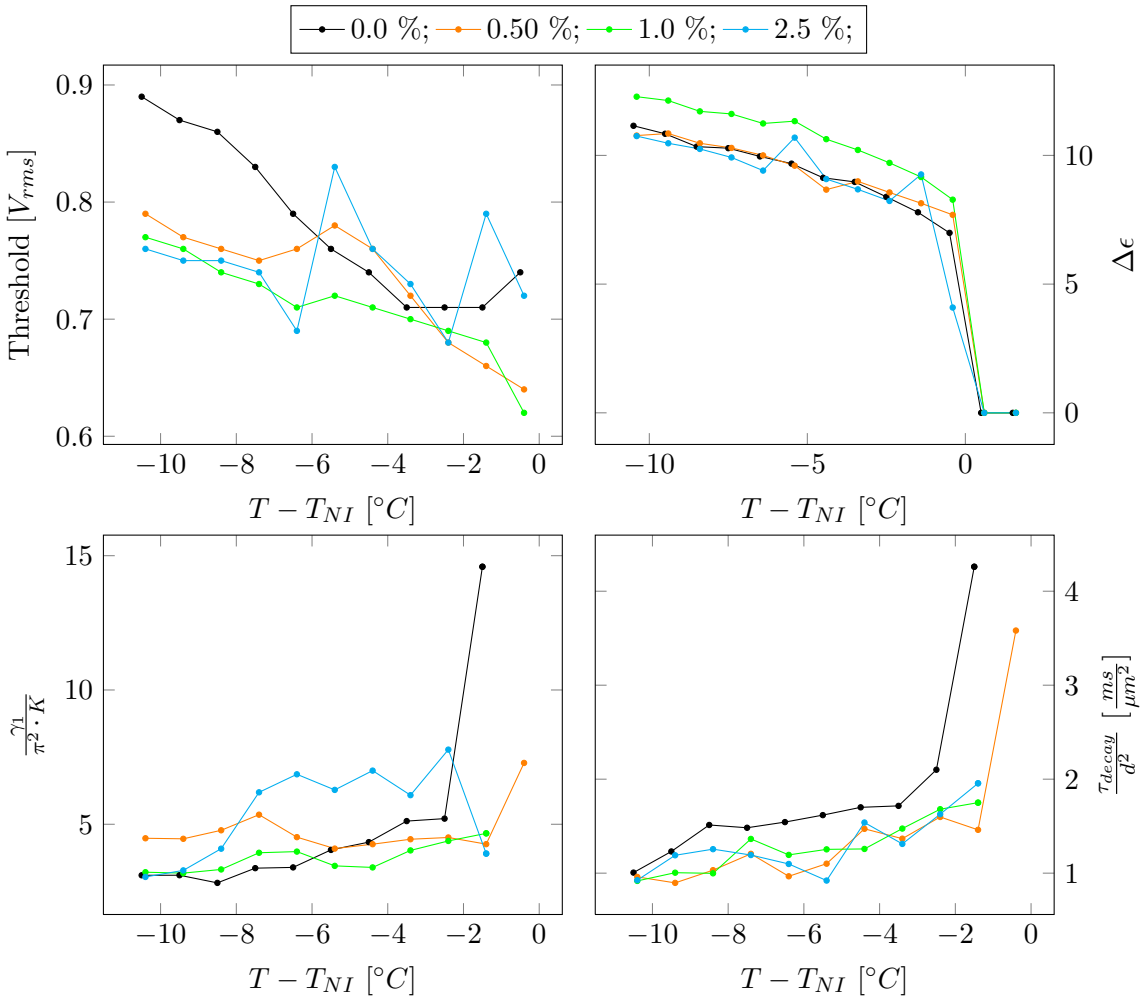

Figure 4.54: Plots of electro-optic data (V_{Th}, $\Delta\epsilon$, τ_{rise} and τ_{decay}) vs. $T - T_{NI}$ for dispersions of CdSe590 particles in 5CB at different particle concentrations.

The analysis of switching times reveals an increase of rise times for doped samples, and a decrease of decay times. This is in contrast to observations made for the gold nanoparticles AuCB and AuSH12$_m$ in the same host. However, again a reliable interpretation of these data appears difficult. A decrease of decay times is either connected to an increase of the effective elastic constant K of the Fréedericksz transition, or a decrease of the rotational viscosity γ_1. However, the observed increase in rise times indicates the opposite behavior, as V_{Th} and $\Delta\epsilon$ show almost no changes compared to the pure host.

The electro-optical analysis of dispersions of CdSe590 particles in 5CB gives very similar results compared to CdSe610 particles, as can be seen in figure 4.54. Again, the presence of nanoparticles leads to a very slight decrease of threshold voltage, which is more pronounced at low temperatures. The temperature dependence of V_{Th} is not altered compared to the pure host. Almost no impact of nanoparticle doping on the dielectric anisotropy $\Delta\epsilon$ is found, except of slightly higher values for the mixture containing 1 % (w) of CdSe590. The impact of CdSe590 doping in 5CB on the switching times of the mixture is comparable to the effects observed for CdSe610 particles. While the rise time is slightly increased, decay

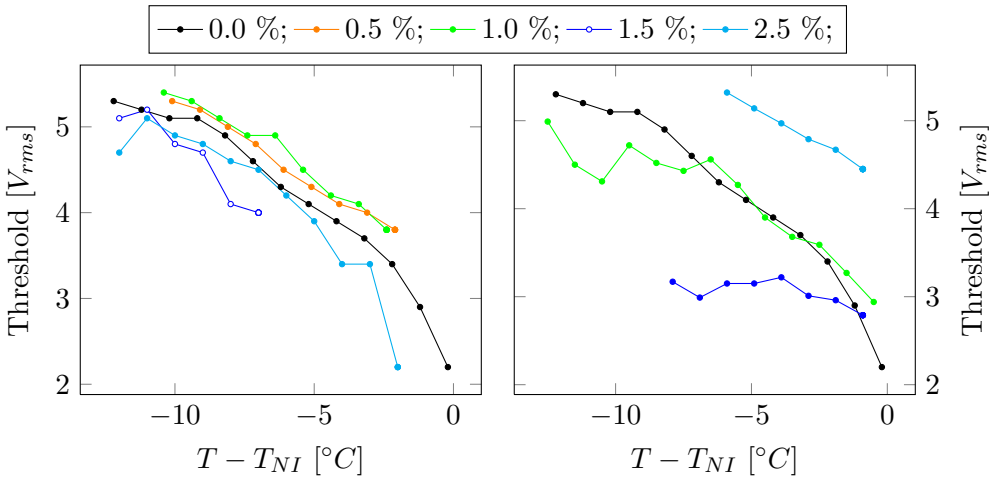

Figure 4.55: Left: Plot of threshold voltages $V_{Th,T}$ vs. $T - T_{NI}$ for CdSe590 nanoparticles in the host FELIX-2900-03. Right: Plot of threshold voltages $V_{Th,T}$ vs. $T - T_{NI}$ for CdSe610 nanoparticles in the host FELIX-2900-03.

times of doped samples are faster than for the pure host.

Comparing these results to effects on the electro-optic response when doping a nematic host with CdSe590 or CdSe610 particles reported by Kinkead et al. in reference [13], several similarities occur. The authors of latter study report that especially CdSe590 particles have no distinct effect on the threshold voltage or the elastic constants of the nematic host FELIX-2900-03 used in their study. This can be confirmed also for the host 5CB by the results presented here. However, Kinkead et al. also report a more pronounced effect for the larger CdSe610 particles on the electro-optical performance of the mixture, and suggest a unique relationship between the size of the particles and observable electro-optical effects. This could not be confirmed for the host 5CB, as both particles CdSe610 and CdSe590 induce roughly the same changes in the electro-optical response.

Own data of threshold voltages for dispersions of CdSe590 and CdSe610 in the nematic host FELIX-2900-03 are shown in figure 4.55. However, as reported in section 4.4.3, these particles have a strong influence on the polyimide alignment layer of the electro-optical test cells used for these experiments. The nanoparticles cause a strong surface coverage on the initial alignment layer and thereby induce homeotropic alignment or reduce the strong boundary conditions to weak anchoring. As a result, dielectric measurements are not possible, and light transmission measurements can only be performed on regions with no detectable surface coverage.

The threshold data obtained for CdSe590 particles are plotted in the left diagram of figure 4.55 and show only slight changes of V_{Th} with increasing particle concentration. At the lowest doping concentrations of 0.5 % (w) and 1.0 % (w), the threshold is slightly increased, while for all higher concentrations V_{Th} is slightly lower than for the pure host. This concentration dependency is in accordance to the model of surface coverage shown in figure 4.26, as

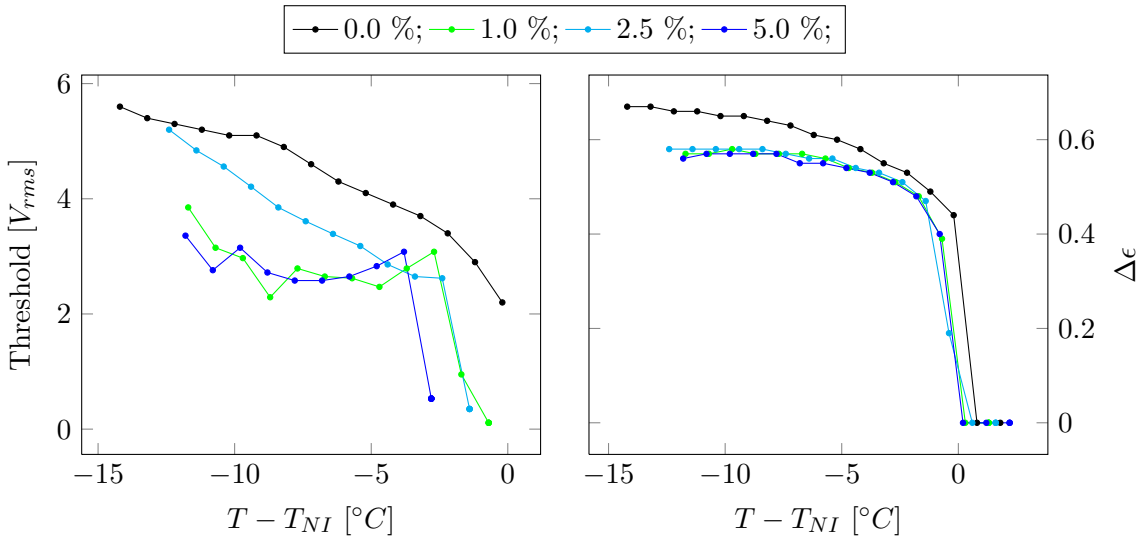

Figure 4.56: Plots of V_{Th} vs. $T - T_{NI}$ (left) and $\Delta\epsilon$ vs. $T - T_{NI}$ for dispersions containing different concentrations of msCdSe quantum dots in the host FELIX-2900-03.

a slight surface coverage with onsetting loss of threshold leads to lower calculated threshold voltages. In general, although the area for measuring the field dependent light transmission between crossed polarizers is chosen very carefully, the obtained data is connected to comparable large uncertainities. Hence, small changes in V_{Th} should not be overemphasized. This is also valid for data obtained for dispersions containing CdSe610 nanoparticles, as shown in the right diagram of figure 4.55.

Referring to the considerations about a connection between core diameters, ligand shell composition and the miscibility of particles in a nematic host, a difference in miscibility and stability between the larger CdSe610 particles and the smaller CdSe590 particles would be expected. However, in the polar host 5CB both particles show similar miscibility, stability and electro-optical properties. In the non-polar host FELIX-2900-03, the strong interaction between the particles and the polyimide alignment layer of the electro-optic test cells prevents both the proper observation of stability and the measurement of electro-optical properties.

The observed similarities between CdSe590 and CdSe610 despite different core diameters can be explained by the small difference in core diameters between CdSe590 and CdSe610 of only 0.8 nm. Although Kinkead et al. suggest an unique relationship between the size of the CdSe particles and observable electro-optical effects (see reference [13]), and Soulé et al. and Milette et al. support this expectations with their work, a certain size difference seems to be necessary to obtain visible effects. Additionally, CdSe590 and CdSe610 particles are not monodisperse, but feature a certain width of size diameter distribution. This hampers size effects to be clearly visible, as an interaction of particles with different cores sizes occurs.

The magic sized quantum dots msCdSe and msCdSe:Zn overcome the problem of polydispersity, as they feature very narrow size distributions.

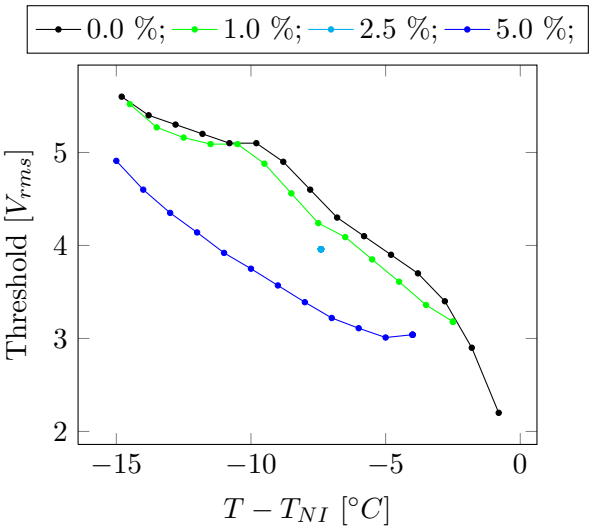

Figure 4.57: Plot of V_{Th} vs. $T - T_{NI}$ for dispersions containing different concentrations of msCdSe:Zn nanoparticles in the host FELIX-2900-03.

The electro-optical analysis of dispersions of FELIX-2900-03 containing the magic-sized quantum dots msCdSe and msCdSe:Zn has been performed in collaboration with Javad Mirzaei from Prof. Hegmann's group, results have been published in reference [65] already. As reported in latter reference, neither msCdSe particles nor msCdSe:Zn particles show a significant effect on the threshold voltage of the Fréedericksz transition $V_{Th,D}$, when determined by dielectric measurement. However, threshold voltages obtained by light transmission measurements show a clear decrease of $V_{Th,T}$ for doped samples (see figures 4.56 (left), and figure 4.57). The origin of this contradiction can be found by a close analysis of the field-dependent light transmission characteristics (see figure 4.58). The doped samples both of msCdSe and msCdSe:Zn mixtures do not exhibit a sharp threshold as the undoped host, but show a gradually increase of light transmission with increasing field strength. This loss of threshold occurs independently from the particle concentration, and is probably caused by a partial surface coverage of nanoparticles on the polyimide alignment layer of the electro-optic test cell, as discussed in section 4.4.3. This effect is more pronounced for the more sensitive light transmission measurements as for dielectric measurements. In consequence, the calculated threshold voltages $V_{Th,T}$ appear lower than data obtained from dielectric measurements, $V_{Th,D}$.

The partial surface coverage and the thereby altered alignment conditions also influence on the dielectric anisotropy values. As reported in reference [65], an increasing concentration of nanoparticles gradually lowers the dielectric anisotropy compared to the pure host. Except for a concentration dependency, own measurements confirm lower dielectric anisotropies for msCdSe doped samples (see figure 4.56, right). However, this decrease in $\Delta\epsilon$ is caused more by an increase of $\epsilon_\perp$ than by a decrease of $\epsilon_\parallel$ (see figure 4.59). This again indicates that the strong boundary conditions in the electro-optic test cell are weakened, and the molecules are not strongly bound parallel to the surface. An increased tilt angle would lead to contributions of ϵ_l to the measurement of $\epsilon_\perp$, and hence gives an explanation for the observed

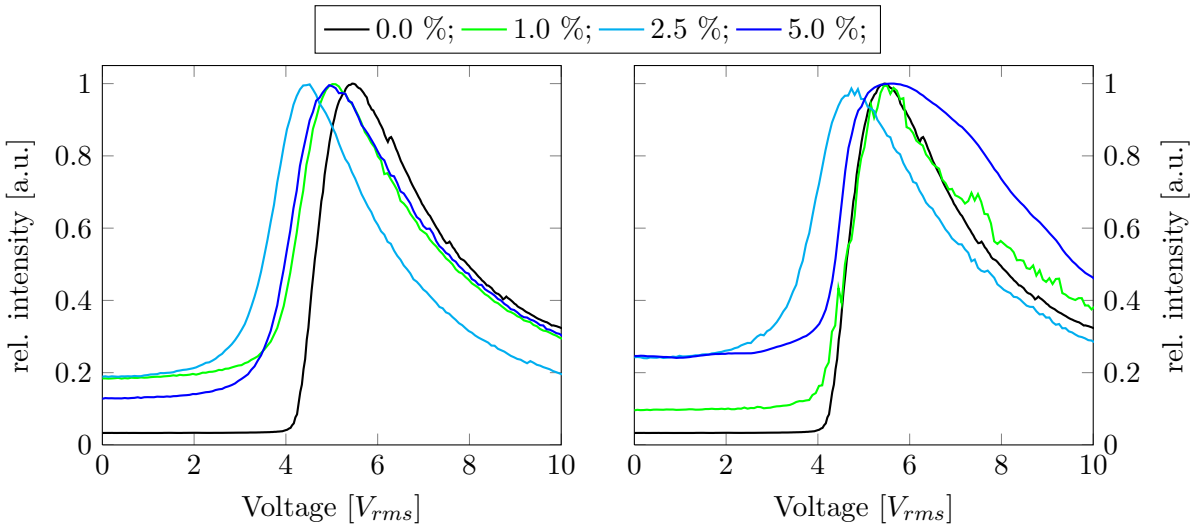

Figure 4.58: Left: Temperature dependent light transmission characteristics of the liquid crystal FELIX-2900-03 doped with different amounts of msCdSe nanoparticles. Right: Temperature dependent light transmission characteristics of the liquid crystal FELIX-2900-03 doped with different amounts of msCdSe:Zn nanoparticles. All measurements are performed at $T_{NI} - T = 3\,\mathrm{K}$ with an interference filter for monochromatic light ($\lambda = 542\,\mathrm{nm}$).

permittivity changes.

Referring to the influence of core curvature and monodispersity, the particles msCdSe and msCdSe:Zn would be promising candidates for stable dispersions in a apolar host like FELIX-2900-03. With core diameter of 2.0±0.1 nm they should feature enough spacing between the ligands for sufficient interaction with the aliphatic side chains of the nematic host. However, the data obtained from these dispersions do not confirm this impression. Dispersions of both particles show defect textures when filled in electro-optical test cells, and the electro-optical data obtained do not give a reliable trend for threshold voltage or dielectric anisotropy. Although only a limited number of samples could be investigated, as the samples were prepared by Javad Mirzaei in Prof. Hegmann's group and kindly provided for own experiments, this might indicate that a certain size distribution of diameters even facilitates the interaction between particles and host.

The electro-optic results for AuSi particles in the nematic host FELIX-2900-03 are shown in figure 4.60. Neglecting the dispersions with 5.0 % (w) and 7.5 % (w) of particles which show a coexistence of nematic and isotropic domains (see section 4.4.3), the presence of AuSi nanoparticles slightly reduces the threshold voltage of the Fréedericksz transition. The temperature dependency of V_{Th} remains approximately unchanged by nanoparticle doping, with increasing temperatures the threshold decreases comparable to the pure host FELIX-2900-03. Especially the mixture containing 1.0 % (w) of AuSi particles shows the most distinct reduction in threshold, and it should be noted that this mixture also shows the most distinct stabilization of the nematic phase as shown by phase transition temperatures in section 4.3. The same concentration of AuSi particles also leads, together with the sample containing

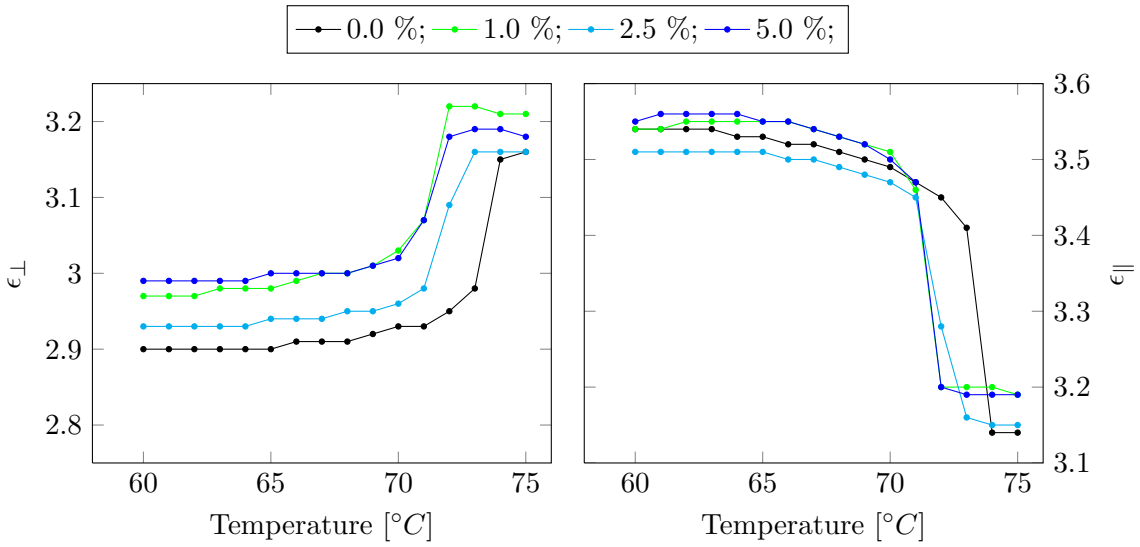

Figure 4.59: Left: Plot of $\epsilon_\perp$ vs. temperature for test cells filled with the liquid crystal FELIX-2900-03 doped with different concentrations of msCdSe nanoparticles. Right: Plot of $\epsilon_\parallel$ vs. temperature for test cells filled with the liquid crystal FELIX-2900-03 doped with different concentrations of msCdSe nanoparticles.

2.5 % (w) of particles, to the most distinct increase of dielectric anisotropy. In general, for concentrations up 2.5 % (w) of nanoparticles, an increase of $\Delta\epsilon$ is found, while samples containing 5.0 % (w) and 7.5 % (w) of particles reduce the dielectric anisotropy. A closer look on the permittivities perpendicular and parallel to the director ($\epsilon_\perp$ and $\epsilon_\parallel$, respectively, see figure 4.61) reveals that latter samples deviate from the expected temperature dependency. While samples with lower particle concentrations show an increase of $\epsilon_\perp$ and a decrease of $\epsilon_\parallel$ similar to the pure host for increasing temperatures, dispersions with 5.0 % (w) and 7.5 % (w) of AuSi particles show a general increase of $\epsilon_\perp$ and $\epsilon_\parallel$ (see figure 4.61). This behavior has also been observed to occur even more pronounced for all concentrations of AuSH12$_m$ particles in 5CB (see figure 4.49) and is presumably connected to the formation of charged particles at higher concentrations. As discussed for latter particle dispersions, the maximum value of $\epsilon_\parallel$ for the host is given by ϵ_l for a nematic order parameter of $S = 1$. According to Barbero et al. (see reference [110]), the presence of gold nanoparticles does not affect the permittivity of the dispersion. Hence, the observation of increasing permittivities for highly doped dispersions is most likely connected to the formation of electric double layers, as reported for AuCB and AuSH12$_m$ particles before.

For the same reason, the increase of $\Delta\epsilon$ at medium concentrations of AuSi particles is surprising. Assuming that the slight shift of $\epsilon_\perp$ and $\epsilon_\parallel$ to higher values (see left diagram in figure 4.61) is connected to very low concentrations of charged particles forming electric double layers, this effect seems to be negligible compared to effects reported for AuCB and AuSH12$_m$ particles. Higher values for $\Delta\epsilon$ are then presumably caused by an increase of the nematic order parameter S. As shown by the Maier-Meier equation 2.23, the dielectric anisotropy $\Delta\epsilon$ scales linearly with the order parameter S. However, the elastic constant K_{11} is proportional to the square of the order parameter, $K_{11} \propto S^2\,(T)$ [24]. According

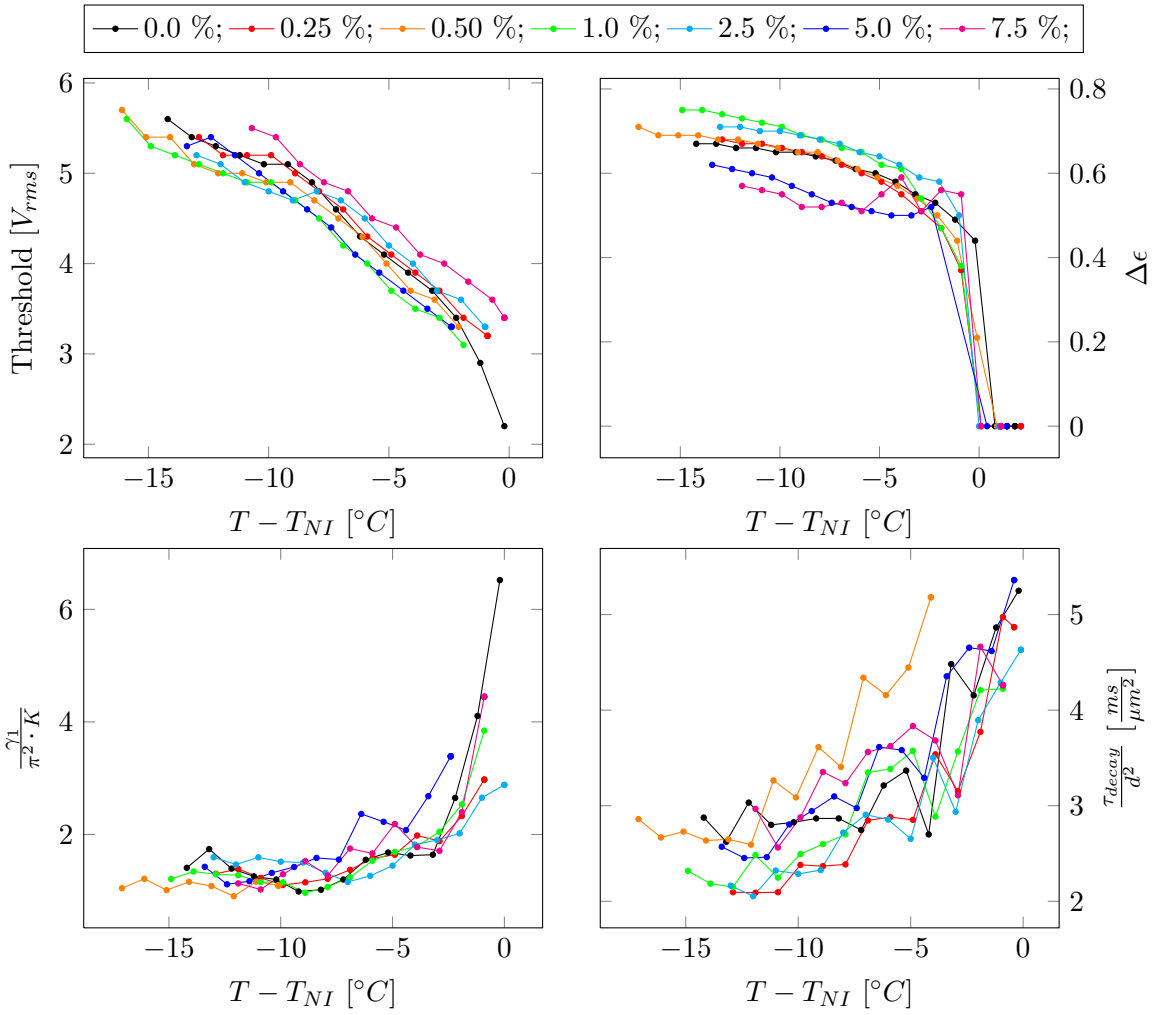

Figure 4.60: Plots of electro-optic data (V_{Th}, $\Delta\epsilon$, τ_{rise} and τ_{decay}) vs. $T - T_{NI}$ for dispersions of AuSi particles in FELIX-2900-03 at different particle concentrations.

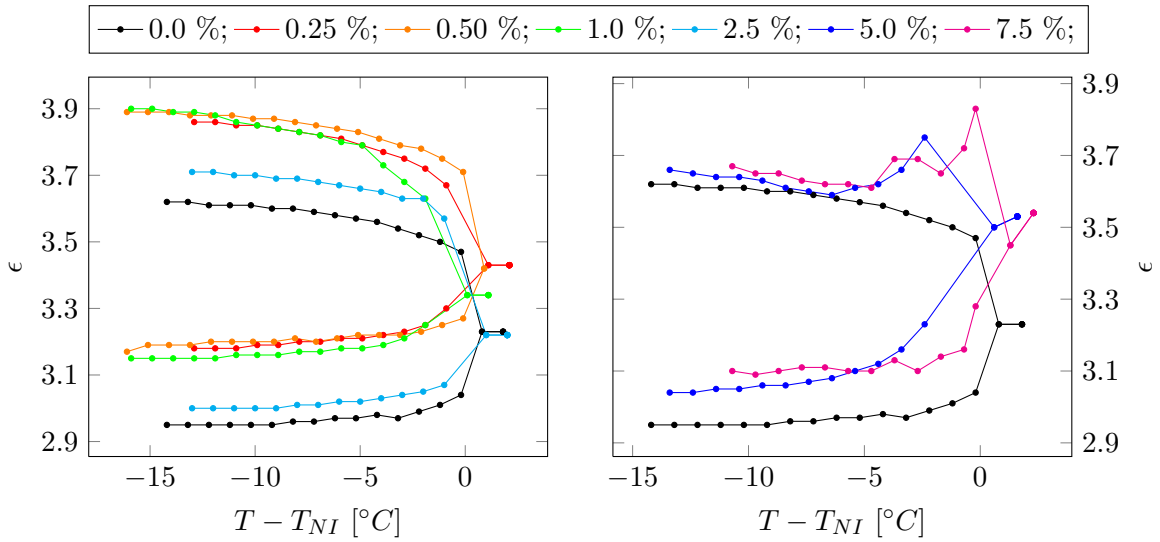

Figure 4.61: Analysis of temperature dependent permittivity changes for dispersions of AuSi nanoparticles in the host FELIX-2900-03.

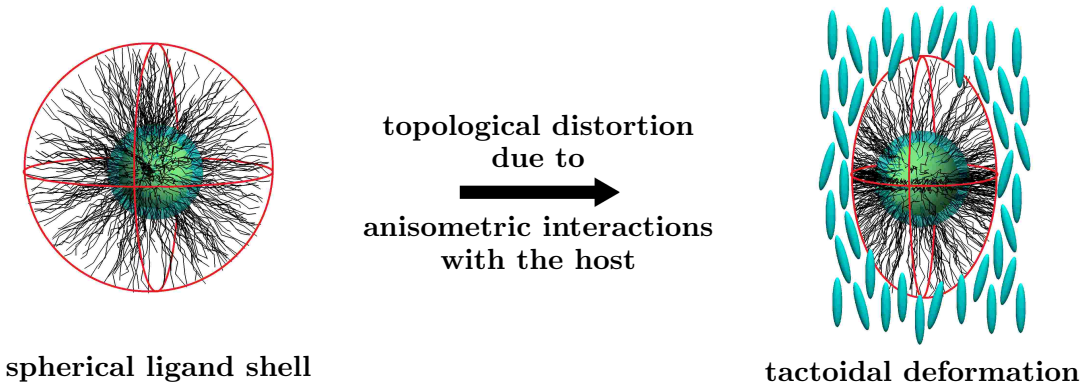

Figure 4.62: Schematic drawings of the expected tactoidal deformation of ligand shell of AuSi particles in the nematic host FELIX-2900-03. Left: Spherical ligand shell of single particle. Right: Tactoidal deformation by a folding of equatorial ligands of the particle due to anisometric interactions with the host molecules.

to equation 2.48 for the threshold voltage, an increase of the nematic order parameter S should then lead to higher values of V_{Th}. The observed decrease is presumably attributed to the presence of dispersed nanoparticles in the bulk, which facilitate the reorientation of host molecules by specific interactions with the ligand shell and thereby decrease the elastic constant K_{11}. Considering the model about anisometric particles shown in figure 4.8 and the notes about the importance of interactions between ligands and host molecules in a soft ligand shell, a model is derived to explain a possible increase in S and decrease in V_{Th} due to the presence of AuSi nanoparticles.

The increase of nematic order by the presence of AuSi particles could be connected to anisometrically shaped nanoparticles, similar as depicted in the combined model in figure 4.51. A tactoidal ligand shell would induce additional orientational order parallel to the long axis of the ligand shell, and therefore increase the total order parameter S in the dispersion. The anisometric shape presumably originates by aliphatic chains in the axial position of the particle being fully unfolded, while ligands in the equatorial region fold to coils. By applying external electric fields, small distortions in the surrounding director field could induce a flip of equatorial and axial orientation, where coils unfold and unfolded ligands fold up. In this manner, the reorientation of host molecules is facilitated by the presence of AuSi nanoparticles even without a rotation of the particle's core, but by anisometric interactions of ligands and host molecules. Hence, the formation of anisometrically shaped ligand shells would also be responsible for the observed slight decrease in threshold voltages.

In analogy to the tactoidal particle shape reported by Draper et al. (see reference [14]), it is assumed that the spherical ligand shell of AuSi particles deforms to a tactoidal shape what also facilitates the interdigitation between ligand molecules and host molecules. A schematic illustration of this ligand shell deformation is given in figure 4.62.

The silanization step in the synthesis of AuSi particles also influences positively on the stability and miscibility in the nematic host FELIX-2900-03. The additional cross-linking

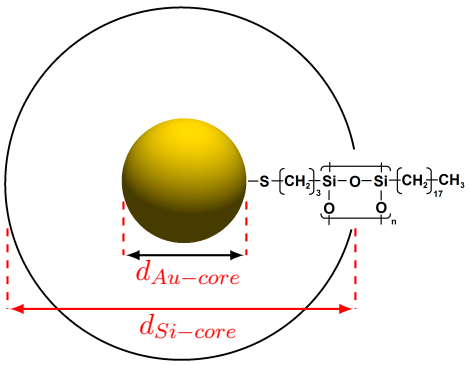

Figure 4.63: Schematic drawing of a silanized AuSi particle with different core and shell diameters. While the curvature of the smaller gold core determines the density of ligands, the outer silanization shell fixes the ligands to the molecules and stabilizes the spatial separation of single coils.

of ligands via Si-O bondings increases the stability of the ligand shell and prevents a loss of ligands or ligand exchange reactions. This gives rise to a high stability also under the influence of electric fields and prevents the decomposition of particles and precipitation onto the substrate's surface as observed for AuCB and AuSH12$_m$ particles. The cross-linking via silanization also influences positively on the ligand density on the particle's surface. As shown in figure 4.63, the silane shell forms a second rigid surface with lower curvature than the gold core. However, the amount of ligands on one particle is determined by the Au-S bondings of ligands onto the smaller core. This leads to a general increase of spatial distance between the aliphatic C_{18}-carbon chain ligands on the silane shell, which promotes the interdigitation with the aliphatic side chains of the FELIX-2900-03 host molecules.

The analysis of switching times of AuSi doped FELIX-2900-03 samples reveals a temperature dependency of nanoparticle induced changes on rise and decay times. Concerning rise times, nanoparticle doping increases the switching speed compared to the pure host only for temperatures far away from the clearing temperature, while they show slower switching speed at higher temperatures. However, clear concentration dependencies could not be identified. Decay times slightly decrease for all doped samples, showing a stronger temperature dependency than the pure nematic host. Again the doped samples show faster switching times than the undoped host especially at low temperatures.

A concentration of approximately 5.0 % (w) AuSi particles presumably represents the upper doping concentration leading to improved electro-optic properties. The optimum concentration for doping the host FELIX-2900-03 with AuSi particles could be identified to be at around 1.0 % (w) of particles. Mixtures containing this amount of nanoparticles show improved stability of the nematic phase as well as superior electro-optical switching behavior.

5 Conclusions and outlook

In this work, the influence of nanoparticle doping on the physical properties of a nematic host was investigated by alignment studies and analysis of electro-optical properties. A measuring setup for the simultaneous measurement of field-induced permittivity and birefringence changes was set up, and the data analysis routine following the Single-Cell method by Wu et al. [69] was developed to yield reliable switching times from transmission measurements. Confocal microscope techniques were used to study the distribution of luminescent quantum dots within nematic dispersions and to clarify the director field distribution in particle induced-disclination lines. Conventional optical polarizing microscopy was used to study phase transition temperatures and the influence of nanoparticles on the alignment of the liquid crystalline host between plain glass slides and in polyimide coated electro-optic test cells.

The dispersions investigated in this work cover metallic gold particles and semiconducting CdSe particles of different diameters up to 5 nm and with different hydrophobic organic functionalizations. The investigated gold particles exhibit thiol-ligands with aliphatic or mesogenic capped spacer chains of different chain length, as well as particles with aliphatic ligands and an additional silanization shell around the gold core. The CdSe particles exhibit aliphatic chains as ligands, bound to the semiconducting core by amino- or acid groups. As host materials, the polar mesogen 5CB and the apolar mesogen FELIX-2900-03 were used to study the interactions of hydrophobic ligands with hosts of different polarity.

The passivation of nanoparticles by organic functionalization was found not to fully prevent agglomeration of particles during the preparation process of nematic dispersions. Additionally, the concentration of particles in the bulk of the nematic material is reduced by particles residing at the interfaces of preparation vial or liquid crystal test cell. In consequence, the actual nanoparticle concentration within a sample is lower than the weighted amount of particles. A study of reproducibility showed that although the precise concentration within the dispersions is unknown, test cells filled with dispersions from the same batch show very good agreement in physical properties, while the physical properties of test cells filled with separately prepared dispersions can slightly differ. In any case, a general concentration trend is maintained, a higher weighted amount of particles leads also to a higher particle concentration in the dispersion.

It was found that the interactions between organic capping and host molecules are crucial for the miscibility and stability of the host. In general, alkylthiol capped gold particles showed higher miscibility and stability in the apolar host FELIX-2900-03 than in 5CB, which is presumably connected to the hydrophobic character of host and ligand shell. A pure mesogenic ligand shell facilitates a tactoidal deformation of the ligand shell, but does not improve the miscibility or stability of dispersions. A comparison with data from literature

showed that the highest miscibility of functionalized nanoparticles in a nematic host can be expected for mixed ligand shells with longer mesogenic ligands and shorter aliphatic ligands. A very high stability was observed for silanized particles with C_{18} ligand chain length, so it can be assumed that also the length of functionalization influences on the interactions between particles and host molecules. An influence of the core material on the stability or physical properties of the dispersion could not be confirmed. No general difference between gold and CdSe particles was found. A possible explanation is the high density of ligands on the surface of the nanoparticles, which prevents a direct interaction between core material and host molecules. Therefore it should be possible to replace the core material without changing the liquid crystalline properties of the dispersion, which can be used to change for example the wavelength regime of plasmon resonances of metallic cores.

The particle size influences the interactions between ligand shell and host molecules due to different surface curvatures. While small core diameters show a high curvature and allow interdigitation between ligands and host molecules, the ligand shell of larger particles shows similarity to a dense monolayer of ligands which prevents interdigitation. However, this effect is not visible for small differences in core diameter, as the particles usually show a comparably broad size distribution. The analysis of magic sized, truly monodisperse CdSe particles did not show an improvement of stability or electro-optic properties. So it can be assumed that a certain size distribution is not a disadvantage for the interaction between particles and host.

On untreated glass, all nanoparticles investigated in this work induce homeotropic alignment, indicating that even a slight surface coverage of hydrophobic coated particles suffices to reduce the surface energy of the glass interface. An insufficient chemical compatibility between ligand shell and nematic host leads to a strong deposition of particles from the bulk onto the substrates and induces homeotropic alignment also in electro-optical test cells by superimposing initial alignment layers for planar alignment. Partial surface coverage was found to induce a tilted alignment of molecules at the interface, which leads to a loss of threshold of the Fréedericksz-transition.

The analysis of nanoparticle-induced birefringent stripe textures in homeotropic surrounding by means of confocal fluorescence polarizing microscopy revealed that the birefringent stripes correspond to twist disclination lines, which form during the phase transition from the isotropic to the nematic phase and can be stabilized by agglomerations of nanoparticles. An accumulation of particles within the stripes as suggested by Qi et al. [12] could neither be confirmed nor negated by confocal fluorescence measurements on luminescent CdSe quantum dots in FELIX-2900-03, so that further research on this question seems necessary.

Results obtained for mesogenic capped gold particles and dodecanethiol capped gold particles in the host 5CB indicate the formation of charged species, which form electric double layers at the interfaces of the electro-optic test cells. This leads to an appearing increase of $\epsilon_\perp$ and $\epsilon_\parallel$ as well as to high threshold voltages for the Fréedericksz-transition. Applying sufficiently high fields induces an irreversible alignment change from homogeneous planar to homeotropic alignment and after long exposure to external fields to an optically isotropic behavior. This is presumably caused by particles being driven and precipitated onto the

initial alignment layer and decomposed under the influence of external electric fields. The origin of charged species has not been successfully enlightened, but is presumably connected to different bonding mechanisms of ligands onto the particle's cores. Another open question is the sign of charges, as the precipitation of particles occurs under DC fields as well as AC fields of a frequency of 1 kHz. The targeted deposition of nanoparticles for the fabrication of a two-dimensional liquid crystal phase grating was not successful due to a lack of control over the deposition process. Certainly the question of charged species in a nanoparticle / liquid crystal dispersion requires additional research, also with respect to possible applications of nanoparticles in electric double-layer capacitors with comparable high energy storage capacitance.

Presumably, the reverse switching modes of alkylthiol capped gold particles in the host FELIX-2900-03 as reported by Qi et al. in reference [62] is also connected to charged dopants in the nematic host. The reverse switching was identified to be an example of electroconvection rolls in a (+,-) material with positive dielectric anisotropy $\Delta\epsilon$ and negative anisotropy of conductivity $\Delta\sigma$. As the nematic host is intrinsically non-conductive, the necessary conductivity as well as the unusual sign of $\Delta\sigma$ are presumably caused by nanoparticle doping.

A clear stabilization of the nematic phase by the presence of nanoparticles was only found for silanized gold particles in the apolar host FELIX-2900-03 at medium concentrations of particles, while the presence of other particles slightly decreases the clearing temperature of the dispersions and leads to a broadening of the biphasic temperature region. According to observations reported in literature, a stabilization of nematic order can be expected especially for anisometrically shaped particles, therefore also for the silanized particles a tactoidal deformation of the ligand shell is assumed.

Evidently, the silanization between ligands is a versatile tool to increase the stability of the ligand shell and to prevent ligand losses and the formation of charged particles by heterolytic breaking of bonds. An additional benefit from the silane conjugation is the lower ligand density on the silane shell, which supports the interdigitation between ligands and host molecules. Dispersions of silanized gold particles in FELIX-2900-03 also showed an improved electro-optical performance due to lower threshold voltages for the Fréedericksz-transition and larger dielectric anisotropies.

Future research therefore should focus on the synthesis and analysis of nanoparticles with stabilized ligand shells, which combine the benefits of mixed ligand shells of mesogenic and aliphatic ligands, the possibility of tactoidal deformation of the ligand shell and a high chemical compatibility with the desired host material. According to the results of this work, these materials are expected to enable overcoming problems in miscibility and stability and lead to new materials with superior electro-optical properties.

Appendix

A. List of symbols

Symbol	Explanation
α	molecular polarizability
β	angle between μ and a nematogen's long axis
δ	phase retardation
Δn	birefringence
Δr_{conf}	lateral resolution in confocal microscopy
Δz_{conf}	axial resolution in confocal microscopy
$\Delta\epsilon$	dielectric anisotropy
$\Delta\sigma$	anisotropy of conductivity
ϵ	permittivity tensor
ϵ_0	permittivity of vacuum
γ	surface tension
γ_1^{eff}	effective rotational viscosity
γ_1	rotational viscosity
κ	inverse Debye length
λ	wavelength
λ_D	Debye length
μ	dipole moment of a molecule
ρ	density
σ	conductivity
τ_{decay}	decay time of the Fréedericksz-transition
τ_{elast}	elastic torque density
τ_{elec}	electrostatic torque density
τ_{rise}	rise time of the Fréedericksz-transition
θ	polar angle
Θ	$\frac{\pi}{2} - \theta$
θ_0	polar angle of the easy direction
φ	azimuthal angle
φ_0	azimuthal angle of the easy direction
$\vec{M}$	transition dipole moment
$\vec{M}_{abs}$	transition dipole moment of absorbtion
$\vec{M}_{em}$	transition dipole moment of emission
ξ_E	field coherence length
ζ	angle between $\vec{M}$ and $\vec{E}$
index $_{\parallel}$	quantity parallel to n

index $_\perp$	quantity perpendicular to n
index $_l$	quantity parallel to the molecule's long axis
index $_t$	quantity perpendicular to the molecule's long axis
a	molecular lengthscale
b	surface extrapolation length
C	capacitance
D	electric displacement field
d	cell gap, thickness of liquid crystal material
E	electric field
E_{pot}	potential mean field energy
E_{Th}	critical field strength for the Fréedericksz-transition
F	Frank-Oseen energy
F_{sur}^{θ}	polar surface energy
F_{sur}^{φ}	azimuthal surface energy
f_{elast}	elastic free energy density
f_{elec}	electric free energy density
f_{sur}	surface anchoring energy density
F_0	Frank-Oseen energy of undistorted liquid crystal
f_0	free energy density of undistorted liquid crystal
I	light intensity
K_{11}	elastic constant of splay deformation
K_{22}	elastic constant of twist deformation
K_{24}	saddle-splay elastic constant
K_{33}	elastic constant of bend deformation
k_B	Boltzmann's constant
L	lengthscale of significant changes in $\mathbf{n}$
M	molar mass
$\mathbf{n}$	nematic director
n	refractive index
N	number of molecules
n_{eff}	effective refractive index
N_A	Avogadro's constant
n_e	extraordinary refractive index
n_o	ordinary refractive index
NA	numerical aperture
P	polarization
Q	charge
q_0	cholesteric pitch length
r_c	critical radius for Ostwald-ripening
S	scalar order parameter
T	temperature
T_{NI}	clearing temperature
U	potential difference
U_{bulk}	energy of nematic bulk interactions

V_m	molar volume
$V_{m,NI}$	molar volume at $T = T_{NI}$
V_{Th}	threshold voltage for the Fréedericksz-transition
v_p	normalized pinhole diameter
W^{θ}_{anchor}	polar part of the anchoring energy
W^{φ}_{anchor}	azimuthal part of the anchoring energy
W_{anchor}	anchoring energy

B. List of abbreviations

Symbol	Explanation
5CB	4-n-pentyl-4'-cyanobiphenyl
BTBP	n,n'-bis(2,5-di-tert-butylphenyl)-3,4,9,10-perylendicaboximid
DCM	Dichloromethane
DSC	Differential scanning calorimetry
FCM	Fluorescence confocal microscopy
FCPM	Fluorescence confocal polarizing microscopy
FELIX-2900-03	5-n-heptyl-2-(octyloxy-phenyl)pyrimidine
FWHM	Full width at half maximum
ITO	Indium tin oxide
POM	Polarizing optical microscopy

C. Molecular structures of nematic hosts and dichroic dye

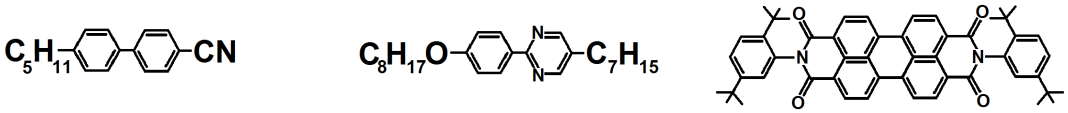

5CB **FELIX-2900-03** **BTBP**

Figure 5.1: Molecular structures of the two nematic hosts 5CB (left) and FELIX-2900-03 (middle) and the dichroic dye BTBP (right) used in this work.

D. Contributions in peer reviewed journals

J. Mirzaei, M. Urbanski, H.-S. Kitzerow and T. Hegmann, "Hydrophobic gold nanoparticles via silane conjugation - chemically and thermally robust nanoparticles as dopants for nematic liquid crystals", *Phil. Trans. R. Soc. A*, **371**, (2013) (10.1098/rsta.2012.0256).

J. Mirzaei, R. Sawatzky, A. Sharma, M. Urbanski, K. Yu, H.-S. Kitzerow and T. Hegmann, "New developments in nanoparticle-liquid crystal composites: from magic-sized semiconductor nanoclusters to alignment pattern formation via nanoparticle stenciling", *Proc. SPIE*, **8279**, 827983, (2012).

J. Mirzaei, M. Urbanski, H.-S. Kitzerow and T. Hegmann, "Nanocomposites of a nematic liquid crystal doped with magic-sized CdSe nanocrystals as nanoscale additives", *J. Mater. Chem.*, **21**, 12710-12716, (2011).

M. Urbanski, K. A. Piegdon, C. Meier and H.-S. Kitzerow, "Investigations on the director field around microdisc resonators", *Liquid Crystals*, **38**, 4, 475-482, (2011).

M. Urbanski, B. Kinkead, T. Hegmann and H.-S. Kitzerow, "Director field of birefringent stripes in liquid crystal / nanoparticle dispersions", *Liquid Crystals*, **37**, 9, 1151-1156, (2010).

M. Urbanski, B. Kinkead, H. Qi, T. Hegmann and H.-S. Kitzerow, "Electroconvection in nematic liquid crystals via nanoparticle doping", *Nanoscale*, **2**, 7, 1118-1121, (2010).

K. A. Piegdon, S. Declair, J. Förstner, T. Meier, H. Matthias, M. Urbanski, H.-S. Kitzerow, D. Reuter, A. D. Wieck, A. Lorke and C. Meier, "Tuning quantum-dot based photonic devices with liquid crystals", *Opt. Express*, **18**, 8, 7946-7954, (2010).

K. A. Piegdon, M. Offer, A. Lorke, M. Urbanski, A. Hoischen, H.-S. Kitzerow, S. Declair, J. Förstner, T. Meier, D. Reuter, A. D. Wieck and C. Meier, "Self-assembled quantum dots in a liquid-crystal-tunable microdisk resonator", *Physica E*, **42**, 10, 2552-2555, (2010).

B. Kinkead, M. Urbanski, H. Qi, H.-S. Kitzerow and T. Hegmann, "Alignment and electro-optic effects in nanoparticle-doped nematic liquid crystals", *Proc. SPIE*, **7775**, 77750C-1 - 77750C-11, (2010).

C. Conference contributions

E1. Oral contributions

(Presenting author underlined)
M. Urbanski and H.-S. Kitzerow, "Prospects of Nanostructures and Nanocomposites with Liquid Crystals", Young Scientist Forum, BIT's 2nd Annual World Congress of Nanoscience and Nanotechnology, Qingdao, PR China (October 26-28 2012), invited talk.

M. Urbanski, B. Kinkead, T. Hegmann, M. Draper, J. W. Goodby and H.-S. Kitzerow, "Investigations on nematic liquid crystals / gold nanoparticle dispersions", 5th Convention of the DFG Graduate Program 1464, Paderborn (July 05-06 2011).

M. Urbanski and H.-S. Kitzerow, "Microdisk resonators embedded in nematic liquid crystals: Investigations on the director field", 4th Convention of the DFG Graduate Program 1464, Darmstadt (November 18-19 2010).

H.-S. Kitzerow, K. Piegdon, H. Matthias, A. Hoischen, M. Urbanski and C. Meier, "Photoluminescent microresonators embedded in liquid crystals", 37th Topical Meeting on Liquid Crystals, Stuttgart (April 1-3 2009).

E2. Poster contributions

(Presenting author underlined)
M. Urbanski, M. Draper, J. W. Goodby, J. Mirzaei, T. Hegmann and H.-S. Kitzerow, "Effects of functionalization of gold nanoparticles dispersed in liquid crystals", 24th International Liquid Crystal Conference, Mainz (August 19-24 2012).

J. Mirzaei, M. Urbanski, H.-S. Kitzerow and T. Hegmann, "Nanocomposites of N-LCs with Silanized Gold Nanoparticles", 24th International Liquid Crystal Conference, Mainz (August 19-24 2012).

M. Urbanski, M. Wahle, A. Lorenz, C. Meier and H.-S. Kitzerow, "Tunable Photonic Structures using Liquid Crystals", 1st Europhotonics Spring School, Barcelona, Spain (March 25-31 2012).

M. Urbanski, K. A. Piegdon, C. Meier and H.-S. Kitzerow, "Microscopic study of the Fréedericksz transition in a liquid crystal embedding a microdisk resonator", 39th Topical Meeting on Liquid Crystals, Hamburg (March 30- April 1st 2010).

M. Urbanski, B. Kinkead, H. Qi, T. Hegmann and H.-S. Kitzerow, "Nanoparticle doping leads to electroconvection in nematic liquid crystals", 23rd International Liquid Crystal Conference, Krakow, Poland (July 11-16 2010).

M. Urbanski, B. Kinkead, T. Hegmann and H.-S. Kitzerow, "Fluorescence confocal polarizing microscopy studies on liquid crystal / nanoparticle dispersions", 38th Topical Meeting on Liquid Crystals, Mainz (March 10-12 2010).

Bibliography

[1] F. Reinitzer. Beiträge zur kenntniss des cholesterins. *Monatshefte für Chemie (Monatshefte für Chemie)*, 9(1):421–441, 1888.

[2] O. Lehmann. Über fliessende kristalle. *Zeitschrift für Physikalische Chemie*, 4:462–472, 1889.

[3] T. Sluckin, D. Dunmur, and H. Stegemeyer. *Crystals that flow: Collected papers from the history of liquid crystals*. Taylor & Francis, London, 2003.

[4] W. Helfrich and M. Schadt. Lichtsteuerzelle, 1972.

[5] E. Ouskova, O. Buchnev, V. Reshetnyak, Y. Reznikov, and H. Kresse. Dielectric relaxation spectroscopy of a nematic liquid crystal doped with ferroelectric sn 2 p 2 s 6 nanoparticles. *Liquid Crystals*, 30(10):1235–1239, 2003.

[6] F. Li, O. Buchnev, C. Cheon, A. Glushchenko, V. Reshetnyak, Y. Reznikov, T. Sluckin, and J. West. Orientational coupling amplification in ferroelectric nematic colloids. *Physical Review Letters*, 97(14), 2006.

[7] J. Rault, P. E. Cladis, and J.P Burger. Ferronematics. *Physics Letters A*, 32(3):199–200, 1970.

[8] C. F. Hayes. Magnetic platelets in a nematic liquid crystal. *Molecular Crystals and Liquid Crystals*, 36(3-4):245–253, 1976.

[9] B. Liang and S.-H Chen. Electric-field-induced molecular reorientation of a magnetically biased ferronematic liquid-crystal film. *Physical Review A*, 39(3):1441–1446, 1989.

[10] I. Dierking, G. Scalia, and P. Morales. Liquid crystal–carbon nanotube dispersions. *Journal of Applied Physics*, 97(4):044309, 2005.

[11] S. Y. Jeon, S. H. Shin, S. J. Jeong, S. H. Lee, S. H. Jeong, Y. H. Lee, H. C. Choi, and K. J. Kim. Effects of carbon nanotubes on electro-optical characteristics of liquid crystal cell driven by in-plane field. *Applied Physics Letters*, 90(12):121901, 2007.

[12] H. Qi and T. Hegmann. Formation of periodic stripe patterns in nematic liquid crystals doped with functionalized gold nanoparticles. *Journal of Materials Chemistry*, 16(43):4197, 2006.

[13] B. Kinkead and T. Hegmann. Effects of size, capping agent, and concentration of cdse and cdte quantum dots doped into a nematic liquid crystal on the optical and electro-optic properties of the final colloidal liquid crystal mixture. *Journal of Materials Chemistry*, 20(3):448, 2009.

[14] M. Draper, I. M. Saez, S. J. Cowling, P. Gai, B. Heinrich, B. Donnio, D. Guillon, and J. W. Goodby. Self-assembly and shape morphology of liquid crystalline gold metamaterials. *Advanced Functional Materials*, 21(7):1260–1278, 2011.

[15] E. B. Kim, O. Guzman, S. Grollau, N. L. Abbott, and J. J. de Pablo. Interactions between spherical colloids mediated by a liquid crystal: A molecular simulation and mesoscale study. *The Journal of Chemical Physics*, 121(4):1949, 2004.

[16] P. J. Collings. *Liquid crystals: Nature's delicate phase of matter*. Princeton University Press, Princeton and N.J, 2 edition, 2002.

[17] P.-G de Gennes. *The physics of liquid crystals*. Clarendon Press, Oxford [Eng.], 1974.

[18] A. Saupe. Recent results in the field of liquid crystals. *Angewandte Chemie International Edition in English*, 7(2):97–112, 1968.

[19] W. Martienssen, O. Madelung, K.-H Hellwege, and S. Pestov. *Landolt-Börnstein - Group VIII Advanced Materials and Technologies*, volume 5. Springer Berlin Heidelberg, Berlin and Heidelberg, 2003.

[20] F. C. Frank. On the theory of liquid crystals. *Discussions of the Faraday Society*, 25:19, 1958.

[21] C. W. Oseen. The theory of liquid crystals. *Transactions of the Faraday Society*, 29(140):883, 1933.

[22] P. Yeh and C. Gu. *Optics of liquid crystal displays*. Wiley, Hoboken and N.J, 2 edition, 2010.

[23] H. Stegemeyer. *Liquid crystals*. Steinkopff and Springer, Darmstadt and New York, 1994.

[24] L. M. Blinov and V. G. Chigrinov. *Electrooptic effects in liquid crystal materials*. Springer, New York, 1996.

[25] W. Urbach. Alignment of nematics and smectics on evaporated films. *Applied Physics Letters*, 25(9):479, 1974.

[26] D. Berreman. Solid surface shape and the alignment of an adjacent nematic liquid crystal. *Physical Review Letters*, 28(26):1683–1686, 1972.

[27] D. Demus, J. W. Goodby, and G. W. Gray. *Handbook of liquid crystals*. Wiley-VCH, Weinheim and and New York and and Chichester, 1998.

[28] L. Onsager. Electric moments of molecules in liquids. *Journal of the American Chemical Society*, 58(8):1486–1493, 1936.

[29] V. Fredericksz and V. Zolina. Forces causing the orientation of an anisotropic liquid. *Transactions of the Faraday Society*, 29(140):919, 1933.

[30] D. Demus. *Physical properties of liquid crystals*. Wiley-VCH, Weinheim and and New York, 1999.

[31] H.-J Butt, K. Graf, and M. Kappl. *Physics and chemistry of interfaces*. Wiley-VCH, Weinheim, 2 edition, 2006.

[32] D. Demus, J. W. Goodby, G. W. Gray, H.-W Spiess, and V. Vill. *Handbook of Liquid Crystals Set*. Wiley-VCH Verlag GmbH, Weinheim and Germany, 1998.

[33] W. H. Jeu. *Physical properties of liquid cristalline materials*. Gordon and Breach Science Publishers, New York and and London and and Paris, 1980.

[34] D. Krüerke. *Experimentelle Untersuchungen nematischer und cholesterischer Phasen diskotischer Flüssigkristalle*. Mensch-und-Buch-Verl, Berlin, 1999.

[35] F. Brochard. Backflow effects in nematic liquid crystals. *Molecular Crystals and Liquid Crystals*, 23(1-2):51–58, 1973.

[36] T. C. Lubensky, D. Pettey, and N. Currier. Topological defects and interactions in nematic emulsions. *Physical Review E*, 57(1):610–625, 1998.

[37] P. Poulin, H. Stark, T. C. Lubensky, and D. A. Weitz. Novel colloidal interactions in anisotropic fluids. *Science*, 275(5307):1770–1773, 1997.

[38] J.-I Fukuda, M. Yoneya, and H. Yokoyama. Nematic liquid crystal around a spherical particle: Investigation of the defect structure and its stability using adaptive mesh refinement. *The European Physical Journal E - Soft Matter*, 13(1):87–98, 2004.

[39] H. Matthias and H.-S Kitzerow. Director fields around spherical and cylindrical micro particles in a liquid crystal host. *Molecular Crystals and Liquid Crystals*, 508(1):127–136, 2009.

[40] M. Tasinkevych, N. M. Silvestre, and M. M. Telo da Gama. Liquid crystals boojum-colloids. *Soft Condensed Matter*, 2012.

[41] M. Urbanski, K. A. Piegdon, C. Meier, and H.-S Kitzerow. Investigations on the director field around microdisc resonators. *Liquid Crystals*, 38(4):475–482, 2011.

[42] M. Ravnik, M. Skarabot, S. Zumer, U. Tkalec, I. Poberaj, D. Babic, N. Osterman, and I. Musevic. Entangled nematic colloidal dimers and wires. *Physical Review Letters*, 99(24), 2007.

[43] D. Voloschenko, O. Pishnyak, S. Shiyanovskii, and O. D. Lavrentovich. Effect of director distortions on morphologies of phase separation in liquid crystals. *Physical Review E*, 65(6), 2002.

[44] J. West, A. Glushchenko, G. Liao, Y. Reznikov, D. Andrienko, and M. Allen. Drag on particles in a nematic suspension by a moving nematic-isotropic interface. *Physical Review E*, 66(1), 2002.

[45] C. Bréchignac, P. Houdy, and M. Lahmani. *Nanomaterials and nanochemistry*. Springer, Berlin and and New York, 2007.

[46] J. Kolny. *Elektrostatische Wechselwirkung zwischen positiv und negativ geladenen Nanoteilchen und deren Aggregationsverhalten*. PhD thesis, University of Hamburg, Hamburg, 2002.

[47] L. Cseh and G. H. Mehl. Structure-property relationships in nematic gold nanoparticles. *Journal of Materials Chemistry*, 17(4):311, 2007.

[48] M. Wojcik, W. Lewandowski, J. Matraszek, J. Mieczkowski, J. Borysiuk, D. Pociecha, and E. Gorecka. Liquid-crystalline phases made of gold nanoparticles. *Angewandte Chemie International Edition*, 48(28):5167–5169, 2009.

[49] M. Draper. *Golden Liquid Crystal Nanoparticles*. PhD thesis, University of York, York, 2009.

[50] M. Minsky. Memoir on inventing the confocal scanning microscope. *Scanning*, 10(4):128–138, 1988.

[51] M. Minsky. Microscopy apparatus, 1975.

[52] J. K. Stevens, L. R. Mills, and J. E. Trogadis. *Three-dimensional confocal microscopy: Volume investigation of biological specimens*. Academic Press, San Diego, 1994.

[53] C. E. Bigelow. *Biological Applications of Confocal Flourescence Polarization Microscopy*. PhD thesis, University of Rochester, Rochester, 2005.

[54] O. Hollricher and W. Ibach. *High Resolution Optical Microscopy*. WITec, 2002.

[55] O. D. Lavrentovich. Fluorescence confocal polarizing microscopy: three-dimensional imaging of the director. *Pramana - Journal of Physics*, 61(2):373–383, 2003.

[56] M. Brust, M. Walker, D. Bethell, D. J. Schiffrin, and R. Whyman. Synthesis of thiol-derivatised gold nanoparticles in a two-phase liquid / liquid system. *Journal of the Chemical Society, Chemical Communications*, page 801, 1994.

[57] J. Milette, V. Toader, L. Reven, and R. B. Lennox. Tuning the miscibility of gold nanoparticles dispersed in liquid crystals via the thiol-for-dmap reaction. *Journal of Materials Chemistry*, 21(25):9043, 2011.

[58] M. Wojcik, M. Kolpaczynsky, D. Pociecha, J. Mieczkowski, and E. Gorecka. Multidimensional structures made by gold nanoparticles with shape-adaptive grafting layers. *Soft Matter*, 6(21):5397, 2010.

[59] M. Urbanski, B. Kinkead, T. Hegmann, and H.-S Kitzerow. Director field of birefringent stripes in liquid crystal/nanoparticle dispersions. *Liquid Crystals*, 37(9):1151–1156, 2010.

[60] M. Urbanski, B. Kinkead, H. Qi, T. Hegmann, and H.-S Kitzerow. Electroconvection in nematic liquid crystals via nanoparticle doping. *Nanoscale*, 2(7):1118, 2010.

[61] J. Mirzaei, M. Urbanski, H.-S Kitzerow, and T. Hegmann. Hydrophobic gold nanoparticles via silane conjugation - chemically and thermally robust nanoparticles as dopants for nematic liquid crystals. *Phil. Trans. R. Soc. A*, 371, 2013.

[62] H. Qi, B. Kinkead, and T. Hegmann. Unprecedented dual alignment mode and freedericksz transition in planar nematic liquid crystal cells doped with gold nanoclusters. *Advanced Functional Materials*, 18(2):212–221, 2008.

[63] W. W. Weare, S. M. Reed, M. G. Warner, and J. E. Hutchison. Improved synthesis of small phosphine-stabilized gold nanoparticles. *Journal of the American Chemical Society*, 122(51):12890–12891, 2000.

[64] J. Mirzaei, M. Reznikov, and T. Hegmann. Quantum dots as liquid crystal dopants. *Journal of Materials Chemistry*, 2012.

[65] J. Mirzaei, M. Urbanski, Kui Yu, H.-S Kitzerow, and T. Hegmann. Nanocomposites of a nematic liquid crystal doped with magic-sized cdse quantum dots. *Journal of Materials Chemistry*, 21(34):12710, 2011.

[66] Y. Q. Wang, W. S. Liang, and C. Y. Geng. Coalescence behavior of gold nanoparticles. *Nanoscale Research Letters*, 4(7):684–688, 2009.

[67] W. Demtröder. *Elektrizität und Optik*. Springer, Berlin, 4 edition, 2006.

[68] S. V. Shiyanovskii, M. Gu, and O. D. Lavrentovich. Liquid crystal device and method thereof, 2009.

[69] S.-T Wu, D. Coates, and E. Bartmann. Physical properties of chlorinated liquid crystals. *Liquid Crystals*, 10(5):635–646, 1991.

[70] S.-T Wu and C.-S Wu. Experimental confirmation of the osipov-terentjev theory on the viscosity of nematic liquid crystals. *Physical Review A*, 42(4):2219–2227, 1990.

[71] M. G. Clark, E. P. Raynes, R. A. Smith, and R. J. A. Tough. Measurement of the permittivity of nematic liquid crystals in magnetic and electric fields using extrapolation procedures. *Journal of Physics D: Applied Physics*, 13(11):2151–2164, 1980.

[72] K. R. Welford and J. R. Sambles. Analysis of electric field induced deformations in a nematic liquid crystal for any applied field. *Molecular Crystals and Liquid Crystals*, 147(1):25–42, 1987.

[73] R. T. Klingbiel, D. J. Genova, and H. K. Bücher. The temperature dependence of the dielectric and conductivity anisotropies of several liquid crystalline materials. *Molecular Crystals and Liquid Crystals*, 27(1-2):1–21, 1974.

[74] F. V. Podgornov, A. V. Ryzhkova, and W. Haase. Influence of gold nanorods size on electro-optical and dielectric properties of ferroelectric liquid crystals. *Applied Physics Letters*, 97(21):212903, 2010.

[75] K. K. Vardanyan, R. D. Walton, and D. M. Bubb. Liquid crystal composites with a high percentage of gold nanoparticles. *Liquid Crystals*, 38(10):1279–1287, 2011.

[76] G. A. Oweimreen and D. E. Martire. The effect of quasispherical and chainlike solutes on the nematic to isotropic phase transition in liquid crystals. *The Journal of Chemical Physics*, 72(4):2500, 1980.

[77] B. Ullrich, G. K. Auernhammer, E. M. Sam, and D. Vollmer. Tracer colloids close to an isotropic–nematic domain interface with phase transition-induced solute transport. *Colloids and Surfaces A: Physicochemical and Engineering Aspects*, 354(1-3):298–307, 2010.

[78] H. Qi, B. Kinkead, V. M. Marx, H. R. Zhang, and T. Hegmann. Miscibility and alignment effects of mixed monolayer cyanobiphenyl liquid-crystal-capped gold nanoparticles in nematic cyanobiphenyl liquid crystal hosts. *ChemPhysChem*, 10(8):1211–1218, 2009.

[79] D. E. Martire. The effect of quasispherical solutes on the nematic to isotropic transition in liquid crystals. *The Journal of Chemical Physics*, 64(4):1456, 1976.

[80] H. Duran, B. Gazdecki, A. Yamashita, and T. Kyu. Effect of carbon nanotubes on phase transitions of nematic liquid crystals. *Liquid Crystals*, 32(7):815–821, 2005.

[81] L. Lopatina and J. Selinger. Theory of ferroelectric nanoparticles in nematic liquid crystals. *Physical Review Letters*, 102(19), 2009.

[82] S. Khatua, P. Manna, W.-S Chang, A. Tcherniak, E. Friedlander, E. R. Zubarev, and S. Link. Plasmonic nanoparticles−liquid crystal composites †. *The Journal of Physical Chemistry C*, 114(16):7251–7257, 2010.

[83] K. K. Vardanyan, Ethan D. Palazzo, and Robert D. Walton. Nematic nanocomposites with enhanced optical birefringence. *Liquid Crystals*, 38(6):709–715, 2011.

[84] T. Bezrodna, I. Chashechnikova, T. Gavrilko, G. Puchkovska, Y. Shaydyuk, A. Tolochko, J. Baran, and M. Drozd. Structure formation and its influence on thermodynamic and optical properties of montmorillonite organoclay–5cb liquid crystal nanocomposites. *Liquid Crystals*, 35(3):265–274, 2008.

[85] E. R. Soulé, J. Milette, L. Reven, and A. D. Rey. Phase equilibrium and structure formation in gold nanoparticles—nematic liquid crystal composites: experiments and theory. *Soft Matter*, 8(10):2860, 2012.

[86] C. Da Cruz, O. Sandre, and V. Cabuil. Phase behavior of nanoparticles in a thermotropic liquid crystal. *The Journal of Physical Chemistry B*, 109(30):14292–14299, 2005.

[87] D. Coursault, J. Grand, B. Zappone, H. Ayeb, G. Lévi, N. Félidj, and E. Lacaze. Linear self-assembly of nanoparticles within liquid crystal defect arrays. *Advanced Materials*, 24(11):1461–1465, 2012.

[88] R. Bitar, G. Agez, and M. Mitov. Cholesteric liquid crystal self-organization of gold nanoparticles. *Soft Matter*, 7(18):8198, 2011.

[89] H.-S Kitzerow, P.P Crooker, S.L Kwok, and G. Heppke. A blue phase with negative dielectric anisotropy in an electric field. statics and dynamics. *Journal de Physique*, 51(12):1303–1312, 1990.

[90] J. Turkevich. Colloidal gold. part ii. *Gold Bulletin*, 18(4):125–132, 1985.

[91] J. C. Love, L. A. Estroff, J. K. Kriebel, R. G. Nuzzo, and G. M. Whitesides. Self-assembled monolayers of thiolates on metals as a form of nanotechnology. *Chemical Reviews*, 105(4):1103–1170, 2005.

[92] R. G. Nuzzo, B. R. Zegarski, and L. H. Dubois. Fundamental studies of the chemisorption of organosulfur compounds on gold(111). implications for molecular self-assembly on gold surfaces. *Journal of the American Chemical Society*, 109(3):733–740, 1987.

[93] J. K. Cooper, A. M. Franco, S. Gul, C. Corrado, and J. Z. Zhang. Characterization of primary amine capped cdse, znse, and zns quantum dots by ft-ir: Determination of surface bonding interaction and identification of selective desorption. *Langmuir*, 27(13):8486–8493, 2011.

[94] G. A. Jeffrey. *An introduction to hydrogen bonding*. Oxford University Press, New York, 1997.

[95] N. R. Jana, C. Earhart, and J. Y. Ying. Synthesis of water-soluble and functionalized nanoparticles by silica coating. *Chemistry of Materials*, 19(21):5074–5082, 2007.

[96] N. R. Jana and X. Peng. Single-phase and gram-scale routes toward nearly monodisperse au and other noble metal nanocrystals. *Journal of the American Chemical Society*, 125(47):14280–14281, 2003.

[97] L. Gu. High-spatial-frequency liquid crystal phase gratings with double-sided striped electrodes. In L.-C Chien, editor, *Proceedings of SPIE*, pages 180–189. SPIE, 2005.

[98] R. A. Kashnow and J. E. Bigelow. Diffraction from a liquid crystal phase grating. *Applied Optics*, 12(10):2302, 1973.

[99] Orsay Liquid Crystal Group. Hydrodynamic instabilities in nematic liquids under ac electric fields. *Physical Review Letters*, 25(24):1642–1643, 1970.

[100] D. P. Resler, D. S. Hobbs, R. C. Sharp, L. J. Friedman, and T. A. Dorschner. High-efficiency liquid-crystal optical phased-array beam steering. *Optics Letters*, 21(9):689, 1996.

[101] H. Sakata and M. Nishimura. Switchable zero-order diffraction filters using fine-pitch phase gratings filled with liquid crystals. *Japanese Journal of Applied Physics*, 39(Part 1, No. 3B):1516–1521, 2000.

[102] J.-H Park, C.-J Yu, J. Kim, S.-Y Chung, and S.-D Lee. Concept of a liquid-crystal polarization beamsplitter based on binary phase gratings. *Applied Physics Letters*, 83(10):1918, 2003.

[103] C. Yu, J.-H Park, J. Kim, M.-S Jung, and S.-D Lee. Design of binary diffraction gratings of liquid crystals in a linearly graded phase model. *Applied Optics*, 43(9):1783, 2004.

[104] B. Apter, U. Efron, and E. Bahat-Treidel. On the fringing-field effect in liquid-crystal beam-steering devices. *Applied Optics*, 43(1):11, 2004.

[105] U. Schnabel, C.-H Fischer, and E. Kenndler. Characterization of colloidal gold nanoparticles according to size by capillary zone electrophoresis. *Journal of Microcolumn Separations*, 9(7):529–534, 1997.

[106] A. Buka, B. Dressel, W. Otowski, K. Camara, T. Toth-Katona, L. Kramer, J. Lindau, G. Pelzl, and W. Pesch. Electroconvection in nematic liquid crystals with positive dielectric and negative conductivity anisotropy. *Physical Review E*, 66(5), 2002.

[107] A. Buka, B. Dressel, L. Kramer, and W. Pesch. Direct transition to electroconvection in a homeotropic nematic liquid crystal. *Chaos: An Interdisciplinary Journal of Nonlinear Science*, 14(3):793, 2004.

[108] A. Buka, B. Dressel, L. Kramer, and W. Pesch. Isotropic convection scenarios in an anisotropic fluid. *Physical Review Letters*, 93(4), 2004.

[109] O. Kurochkin, H. Atkuri, O. Buchnev, A. Glushchenko, O. Grabar, R. Karapinar, V. Reshetnyak, V. West, and Y. Reznikov. Nano-colloids of sn2p2s6 in nematic liquid crystal pentyl-cianobiphenile. *Condensed Matter Physics*, 13(3):33701, 2010.

[110] G. Barbero, F. C. M. Freire, C. Vena, and C. Versace. Dielectric characterization of doped m5. *The Journal of Physical Chemistry B*, 112(35):11049–11053, 2008.

[111] O. Stern. Zur theorie der elektrischen doppelschicht. *Zeitschrift für Elektrochemie und Angewandte Physikalische Chemie*, 30:508–516, 1924.

[112] H.-J Butt and M. Kappl. *Surface and Interfacial Forces*. Wiley-VCH Verlag GmbH & Co. KGaA, Weinheim and Germany, 2010.

[113] R. Kötz and M. Carlen. Principles and applications of electrochemical capacitors. *Electrochimica Acta*, 45:2483–2498, 2000.

[114] X. Mang, X. Zeng, B. Tang, F. Liu, G. Ungar, R. Zhang, L. Cseh, and G. H. Mehl. Control of anisotropic self-assembly of gold nanoparticles coated with mesogens. *Journal of Materials Chemistry*, 22(22):11101, 2012.